Chemical and optical properties of particulate pollution in the Lille area, Northern France based on ATOLL observations

Alejandra Velazquez Garcia

N° d'ordre : 2023MTLD0001

THÈSE

présentée en vue d'obtenir le grade de

DOCTEURE

en

Discipline : Sciences de la terre et de l'univers, espace

Spécialité : Terre, enveloppes fluides

par

Alejandra VELAZQUEZ GARCIA

Doctorat de l´Université de Lille délivré par IMT Nord Europe

« Chemical and optical properties of particulate pollution in the Lille area, Northern France based on ATOLL observations»

Soutenue le 14 mars 2023 devant le jury d'examen :

Rapporteur	LEON Jean-François	CR HDR, CNRS Laboratoire d'Aérologie
Rapporteur	POULAIN Laurent	Chercheur senior, TROPOS
Examinatrice	FRENEY Evelyn	CR, UMR6016 – OPGC -LaMP
Examinateur	FLAMENT Pascal	PR, LPCA ULCO
Directrice de Thèse	RIFFAULT Véronique	PR, CERI EE IMT Nord Europe
Co-Directrice de Thèse	CHIAPELLO Isabelle	CR HDR, CNRS LOA
Invitée, encadrante	CRUMEYROLLE Suzanne	MCF, LOA ULille
Invité, encadrant	FERREIRA DE BRITO Joel	MA, CERI EE IMT Nord Europe

Laboratoires d'accueil : Centre Energie et Environnement (CERI EE), IMT Nord Europe

Laboratoire d'Optique Atmosphérique (LOA), CNRS UMR 8518 Université de Lille

École doctorale Sciences de la Matière, du Rayonnement et de l'Environnement (ED - SMRE)

(Université de Lille, Centrale Lille, IMT Nord Europe)

Abstract

The link between fine aerosol optical properties and their chemical composition is not yet well understood, and was investigated using long-term in situ observations performed at the "ATmospheric Observations in liLLe" platform from 2016 to 2020 using a combination of aerosol mass spectrometer, aethalometer, and nephelometer. Highly absorbing aerosols and a marked seasonality of the mass contribution of ammonium nitrate (AN) in spring were observed. We evidence that AN (35%) and carbonaceous aerosols (51%) are predominant regarding light extinction at 525 nm. Besides, a novel approach combining these in situ measurements to backtrajectories and emission inventories identifies a Brown Carbon (BrC) decrease within 24 hours after emission even during wintertime, pointing at a likely systematic underestimation of the contribution of residential heating (identified by the presence of BrC) to the aerosol absorption in the region.

Keywords

Atmospheric pollution, climate impact, in situ observations, PM_1, extinction coefficient, aerosol origins

Résumé

Le lien entre les propriétés optiques des aérosols fins et leur composition chimique n'est pas encore bien compris. Il a été étudié ici en utilisant des mesures in situ (spectromètre de masse d'aérosol, aethalomètre et néphélomètre) réalisées sur la plateforme 'ATmospheric Observations in liLLe' de 2016 à 2020. On a pu observer des aérosols très absorbants et une saisonnalité marquée pour la contribution massique du nitrate d'ammonium (AN) au printemps. Nous avons montré que l'AN (35%) et les aérosols carbonés (51%) prédominent dans l'extinction du rayonnement à 525 nm. Enfin, une nouvelle approche combinant ces mesures in situ à des rétrotrajectoires, et des inventaires d'émissions ont révélé une diminution du carbone brun (BrC) dans les 24 heures suivant son émission, même en hiver, ce qui implique une probable sous-estimation systématique de la contribution attribuée au chauffage résidentiel (lié à la présence de BrC) dans l'absorption des aérosols de la région.

Mots clés

Pollution atmosphérique, impact sur le climat, observation in situ, PM_1, extinction du rayonnement, origines des aérosols

Acknowledgments

This study was carried out in collaboration between the Laboratory of Atmospheric Optics (LOA) of the University of Lille and the Centre for Energy and Environment of IMT Nord Europe. Thus, I would like to thank both laboratories and, permanent members (laboratory directors, professors, technicians, engineers, and secretaries, among others) for welcoming me during the period of work during the elaboration of my thesis. Likewise, I would like to thank the funders of my doctorate project: The Regional Council “Hauts-de-France” and the CONACYT Mexican grant (2019-000004-01EXTF-00001).

I sincerely thank the members of the jury for agreeing to examine this work, and for the time they devoted to read this manuscript.

Words cannot express my gratitude towards my supervisors, Joel, Suzanne, Véronique, and Isabelle for their continuous support during this process and most importantly, for the patience they had whenever my knowledge gaps appeared during my Ph.D. I feel really honored and lucky to have you all as supervisors, for the quality of your supervision, for sharing your amazing knowledge, and for your rigor in science.

To my family, especially my parents and brother, as they persuaded me to be a doctor in science and, they supported me no matter what the circumstances of the situation. To my dearest partner, for his motivation, patience, and support in the process to be here and obtain my Ph.D. degree.

Throughout this work, I had the immense pleasure of meeting and rubbing shoulders with doctoral and post-doctoral students from all walks of life. I would like to thank them all for their friendliness and for the richness of the resulting exchanges, especially those who became my closest friends.

Last but not least, I would like to thank all my friends in Mexico who always have been supportive in the distance. To my Mexican professors who induced me to the air pollution, meteorology, mathematics, and earth science during my engineering degree, and, to my British supervisor during my engineering internship, who impulse to do my Ph.D. abroad.

I cannot thank all of you enough for helping me get here.

Index

Glossary

AE – Ångstrom Exponent

AAE – Absorption Ångstrom Exponent

AN – Ammonium nitrate

AOD – Aerosol Optical Depth

AS – Ammonium sulfate

ATOLL – Atmospheric Observation in liLLe platform

AQG – Air Quality Guidelines

BB – Biomass Burning

BBOA - Biomass Burning Organic Aerosol

BLH – Boundary Layer Height

BVOC – Biogenic Volatile Organic Compounds

BrC – Brown Carbon

BC_{ff} – Black Carbon from fossil fuel

BC_{wb} – Black Carbon from wood burning

COA – Cooking-like Organic Aerosol

CCOA – Coal Combustion Organic Aerosol

EC – Elemental Carbon

EAE – Extinction Ångstrom Exponent

eBC – Equivalent Black Carbon

HdF – Hauts-de-France

HOA – Hydrocarbon-like Organic Aerosol

LOOA – Less-Oxygenated Organic Aerosol

MAC – Mass Absorption Cross-section

MAE – Mass Absorption Efficiency

MEE – Mass Extinction Efficiency

MOOA – More-Oxygenated Organic Aerosol

MSE – Mass Scattering Efficiency

NMVOC – Non-Methane Volatile Organic Compounds

NR-PM_1 – Non-refractory submicron aerosol

OA – Organic Aerosol

OC – Organic Carbon

OOA – Oxygenated Organic Aerosol

PHA – Polycyclic Aromatic Hydrocarbons

PM_{10} – Particulate Matter of aerodynamic diameter ≤ 10 µm

$PM_{2.5}$ – Particulate Matter of aerodynamic diameter ≤ 2.5 µm

PM_1 – Particulate Matter of aerodynamic diameter ≤ 1 µm

PMF – Positive Matrix Factorization

POA – Primary Organic Aerosol

RF – Radiative Forcing

SAE – Scattering Ångstrom Exponent

SIA – Secondary Inorganic Aerosols

SLCFs – Short-lived climate forcers

SOA – Secondary Organic Aerosols

SSA – Single Scattering Albedo

VAM – Volume Aerosol Mixing

VOCs – Volatile Organic Compounds

WHO – World Health Organization

Introduction

Aerosol particles (sulfate, nitrate, ammonium, carbonaceous aerosols, mineral dust, and sea spray, etc.), also called particulate matter (PM), and chemically reactive gases (methane, ozone halogenated compounds, nitrogen oxides, carbon monoxide, non-methane volatile organic compounds - NMVOCs, sulfur dioxide, and ammonia) affects climate, visibility, and, human health. The so-called short-lived climate forcers (SLCFs) listed above are highly spatially heterogeneous given their different sources and fairly short lifetimes from seconds up to weeks and, they can either absorb/scatter light effectively or influence the abundances of radiatively active compounds through chemistry.

The increase in the Earth's average temperature is a major scientific and societal issue. According to the latest IPCC report (Forster et al. 2021), each of the last four decades has been successively warmer than any decade that preceded it since 1850. The global surface temperature in the first two decades of the 21st century (2001 – 2020) was 0.99 (0.84 – 1.10) degrees Celsius higher than in 1850 – 1900, with increases over land (1.34 to 1.83°C) larger than over the ocean (0.68 to 1.01°C).

The IPCC also reports low confidence in the response of surface PM to future climate change due to the uncertainty in the response of the natural processes (e.g. stratosphere-troposphere exchange, natural precursor emissions, particularly including biogenic volatile organic compounds - BVOC, wildfire-emitted precursors, land and marine aerosols, and lightning NO_x) to climate change. Changes in the atmospheric distribution of SLCFs determine their impact on climate and air quality. Hence, to better understand the climate variations observed today and to predict those that will occur in the years to come, it is important to acquire a complete vision of the atmospheric compounds and parameters that influence their variations.

Therefore, this PhD work has been done in the context of current climate change and poor air quality, its main objective being to better understand aerosol particle sources and their impacts, notably in the region Northern France. Here, we analyze a long-term dataset of aerosol optical properties and chemical composition, based on the comprehensive set of measurements performed on the ATOLL (ATmospheric Observations in liLLe) platform.

To achieve the goal described above, we first target the aerosol optical properties (absorption, scattering, and extinction) and their relation to PM_1 particle chemical composition. Such an objective is expected to provide a robust parametrization to link aerosol properties at the surface, that would also allow to improve aerosol properties retrievals from remote sensing techniques. At present, the methods that involve retrieval of optical properties from in situ measurements use fixed aerosol mass efficiency, yet, those values vary according to aerosol types and properties which are depending on site, season but also on derivation method. Here, the coincident in situ measurements are combined to assess the particulate pollution specificities at the ATOLL platform via the IMPROVE algorithm, a method applied to estimate the extinction coefficient from chemical composition at remote and urban sites, notably in the US and China (Hand and Malm 2007; Pitchford et al. 2007). In the approach suggested in this objective, we derived specific Mass Extinction Efficiencies (MEEs) for ATOLL, using the measured optical properties and the aerosol

mass concentration of the various chemical species. Furthermore, we evaluated the relative bias when applying MEEs reported for suburban and urban sites from the literature. The developed site-specific aerosol mass efficiency should then consider aerosol heterogeneity among different seasons, and parameters that reflect various influences such as mixing state and size distribution of aerosol components, relevant for better assessment of their role on climate.

Indeed, Northern France is affected by relatively high PM concentrations exceeding the new daily $PM_{2.5}$ concentration threshold of 15 $\mu g\ m^{-3}$, recommended by WHO (World Health Organization 2021), due to heavy traffic, high urban density, and significant agricultural activities overlapping with transnational pollution transport. Although significant progress has been made regarding air quality, only a few chemical particulate species are regulated and monitored (e.g. some heavy metals, and polycyclic aromatic hydrocarbons in Europe; (Directive 2008/107/EC). However, these species account for a small fraction of PM, while others such as carbonaceous PM (e.g. Black Carbon – BC, Organics) and Secondary Inorganic Aerosols (SIA) are found in higher abundance. Designing air pollutant emission abatement strategies and evaluating their efficiencies requires knowledge of the main PM origins and their associated properties. Hence, this study addresses aerosol sources, their geographical origins, and the optical properties of light-absorbing aerosols (BC and Brown Carbon – BrC), an important component of the climate system due to their effect on solar radiation and the associated impact on cloud properties. The method developed in this thesis aims at assessing the emission sources associated with the local vs. transboundary origins, allowing the characterization of the corresponding optical properties of light-absorbing aerosols measured at ATOLL. The purpose is also that the proposed method in this thesis will become a useful tool for the in-situ community to exploit their measurements over a higher spatial coverage.

Overall, the objectives of this work will therefore answer scientific questions, dedicated to particulate pollution measured at the ATOLL platform:

a) What is the temporal variability of the chemical composition and optical properties of fine aerosols at various time scales (from diel to seasonal), and how does it change with specific particulate pollution events?
b) Can we parametrize aerosol optical properties from the chemical composition of the fine fraction at the surface level?
c) What are the sources, geographical origins, and associated optical properties of light-absorbing aerosols in Northern France?
d) What are the sources and lifetime of brown carbon in Northern France?

This PhD thesis is structured into five chapters:

- The first chapter discusses the atmospheric framework, describing key microphysical, chemical, and optical properties of aerosols, their possible sources and their relation with the climate system. Additionally, this chapter discusses particulate pollution and previous studies in the area of northern France.

- The second chapter will provide a detailed description of the ATOLL site, namely its location and analytical methods used, with a particular focus on the in-situ instrumentation.

- The third chapter describes the temporal variability of aerosol chemical and optical properties, as well as meteorological conditions at the site. The observations are analyzed at different time scales, from multi-annually, seasonally, and down to the diel cycle.

- The fourth chapter aims to parametrize optical properties from chemical composition. Results support the use of site-specific parameters along with long-term field observations to derive key aerosol optical properties. The IMPROVE equation is employed for retrieving the light extinction by applying different literature-based mass extinction coefficients. Furthermore, the reconstructed extinction is compared with the observed one and the composition-dependent optical properties are illustrated and discussed.

- The fifth chapter presents the results of using the INTERPLAY approach developed here, aiming at assessing the emission sources associated with local vs. transboundary origins. It allows us to characterize the corresponding optical properties of aerosols measured at the ground level. Specifically, the light-absorbing aerosols, and associated absorption Ångström exponent, and lifetime are analyzed.

CHAPTER 1

1. Aerosol particles

1.1 Definition, types and sources

The atmosphere is a mixture of gaseous and particulate components. Atmospheric aerosols are defined as solid or liquid particles (also known as Particle Matter, PM) suspended in the air excluding rain droplets or ice crystals. Their *aerodynamic diameter* (D_a) ranges between a few nm to 100 µm. A distinction is further made between different size fractions: PM_{10} (D_a < 10 µm), $PM_{2.5}$ (D_a < 2.5 µm), and PM_1 (D_a < 1 µm). In this manuscript, the terms aerosol particles and PM will be used interchangeably. Aerosol particles can be classified according to their properties: microphysical (e.g. size distribution), optical (e.g. scattering and absorption coefficients, single scattering albedo, Ångström exponent), and chemical (e.g. their composition such as nitrate, sulfate, organic matter, etc.), described in section 1.2. They can be formed by several processes such as nucleation, coagulation, condensation of vapors, surface adsorption, and deliquescence/dehydration phenomena.

Figure 1.1 by Buseck & Adachi (2008) summarizes the mechanisms of aerosol formation. During the nucleation process, particles from 1 to 10 nm are formed (in the nucleation mode) from gases either by lowering the temperature (e.g. condensation of hot vapors from combustion processes) or via an increase in the abundance of low vapor pressure species. The formation of a cluster of molecules starts when they react and collide (Sipilä et al. 2010). The low size favors the evaporation, therefore small clusters may be not stable, yet, when clusters grow under saturated conditions, they might reach a critical diameter and develop as stable nuclei (Finlayson-Pitts and Jr 1999). For instance, an important aerosol nucleation route in the atmosphere is the ternary system H_2SO_4-NH_3-H_2O (Kürten et al. 2018; Nøjgaard et al. 2012). The organic compounds can also favor the nucleation and growth of new particles (Chu et al. 2022; Tröstl et al. 2016). Furthermore, newly-formed particles can also act as nuclei for the condensation of low-vapor pressure gases leading to particles between 10 to 100 nm (Aitken mode). Both the nucleation and Aitken modes have a large impact on the aerosol microphysical properties (e.g. number size distribution) which are described in section 1.2.1. The lifetime of ultrafine particles (< 0.1 µm) is generally short (a few hours, Seinfeld and Pandis, 2012) due to surface condensation and coagulation onto larger particles.

The surface condensation process consists of the sorption of low-pressure products onto preexisting particles with D_a between ~0.1 µm and 2 µm, leading them to grow. Evaporation occurs if the ambient conditions are favorable (Finlayson-Pitts and Jr 1999). On the other hand, the formation of a single particle by collision between two smaller ones correspond to coagulation, which is promoted by the fact that small particles go through fairly rapid Brownian diffusion, leading to sufficient particle-particle collisions. This process is more effective when the difference in particle size is large, as smaller particles present a large diffusion coefficient, and therefore can diffuse fast onto the large surface area of bigger particles (Finlayson-Pitts and Jr 1999). An important process impacting the aerosol optical properties occurs when various atmospheric gases nucleate to form new aerosol mass, then these small particles coagulate in the atmosphere. For

instance, water vapor can condense on an airbone particle, which plays the role of a condensation nucleus forming fog (Hussein et al., 2018).

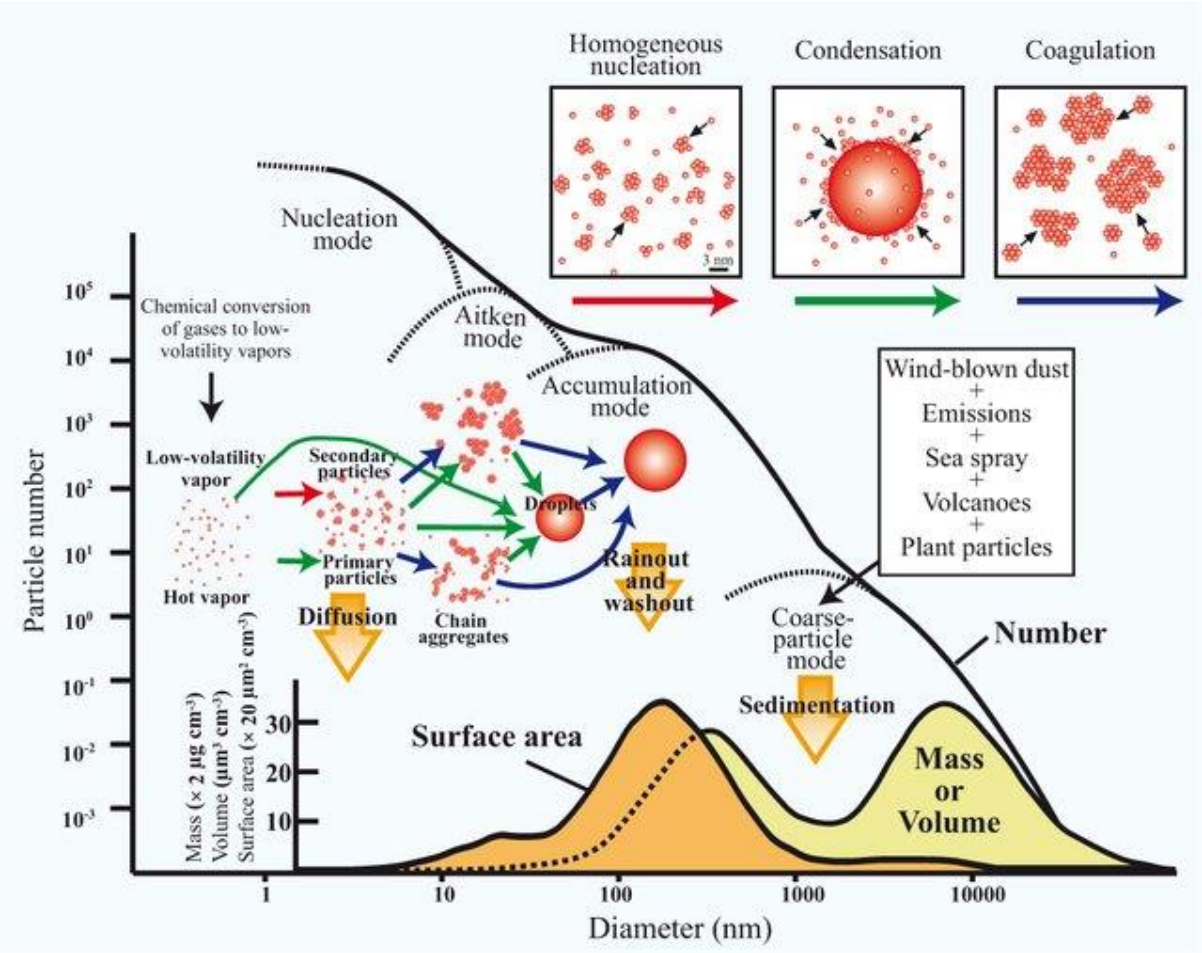

Figure 1.1 Mechanisms of aerosol formation and schematization of the distribution in number, surface area and mass (or volume) of aerosols (Buseck and Adachi 2008).

Once in the atmosphere, aerosol particles can be transported across areas, but they are also subject to removal pathways, called *atmospheric sinks*. Depending on their characteristics and properties as well as meteorological conditions, aerosol particles can stay suspended for very different times in the atmosphere (days to weeks), hence the concept of atmospheric *residence time*, i.e. the average amount of time aerosols spend in the atmosphere (Seinfeld and Pandis 2012). The most important sinks are *dry deposition* at the surface and *wet deposition* from precipitation (Boucher 2016). Aerosol properties reflect the strength of the time spent in the atmosphere before removal. For instance, as ultrafine particles grow rapidly due to coagulation or condensation into the accumulation mode, the main size range which accumulates in the atmosphere is ~ 0.1 - 2 μm. The typical atmospheric lifetime for this mode is several days in the lower troposphere, only wet deposition is an efficient removal mechanism for this mode. On the contrary large particles (> 2 μm) sediment rapidly under the gravitational influence (Seinfeld and Pandis 2012).

Overall, there is a marked seasonality in the aerosol quantities but also between years, which may depend on the variations of sources and sinks in response to changes in the meteorology and human activity. Thus, aerosols form an integral part of the climate system and interact with the atmosphere, the cryosphere, the biosphere, and the ocean. They interact strongly with the water cycle and biogeochemical cycles.

Since the amount and properties (e.g. microphysical, optical, and chemical composition) of aerosols are extremely variable in space and time, it is useful to classify aerosols into different categories according to their origins. Those possible classifications are:

1. *Primary vs secondary*. *Primary aerosol particles* have been emitted into the atmosphere as particles while, s*econdary aerosol particles* come from the processes described previously in Figure 1.1 (e.g. condensation, nucleation of gases, coagulation of nuclei, etc.) related to atmospheric gas-phase species called *aerosol particle precursors*.
2. Aerosol particles can also be classified according to their origin: *natural* vs. *anthropogenic* sources.
3. Chemical composition: *inorganic* (e.g. nitrate, sulfate) and *organic* aerosol particles (e.g. PAH and levoglucosan).

On a global scale, the total mass of suspended particles of natural origin is significantly higher than that of anthropogenic particles, as shown by the global emissions listed in Table 1.1. According to Delmas et al. (2015), natural sources would represent 70 to 90% of the total mass emissions of aerosols.

Table 1.1 Approximative emission fluxes from different types of primary aerosols and gaseous precursors of secondary aerosols. Estimates are compiled from different authors (Burrows et al. 2009; Dentener et al. 2006; Guenther et al. 1995; Heald and Spracklen 2009; Jaenicke 2005; Penner et al. 2001). Taken from (Boucher 2016).

Aerosol type	Emission flux (per year)
Natural primary aerosols	
Desert dust	1000-3000 Tg
Sea spray	1000-6000 Tg
Biomass burning aerosols	20-35 Tg
Terrestrial primary biogenic aerosols	Order of 1000 Tg
Including bacteria	40-1800 Gg
Including spores	30 Tg
Precursors of natural secondary aerosols	
Dimethylsulphide (DMS)	20-40 Tg S
Volcanic (SO_2)	6-20 Tg S
Terpenes	40-400 Tg
Anthropogenic primary aerosols	

Industrial dust	40-130 Tg
Biomass burning aerosols	50-90 Tg
Black carbon (from fossil fuel)	6-10 Tg
Organic carbon (from fossil fuel)	20-30 Tg
Anthropogenic secondary aerosols	
SO_2	70-90 Tg S
Volatile organic compounds (VOCs)	100-560 Tg C
NH_3	20-50 Tg N
NOx	30-40 Tg N

In the following, the main natural and anthropogenic sources of aerosols are described, by successively considering their primary and then secondary formation processes.

Marine aerosols

The wind friction at the ocean surface ejects particles (< 10 µm) of salty marine water into the atmosphere. The phenomenon called *bubbling* occurs when a fraction of the water evaporates, so the concentration of sea salt in the particle matter, which is more or less hydrated according to ambient humidity, increases (Fitzgerald 1991). Although these particles are often called sea salt aerosols, this is yet another misuse of language because these particles may also contain biological material and other impurities. In contrast, jet drops formed from the base of bursting bubbles are postulated to produce particles from bulk seawater, enriched largely in salts and water-soluble organic species. It is therefore more appropriate to refer to sea spray aerosol particles which cover size ranges from ~100 nm to several tens of µm. The largest particles (Woolf et al., 1987) fall back fairly quickly to the ocean surface and are therefore of lesser climatic importance, whereas submicron particles (Wang et al. 2017) play a critical role in determining cloud properties in marine environments (Andreae et al. 1986; Facchini et al. 2008; Fitzgerald 1991; Heintzenberg et al. 2000; Zhuang et al. 1992).

Desert dust

S*altation* can occur when the wind friction on continental surfaces detaches soil particles and suspend them in the atmosphere. This is particularly the case in desertic, arid and semiarid regions where the wind is not slowed down by vegetation. The emission of soil particles span sizes that range from typically 100 nm to tens of µm (Maring et al. 2000). Larger particles can also be lifted but they tend to fall back quickly (Maring et al. 2003). Emissions of desert dust depend very much on environmental and meteorological conditions. They are sporadic and can travel long distances (Zwaaftink et al. 2022; Knippertz and Todd 2012; Kok et al. 2021; Zhao et al. 2022).

Volcanic aerosols

Volcanoes can emit fragments of pulverized rocks and minerals, usually called *volcanic ash*, during explosive eruptions. These particles have sizes typically ranging from micrometers to millimeters (< 0.6 µm) (Brown et al. 2012). Volcanic ash can be transported over distances of a few hundred to a few thousand kilometers but due to its size, it tends to fall down rapidly (Sellitto

et al. 2020), hence limiting its climate effect. Volcanoes also emit sulfur-containing gases (in the form of sulfur dioxide, SO_2, and hydrogen sulfide, H_2S) that get oxidized in the atmosphere to form submicron sulfate aerosols. If these sulfur-containing gases are emitted in the troposphere, the residence time of the subsequent aerosols will be relatively short, a few weeks at most (Hofmann and Rosen 1980). If the eruption is powerful enough to inject the sulfur gases in the stratosphere (Textor et al. 2003), then the volcanic aerosols have a much longer residence time, of the order of a few months to more than a year, depending on the region (Carn et al. 2011; Frogner et al. 2006; Handler 1989; Mills et al. 2016; Nee et al. 2021; Rind et al. 1992).

Biogenic aerosols

The terrestrial biosphere is a source of primary biogenic aerosol particles. They comprise plant and insect debris, pollen, spores, bacteria, and viruses. Debris is usually larger than 100 µm, while pollen, spores, and large bacteria are generally in the range of 1-100 µm, and small bacteria and viruses are generally smaller than 1 µm (Amato et al. 2017; Fröhlich-Nowoisky et al. 2016).

Seawater also contains biological material, some of which is transferred to sea spray aerosols during the emission process, as discussed previously. This primary biological matter is found preferentially in particles smaller than 200 nm in diameter (Leck and Bigg 2008) and its amount has been found to depend on the biological activity in ocean waters (Facchini et al. 2008).

Terrestrial and marine ecosystems are also important sources of aerosol precursors. Some species of phytoplankton produce dimethylsulfide (DMS; CH_3SCH_3), a gaseous compound that is oxidized in the atmosphere to form sulfur-containing aerosols. Plants and algae emit Volatile Organic Compounds (VOCs), i.e. compounds which have a high vapor pressure and low water solubility. Those VOCs are oxidized in the atmosphere and further contribute organic material to the atmospheric aerosol (He et al. 2021; Laskin, and Nizkorodov 2015; de Sá et al. 2019). These aerosols are referred to as secondary biogenic aerosols.

Combustion aerosols

Typically submicron and visible in smoke plumes (Liu et al. 2020), carbonaceous aerosol particles are emitted from combustion processes and have two separate origins: 1) they either come from the living world (i.e. vegetation), or 2) they are emitted from fossil fuels (coal, gas, and oil) that are formed on geological timescales. For instance, biomass burning (BB) emissions generate primary aerosols that stem from the incomplete combustion of organic matter, comprising elemental carbon (EC) and organic carbon (OC) associated with hydrogen and other atoms. The combustion of biomass also emits gaseous compounds, such as VOCs and sulfur dioxide, which are aerosol precursors (Adam et al. 2021; Brown et al. 2021; Bui et al. 2022; Jahl et al. 2021; Karanasiou et al. 2021; Washenfelder et al. 2015).

1.2 Properties

1.2.1 Microphysical properties

Atmospheric aerosols are polydisperse, i.e. they exhibit a range of sizes. Commonly, they are considered spherical with diameters relative to equivalent spheres. Three approaches are used to describe *size*, including the aerodynamic diameter (D_a), defined previously in section 1.1, the

optical diameter (D_o), and the (electrical) mobility diameter (D_m). D_o is defined by the radiative properties in comparison to a spherical particle of PolyStyrene Latex (PSL, $m = 1.598 + 0i$ at 532 nm, Pettersson et al., 2004), whereas D_m corresponds to the diameter of a sphere with the same migration velocity in a constant electric field as the particle of interest.

An aerosol population can be characterized depending on its size and it is possible to distinguish four modes according to the processes described in section 1.1. The number of modes that are visible in the observations can however vary, but it is usual to see two to three.

For polydisperse aerosol particles, the *number* size distribution is defined as the particle number for different size bins. The total particle number concentration is the integrated number concentration across all size bins:

$$N = \int N(D_p) dD_p \qquad \text{eq. 1.1}$$

where D_p is the particle diameter, $N(D_p)$ is the number concentration of particles with a diameter ranging within dD_p, and N is the total number concentration.

Under the assumption of spherical particles, we can also calculate the aerosol *surface* area (S) and *volume* concentrations (V) following eq. 1.2 and eq. 1.3.

$$S = \pi \int N(D_p) D_p^2 \, dD_p \qquad \text{eq. 1.2}$$

$$V = \frac{\pi}{6} \int N(D_p) D_p^3 dD_p \qquad \text{eq. 1.3}$$

Generally, aerosol *size distribution* can be described as a multi-modal log-normal distribution. Those are determined by particle Geometric Mean Diameter (GMD, D_{pg}) and Geometric Standard Deviation (GSD, σ_{pg}) represented in eq. 1.4, where D_{pg} and σ_{pg} could be given as equations 1.5 and 1.7.

$$\frac{dN}{d \ln D_p} = N_0 \frac{1}{\sqrt{2\pi} \ln \sigma_{pg}} \exp\left(-\frac{1}{2} \left(\frac{\ln\left(D_p / D_{pg}\right)}{\ln \sigma_{pg}} \right) \right) \qquad \text{eq. 1.4}$$

where N_0 is the total aerosol concentration,

$$\log D_{pg} = \frac{\int \ln D_p N(D_p) d \ln D_p}{\int N(D_p) \, d \ln D_p} \qquad \text{eq. 1.5}$$

$$\log \sigma_{pg} = \sqrt{\frac{\int N(D_p) (\ln D_p - \ln D_{pg})^2 d \ln D_p}{\int N(D_p) d \ln D_p}} \qquad \text{eq. 1.6}$$

Under the assumption of log-normal distribution, the particle GMD equals its geometric median diameter. For particles with two or more modes, the new mode size distribution could be added to the previous knowing its GMD, number concentration and GSD. Due to these advantages, the log-normal distribution is widely used to simplify theoretical calculations of optical properties e.g. in the Mie theory (Chen et al. 2018).

1.2.2 Chemical composition

The chemical composition of aerosol is a key parameter that controls the optical properties or the ability to serve as cloud condensation nucleus or ice nucleus. Before discussing the chemical composition of atmospheric aerosols, it is important to introduce the concept of mixing state.

It is usual to distinguish *external* and *internal* mixtures. In an external mixture, particles are chemically pure and the mixture is composed of particles of different chemical compositions. It is therefore possible to differentiate the particles according to their chemical composition (e.g. black carbon, ammonium nitrate, organics). In the case of an internal mixture, different chemical species are mixed within each particle. If the internal mixture is perfect, all particles have the same chemical composition.

External and internal mixtures are conceptual models, the reality lies somewhere in between these two extremes as schematized in Figure 1.2. Certainly, as a general rule, the aerosol chemical composition varies both as a function of size (some chemical species are found preferentially in some size ranges) and within a size class (there are different degrees of mixture for a given size range).

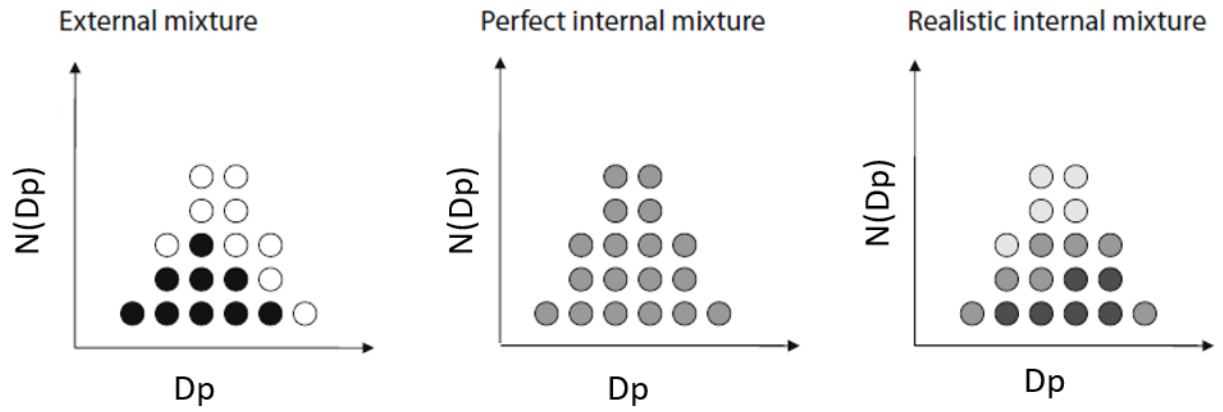

Figure 1.2 Schematic representation of three different aerosol mixtures. The more realistic internal mixture is composed of internally-mixed particles but with varying degrees of mixing for a given aerosol size and across the size distribution. This figure is reproduce from Boucher, (2016).

Aerosol mixing occurs through the *coagulation* of particles of different chemical compositions, and by the *condensation* of semi-volatile compounds onto pre-existing particles. For instance, non-soluble primary aerosols, such as black carbon and mineral dust, can be covered by a coating of soluble species, which changes their properties such as hygroscopicity (Crumeyrolle et al. 2008). Boucher (2016) identifies three main categories of fine-mode aerosol particles when considering their chemical composition, which are described in the sections below.

Inorganic Aerosols (IA)

In submicron aerosol particles, the presence of inorganic material is very common, notably in secondary processes. The chemical composition of sulfate, for example, varies between pure

sulfuric acid (H_2SO_4), ammonium bisulfate (NH_4HSO_4), and ammonium sulfate ($(NH_4)_2SO_4$). Beyond the sulfate (SO_4^{2-}) and ammonium (NH_4^+) ions, one can also find the nitrate ion (NO_3^-), which will also be neutralized by ammonia (NH_3). Inorganic aerosols are generally very hygroscopic and are mostly scattering, typically not absorbing solar radiation (Seinfeld and Pandis 2012).

Black Carbon (BC) aerosols

Black carbon is an aerosol component (Petzold et al. 2010) with unique properties. It is produced during the combustion of long carbon-chain fuels when the combustion is incomplete due to a lack of oxygen. The reaction chain starts with the production of polycyclic aromatic hydrocarbons (PAHs) which serve as nuclei to form small particles of a few nanometers with graphite layers and a large carbon-to-hydrogen ratio (Bond et al. 2013). The density of BC is not well measured and is likely to vary with the combustion conditions, with generally a recommended value between 1.7 and 1.9 g cm^{-3} (Bond and Bergstrom 2006). The size of BC particles varies with the source type and age but is typically at 100 nm or lower (Bond and Bergstrom 2006). Incomplete combustions are common, e.g., when biomass is burned, but also in stoves or even in certain parts of the most sophisticated engine. In this thesis, we refer to BC_{ff} for soot-like particles generated by fossil fuel combustion sources, whereas BC_{wb} refers to particles generated from biomass (wood) burning. The sources of BC_{wb} can be natural (e.g. naturally occuring wildfires) or anthropogenic (e.g. deforestation, controlled burns, residential heating) while BC_{ff} is mostly from anthropogenic sources (e.g. traffic, industries). Shortly after its emission, BC can get coated with organics or inorganics (sulfate), thus creating an internal mixture that modifies the microphysical and optical properties of BC, generally becoming more hygroscopic (Laborde et al. 2013; Zhang et al. 2021).

Organic (Org) Aerosols

Although the presence of organic material in aerosol particles has been known for a long time, it has taken decades for scientists to measure the concentration and composition of organics more accurately (Jacobson et al. 2000). Mass spectrometry on bulk and individual aerosol particles has permitted substantial progress in the characterization and understanding of Org particles (Pratt and Prather 2012b, 2012a). Those particles contain a tremendous variety of chemical compounds (alkanes, alcohols, aromatic compounds, carbonyl compounds, organic acids, amines, organosulfur compounds, etc.), whose full complexity cannot be monitored and represented through continuous observations. It is therefore important to seek to simplify the way the chemical composition of these compounds is characterized. One can distinguish primary (POA) from secondary organic aerosols (SOA). SOAs originate from VOCs that are oxidized in the atmosphere, and those gaseous precursors can originate from different sources, be co-emitted with the particle to serve as a condensable surface, or evaporate from another POA (Bian et al. 2017).Further processing of mass spectrometry data allows for the distinction between different types of Org (Drosatou et al. 2019; Ulbrich et al. 2009). These spectra can be used in factor analysis to acquire information about Org sources, processes, and properties (Zhang et al. 2011). Several factor analysis techniques have been developed to estimate the contributions of sources and processes to the observed Org. These techniques include custom principal component analysis (Zhang et al. 2005), multiple component analysis (Zhang et al. 2007), positive matrix factorization

(Lanz et al. 2007; Paatero and Tapper 1994), and the multilinear engine (ME-2) (Canonaco et al. 2013; Lanz et al. 2008; Paatero 1999). The chemical composition of Org originating from the combustion of fossil hydrocarbons (hydrocarbon-like Org, or HOA) differs from that of Org produced by the combustion of biomass (biomass burning organic aerosols or BBOA). Org particles with high oxygen-to-carbon ratio are called oxygenated organic aerosols (or OOA). The O:C ratio is larger than 0.25 in OOA and can reach values as large as 1 for the more aged aerosols (Aiken et al. 2008). Several authors (Laskin, and Nizkorodov 2015; Moise et al. 2015; Tasoglou et al. 2017; Taylor et al. 2020; Yus-Díez et al. 2022) showed that, as they age in the atmosphere, organic aerosols become more oxygenated, less volatile and more hygroscopic.

1.2.3 Optical properties

Following the theory of Kerker (1969) and Bohren & Huffman (1998), the key parameters that govern the scattering and absorption of light by a particle are the *wavelength* (λ) of the incident radiation, the size of the particle, the ratio of the circumference of the particle to the wavelength of light, and the particle optical property relative to the surrounding medium, the *complex refractive index (RI)*:

$$N(\lambda) = n(\lambda) + ik(\lambda) \qquad \text{eq. 1.7}$$

Both the *real part (n)* and the *imaginary part (k)* of the refractive index are functions of λ. When a beam of light impinges on a particle, electric charges in the particle are excited into oscillatory motion. The excited electric charges radiate energy in all directions (*scattering*) and may convert a part of the incident radiation into thermal energy (*absorption*). Electromagnetic radiation transports energy which can be measured by a detector perpendicular to its direction of propagation in W m^{-2} (incident intensity of radiation).

The energy scattered by a particle (F_{scat}) is proportional to the incident intensity:

$$F_{scat} \approx C_{scat} F_0 \qquad \text{eq. 1.8}$$

where C_{scat} in units of m^2 is the single-particle scattering cross-section and F_0 is the incident intensity of radiation.

For absorption, the energy absorbed (F_{abs}) is described by:

$$F_{abs} \approx C_{abs} F_0 \qquad \text{eq. 1.9}$$

where C_{abs} (m^2) is the single-particle absorption cross-section.

The combined effect of scattering and absorption is referred to as extinction, and the extinction cross-section (C_{ext}) can be defined by:

$$C_{ext} = C_{scat} + C_{abs} \qquad \text{eq. 1.10}$$

C_{ext} has the unit of area; in the language of geometric optics, one would say that the particle casts a "shadow" of area C_{ext} on the radiative energy passing the particle. This shadow, however, can be considerably greater, or much less, than the particle geometric shadow. The dimensionless *scattering efficiency* (σ_{scat}) of a particle is C_{scat} / A, where A is the cross-sectional area of the particle. Defining σ_{ext} and σ_{abs} in the same way, we obtain:

$$\sigma_{ext} = \sigma_{scat} + \sigma_{abs} \quad \text{eq. 1.11}$$

The σ_{ext} at a given wavelength λ can be expressed as the sum of scattering and absorption coefficients of particles and gases in the atmosphere:

$$\sigma_{ext,\lambda} = \sigma_{ap,\lambda} + \sigma_{sp,\lambda} + \sigma_{ag,\lambda} + \sigma_{sg,\lambda} \quad \text{eq. 1.12}$$

where subscripts "s" and "a" indicate scattering and absorption, and "p" and "g" denote particles and gases, respectively.

The ratio of σ_{scat} and σ_{ext} is called the *Single-Scattering Albedo (SSA)*:

$$SSA = \frac{\sigma_{scat}}{\sigma_{ext}} \quad \text{eq. 1.13}$$

Thus, the fraction of light extinction that is scattered by a particle is equal to SSA, and the fraction absorbed is (1-SSA). Another key parameter useful to represent the wavelength dependence of the aerosol optical properties is the *Ångstrom exponent (AE)* which is calculated from the measured values of the extinction (EAE), absorption (AAE), and scattering (SAE) as a function of wavelength by:

$$AE = -\frac{dlog^2\sigma_i}{dlog^2\lambda} \cong -\frac{log\left(\frac{\sigma_{i\,1}}{\sigma_{i\,2}}\right)}{log\left(\frac{\lambda_1}{\lambda_2}\right)} \quad \text{eq. 1.14}$$

where i is either extinction, absorption, or scattering.

Furthermore, the *mass extinction (MEE), scattering (MSE) and absorption (MAE) efficiencies* (α_i) of different aerosol chemical species are key parameters used to estimate aerosol radiation impact from chemical properties and within radiation models (Seinfeld and Pandis, 2012). The MEE/MSE/MAE depend on particle composition and size distribution which determines its refractive index (particles with a higher refractive index scatter more light) and hygroscopic properties. For instance, fine mode particles (< 1.0 or 2.5 μm) have higher MEE compared to coarse mode particles (> 1.0 or 2.5 μm) because smaller particles scatter light more efficiently at visible wavelengths. The particle MEE increases with water adsorption (thus with varying ambient RH) because of the increase of the particle cross-section. These parameters can be expressed as:

$$\alpha_i(m^2g^{-1}) \equiv \frac{Optical\ property_i\ (M\ m^{-1})}{Mass\ concentation\ (\mu g\ m^{-3})} \quad \text{eq. 1.15}$$

where i is either extinction, absorption, or scattering.

1.3 Impacts

1.3.1 Air quality

Research has shown the impacts of aerosol on air quality degradation and their subsequent adverse health effects (Araujo 2011; Khomenko et al. 2021; Kim et al. 2015; Tarín-Carrasco et al. 2021). Indeed, PM is one of the main pollutants responsible for an increased incidence of several respiratory and cardiovascular diseases, leading to significant reductions in human life expectancy. Particle size has been directly linked to the potential of PM for causing health problems, with

smaller particles likely to be deposited in deeper parts of the respiratory system. Figure 1.3 shows how deep PM of different sizes reaches the respiratory tract. Health effects of PM result in short-term (e.g. allergies) and long-term exposure (e.g. asthma and lung cancer).

The toxicity of particles depends not only on their size but also on their concentration and chemical composition. Ultrafine particles are the most dangerous size, since they can penetrate deeply into the lung tissues, then diffuse into the bloodstream and be transported to other body parts, causing serious health problems like heart attacks (Anderson, Thundiyil, and Stolbach 2012). According to recent studies, long-term exposure to high levels of PM can be also associated to dementia, obesity, loss of fertility, or even type 2 diabetes in adults among other effects (Calderón-Garcidueñas and Villarreal-Ríos 2017; Rao et al. 2015).

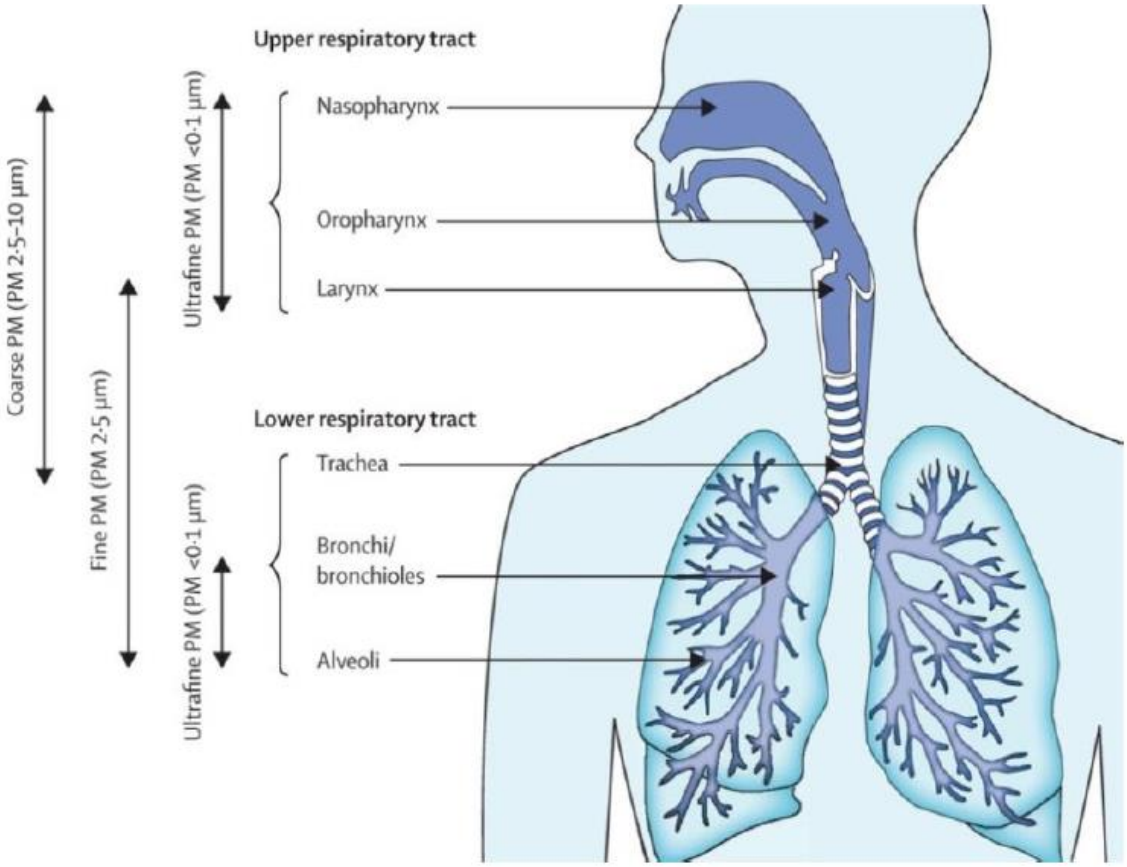

Figure 1.3 Penetration in the respiratory tract of different PM size ranges (Guarnieri and Balmes 2014).

Since 1987, the World Health Organization (WHO) has periodically issued health-based air quality guidelines (AQG) to assist governments and civil society to reduce human exposure to air pollution and its adverse effects. However, despite some notable improvements in air quality, the global death toll has barely declined since the 1990s (World Health Organization 2021). More than 15 years have passed since the WHO AQG were published in 2005, focusing on PM, ozone, nitrogen dioxide, and sulfur dioxide. Since then, there has been a marked increase in evidences on the

adverse health effects of air pollution, built on advances in air pollution measurement and exposure assessment and an expanded global database of air pollution measurements (World Health Organization 2021). Therefore, new recommendations on AQG levels have recently been published (Table 1.2) for annual and daily concentration of $PM_{2.5}$, PM_{10}, ozone (O_3), nitrogen dioxide (NO_2), sulfur dioxide (SO_2), and carbon monoxide (CO). One note that PM_1 threshold is not yet existing.

Table 1.2 Latest recommended Air Quality Guideline (AQG) levels and interim targets by the World Health Organization.

Pollutant	Averaging time	Interim target				AQG level
		1	2	3	4	
$PM_{2.5}$ ($\mu g\ m^{-3}$)	Annual	35	25	15	10	5
	24-hour[a]	75	50	37,5	25	15
PM_{10} ($\mu g\ m^{-3}$)	Annual	70	50	30	20	15
	24-hour[a]	150	100	75	50	45
O_3 ($\mu g\ m^{-3}$)	Peak season[b]	100	70	-	-	60
	8-hour[a]	160	120	-	-	100
NO_2 ($\mu g\ m^{-3}$)	Annual	40	30	20	-	10
	24-hour[a]	120	50	-	-	25
SO_2 ($\mu g\ m^{-3}$)	24-hour[a]	125	50	-	-	40
CO ($mg\ m^{-3}$)	24-hour[a]	7	-	-	-	4

[a] 99th percentile (i.e. 3-4 exceedance days per year).

[b] Average of daily maximum 8-hour mean O_3 concentration in the six consecutive months with the highest six-month running-average O_3 concentration.

The interim target supports the planning of incremental milestones toward clear air, particularly in countries struggling with high air pollution levels.

The WHO estimates that almost 99% of the global population is exposed to air pollution levels exceeding their safe guideline level for $PM_{2.5}$, with low-and middle-income countries suffering from the highest levels of exposure. Approximately 86% of the global population (2.5 billion people) lived in urban areas that exceeded WHO's 2005 guideline annual average $PM_{2.5}$ (10 $\mu g\ m^{-3}$), resulting in an excess of 1·8 million (95% CI 1·34 million–2·3 million) deaths in 2019. Furthermore, 4.2 million deaths globally are linked to ambient air pollution, 43% of deaths and disease from chronic obstructive pulmonary disease, 25% of deaths and disease from ischemic heart disease, 24% of deaths from stroke, 14% of deaths and disease from an acute lower respiratory infection and 29% of deaths and disease from lung cancer (World Health Organization 2022). In France, nearly 40,000 deaths are attributable each year to exposure of people aged 30 and over to $PM_{2.5}$, according to the latest estimate published in 2021 (Medina et al. 2021).

In Europe, more than 70% of European Union (EU) citizens live in urban areas (Eurostat 2016), where population density and economic activities cause high levels of air pollution. This leads to an estimated 90% of city dwellers in Europe being exposed to pollutant levels higher than current

guidelines. The European Environment Agency (EEA) is the European Union's air pollution data center and it supports the implementation of EU legislation linked to air emissions and air quality. The EEA also contributes to the evaluation of the EU air pollution policies and to the development of long-term strategies to improve air quality in Europe, aiming to protect health, vegetation, and natural ecosystems by setting limits and target values (e.g. Directive 2008/50/EC) for air pollutants.

Moreover, the latest EEA air quality status of Europe (European Environment Agency 2022) shows that exceedances of air quality standards are common across the EU, with 96% of the urban population exposed to higher PM levels than those recommended (Figure 1.4). For instance, the EEA analyzed the daily limit value of PM_{10} concentration in 2 979 stations. They report 16% of monitoring stations with PM_{10} concentrations above the EU daily limit value, 84% of which were urban and 11% suburban.

The emissions of all key air pollutants in the EU continued to decline despite an increase in gross domestic production (European Environment Agency 2022). For instance, the percentage of the urban population exposed to SO_2 levels above the recommended limit value decreased from 2% in 2006 to less than 0.1% in 2020. For the period 2015-2020, the EEA (European Environment Agency 2022) reported high concentrations of PM and benzo[a]pyrene (a carcinogen compound) in Central-eastern Europe and Italy. The high concentrations in Central-eastern Europe are mainly driven by the use of solid fuels for domestic heating and industry while, in Italy, the combination of a high density of anthropogenic emissions and meteorological and geographical conditions favors the accumulation of air pollutants in the atmosphere. For ozone, the levels reported in 2020 were lower than in previous years (2015), but are still significant in some of the Mediterranean areas. Despite overall improvements in air quality, air pollutant levels remain a major health concern for a large fraction of Europeans.

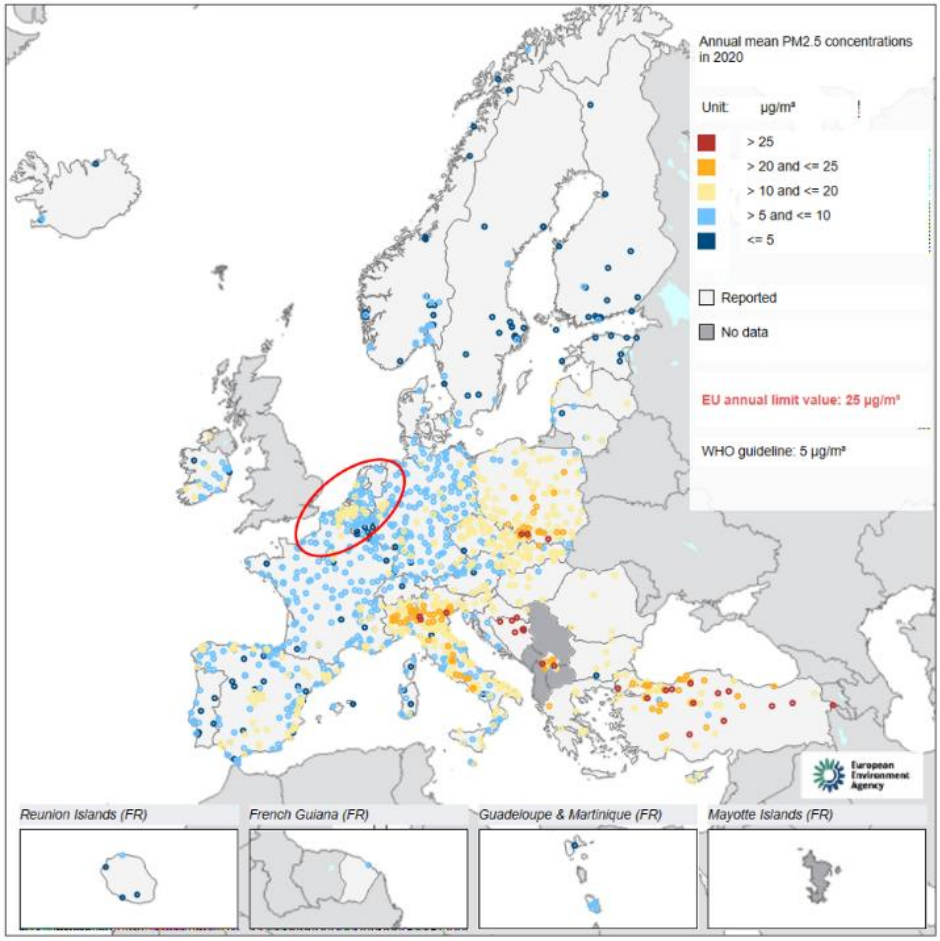

Figure 1.4 Concentrations of $PM_{2.5}$ in 2020 and 2021 in relation to the EU annual limit value and the WHO annual guideline. Source: European Environment Agency, (2022). The red ellipse highlights the continental Northwestern part of Europe.

It is important to point out that, in 2020, after the start of the COVID-19 pandemic, most European countries implemented lockdown measures to stop or minimize the spread of the disease. Those measures led to a reduction in activity in road transport, aviation, and international shipping, which in turn led to falls in emissions of some air pollutants, e.g. NO_2 concentrations monitored at traffic stations decreased by up to 70% (European Environment Agency 2022). Some industrial sectors also reduced activity levels, the level of agricultural production stayed more or less steady and emissions from domestic heating increased slightly as people stayed at home (European Environment Agency 2022).

In France, regional air quality monitoring networks (AASQA – Association Agréée de Surveillance de la Qualité de l'Air) are responsible for applying the recommendations explained above under the supervision of the Ministry of Environment (MTE), which is responsible for setting the strategies to implement EU directives at the national scale, although the PM levels are frequently exceeded in the territory, as in many European countries. According to the latest report of the Interprofessional Technical Centre for Studies on Air Pollution (Citepa 2021) by sector of activity, primary anthropogenic emissions have decreased in France for the majority of the

pollutants studied over the period 2000-2020. For instance, PM_{10} and $PM_{2.5}$ emissions decreased by 55% and 65%, respectively. Sulfur dioxide emissions, mainly from industrial activities, decreased seven-fold over the period. The development of renewable energy, energy-saving actions, regulation of emissions from industrial installations, improvement of the energy efficiency of the latter and regulation of sulfur content in fuels have in particular made it possible to reduce the discharge of this pollutant in the air. Vestreng et al. (2007) report a decrease over the last twenty-five years of anthropogenic sulfur emissions of more than 60% between 1980 and 2004.

Unlike SO_2, the emission sources of NO_x and particles are multiple and diffuse on the territory, which complicates the implementation of reduction measures. Nonetheless, the emission of NOx, for example, has fallen by 62% over the period 2000-2020. The progress made in the road transport sector with catalytic converters and other technologies explains some of that decrease. In contrast, anthropogenic NH_3, mainly from agriculture (fertilizers and manure) have only slightly decreased since 2000 (-11%), and in steps: decreasing between 2000 and 2006, stabilizing from 2006 till 2016, then a further reduction since 2016. Indeed, NH_3 is a precursor of ammonium sulfate and nitrate (AS, AN) aerosols, which are formed when atmospheric NH_3 reacts with sulfuric acid (H_2SO_4) and nitric acid (HNO_3). In urban areas, HNO_3 is formed primarily from the oxidation of NO_x, mostly emitted by traffic. The thermodynamic relationships governing the partitioning between the gas and aerosol phases depend on the quantities of NH_3 and acid precursors (i.e., SO_2 and NO_x) and the meteorological conditions (heat, solar radiation, and humidity) (Hauglustaine et al. 2014).

On the biosphere, there are two main effects of aerosols: 1) acidification of soils and waters, 2) eutrophication (i. e. the enrichment of nitrogen-containing nutrients). The first occurs when sulfate and nitrate aerosols are deposited on the surface, changing the soil and water conditions of basic cations by replacing them with H^+ (Bowman et al. 2008; Xu et al. 2016). In aquatic environments (e.g. freshwaters), the water pH lowers, affecting biodiversity (Lovett et al. 2009). Eutrophication is more related to nitrate aerosols, as their excess in aquatic bodies lead to the development of algae populations, including toxic ones, and the depletion of oxygen concentrations critical to fish populations, thus leading to the loss of biodiversity (Burt 2012). The EEA report (European Environment Agency 2021) shows that about 563,000 km² of European seas (23% of the total area) have a eutrophication problem, including areas in all regional seas. The situation is worst in the Baltic Sea where 99% of the assessed areas suffer from eutrophication, followed by the Black Sea (53%) and some coastal areas in the Mediterranean Sea (12%), mainly close to densely populated coasts or catchments that are downstream from agricultural activities.

1.3.2 Radiative effects

Clouds and aerosols continue to contribute to the largest uncertainties in estimates of the Earth's changing energy budget (Forster et al. 2021). This section focuses on understanding how clouds and aerosols contribute to, and may respond to climate change.

Cloud formation usually takes place in rising air, which expands and cools, thus permitting the activation of aerosol particles into cloud droplets and ice crystals in supersaturated air. Cloud particles are generally larger than aerosol particles and composed mostly of liquid water or ice. The evolution of a cloud is governed by the balance between a number of dynamical, radiative,

and microphysical processes. Cloud particles of sufficient size become falling hydrometeors (e.g. drizzle, raindrops, snow crystals, graupel, and hailstones). Precipitation is an important and complex climate variable that is influenced by the distribution of moisture and cloudiness, and to a lesser extent by the concentrations and properties of aerosol particles (Solomon et al. 2007; Stocker et al. 2013).

As discussed in the previous section, aerosol particles interact with solar radiation through absorption and scattering, and to a lesser extent with terrestrial radiation via absorption, scattering and emission. Aerosols can serve as cloud condensation nuclei (CCN) and ice nuclei (IN) upon which cloud droplets and ice crystals form. Overall, aerosol particles of anthropogenic origin are responsible for radiative forcing (RF) of climate change through their interaction with radiation, and also as a result of fraught with uncertainties (Haywood et al. 2000; Lohmann and Feichter 2001), aerosols dominate the uncertainty in the total estimates of anthropogenic RF (Forster et al. 2021; Haywood and Schulz 2007). Furthermore, current difficulties in accurately quantifying non-greenhouse gas RFs, primarily those that result from aerosol-cloud interactions, underlie the complexity of constraining climate sensitivity from observations even if there is a robust knowledge of the temperature records (Andreae et al. 2005). Thus, a complete understanding of past, current, and future climate changes requires a thorough assessment of *aerosol-cloud–radiation interactions* (Figure 1.5).

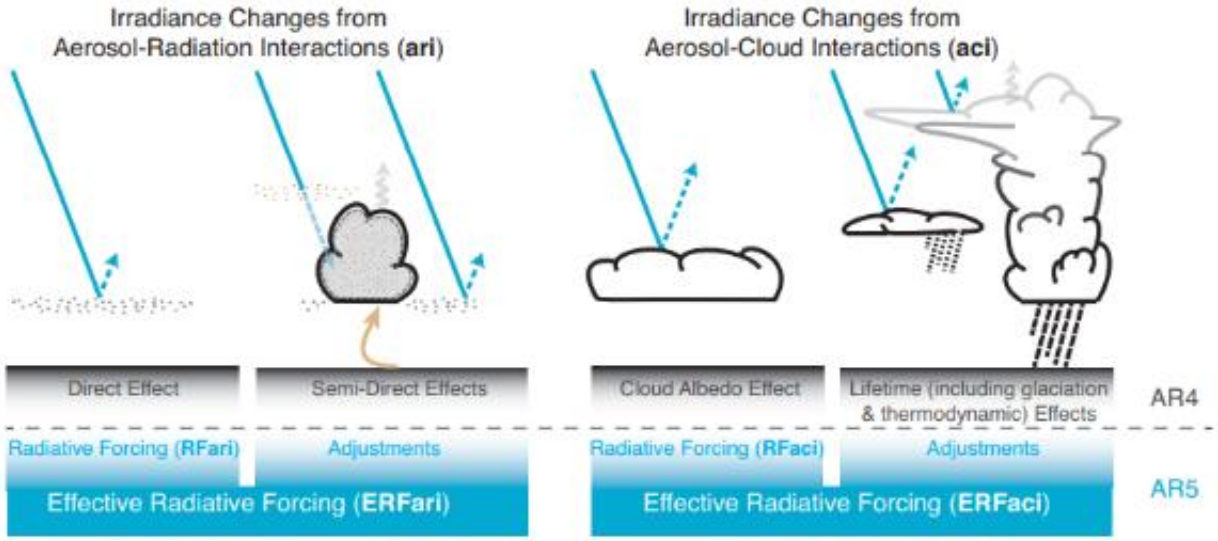

Figure 1.5 Schematic of the terminology used in the fifth assessment report (AR5) of the IPCC (Stocker et al. 2013) for aerosol–radiation and aerosol-cloud interactions and how they relate to the terminology used in the previous report (AR4) (Solomon et al. 2007). The blue arrows depict solar radiation, the grey arrows terrestrial radiation and the brown arrow symbolizes the importance of couplings between the surface and the cloud layer for rapid adjustments. See Chapter 7 of AR5 from the IPCC (Stocker et al. 2013) for further details.

The Effective RF from *aerosol–radiation interactions* (ERFari) is usually referred to as the aerosol direct effect; it includes radiative effects from anthropogenic aerosols before any adjustment takes

place. The Effective RF from *aerosol-cloud interactions* (ERFaci) arises from the prompt effect on cloud albedo changing concentrations and size of cloud droplets (and ice nuclei), also known as the Twomey effect (Lohmann and Feichter 2005).

According to Bellouin et al. (2020) total aerosol effective radiative forcing is -1.6 to -0.6 W m^{-2} (68% confidence interval), or -2.0 to -0.4 W m^{-2} with a 90% likelihood. Those intervals are of similar width to the last Intergovernmental Panel on Climate Change (IPCC) assessment but shifted toward more negative values. According to the latest IPCC report (Masson-Delmotte et al. 2021), there is still low confidence in the response of the surface to future climate change due to the uncertainty in the response of the natural processes (e.g. stratosphere-troposphere exchange, natural precursor emissions, particularly including biogenic volatile organic compounds, wildfire-emitted precursors, land and marine aerosols, and lightning NOx) to climate change. Changes in the atmospheric distribution of short-lived climate forcers determine their radiative forcing (Figure 1.6) on climate as well as their impacts on air quality. Hence, a process-level understanding of tropospheric gas and aerosol chemistry developed through laboratory and simulation chamber experiments as well as quantum chemical theory is used to generate chemical mechanisms.

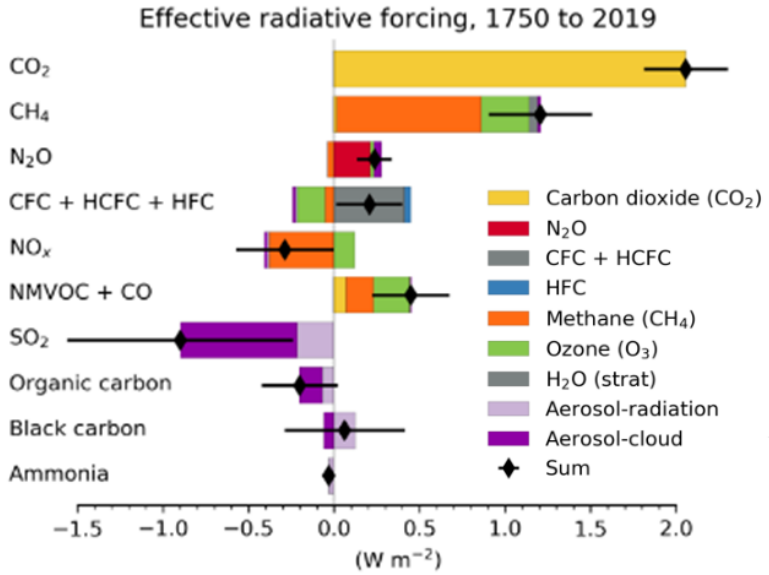

Figure 1.6 Contribution to effective radiative forcing from component emissions between 1750 and 2019 based on CMIP6 models. Effective radiative forcing due to aerosol radiation and cloud effects are calculated for clear-sky and aerosol-free conditions. Further details on data sources and processing are available in the 6th assessment report of the IPCC (Masson-Delmotte et al. 2021).

1.4 Observations types

Aerosol loads and physico-chemical properties are variable in space and time, thus causing strong heterogeneities of their impacts (air quality and radiative effects). A wide range of in situ and remotely sensed observations are used to characterize atmospheric aerosol loads and optical properties (Masson-Delmotte et al. 2021). Measurements made routinely as part of long-term monitoring programs are particularly useful for assessing long-term trends and variability, along with spatial distributions. While remote sensing techniques are optically-based to monitor aerosol

optical properties, in-situ measurements are not only limited to the optical properties of aerosol particles but also include microphysical and chemical properties monitoring. Furthermore, retrieval of atmospheric aerosol concentrations from satellites has been useful for providing global and frequent coverage, although the retrievals themselves depend on prior information on atmospheric composition usually derived from models.

Over the last decade or so, observations of atmospheric pollutant concentrations have been combined with information from global chemistry-climate models to produce global assimilation and forecasting systems and therefore to provide chemical reanalysis or improve model inputs and forecasts. However, uncertainty remains large because of observation limitations (errors and uncertainties, or partial spatial and temporal coverages), model parameterizations (e.g., chemical mechanisms, photolysis schemes, parameterization for mixing and convective transport, and deposition), as well as physical and chemical processes that determine short-lived climate forcer distributions.

1.4.1 Remote sensing (ground-based and satellite)

The aerosol remote sensing approach allows measurements of columnar and vertically resolved aerosol optical properties based on ground-based, airborne or space-based instruments. For example, the sun photometer is a passive ground-based instrument that provides columnar aerosol optical properties. The AERONET (AErosol RObotic NETwork, https://aeronet.gsfc.nasa.gov/) is a network of ground-based aerosol remote sensing networks developed by NASA using the CIMEL CE-318 sun/lunar/sky photometers. For varying periods of time, it has deployed over 1000 observation sites around the world (Figure 1.7), providing globally-distributed observations of Aerosol Optical Depth (AOD) at several wavelengths between 340 and 1640 nm (440, 670, 870, 940, and 1020 nm are commonly used) and additional inversions (Figure 1.8 that include aerosol properties and volume size distributions) (Dubovik et al. 2002; Holben et al. 2006). In the study by Dubovik et al. (2002), eight years of vertically-integrated radiometric measurements from the ground were carried out on various sites of the global AERONET network, making it possible to determine the optical properties of the main types of tropospheric aerosols.

Figure 1.8 presents the average single scattering albedo spectral profiles (440 and 1020 nm) and the associated size distributions of urban/industrial type aerosols, biomass fires, desert, and ocean dust. We can see that urban/industrial and biomass fires aerosols have overall a lower SSA than those of desert and ocean aerosols, highlighting the more absorbing properties of these type of particles. Differences in their spectral dependence are also observed with positive dependencies for desert aerosols and negative for other types of aerosols, with very marked dependencies for biomass fire aerosols. Some difficulties to validate these algorithms are the current uncertainties in the inversions associated with low to moderate aerosol loads (AOD < 0.4) and the lack of measurements and inversions in cloudy sky conditions.

Figure 1.7 Distribution of global AERONET sites (https://aeronet.gsfc.nasa.gov/)

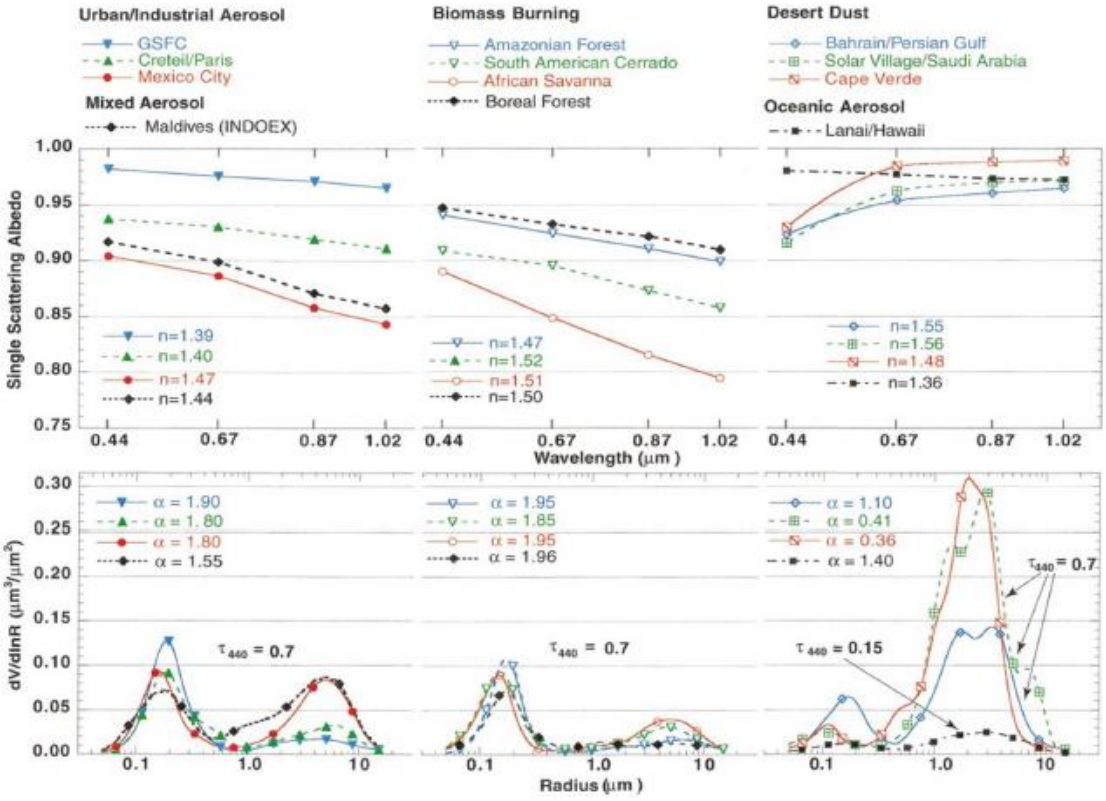

Figure 1.8 Averages of SSA and volume size distributions of the different types of tropospheric aerosols returned by the global AERONET network. Urban/industrial aerosols, aerosols from biomass fires, and mineral dust are represented for an AOD (τ_{440}) of 0.7, the oceanic aerosols for an AOD of 0.15, with the Ångström exponent estimated from the AODs at 440 and 870 nm. Source: Dubovik et al. (2002).

Furthermore, current satellites aerosol algorithms allow frequent and large-scale retrievals of aerosol loads and properties over the globe with only a few geographical limitations, such as cloudy areas and some continental areas, as ice surfaces in polar regions. These observations

display aerosol transports over large regional and global scales, allowing to better estimate the role of aerosols on climate. During the past two decades, aerosol retrievals based on satellite observations have made great progress (Dubovik et al. 2011; Levy et al. 2010). Sensors like Moderate Resolution Imaging Spectro-radiometer (MODIS), Advanced Very High-Resolution Radiometer (AVHRR), Ozone Monitoring Instrument (OMI), and Polarization and Directionality of the Earth's Reflectance (POLDER) are examples of spaced-based instruments providing relevant observations of aerosol loads and properties. Retrieval satellite algorithms continue to make constant progress to retrieve aerosol key parameters (AOD, information on size and absorption) with better accuracy and for a wider range of conditions (as above cloudy scene and various continental surfaces).

1.4.2 In situ measurements

Air quality monitoring stations (e.g. in France: https://www.atmo-france.org/) are generally distributed over urban, peri-urban, and rural sites, yet continuous measurements of particles are usually limited to mass concentrations of PM_{10} and $PM_{2.5}$ and other regulated pollutants (Guerreiro et al. 2014; Putaud et al. 2010).

Efforts on monitoring aerosol properties over the world have formed networks such as ACTRIS (Aerosol, Clouds, and Trace Gases Research Infrastructure, https://www.actris.eu/about) at the European level, and GAW (Global Atmosphere Watch, https://www.gaw-wdca.org/). The goal of those research infrastructures is to produce high-quality data and information on short-lived atmospheric constituents and the processes leading to the variability of these constituents in natural and controlled atmospheres. Under the leadership of the Scientific Advisory Group (SAG) – Aerosols, the GAW aerosol network grew slowly through the decade 1997–2007, with the refinement of recommended measurements and sampling procedures (World Meteorological Organization, World Meteorological Organization, and Global Atmosphere Watch 2016), and the establishment of the World Data Center of Aerosols (WDCA) and the World Calibration Center for Aerosol Physical Properties (WCAAP). The GAW aerosol network was greatly strengthened, particularly in Europe, by the establishment of the EUSAAR program (European Supersites for Atmospheric Aerosol Research) in 2006. Its expansion was further enhanced by the NOAA Federated Aerosol Network (Andrews et al. 2019), which currently supports nearly 30 GAW aerosol stations (Figure 1.9) with scientific and technical advice, data acquisition software, and streamlined procedures for submitting quality-controlled data to the WDCA.

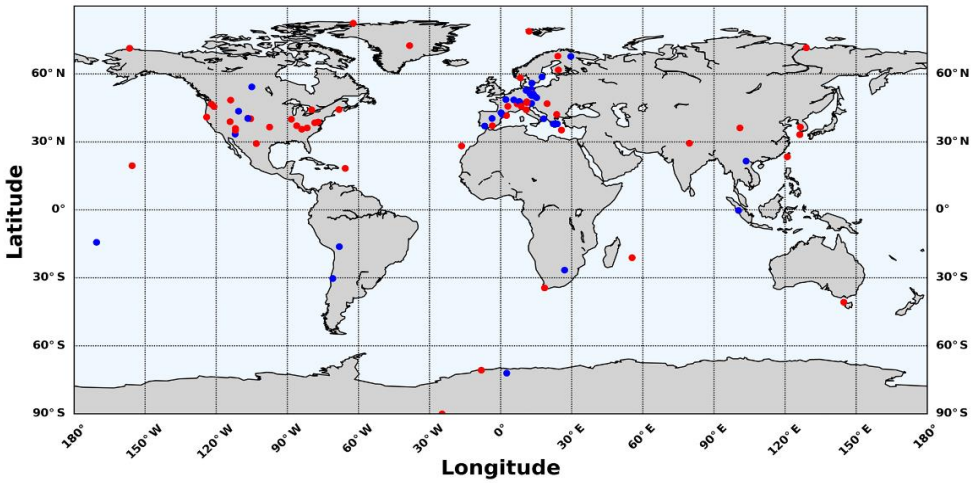

Figure 1.9 Location of sites contributing to the GAW (Global Atmosphere Watch) network. Shown in blue are the sites which provided information for the reference year 2017 and shown in red are the sites that in addition, provided > 10-year time series for optical properties. (Source: Collaud Coen et al., 2020; Laj et al., 2020)

The 'Chemical On-Line cOmpoSition and Source Apportionment of the fine aerosoL' project of the COST program (COLOSSAL, https://cost-colossal.eu/) was based on measurements performed mostly within ACTRIS sites. Chen et al. (2022) used 22 year-long datasets of online mass spectrometers from 14 different countries since 2013 to retrieve source apportionment of PM_1 as illustrated in Figure 1.10. In general, this work provides a comprehensive overview of the organic aerosol sources in Europe with highly time-resolved results. Most primary organic aerosol factors show enhanced contribution/mass concentrations during cold seasons compared to warm seasons. Chen et al. (2022) explain this enhancement with the growth in residential heating combined with lower boundary layer heights (lower temperature) causing stagnant conditions and accumulation of pollutants. In addition, Oxygenated Organic Aerosol components make up most of the submicron Org mass (average = 71.1%, ranging from 43.7 to 100%). Solid fuel combustion-related Org components (i.e., Biomass Burning - Org, Cooking - Org, and Solid Fuel - Org) are important with a total of 16.0% yearly contribution to the Org, increasing during winter months (21.4%).

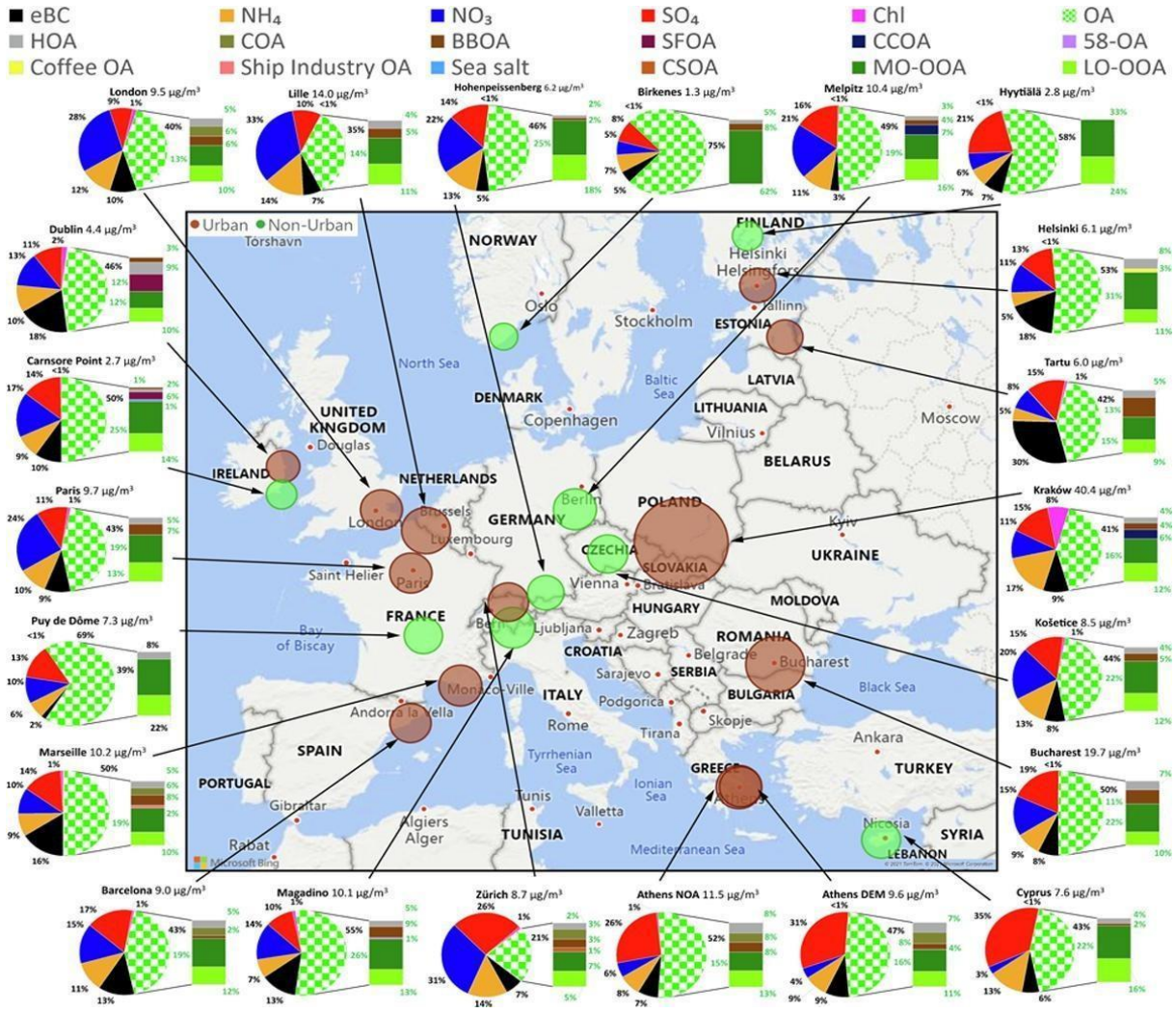

Figure 1.10 Submicron particulate matter (PM_1) mass concentration (in $\mu g/m^3$) and mass fractions of non-refractory inorganic species, equivalent black carbon (measured by online filter-based methods), and organic aerosol measured with the 22 online mass spectrometers at multiple locations in Europe covering all seasons. The size of the markers corresponds to the PM_1 mass concentration. The brown color of the marker indicates an urban site, while the green marker indicates a non-urban site. The checkered green/white shading of the pie charts denotes the organic aerosol fraction in PM_1, and the bar charts represent the contributions of each Org factor to the total Org mass. Source: Chen et al. (2022).

Regarding the aerosol optical properties at the surface level, Laj et al., (2020) collected high-quality data from almost 90 stations worldwide, controlled for quality, and reported for a reference year in 2017, providing a very extended and robust view of the variability of these variables worldwide. The range of variability observed for light scattering and absorption coefficients (Figure 1.11) and single-scattering albedo (Figure 1.12) are presented together with preliminary information on their long-term trends and comparison with model simulation for the different stations.

Overall, the variability in absorption and scattering (Figure 1.11) is high, the range covers several orders of magnitude explained by a few main drivers such as site latitude, site geographic localization/footprint, and the distance from the main anthropogenic sources. Some similarities can be observed globally, being both parameters featured by the largest variability at mountain sites whereas the minimum variability is observed at urban polluted sites (e.g. LEI – Germany, IPR – Italy) Regarding the mid-latitudes, the values of absorption and scattering increase from sites with a rural forest footprint towards those in mixed and urban conditions. The lowest values are related to polar sites both in the Arctic and Antarctic as well as in high altitude sites (e.g. JFJ – Switzerland, ZSF – Germany, and MLO – United States).

The higher variability at sites with low absorption and scattering reflect the contrasting transport, in the case of pristine sites, between the very low background values and the increase to advection of less clean air masses. For mountain sites, the contrasting diel or seasonal transport patterns. For instance, the site TIK (Tiksi - Russia) shows the largest medians among polar sites, where absorption spans over 1 order of magnitude, this reflects both clean and polluted air masses, most likely affected by biomass burning at the high latitudes.

The urban/peri-urban sites (e.g. LEI, UGR, IPR) exhibit the highest values and the smallest variability in both absorption and scattering. It is interesting to note that, occasionally the rural stations as AMY (East Asia) and KOS (Central Europe) show similar values of absorption to urban sites, despite being located in rural areas supposedly far from local sources. Looking at the temporal variability, the season median is much lower than the yearly variability reflecting the role of transport in the variability. High altitude sites have the most pronounced annual seasonality due to the seasonal variation of the boundary layer height and the local circulation induced by thermal winds that follow the ground temperature cycle. Urban sites (e.g. UGR, NOA, LEI-M) and those recurrently influenced by transport of either local or distant anthropogenic emissions (e.g. IPR, GSN) display a larger seasonality. BB can have a large influence on absorption seasonality and absolute levels too (Laj et al. 2020).

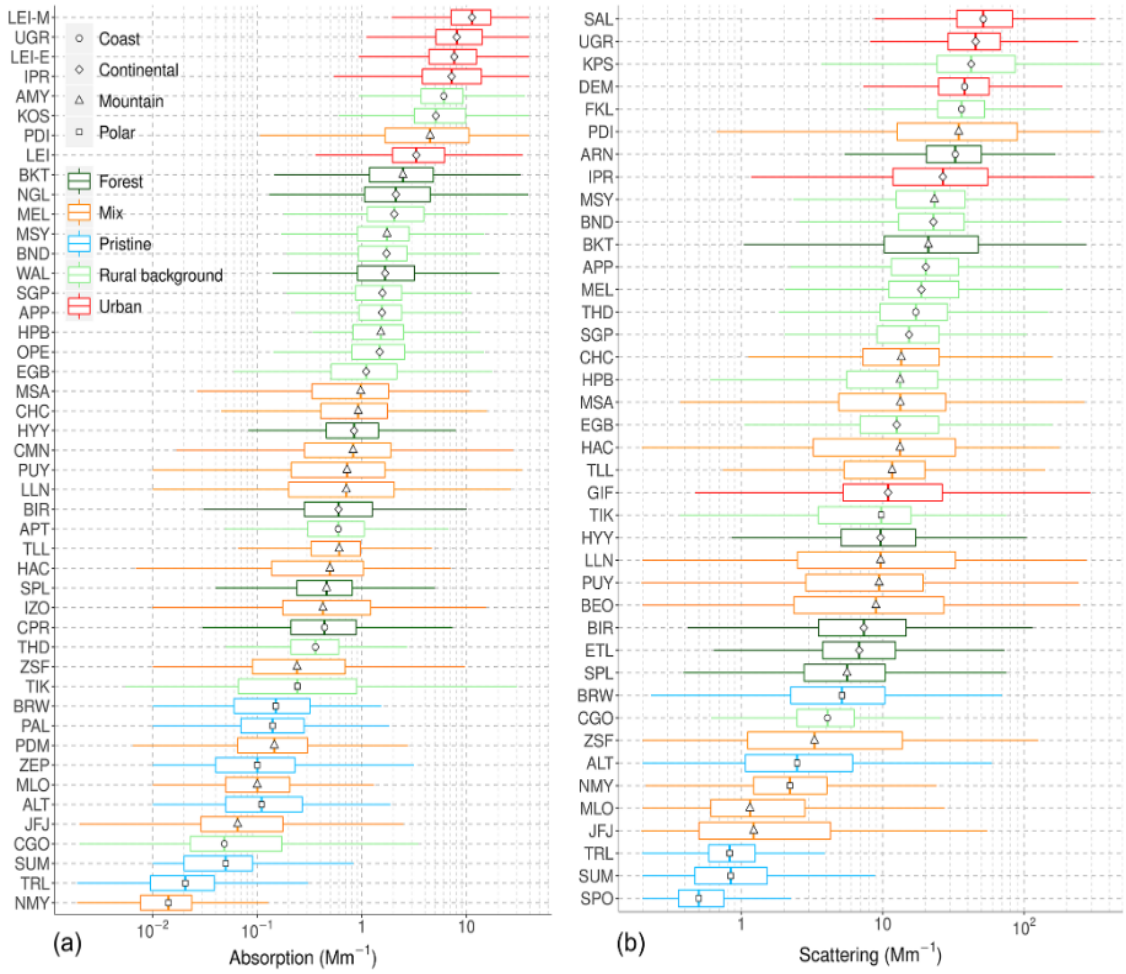

Figure 1.11 Boxplot of hourly aerosol absorption (a) and scattering (b) coefficients at the SARGAN (in-Situ AeRosol GAW observing Network) sites with sufficient annual coverage over the considered period (see Laj et al., 2020 for details). Boxplot color indicates the footprint and the symbol at the median indicates the geographical category; both color and symbol follow Table 3 in Laj et al., 2020

For stations providing simultaneous measurements of scattering and absorption coefficients, it is possible to derive the SSA (Figure 1.12), which is an important parameter for assessing aerosol radiative effects. Thus Laj et al. (2020) have summarized SSA ranges of values at 550 nm from measurements available at 31 stations. In general, the median values of SSA range from slightly less than 0.8 to almost purely scattering particles with SSA close to 1.

The highest SSA values are found at coastal and polar sites influenced by inorganic salts and sulfur-rich particles. The lowest SSA values are measured at sites in southern Europe (IPR and UGR), which are impacted by desert dust, biomass burning, and local anthropogenic emissions. Only six sites have median SSA values below 0.9 but only the coastal, mountain and polar sites exhibit 25th percentiles constantly above 0.9. The variability at sites characterized as “Mixed”, and in particular, the mountain sites, is not higher than at other places. The switch from free

tropospheric air to boundary layer for the mountain sites does not appear to significantly affect the SSA.

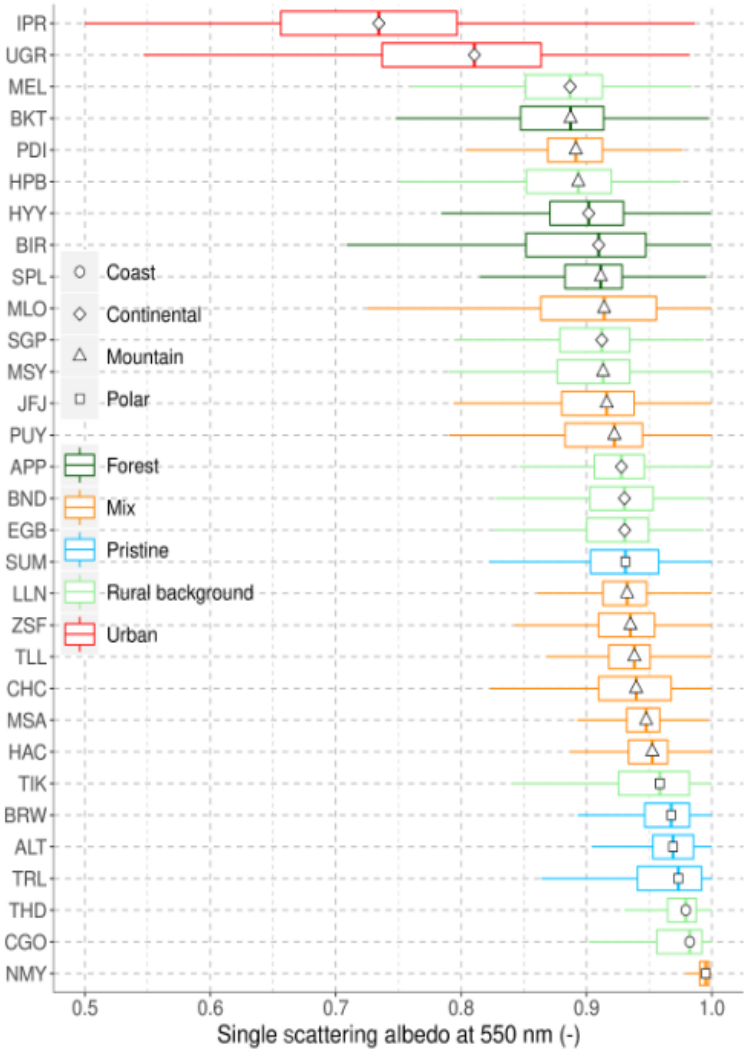

Figure 1.12 Boxplot of quantiles and annual median for single scattering albedo at 550 nm at the analyzed sites. Box color indicates the footprint according to Laj et al., 2020.

One of the current difficulties remains in establishing the relationship between the different types of measurements of the properties of aerosols, especially those derived from in situ and remote sensing approaches. It is important to note that remote sensing observations are generally effective over large spatial distributions, although in situ measurements are the most employed during field campaigns for limited periods or at long-term observation stations but in limited locations. In this thesis, long-term (about 3 years) in situ measurements are analyzed in northern France. Thus, instruments such as mass spectrometers dedicated to aerosol chemistry and those allowing to monitor collocated aerosol optical properties are described in the next chapter.

CHAPTER 2

2. ATmospheric Observations in liLLe (ATOLL) platform

This chapter describes the the ATOLL platform and its observations used throughout this thesis, with a focus on the instrumentation and data availability. This dataset combines both aerosol chemical and optical properties. While the chemical composition is measured only by in situ surface instruments, the optical parameters are derived also from passive remote sensing from the ground. In addition, PM concentration measurements performed at the nearby "Lille Fives" station belonging to the regional air quality network (Atmo Hauts-de-France) will be used.

2.1 Site description

The ATOLL platform (Figure 2.1) is located on the rooftop (Figure 2.2) of a building of the University of Lille in Villeneuve d'Ascq (50.6111° N, 3.1404° E, 70 m a.s.l.). Thanks to the deployment of a wide range of remote sensing and in situ instruments, the site provides near-continuous measurements of atmospheric composition and dynamics. The site, which is located 6 km southeast of the Lille downtown area, can be considered as suburban, without significant influence of local aerosol sources on fine PM concentration levels (Riffault et al. *in preparation*). With more than 1.1 million inhabitants, the metropolitan area of Lille is characterized by a high population density (1,765 inhabitants km^{-2}). As part of the North of France (Figure 2.1), ATOLL is located roughly ~15 km from the Belgium border to the North and East, 110 km from Brussels, 300 km from Amsterdam in the North-Northeast direction, 225 km from London in the Northwest direction, and 230 km from Paris to the South.

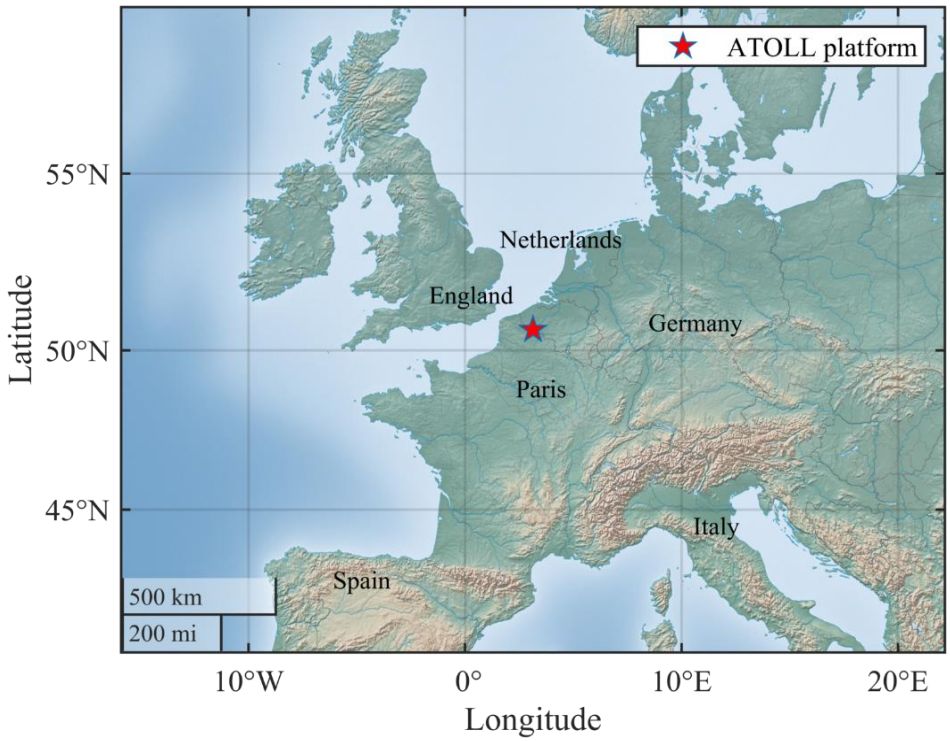

Figure 2.1 Location of the ATOLL platform.

Figure 2.2 ATOLL platform at the University of Lille - Cité Scientifique,Villeneuve d'Ascq

The ATOLL instrumental platform is dedicated to studying aerosol particles, clouds, and, to a lesser extent, gases, bringing together complementary observational tools. A large focus on the research on site has been historically dedicated to the calculation and measurement of radiation transfer in the Earth's atmosphere, essential prerequisites for the efficient development of remote sensing observation methods. In particular, ATOLL has a long-term database of sun/sky photometric measurements from the AERONET network (more than 20 years), as well as LIDAR data back from 2005, and a meteorological station measuring temperature, relative humidity, wind direction and speed, rain since 2005. Thus, ATOLL provides a large dataset of routine measurements of vertically integrated and vertically resolved aerosol optical properties, that include AOD and other aerosol parameters retrievals like particle size distribution over the atmospheric column. The instrumental activity deployed at ATOLL is part of several observational networks at the national level: Service National d'Observation (SNO) – PHOTONS / AERONET (Holben et al. 1998), SNO Network for the Detection of Atmospheric Composition Changes (NDACC) (De Mazière et al. 2018); at the European scale: the European Aerosol Research Lidar Network – EARLINET, ACTRIS (Pappalardo et al. 2014) and also at the international scale (AERONET, NDACC). Besides, ATOLL is part of the CARA program (Favez et al., 2021) and a French National Facility of the European ACTRIS Infrastructure network focusing on high-quality long-term atmospheric data.

2.2 Aerosol in situ instrumentation

Since October 2016 within the Laboratoire d'excellence – Physique et Chimie de l'environnement Atmosphérique (Labex CaPPA) framework, the Laboratoire d'Optique Atmosphérique (LOA) and the Centre for Energy and Environment (CERI EE) of IMT Nord Europe, have performed near real-time in situ aerosol measurements on the ATOLL platform aiming at better assessing the properties and impacts of the fine fraction of particles (PM_1) as well as the temporal variability of their chemical composition, sources, and optical properties. The instruments and measured parameters (Table 2.1) are going to be addressed in this section.

Table 2.1 List of in situ instrumentation and measured parameters in the PM_1 fraction

Instrument	**Measured parameters**	**Time resolution**	**Starting year**
Aerosol Chemical Speciation Monitor (ACSM)	Mass concentrations of Org, NH_4, SO_4, NO_3, Cl ($NR\text{-}PM_1$)	~30 min	2016
Aethalometer (7λ)	σ_{abs} & eBC	1 min	2016
Nephelometer (3λ)	σ_{scat}	1 min	2017
Mobility particle size spectrometer (MPSS)	Particle number concentration and size distribution (15 nm – 1 µm)	5 min	2017

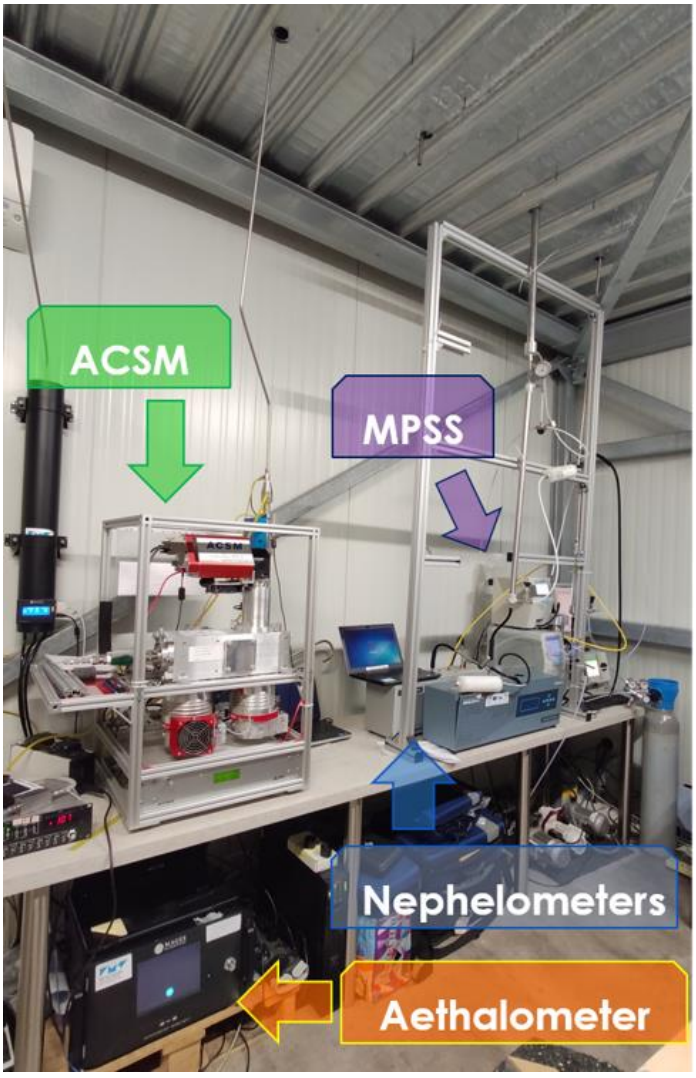

Figure 2.3 In situ instrumentation at the ATOLL platform in November 2022.

2.2.1 Mobility Particle Sizer Spectrometer (MPSS)

Over the past 10-15 years, MPSSs have been increasingly used for long-term measurements of atmospheric particle number size distributions (PNSD) in the submicron range. Depending on the instrument, at the site, the MPSS typically covers diameters from 15 – 800 nm. The atmospheric PNSD is an essential parameter required to assess the aerosol climatic, health, or ecosystem effects. It is also an important parameter concerning the description of aerosol dynamical processes as well as heterogeneous chemical reactions in the atmosphere.

MPSS integrates a setup of a bipolar diffusion charger (neutralizer), a Differential Mobility Analyzer (DMA), and a Condensation Particle Counter (CPC) (Wiedensohler et al. 2012). The neutralizer creates a known charge distribution of the aerosol population, then particles enter an electric field within the DMA. Particles of different electrical mobilities are selected by setting different voltages so their number concentration can be measured. The voltage yields an electrical particle mobility distribution, which can be inverted into a PNSD.

The quality of MPSS measurements is subject to the stability of the aerosol and sheath air flow rates as well as the performance of the CPC. An important issue for PNSD is the relative humidity in the instrument. Therefore, a means to achieve comparability between measurements is to limit the RH below 40%, minimizing the diameter changes due to hygroscopic growth to less than 5% (Swietlicki et al. 2008).

Figure 2.4 shows the MPSS scheme used at ATOLL. Crumeyrolle et al. (2022) described the MPSS system, consisting of a TSI model 3775 condensation particle counter, a TSI 3082 – type DMA, and a Nickel aerosol neutralizer (Ni-63; 95 MBq) downstream a $PM_{2.5}$ sampling head (URG-2000-30ED, URG Corp). The sheath flow rate is controlled with a critical orifice in a closed-loop arrangement (Mäkelä et al. 1997) and includes dryers to reduce RH in the aerosol sample. Furthermore, the sheath air loop contains a heat exchanger and HEPA (High-Efficiency Particle) filters. Sensors continuously record the aerosol and sheath air flow rates, RH and temperature in both flows, and absolute pressure in the aerosol flow entering the DMA. Typically, the scan time was chosen to be 300 seconds. To consider the multiple charge effect and the losses through diffusion, particle concentrations are corrected using the equation given by the manufacturer specifications (AIM 10.2.0.11).

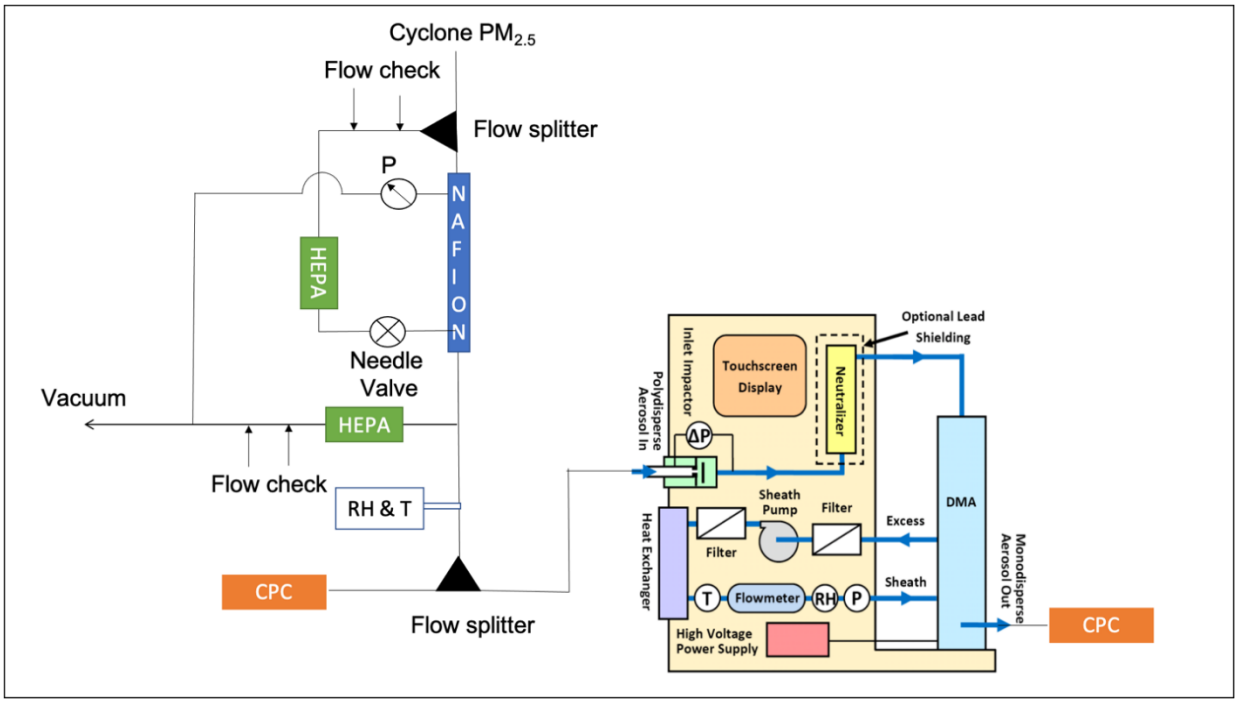

Figure 2.4 Flow schematic of the MPSS used at ATOLL. The setup includes dryers for aerosol and sheath air flows, heat exchanger, particle filters, as well as sensors for aerosol and sheath air flow rate, relative humidity and temperature.

2.2.2 Aerosol Chemical Speciation Monitor (ACSM)

The Aerosol Chemical Speciation Monitor (ACSM) is an instrument that provides chemically speciated mass loadings and aerosol mass spectra data of five non-refractory submicron aerosol particles species: organics, nitrate, sulfate, ammonium, and non-sea salt chloride (Ng et al. 2011). A schematic of the ACSM is shown in Figure 2.5; the instrument consists of three vacuum chambers that are differentially pumped by turbo pumps and backed by a small diaphragm pump. During operation, an aerodynamic lens is used to efficiently sample and focus submicron particles into the ACSM. The focused particle beam is transmitted through the two chambers into the final detection chamber where particles impact and flash vaporize on a hot oven; non-refractory particle material that vaporizes at typically 600°C is subsequently detected and chemically characterized with 70 eV electron impact quadruple mass spectrometry. These ions will be detected by a quadripolar mass spectrometer (RGA, for Residual Gas Analyzer) allowing the characterization of the different species by obtaining mass/charge spectra. The "filtered air" gas mass spectra are then subtracted from the unfiltered spectra to obtain an aerosol-specific mass spectrum. Mineral dust, soot carbon (BC for Black Carbon), and sea salt (SS) must be subjected to temperatures above 600°C to be vaporized, and therefore cannot be detected by the instrument. The detection chamber also contains an effusive source of naphthalene which is used for calibration and routine monitoring of instrument performance.

The ACSM does not measure the size distribution of the particles. The model used here is a Q-ACSM because the detector is a quadrupole analyzer, which also results in lower mass resolution (typically one unit) and lower sensitivity. The detection limits defined by Ng et al. (2011) are, in

μg m^{-3}, 0.28 for ammonium, 0.15 for organic compounds, 0.02 for sulfate, 0.01 for nitrate, and 0.01 for chloride. Since the instrument can be used routinely, its use is favored during long-term field campaigns.

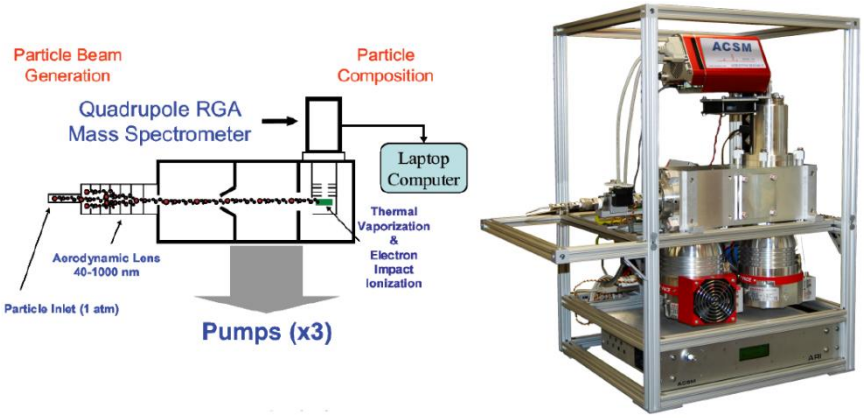

Figure 2.5 Schematic of the ACSM. (see Ng et al. (2011) for more details)

At the ATOLL platform, sampling of the ambient air is carried out through a sampling line oriented vertically to the instrument with a flow of 3L min^{-1}. This line is equipped upstream with a $PM_{2.5}$ sampling head (URG-2000-30ED, URG Corp.) and then through a Nafion dryer with stainless steel tubing (2.3 m) all along, to reduce the relative humidity (RH) of the sample. Particle loss in the sample line was estimated at less than 2% between 50 nm and 1 μm (the size range sampled by the ACSM aerodynamic lens system) using the Particle Loss Calculator developed by von der Weiden et al. (2009)

As the analysis is based on mass spectrometry, the previously mentioned NR species names refer to the sum of the m/z fragments of a species defined in a fragmentation table (Allan et al. 2004; Canagaratna et al. 2007). Therefore, the sums of the fragments $H_{0\leq x\leq 2}S_{0<y\leq 1}O_{0\leq z\leq 4}$ corresponding to sulfate, $NH_{0<x\leq 2}$ to ammonium, $NO_{0\leq x\leq 2}$ and HNO_3 to nitrate, $H_{0\leq x\leq 1}Cl$ to chloride and the rest of the fragments are attributed to Org. Each m/z fragment of the mass spectra is assigned to one or more species based on a fragmentation table developed by Allan et al. (2004) and improved by Canagaratna et al. (2007). The assignment of these spectra makes it possible to obtain the mass concentrations (Cs) of each species using the following equation:

$$Cs = \frac{CE}{Tm_{/z}} \times \frac{10^{12}}{RIE_s} \times \frac{Q_{cal}G_{cal}}{RF_{NOs}} \times \frac{1}{QG} \times \sum_i IC_{s,i} \qquad \text{eq. 2.1}$$

where the CE corresponds to the composition-dependent Collection Efficiency, $T_{m/z}$ is the correction of the transmission efficiency of the quadrupole ions (measured by monitoring the naphthalene peaks, emitted continuously under the vaporization zone), RIE refers to the Relative Ionization Efficiencies for each species compared to NO_3^-, RF_{NO3} is the nitrate Response Factor, Q and G are the volume flow (cm^3 s^{-1}) and the gain of the multiplier during the measurement and their equivalents (Q_{cal} and G_{cal}) obtained during the calibration of the RF_{NO3}, and $IC_{s,i}$ is the signal intensity of each fragment i of the species s.

RF_{NO3} calibrations are performed by measuring the intensity of NO_3^- ACSM signals, in response to the injection of known concentrations of NO_3^-. Aerosols of monodispersed ammonium nitrate are generated by vaporization of an aqueous solution of NH_4NO_3 (Sigma-Aldrich, >99.0%) at 5×10^{-3} mol L^{-1}. These aerosols generated using an atomizer are then dried, then filtered employing a bypass system used to manually regulate the aerosol concentrations, all before being sent to an electrostatic classifier (model 3080, TSI). This classifier is composed of a neutralizer to reduce electrostatic losses of particles and a differential mobility analyzer (DMA) which will make it possible to select particles with a diameter of 300 nm. These monodispersed aerosols are then sent in parallel to a particle counter (CPC model 3788, TSI) and the ACSM. Knowledge of the particle size (300 nm) and the particle number concentration (N_{CPC}) given by the CPC provides access to the NO_3^- concentration (in µg m^{-3}), calculated using the following equation:

$$[NO_3^-] = N_{CPC} \times S \times V_{part} \times \rho \times \frac{M(NO_3^-)}{M(NH_4NO_3)} \quad \text{eq. 2.2}$$

where S is the shape factor (equal to 0.8 in the case of ammonium nitrate), V_{part} is the volume of a particle (in cm^3) considering spherical particles, ρ the density of ammonium nitrate (1.72 g cm^{-3}), and $M(NO_3^-)$ and $M(NH_4NO_3)$ the respective molar masses of nitrate and ammonium nitrate. RF_{NO3} is then obtained by linear regression between the intensity of the NO_3^- signal (in amperes), which corresponds to the sum of the NO^+ (m/z 30) and NO_2^+ (m/z 46) signals measured by the ACSM, and the number concentration (N_{CPC}) obtained via the CPC (eq. 2.2). The RIE of NH_4^+ is obtained in parallel, by replacing in eq 2.2 nitrate by NH_4^+ and dividing the slope obtained in the linear regression between the intensity of the NH_4^+ signal (sum of m/z 15, 16 and 17) and the $[NH_4^+]_{cpc}$ by the value of RF_{NO3}. The RIE values of SO_4^{2-} and Cl^- are obtained in a similar way to that of NH_4^+ using ammonium sulfate and chloride solutions, respectively, however, considering that CE is not necessarily 100% for those aerosols. Calibrations are typically performed once a year, and an average value is used for the ACTRIS annual reporting. The RIE for NO_3 was considered as 1.1 until 2018 then 1.05 from 2019 to account for additional m/z related to NO_3, and the RIE for Org at 1.4, as recommended by the manufacturer and following ACTRIS/COLOSSAL standard operating procedure (European Center for Aerosol Calibration and Characterization 2022). The concentrations measured by the ACSM are determined by applying the RF and RIE values for each species shown in Table 2.2. Values are consistently checked regarding the ion balance (measured versus predicted NH_4) as well as with $PM_{2.5}$ concentrations determined by the regional air quality monitoring network at the Lille Fives station.

Table 2.2 RF and RIE calibration values used for ACSM measurements at the ATOLL platform.

Year	RF(NO_3) $\times10^{-11}$	RIE (NH_4^+)	RIE (SO_4^{2-})	RIE (Cl^-)
2016-2017	3.5	4	0.65	2.3
2018-2020	5.1	4.3	0.86	2.3

Finally, losses can occur during the passage of the particles at the level of the aerodynamic lens (Hoffmann et al. 2016), and throughout the vaporization process, in particular by the bouncing of particles before vaporization or deflection of the non-spherical particles. Indeed, the main factors

influencing CE are microphysical properties (size and sphericity), the acidity of the particles, nitrate content, and RH within the sampling line. Therefore, a correction due to the collection efficiency is applied to the concentrations following the algorithm developed by Middlebrook et al. (2012).

2.2.3 Aethalometer

Equivalent Black carbon (eBC in µg m^{-3}, defined as black carbon concentration derived from optical absorption methods) concentrations and the absorption coefficients (σ_{abs}, in Mm^{-1}) are continuously measured with a seven-wavelength (370, 470, 525, 590, 660, 880 and 950 nm) aethalometer (AE33, Magee Scientific Inc., Figure 2.6) (Cuesta-Mosquera et al. 2021; Drinovec et al. 2015). According to ACTRIS current guidelines (https://actris-ecac.eu/particle-light-absorption.html), σ_{abs} coefficients at each wavelength have been recalculated by multiplying eBC by the mass-specific absorption coefficient (MAC, 18.47, 14.54, 13.14, 11.58, 10.35, 7.7 and 7.19 m^2 g^{-1}, respectively for each wavelength), then dividing by the suitable harmonization factor to account for the filter multiple scattering effects: 2.21 (M8020 filter tape) until the end of 2017 then 1.76 (M8060 filter tape) from 2018. The Aethalometer is sampling at 5 L min^{-1} downstream a PM_1 cyclone (BGI SCC1.197, Mesa Labs) with a stainless-steel line (2.6 m) and flexible tubing (1.85 m) designed to limit the aerosol electrostatic losses at a time resolution of 1 min.

The AE33 principle consists in measuring the optical attenuation of a light beam (Beer-Lambert law) following its transmission through a filter onto which particles are deposited over time. The attenuation coefficient is then converted into an absorption coefficient for each wavelength. In the case of the AE33, two corrections are applied: the first proposed by Weingartner et al, (2003) aims at overcoming artifacts such as the absorption of radiation inside the filter by applying a factor C=1.57, specific to the instrument filter (Drinovec et al. 2015). The second correction uses the "dual spot" technology to get rid of the filter loading effect, all the characteristics of the instrument being developed in more detail in the article by Drinovec et al. (2015).

In this thesis, we apportion black carbon sources at the ATOLL platform in µg m^{-3}, applying the methodology of Sandradewi et al. (2008) to AE33 observations, obtaining eBC from fossil fuel (BC_{ff}) applying an AAE = 1, and from wood burning (BC_{wb}) using an AAE = 2.

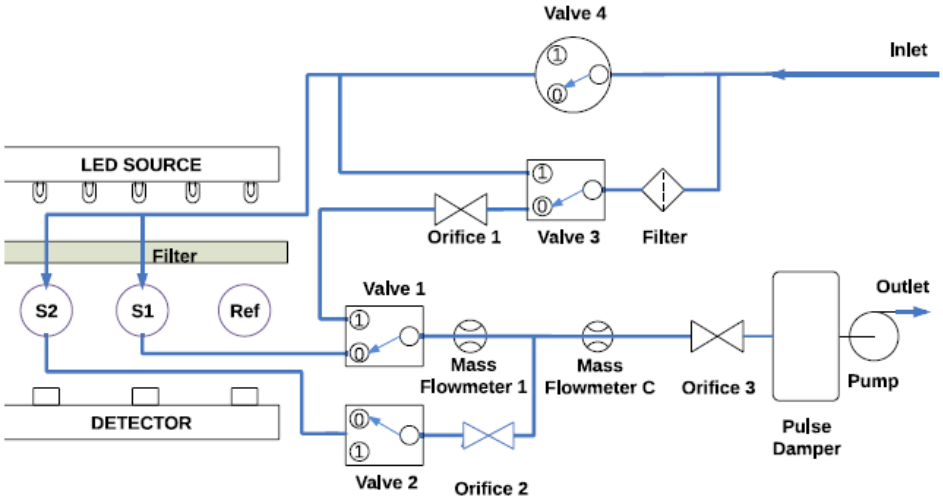

Figure 2.6 AE33 flow diagram (bottom) and instrument (top). During measurement, the inlet air passes through filter spots S1 and S2, each at a different flow rate, as set by the critical orifice 2. Airflow through S1 is measured by the mass flowmeter 1; flow through S2 is calculated as the difference between the total flow (flowmeter C) and flow through S1. The valves are used for routing airflow during different modes of operation. The bypass mode is used during the tape advance procedure with critical orifice 1 mimicking the filter flow resistance. Source: Drinovec et al., 2015.

2.2.4 Nephelometer

Dry scattering coefficient (σ_{scat}, in Mm^{-1}) measurements are performed using two Aurora (ECOTECH) nephelometers (4000 and 3000). Both nephelometers are running in series, with a Nafion dryer upstream of both instruments (<40% RH), and a PM_1 cyclone prior to the Aurora 3000. Therefore, dry scattering coefficients are measured first within the total suspended particle (A-4000) then within the PM_1 (A-3000) fractions. Both nephelometers are calibrated daily using filtered air and monthly using CO_2. For this chapter, the PM_1 fraction is of interest, therefore, here, we present the A-3000 specifications.

The nephelometer (Figure 2.7) allows real-time and continuous measurement of the diffusion coefficient of particles at 450, 525 and 635 nm. The measurement is made by passing a light ray through a volume of air containing aerosols. This radiation will be reflected differently depending on the nature of the compounds, the shape and size of each particle before being detected by means of a photodiode. This step makes it possible to obtain the diffusion coefficients of the air sampled in the cell from the Beer-Lambert law. The diffusion coefficient needs to be corrected for measurement artifacts related to truncation and angular non-ideality of the light intensity. The correction factors applied to the diffusion coefficient are determined with respect to the values proposed by Müller et al. (2011) for each wavelength. These correction factors will also depend on the size of the sampled particles which can be found from the Ångström exponent measurement. Anderson and Ogren, (1998) propose a threshold of the Ångstrom coefficient (0.75) corresponding to sub- and super-micron particles in order to apply the correction factors.

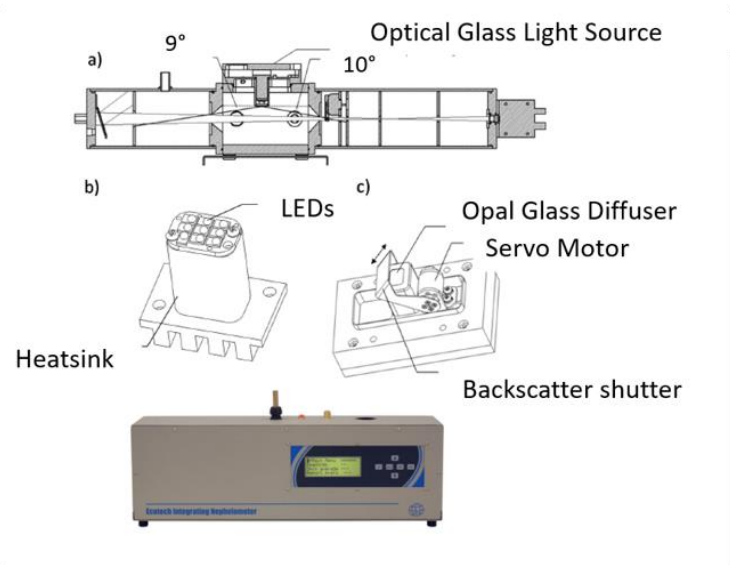

Figure 2.7 Sketch and picture of the Nephelometer – Aurora 3000. (a) Sensing volume and indicated truncation angles, (b) arrangement of LEDs, (c) light source with motor driven backscatter shutter. Source: Müller et al. (2011)

2.3 Aerosol photometer measurements

As previously mentioned, the photometer (Figure 2.8) is a passive remote sensing instrument that performs direct measurements of solar radiation and sky luminance at several wavelengths from the ground; those wavelengths can be 340, 380, 440, 500, 675, 870 and 1020 nm. This instrument performs the retrieval of microphysical and optical properties of aerosol vertically integrated into the atmospheric column. The instrument uses sunlight (and possibly moonlight) as a radiative source and therefore cannot perform measurements under cloudy cover conditions. The photometers present in Lille can make measurements every 15 minutes during clear sky days.

The primary optical parameter returned from the photometer direct solar radiation measurements is the AOD of the atmospheric column. The AOD corresponds to the integration over the column of the total extinction corrected for molecular optical thickness, ozone and Rayleigh scattering calibrated at specific sites. The AOD is available at the multiple wavelengths previously mentioned. AOD uncertainties are lower than 0.01 for wavelengths longer than 440 nm (Holben et al. 1998), thus the Ångstrom Exponent (AE) calculation from a pair of AOD at two different wavelengths is possible. In chapter 3 of this thesis, AE is analyzed at 440-870 nm. Moreover, aerosol size distribution, coarse-to-fine particle volume ratio, fine mode AOD and SSA can be retrieved with an inversion algorithm developed by Dubovik and King (Dubovik and King 2000).

The AERONET data are available for three quality levels: Level 1.0 data are post-processed in near-real time (post-calibration coefficient); Level 1.5 are pre-calibrated data for which a first cloud filter is applied (Smirnov et al. 2000), yet it may be still affected by the presence of anomalies (cloudy or other); Level 2.0 data are corrected by a definitive calibration coefficient (interpolated between pre- and post-calibration) in addition to a manual or automatic quality control. In chapter 3 the AOD and AE used are from Level 2.

Figure 2.8 CIMEL Sun/Sky Photometer. Source : www.cimel.fr.

2.4 Data availability

Table 2.3 summarizes the measured datasets investigated in this thesis. Here, each chapter focuses on a specific period, conditioned by its scientific objectives. For instance, in chapter 3, we analyze the long-temporal series of aerosol optical properties (absorption and scattering coefficients, SSA, AOD, AE), aerosol chemical compositions (NR-PM_1, eBC), and meteorological observations (wind speed, wind direction, temperature, relative humidity), thus, the period of observations vary as a function of the instrument (e.g. AOD is investigated from January 2008 – December 2021). Furthermore, chapter 4 analyzes the period from July 2017 – December 2019, and chapter 5 analyzes the period from December 2016 – December 2019. The MPSS data was only used to compare the PNSD with the extinction coefficient retrieved aiming to look at the effect of size in aerosol retrieval. Further analysis of MPSS data can be found in Crumeyrolle et al. (2022). Finally, the time resolution employed also depends on the type of analysis. The time resolution used in chapter 4 is 30 min for comparison with the ACSM observations, whereas in chapters 3 and 5, the time resolution used is hourly averages.

Table 2.3 Datasets of the various in situ chemical and optical quantities measured and used in this thesis. In parentheses: units of the parameters.

Instrument	Parameter	Period	Time stamp	# of points	30 min avg	Hourly avg
ACSM	Chemical composition of NR-PM_1 (µg m^{-3})	11/Oct/2016 - 31/Dec/2020	~ 30 min	48 025	NA*	25 759
Aethalometer	eBC (µg m^{-3}), σ_{abs} (Mm^{-1})	12/Dec/2016 - 31/Dec/2021	1 min	2 168 230	44 505	37 085
Nephelometer	σ_{scat} (Mm^{-1})	28/Jul/2017 - 31/Dec/2020	1 min	1 316 332	29 661	23 319
Anemometer	Wind direction	01/Jan/2014 - 31/Aug/2022	5 min	810 983	44 104	49 778
	Wind speed					
Davis/RPG station	Temperature		1 min	4 314 643	43 883	51 211
	Relative Humidity			4 318 655	43 902	51 226
Photometer	AOD	01/Jan/2008 - 31/Dec/2021	15 min	94 592	NA*	16 274
	AE					

*NA - not applicable

In this chapter, the operating principles of the main instruments used in the chemical and optical characterization of surface aerosols have been detailed. The setup established at ATOLL allows for a detailed study of particulate pollution in the area. For instance, the long-term observations of the optical parameters vertically integrated (AOD, AE) allow to study the possible changes of pollution levels over more than 10 years. Furthermore, by analyzing the seasonal and daily variability of the chemical and optical measurements at the ground, we are able to identify potential emission sources in the region. Thus, in the following chapter, we present the temporal variability of these observations.

CHAPTER 3

3. Aerosol variability measured in Lille

The aim of this chapter is to analyze the atmospheric conditions at ATOLL over different time scales (annually, seasonally, daily), leading to a better description of the site and its aerosol population over the seasons and years. Moreover, the particle properties (e.g. chemical composition and SSA) observed during pollution events following the latest WHO AQG were analyzed for the period 2013 – 2020. This chapter will serve furthermore as a foundation for the detailed analysis performed in the following chapters.

3.1 Meteorological conditions

The French territory experiences frequent winds coming from the Atlantic Ocean leading to a temperate climate. The Northern France region, and more precisely, Lille, has oceanic weather, as classified by the French National Meteorological Service (MeteoFrance, https://meteofrance.com/), characterized by mild temperatures and relatively abundant rainfall (in connection with the disturbances coming from the Atlantic Ocean), distributed throughout the year with a slight maximum from October to February. Figure 3.1 represents the weather measurements at the ATOLL platform from 2014 until August 2022. The multiannual temperature (T) average and standard deviation registered by the weather station at the site (11.9 °C) are comparable with the temperature registered by the Meteo-France weather station at the Lille-Lesquin airport (10.8 °C), 11 km apart from the ATOLL site. The multiannual minimal and maximum T registered at ATOLL is 40.4°C and -7.4°C. The average precipitation is 5.4 mm, for rain events larger than 1 mm. Figure 3.1c shows the multiannual wind rose highlighting the frequent (18%) winds from south-west with moderate wind speed (2-4 m s^{-1}).

Regarding the seasons (Table 3.1), the average temperature decreases by 70.2% during winter compared to summer. The season with higher relative humidity (RH) is winter with an average of 88.1% and the season with higher precipitation is summer. Figure 3.2 analyzes the diel cycles of temperature and RH, showing that both variables have anti-correlated profiles on a seasonal and daily basis. The temperature shows a large gap between summer and winter while having similar profiles in spring and fall. The maximum temperature is reached during the afternoon, then it decreases in the evening and night until sunrise. On the contrary, RH has its maximum value during nighttime in all seasons, and after sunrise, it decreases until hitting a minimum value at 14:00, when it starts to increase again as the sun goes down.

Table 3.1 Meteorological conditions measured at ATOLL for the period Jan. 2014 – Aug. 2022.

		Winter (DJF)	Spring (MAM)	Summer (JJA)	Fall (SON)
Temperature (°C)	Average	5.6	11.1	18.8	12.3
	Max	18.7	28.9	40.4	31.0
	Min	-7.4	-5.8	8.4	-2.7
RH (%)	Average	88.1	73.6	73.1	84.2
	Min	28	18.3	17	28.6
	Max	100	100	100	100
Rain (mm) from Lille-Lesquin station (5.5 km away)	Average (accumulated)	62.7	55.7	72.2	69.4
	Max (5 days)	65.0	61.8	84.9	76.0
	Averaged ≥ 1	4.8	5.0	6.5	5.2

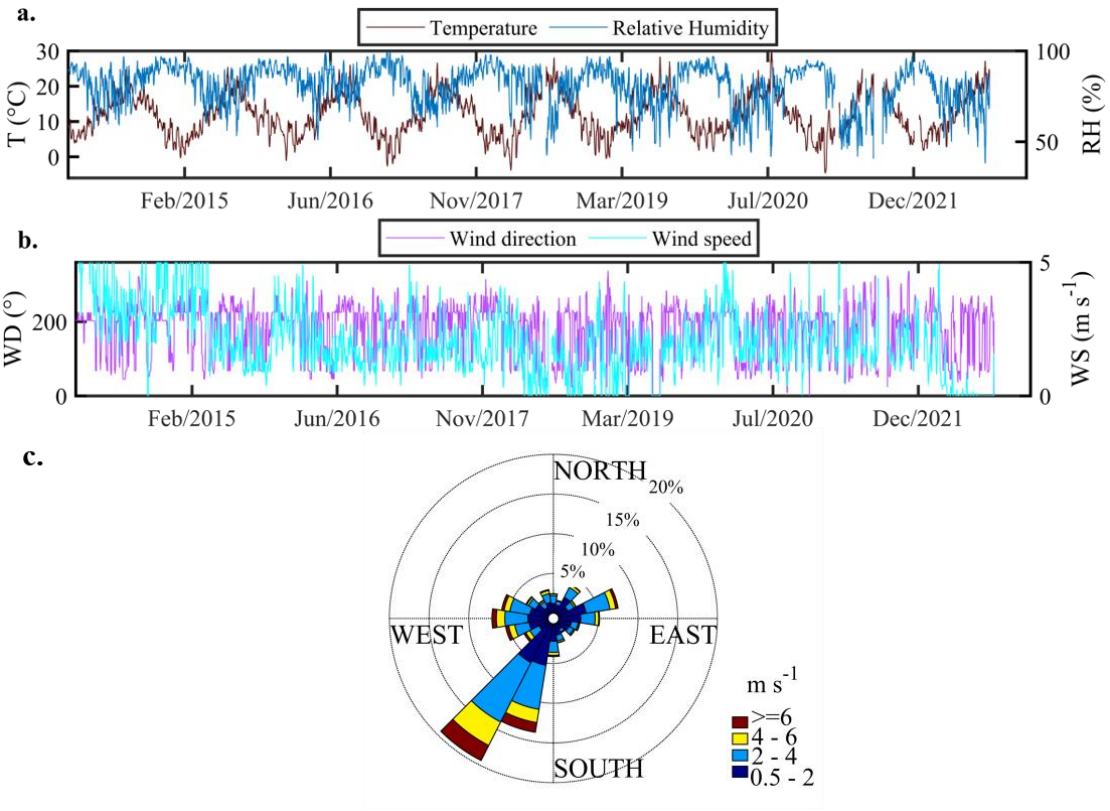

Figure 3.1 a-b) Time series of meteorological conditions (temperature, relative humidity, wind speed and wind direction. c) Multiannual wind roses from the period 2014 – 2021 at ATOLL. Time-frequency used: 1 min.

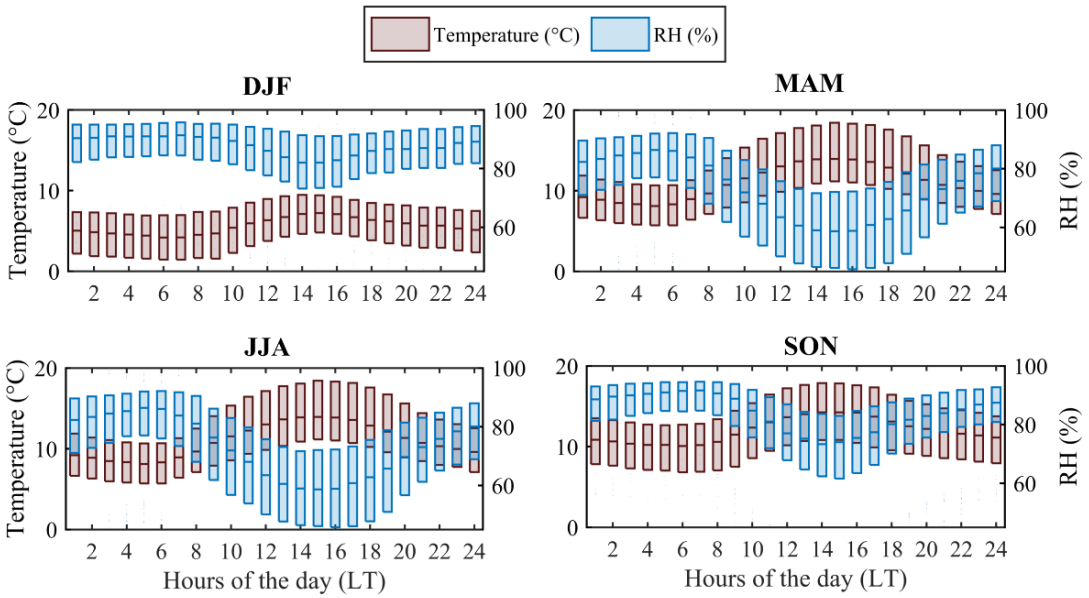

Figure 3.2 Diel cycles by season of the temperature (y axis left) and relative humidity (y axis right) for the period of 2014 – 2021. Time-frequency used: 1 hour average.

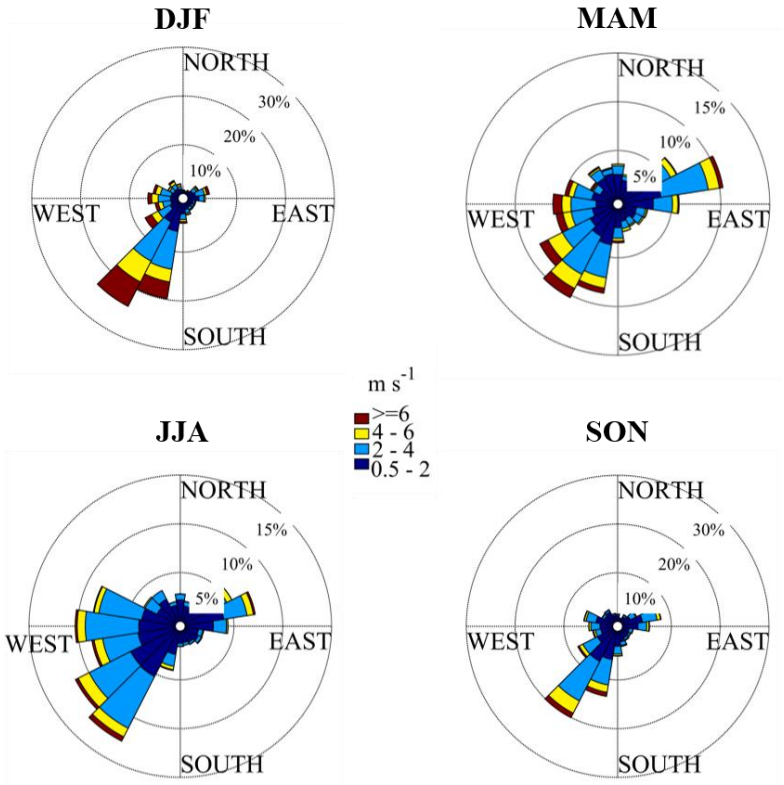

Figure 3.3 Seasonal wind roses with wind speed > 0.5 m s^{-1} at ATOLL for the period 2014 – 2021. Time-frequency used: 1min.

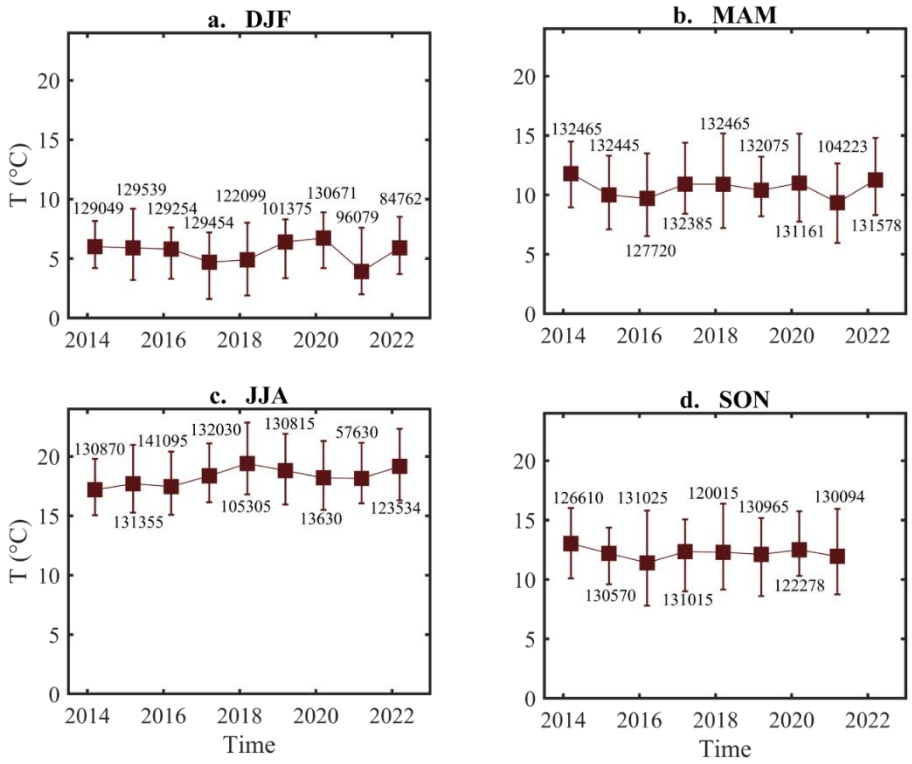

Figure 3.4 Evolution of annual temperature by seasons since 2014 at ATOLL. The square and bars represent the median, the 25th and 75th percentiles, respectively. The numbers within the plot indicate the number of points used. Time-frequency used: 1 min.

It is noteworthy to mention that the variation of the Boundary Layer Height (BLH) is consistent with the temperature diel cycle, as during the afternoon the vertical mixing is maximized due to the convection of warmer air masses. Figure 3.3 displays the seasonal wind roses at the ATOLL platform: the highest wind speeds and most frequent air masses usually come from the south-west (SW) sector. Conversely, during spring, the prevailing wind sector is from the north-east (NE) sector with wind speeds and frequency lower than SW winds. In general, previous field campaigns performed in Northern France agree with our results. For instance, Espina Martin, (2020) compares three different sites ~110 km apart from each other: suburban (Douai), rural (Caillouel-Crepigny), and remote (Revin). All sites have a common predominant SW sector and the main difference is the drier conditions (less rain) at the rural site during the period of study.

Figure 3.4 shows the seasonal temperature statistics observed at the ATOLL platform. Despite the very limited 9-year statistics here, summer temperatures seem to show an upward trend, which would be consistent with the increasing frequency and intensity of heat waves in the region (Météo-France, 2020).

3.2 Particulate matter levels and pollution events

Various authors have investigated the particulate pollution in the Northern France area. For instance, Waked et al. (2014, 2018) studied the frequent PM_{10} pollution episodes in N-WE over the years 2009 – 2013. Their study reports PM_{10} average annual values for all sampling stations ranging from 24.8 ± 14.1 µg m^{-3} to 29.2 ± 14.8 µg m^{-3}, exceeding the WHO current annual guideline value (15 µg m^{-3}) but below the EU annual limit value (40 µg m^{-3}). Nevertheless, 8 out of the 12 sampling sites showed exceedances of the EU daily limit value of 50 µg m^{-3} for more than 35 days per year during the studied period. A median value of 24 µg m^{-3} was reported for $PM_{2.5}$ in North Western Europe for the 1997-

2007 period (Putaud et al. 2010), whereas other sites like Toulouse, France (Calvo et al. 2008) and Erfurt, Germany (Yue et al. 2008) reported lower mean $PM_{2.5}$ concentrations (11 and 19 µg m^{-3}), highlighting that the North Western region is subjected to high concentrations of PM.

In Figure 3.5, PM_{10} and $PM_{2.5}$ concentrations are presented from 2013 – 2021. The observations are from the nearest air quality monitoring station from ATOLL, "Lille-Fives" located roughly 4 km away, as described in section 2.1. The multiannual concentration average and standard deviation are in the range of values reported previously in the north of France by Waked et al. (2014): 20.8 ± 13.5 µg m^{-3} and 15.2 ± 11.7 µg m^{-3} for PM_{10} and $PM_{2.5}$, respectively. Furthermore, the highest PM_{10} and $PM_{2.5}$ concentrations were observed during spring (24.0 µg m^{-3} and 18.1 µg m^{-3}) and winter (21.5 µg m^{-3} and 16.6 µg m^{-3}). The average $PM_{2.5}/PM_{10}$ ratio is 0.73 for the period of analysis, with the highest ratio (0.77) in winter and the lowest (0.66) in summer. A lower $PM_{2.5}/PM_{10}$ ratio indicates domination of coarse particles, generally linked to natural sources (Tian et al. 2018) while a higher $PM_{2.5}/PM_{10}$ ratio points towards particle pollution from anthropogenic sources (Fan et al. 2020; Zhao et al. 2019).

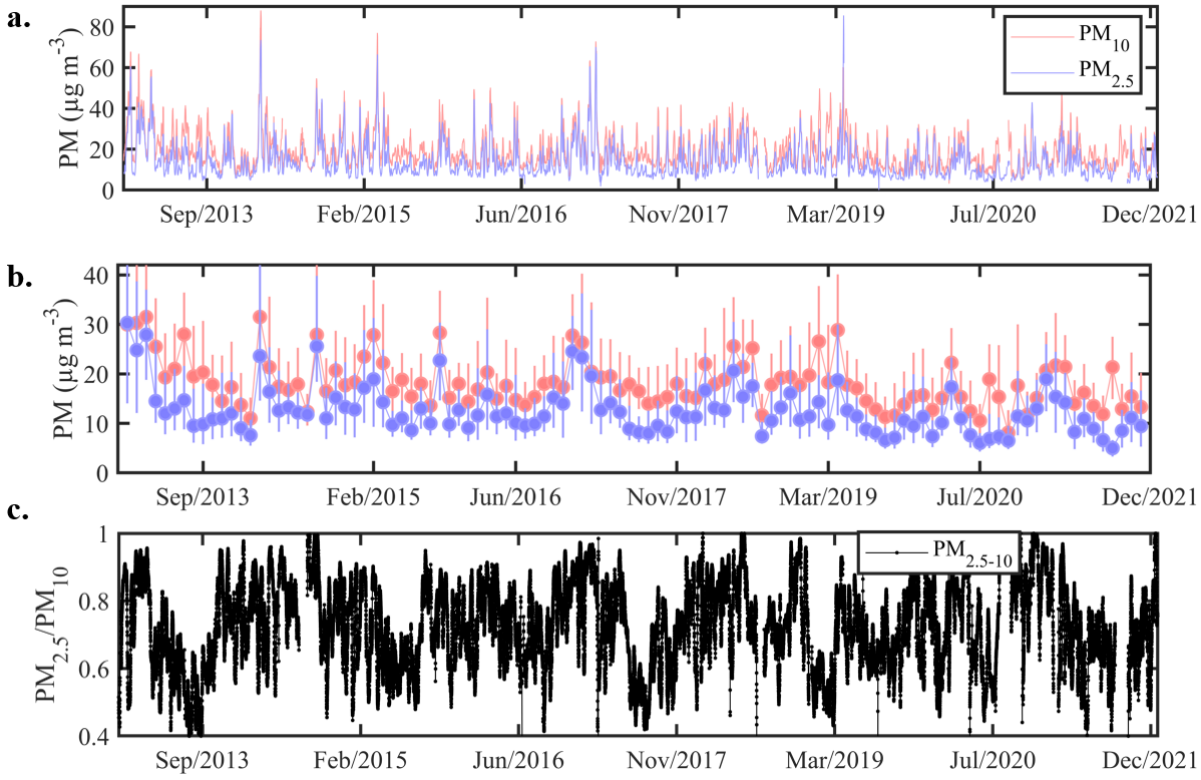

Figure 3.5 PM_{10} and $PM_{2.5}$ time series from the ATMO HdF "Lille Fives" station in Lille for the period Jan/2013 – Dec/2021. a) Hourly concentrations; b) Monthly concentrations (median and 25^{th} - 75^{th} percentile); c) Hourly time series of the $PM_{2.5}/PM_{10}$ ratio.

Figure 3.6 displays the averaged diel cycle of PM_{10} and $PM_{2.5}$ in Lille for each season, showing a co-variability between both PM_{10} and $PM_{2.5}$ concentration with two daily peaks, the morning rush, and an evening peak, highlighting, to some extent, the role of traffic at the Fives site, coupled with potential house heating during the cold months, or BLH influence in the warm months.

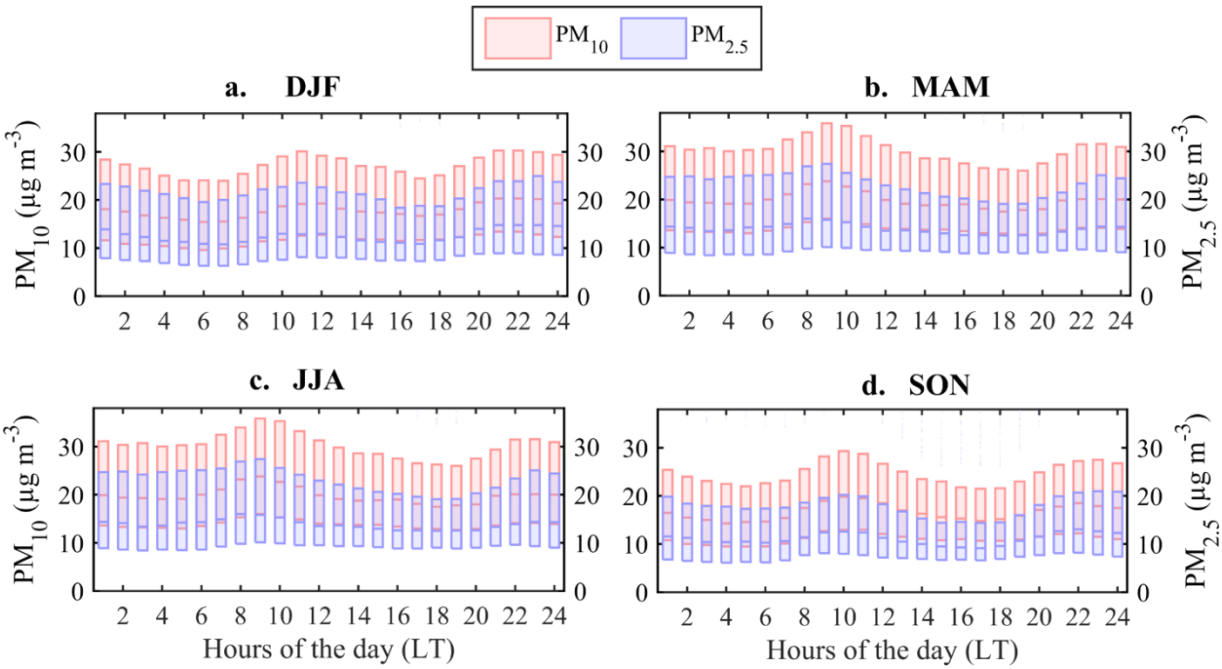

Figure 3.6 Seasonal diel averaged cycles of PM_{10} (red color, left y axis) and $PM_{2.5}$ (blue color, right y axis) concentration (in µg m^{-3}) at the Lille Fives station, binned per hour of the day in local time (LT). a) DJF (December, January and February) – winter. b) MAM (March, April, May) – spring. c) JJA (Jun, July, August) – summer. d) SON (September, October, November) – fall. Time-frequency used: 1 hour.

Here, we calculate the linear trend of the data series by least square fitting employing the climate data toolbox (Greene et al. 2019). It is worth noting that the limited number of years considered in this analysis limits the robustness of the calculated trends. Furthermore, according to Font et al. (2022) including meteorological and temporal variables in this type of analysis is critical, since changes in concentrations can be attributed to emissions but also to changes associated with meteorological parameters and dispersion conditions. Therefore, caution has been exercised when interpreting trends here as an absolute reference in the decay/increase of concentrations linked exclusively to emissions.

Figure 3.7 displays the seasonal trend of PM_{10} and $PM_{2.5}$ concentrations for the 2013 - 2021 period. Overall, we see that both PM fractions suggest decreasing trends over the period across seasons. The PM_{10} seasonal trend is slightly higher (-0.8 µg m^{-3} yr^{-1}) in summer compared to the rest of the seasons (-0.6 µg m^{-3} yr^{-1}). It is noteworthy to mention that, for PM_{10} and $PM_{2.5}$, despite an overall downward trend (-0.7 and -0.5 µg m^{-3} yr^{-1}, respectively), interannual variations are recorded, their presence in the air being linked both to anthropogenic and natural emissions (primary particles), to the formation of secondary particles due to gaseous precursors, weather conditions and long-range transport of pollutants.

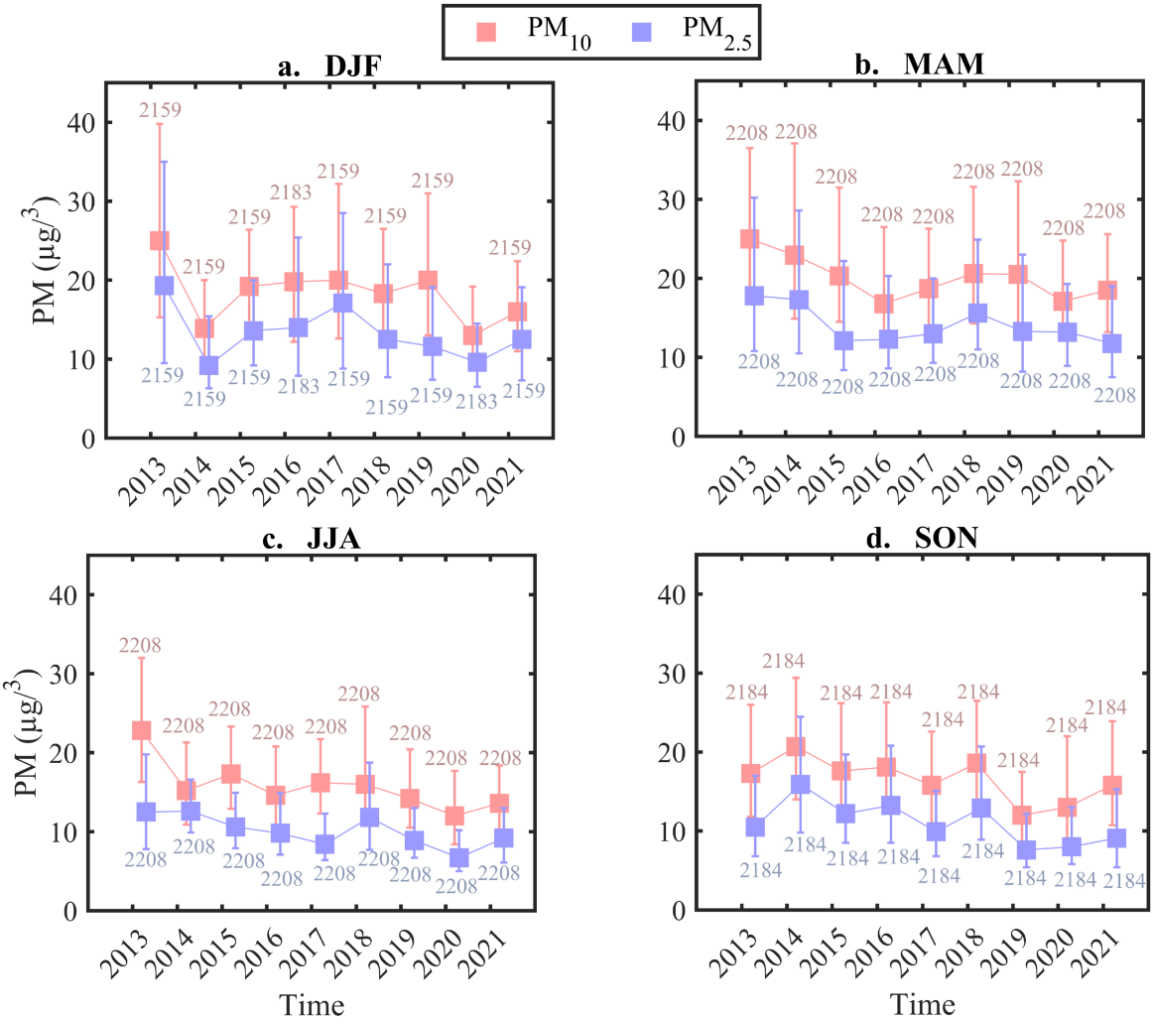

Figure 3.7 Averaged PM_{10} (red) and $PM_{2.5}$ (blue) levels for (a) winter, (b) spring, (c) summer, and (d) fall from 2013 to 2021. The square and the bars represent the median, the 25th and 75th percentiles, respectively. Time-frequency used: 1 hr. The numbers are the datapoints associated with each year.

At the ATOLL site, the chemical speciation is measured over the PM_1 fraction. This fraction accounts for 80% and 64% of $PM_{2.5}$ and PM_{10} concentrations measured at the Fives station (Appendix A3 - 7) and it shows a good correlation with both size fractions ($PM_{2.5}$, r^2: 0.80 and PM_{10}, r^2: 0.72). The $PM_1/PM_{2.5}$ (0.80) and PM_1/PM_{10} (0.64) ratios agree with typical values for urban sites. For instance, in Vienna (Gomišček et al. 2004), for one year of measurements, a $PM_1/PM_{2.5}$ ratio of 0.87 has been reported. Another study in Athens, Greece, shows a slightly lower $PM_1/PM_{2.5}$ ratio of 0.78 (Koulouri et al. 2013). The PM_1/PM_{10} ratio in Lille is in the higher range of values reported in stations nearby source combustion emissions, e.g. Phoenix (0.18 – 0.69, Lundgren et al. 1996), Taipei (0.22 – 0.60, Li and Lin, 2002) and Helsinki (0.46 – 0.65, Vallius et al. 2000).

The Northern France area, localized in the North-West European (N-WE) Megalopolis (Figure 1.4 and Figure 2.1), has been recognized as a hotspot for inorganic precursor gases (Espina Martin 2020) and PM (Hofman et al. 2016; Potier et al. 2019; Waked et al. 2014; 2018), with pollution episodes during winter and spring seasons. According to (Rega et al. 2020), the pollution episodes arise from high population densities (Appendix A3 - 4), extensive vehicular traffic and industries/power plants (emitting, among others, NO_x) (Appendix A3 - 3), as well as intensive agricultural practices maintaining consistently high NH_3 levels (Appendix A3 - 5).

Figure 3.8 shows the annual exceedances of $PM_{2.5}$ and PM_{10} concentrations from 2013 to 2021, following the AQG updated recently by the WHO (World Health Organization 2021). Figure 3.8a shows the number of exceedances days whereas, Figure 3.8b exhibits the trends in averaged concentrations of the exceedances per year. In addition, Figure 3.8c examines during the exceedance days, the PM_1 chemical composition and the single scattering albedo at 525 nm at the ATOLL platform.

Generally, the particulate pollution events also reflect the trend in PM concentration described previously in Figure 3.7. Indeed, the number of exceedance days (Figure 3.8a) for PM_{10} concentration (> 15 µg m^{-3}) has slightly decreased (33%) in time since 2013 (~ 273 events vs 187 in 2021). Similarly, the number of exceedance days for $PM_{2.5}$ concentration (> 5 µg m^{-3}) has slightly decreased (24%) during the period. This can be explained by the decrease in emissions of PM_{10} (e.g. dust from construction sites, industrial plants) and $PM_{2.5}$ sources (e.g. combustion from wood, oil, diesel fuel) discussed in section 3.2. In addition, we explored (Appendix A3 - 8) the difference of number of exceedance days using the previous WHO AQG standards (PM_{10} > 50 µg m^{-3} & $PM_{2.5}$ > 25 µg m^{-3}); as expected the number of exceedances days are lower than when applying the updated AQG. For example, for $PM_{2.5}$ concentration during the year 2021, only 20 pollution events appeared, while using the latest AQG, the number of events increased to 263.

Figure 3.8b shows the trend in mean PM concentrations calculated for the days exceeding the WHO limits, with results comparable to the trends shown in Figure 3.7. The mean PM concentration has decreased over the years since 2013. For the period analyzed here (2013 - 2021), PM_{10} concentration has moderately decreased (20%), having a 2021 average of 21.3 µg m^{-3}, about 40% above the WHO limit (15 µg m^{-3}), while the decrease in $PM_{2.5}$ (19%) still led to a 2021 average of 11.4 µg m^{-3}, more than twice the WHO limit (5 µg m^{-3}).

Figure 3.8c shows the evolution of the mean PM_1 chemical composition and the respective SSA when the PM_{10} or $PM_{2.5}$ concentrations exceed the WHO limits. Concerning the chemical composition when PM_{10} exceeds the 15 µg m^{-3} daily mean, the relative contribution of nitrate to PM_1 is 31% with an average SSA of 0.82. This is comparable when $PM_{2.5}$ exceeds 5 µg m^{-3}, with only 2% of difference in nitrate contribution and comparable average SSA (0.79). The high fraction of nitrate and SSA points out that exceedance days are linked with mild/low temperatures that favor AN formation. On the contrary, the SSA shows generally lower values (< 0.77) during the non-exceedance days, underlying the role of light-absorbing aerosols from combustion sources during “cleaner” site conditions.

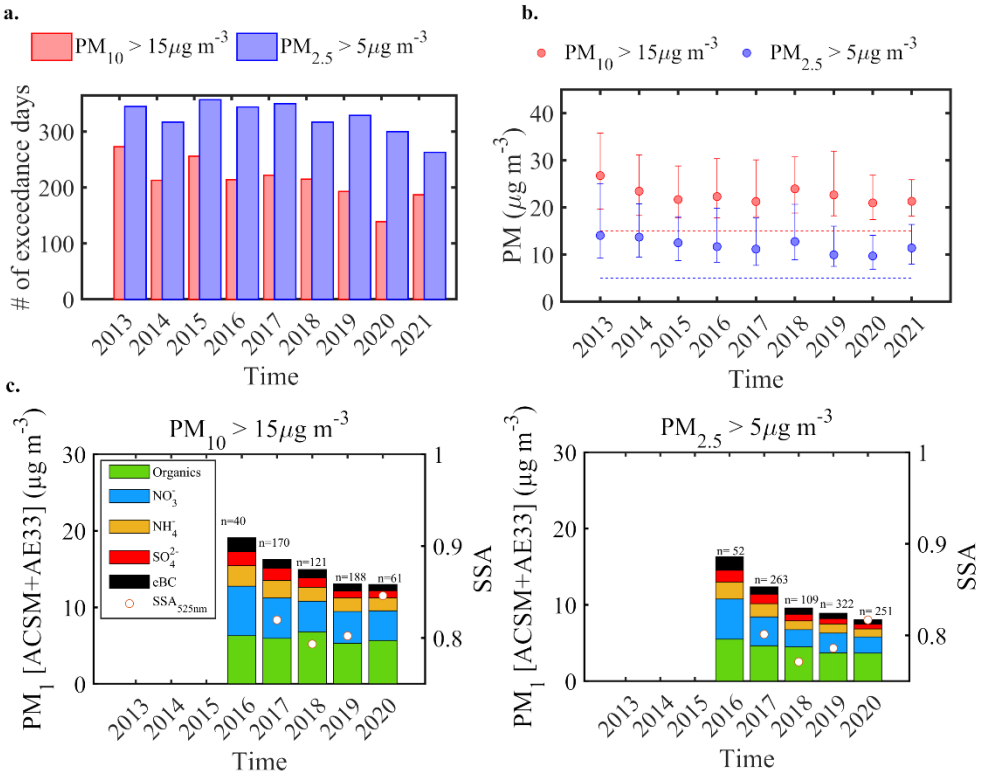

Figure 3.8 WHO exceedance analysis: a) The number of exceedance days for PM_{10} (in red) and $PM_{2.5}$ (in blue) concentrations at Lille Fives station from 2013 to 2021. b) Trend of averaged PM_{10} (in red) and $PM_{2.5}$ (in blue) concentration for days of exceedance at Lille Fives station from 2013 to 2021. c) Chemical composition (y axis left), Single Scattering Albedo at 525 nm (y axis right) in days of exceedance for PM_{10} (left) and $PM_{2.5}$ (right), and the number of points used (n, top of bars) at ATOLL from 2016 to 2020. Time-frequency used: 1 hour average.

Overall, the results presented in this section are consistent with those from the EEA. In their latest Europe's air quality status 2022 (European Environment Agency 2022), they report PM_{10} concentration exceedances for all 32 reporting countries regarding the WHO AQG, while using the EU guidelines, only 8 countries reported concentrations above the annual limit value. The proportion of the EU urban population exposed to concentrations above the 2021 WHO AQG value for PM_{10} decreased from 97% in 2000 to 71% in 2020 (81% in 2019). Although EU legislation has led to improvements in air quality as suggested by the reductions in primary emissions of regulated pollutants, poor air quality remains a problem, and citizens are exposed to pollution levels above WHO standards. In the next sections, we will analyze the long-term measurements of the ATOLL platform aiming at investigating more deeply the changes in chemical and optical properties.

3.3 Aerosol chemical composition

Knowing the physicochemical composition of the atmospheric particles is essential to develop mitigation policies, as well as better constraining their health and climatic effects. Figure 3.9 shows four years (Oct. 2016 – Dec. 2020) of PM_1 chemical composition at the ATOLL platform. For this period, the average PM_1 concentration (calculated as the sum of ACSM species and BC concentrations) is 13.9 ± 10.5 µg m^{-3}, with seasonal averages of 17.8, 15.4, 11.0 and 14.2 µg m^{-3} for winter, spring, summer, and fall, respectively. The most abundant species contributing to PM_1 is organics with 40% followed by nitrate (28%), ammonium (15%), sulfate (8%), eBC (8%), and chloride being negligible (1%). The PM_1 levels observed at the ATOLL site are in the range of typical

values with other European sites. For instance, Chen et al., (2022) based on long-term observations, reported for 13 urban sites in Europe an average mass concentrations of 12.2 ± 9.3 µg m^{-3}. PM_1 levels at ATOLL are much lower than those reported for eastern Europe as in Krakow, Poland (40.4 µg m^{-3}), while significantly higher than those in London, UK (9.5 µg m^{-3}) and Paris (9.7 µg m^{-3}) (see also Figure 1.10 of Chapter 1). The main chemical species contribution to the total submicron aerosol range is also consistent with previous results (Bressi et al. 2021; Chen et al. 2022; Espina Martin 2020; Putaud et al. 2010; Rodelas et al. 2019). Organics contribution is substantial at all sites (21 – 75%) in the work reported by Chen et al., (2022) and Bressi et al. (2021). Sulfate and nitrate present a wider range of annual contributions (12-44% and 5-35%, respectively). At mid-latitudes nitrate shows higher contribution and sulfate lower contribution compared to northern and southern Europe regional background sites (Bressi et al. 2021). According to Chen et al., (2022), eBC shows higher contributions at urban sites (12%) than at non-urban sites (6.8%), ammonium contributions are closely related to those of sulfate and nitrate, as a consequence of sulfuric and nitric acid neutralization by ammonia. Non sea-salt chloride contributions are generally negligible.

As PM_1 changes significantly throughout the year, so can its composition. Whereas sulfate does not show a marked seasonality, with averaged monthly values varying between 1.0 ± 1.8 µg m^{-3} (winter) and 0.9 ± 0.6 µg m^{-3} (summer). In France, emissions of SO_2 are mainly attributed to energy transformation, manufacturing, industry, and residential or tertiary emissions, therefore concentrations can be highly variable at a given site, depending on the presence of local emitters and air mass origins (Rodelas et al. 2019). Carbonaceous aerosols, ammonium, and nitrate variations are more season-dependent. Carbonaceous aerosols showed a higher concentration in winter (5.3 ± 4.9 and 1.1 ± 1.3 µg m^{-3} for organics and eBC, respectively) compared to summer (3.7 ± 3.4 to and 0.6 ± 1.5 µg m^{-3}). This winter increase could be explained by residential heating emissions combined with shallow PBL, stagnant conditions, and lower temperatures, favoring the accumulation of pollutants and potentially supporting the partitioning of semi-volatile organics into particle-phase (Favez et al. 2010; Lanzafame et al. 2021; Sciare et al. 2011; Xu et al. 2020). On the other hand, during summer, organic concentrations are significantly impacted by secondary formation (Laskin, and Nizkorodov 2015). SOA results from the condensation and coagulation of (photo-)oxidized volatile and/or semi-volatile organic compounds which can be emitted by biogenic and anthropogenic sources. Biogenic VOCs (e.g. isoprene, monoterpene, and sesquiterpene) play an important role in SOA formation due to their large emission and high activity during summer (Cao et al. 2022; Lanzafame et al. 2021).

The concentrations of NH_4 and NO_3 exhibit a marked seasonal variation showing maximum during spring with average peaks around 2.0 ± 1.7 µg m^{-3} and 4.4 ± 4.8 µg m^{-3} respectively, even surpassing organics to become the dominating species (37% of NO_3 vs 33% of Org). The levels of ammonium nitrate in the HdF region are related to both local and regional origins. The seasonality of this species arises from the widespread use of fertilizers (rich in ammonia) in the agricultural sector in spring, associated with combustion processes from traffic or industry (Rodelas et al. 2019). Previous studies (Rodelas et al. 2019; Rodelas et al. 2019; Zhang et al. 2020) identified significant contributions of AN and Org from air masses that passed over Belgium, the Netherlands and Germany (North to North-East sectors) associated with high wind speeds and increased farming activities in those areas, suggesting the transport of neutralized and aged aerosols. Finally, non-refractory Cl^- is found typically below the detection limit, representing a negligible fraction of PM_1 at the ATOLL site.

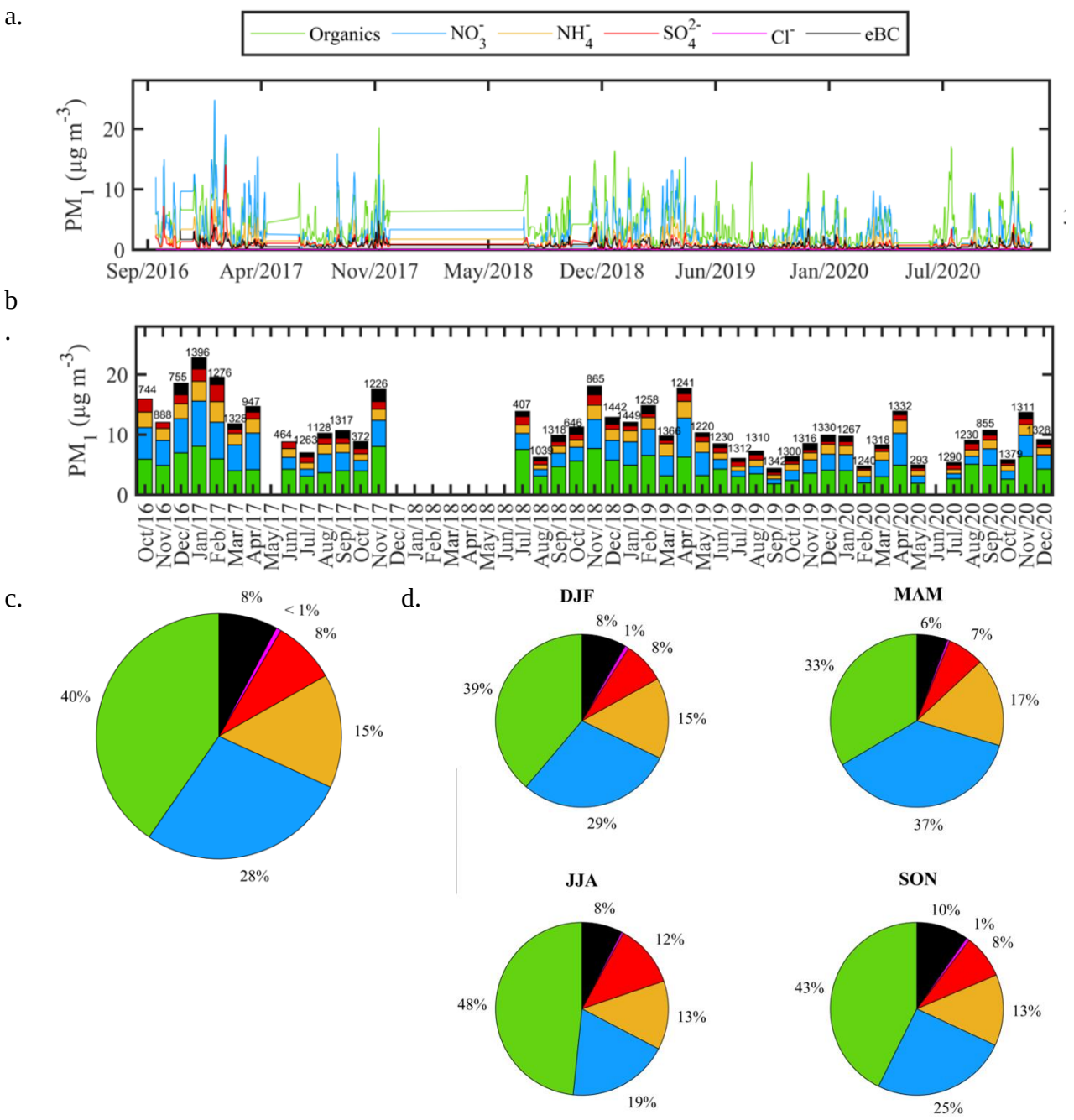

Figure 3.9 PM_1 chemical composition (organics, nitrate, ammonium, sulfate, chloride, and black carbon) at the ATOLL site for the period 2016 – 2020. a) Speciated time series. b) Monthly composition and number of points. c) Multiannual relative composition. d) Seasonal relative composition. Time-frequency used: 30 min average.

Figure 3.10 presents the daily variability of different species. In general, the BLH tends to be lower during winter compared with summer, concentrating pollutants in a narrow mixing layer. The Org and eBC tend to show comparable daily variability (Figure 3.10a), due to their emission during the combustion of liquid and solid fuels. There is generally a pattern following morning and evening rush hours. Chen et al., (2022) analyzed the diel profiles of the major organic components at 22 sites including ATOLL. Results of this study report that, hydrocarbon-like organic aerosol shows morning and evening rush-hour peaks while biomass burning organic aerosol has a low value during the day and a marked evening peak, which indicates that most likely, (residential) heating emissions are the main contributor. In our study, there is a consistent correlation between organics and eBC, with $R^2 = 0.53$ for the whole period, being lower in summer ($R^2 = 0.29$). This is likely related to the larger fraction of biogenic SOA formation in this season (Hama et al. 2022; Laskin, and Nizkorodov 2015; Zhang et al. 2021).

Nitrate and ammonium (Figure 3.10b, c) reach a maximum concentration in the morning for all seasons except for winter, during which the concentration stays more or less constant during the day. The peak during the morning is explained by the accumulation of AN during nighttime as well as low temperature and high RH, favorable conditions for the precursor gases to condense into AN. Thus, when the temperature increases during the afternoon, the concentrations levels decrease in agreement with the thermodynamic equilibrium, being shifted towards the gas phase NH_3 and HNO_3. Following this, summer is the season with the lowest concentrations due to unfavorable environmental conditions and NO_x levels, being at their lowest in the summer period (Rodelas et al. 2019; Shah et al. 2020). Conversely, spring has the highest concentrations, caused by the multiple fertilization of agricultural fields and the often high pollution episodes coming from the transboundary transport of particles (Espina Martin 2020; Waked et al. 2014). The sulfate diel cycle (Figure 3.10d) shows in general a relatively flat trend; in summer during the daytime, an enhancement of SO_4 can be observed. Higher O_3 and T combined with lower RH, as illustrated in Figure 3.2, are favorable conditions for the gas-phase oxidation reaction of SO_2 which play an important role in promoting sulfate diel variations (Han et al. 2021; Rodelas et al. 2019).

Our results are generally comparable to what has been previously reported in the other sites of Northern France, although for more limited sampling periods. For instance, Crenn et al. (2017, 2018) conducted in Douai (39 km apart from ATOLL) two intensive campaigns during the winter of 2010 and summer of 2011 to determine the composition of NR-PM_1. They report a higher contribution to NR-PM_1 for the major inorganic ions (i.e. NO_3, SO_4, and NH_4), with a predominance of NO_3 (about one-third of the total NR-PM_1). Another comparable study (Zhang 2016) monitored the composition of the PM_1 during one year from July 2013 to September 2014 using ACSM and an aethalometer in Dunkirk (80 km apart from the ATOLL platform), at an urban background site largely influenced by industrial and harbor activities. The mean PM_1 mass for the whole period was 9.7 ± 9.0 µg m^{-3}, slightly lower in comparison with the average value reported for ATOLL. In the same study, the average contribution from the major constituents showed also lower values for organics (32.5%), while the other species exhibit values of 26.4% nitrate, 26.0% sulfate, 14.4% ammonium, and 1% chloride. A source apportionment study of the organic fraction of the aerosol evidenced three primary sources, related to traffic, biomass combustion, and domestic cooking.

The studies of Waked et al. (2014) and Barros de Oliveira (2017) focused on the PM_{10} fraction in the region. In the work of Waked et al. (2014), the PM_{10} composition was measured from

March 2011 to March 2012 in Lens (40 km apart), with a mean concentration of 21 µg m^{-3}. A source apportionment analysis showed the main components were Secondary Inorganic Aerosols (SIA, 28% of the total PM_{10} mass; divided in nitrate-rich and sulfate-rich with equal contributions of 14%), aged marine emissions (19%), biomass burning (19%), mineral dust (13%), primary biogenic emissions (9%), fresh salts (8%), primary traffic emissions (6%) and heavy oil combustion (4%). As expected, some factors showed significant seasonal variations such as biomass burning, which presented higher contribution in winter, and primary biogenic emissions, peaking in summer. The work conducted by Barros de Oliveira (2017) at five sites in northern France showed a similar mass composition to that observed by Waked et al. (2014), with the predominance of SIA (particularly nitrate) and organics. A source apportionment analysis showed common sources among the different sites, including nitrate-rich (12-23%), sulfate-rich (7-15%), traffic (10-26%), biomass burning (8-15%), oxalate-rich (4-19%), fresh marine (4-11%), land biogenic (2-9%) and marine biogenic (3-12%). Other sources were identified only at some sites, including an aged marine factor identified at all sites except in Rouen (9-11%) and a road/dust factor identified in Revin (15%) and Roubaix (26%). Both Waked et al. (2014) and Barros de Oliveira (2017) report a higher contribution of SIA in PM_{10} during high pollution episodes.

Most recently, Rodelas et al. (2019) and Espina Martin (2020) studied the chemical composition, sources, and origins of SIA at urban and rural sites in Northern France. In Douai, Rodelas et al. (2019) observed that the main species forming SIA in the $PM_{2.5}$ were AN and AS with a predominance of the former during most of the year except in summer. Espina Martin (2020) reports a contribution of nitrate, sulfate, ammonium, organics, and black carbon to $PM_{2.5}$ of 27%, 14%, 10%, 32%, and 4%, respectively, making SIA the major fraction of $PM_{2.5}$ mas (51%).

In Europe, comparable studies on the measurement of chemical aerosols have already been conducted. For instance, Putaud et al. (2010) studied from 1996 to 2007, the chemical composition of $PM_{2.5}$ samples collected at different sites (urban, rural and natural) across 11 European countries dived into three major groups: Northwest, South, and Central. Results of this study showed in Northwestern Europe sulfate, nitrate and organics as the major constituents of $PM_{2.5}$, no matter whatever the typology, supporting that SIA may account for more than half of the $PM_{2.5}$ mass (Putaud et al. 2004). Bressi et al. (2021) also studied the diel cycles in the contribution to NR-PM_1 of organics, sulfate and nitrate. Early morning minima in organics in concomitance with maxima in nitrate are common features at regional and urban background sites. Finally, looking at NR-PM_1 chemical composition as a function of mass concentration reveals that, although organics account for the major fraction of NR-PM_1 at all concentration levels at most sites, nitrate contribution generally increases with mass concentration and predominates when NR-PM_1 mass concentrations exceed 40 µg m^{-3} at half of the sites, in agreement with ATOLL observations.

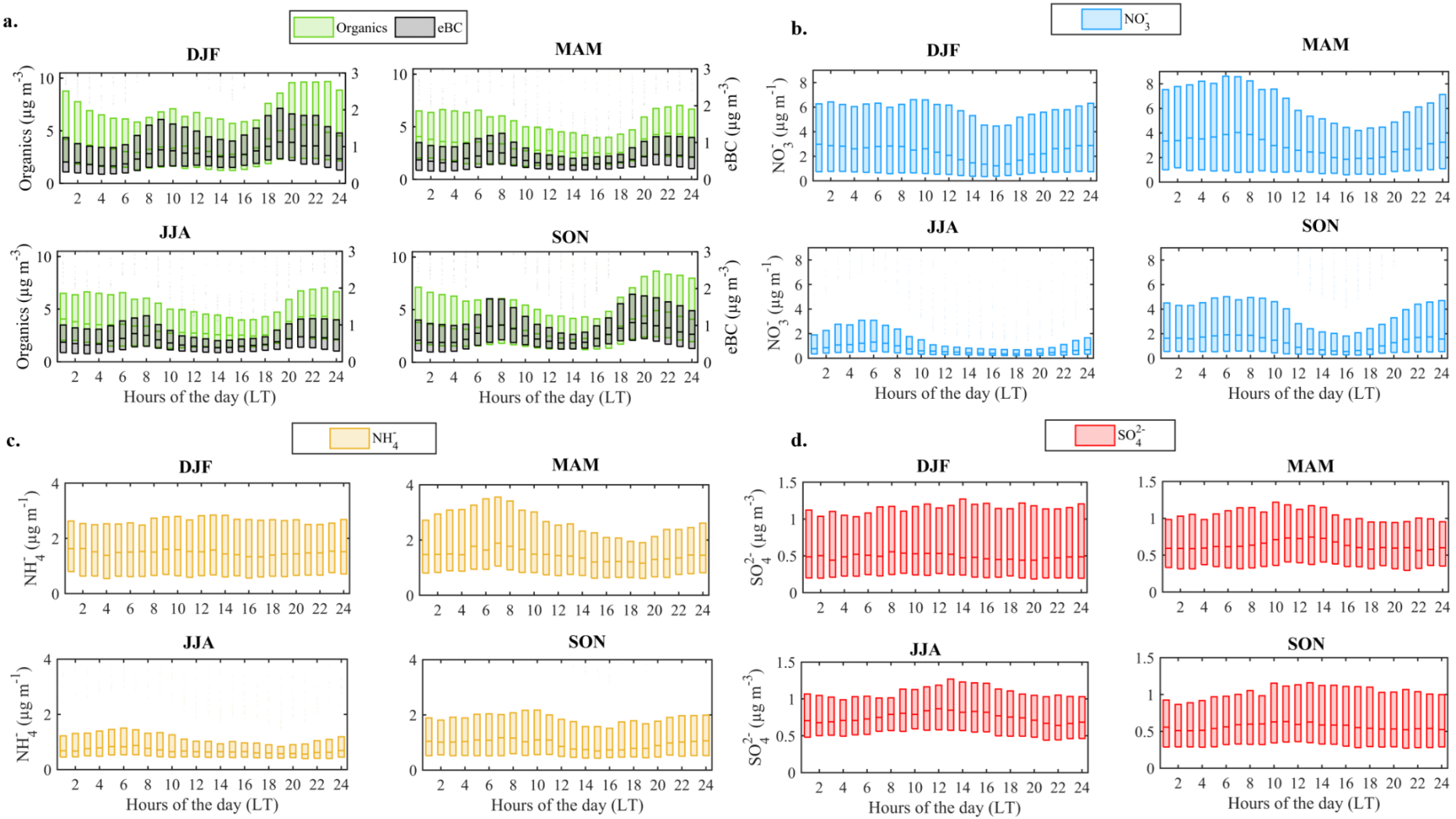

Figure 3.10 Seasonal diel cycles for PM_1 species. a) Carbonaceous aerosols (Organics and Black carbon). b) Nitrate. c) Ammonium. d) Sulfate Time-frequency used: 1 hour average.

As discussed previously, European emissions of pollutants such as sulfur dioxide, carbon monoxide, lead, and benzene have decreased in recent years. On the other hand, air pollutants continue to be emitted copiously by sources such as road transport, industry, power plants, households, and agricultural activities. Figure 3.11 shows the averages of the chemical species concentrations observed from 2016 to 2020 at the ATOLL platform. Overall, the PM_1 suggests a decreasing tendency, especially evident for eBC and organics in winter, and in agreement with PM_{10} and $PM_{2.5}$ evolution described in section 3.2, albeit on a shorter period. Due to the limited number of years, trend analysis will not be performed within the scope of this thesis, but should be the study of a future, and more comprehensive analysis of this topic.

It is important to mention that the European Environment Agency (2020) reports a significant increase (64%) in biomass as a fuel input since 2010. While this has its origin in climate mitigation goals, it can result in increases in air pollution, particularly PM and VOCs during wintertime. On the other hand, increased intensity and frequency of heat events during summer time are expected to lead to higher mean ozone concentrations in urban and rural areas (Ministère de la Transition Ecologique 2021; Sicard 2021), also exacerbated by wildfires across Europe, especially in southwestern France, Italy, Spain and Portugal. Thus, primary carbonaceous aerosols and SOA concentrations are expected to be enhanced under these conditions (Brito et al., *in preparation*).

To conclude, declines in emissions and improvements in environmental performance were largely driven by European policy, which sets legally binding emission limit values (European Environment Agency 2020). Emission reductions resulted in a notable reduction of ambient concentrations of SO_2 and NO_x, decreasing by 91% and 68% between 2004 and 2020 (European Environment Agency 2020). While continuous progress has been observed in other sectors, air pollutant emissions from agriculture and the combustion of fuels to produce energy for domestic needs have either decreased very little (in the case of agriculture), or not decreased (in the case of domestic fuel combustion) in the last decade (Guerreiro 2014). Although the amount of fossil fuel used has also decreased by 26%, as energy production shifts to climate-friendlier sources, the two fossil fuels (natural gas and coal) are still very significant in the overall mix, covering over 70% of the total fuel input (European Environment Agency 2020). BB has become an important source since wood burning is often relatively cheap, and considered as climate-friendly source of energy since it is renewable and often considered as carbon-neutral, coupled with the important open fires occurring in the latest years (European Environment Agency 2020). Stricter emission limit values and policies aimed at increasing the use of renewable or cleaner fuels are expected to drive further declines in combustion plant emissions in the coming years.

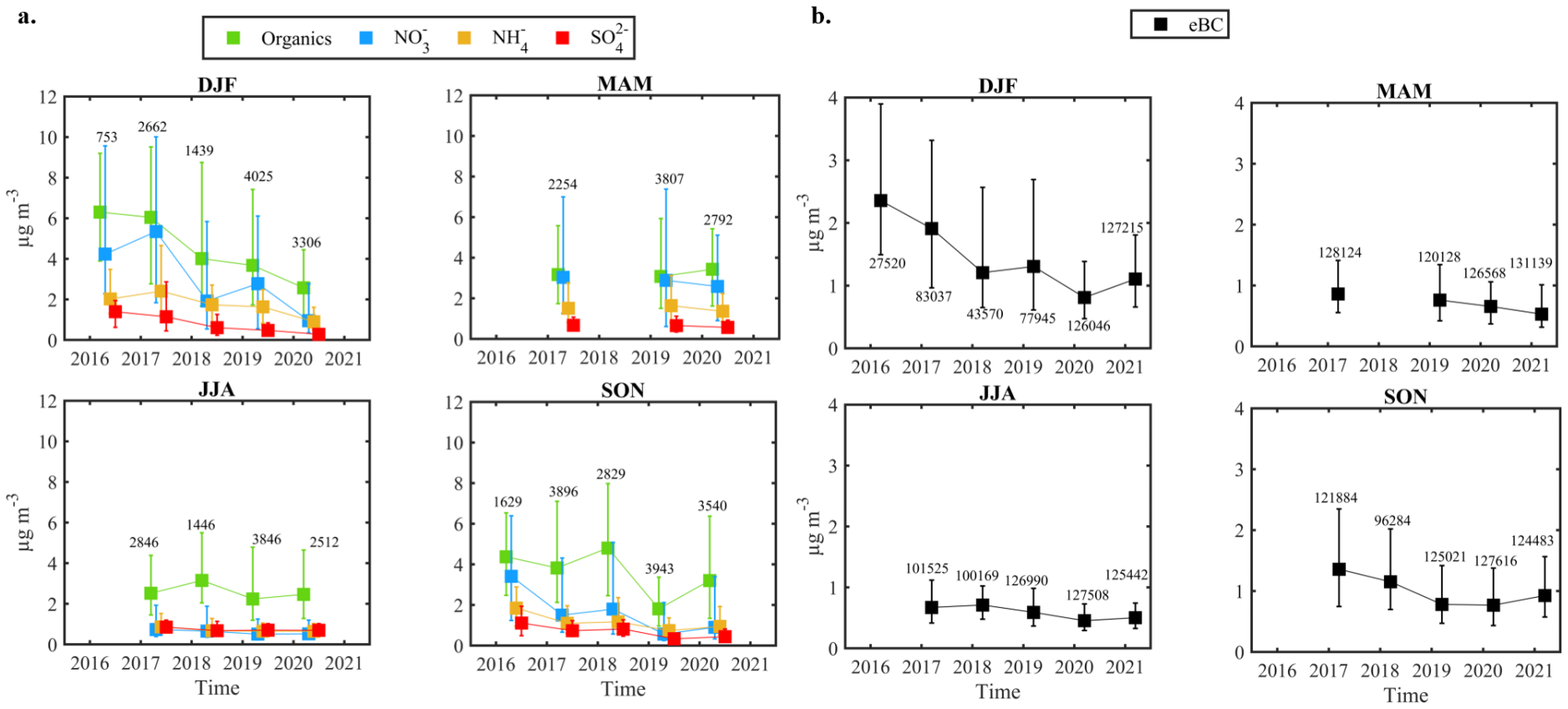

Figure 3.11 Seasonal averages of PM_1 in µg m^{-3} from 2016 – 2021.a) Non-refractory PM_1 (organics, nitrate, ammonium, sulfate). b) Equivalent black carbon (eBC). Time-frequency used: NR-PM_1 - 30 min and eBC 1 min.

3.4 Aerosol optical properties

3.4.1 AERONET-based analysis

The passive remote sensing from ground-based observations at the ATOLL platform became continuous in 2008. Figure 3.12 presents observations for Aerosol Optical Depths at 3 wavelengths (380 nm, 500 nm, 675 nm) and the Ångström Exponent calculated for the pair of wavelengths 440-870 nm. The average and standard deviation of AOD_{380nm}, AOD_{500nm}, AOD_{675nm}, and $AE_{440\text{-}870nm}$ are 0.224 ± 0.159, 0.163 ± 0.125, 0.110 ± 0.089, 1.262 ± 0.402, respectively. In Europe, AOD mean values at 550 nm are reported by Yang et al. (2020) for AERONET sites near the English Chanel. The values observed in ATOLL are comparable with Oostende (0.154) and Dunkirk (0.164) and slightly higher than values observed in Plymouth (0.136) and Chilbolton (0.134). It is interesting to see that the AE values retrieved in the pair of wavelengths of 400-870 nm for all these sites are lower (0.797 – 1.119) than the value reported for ATOLL, most probably due to its distance from the coast.

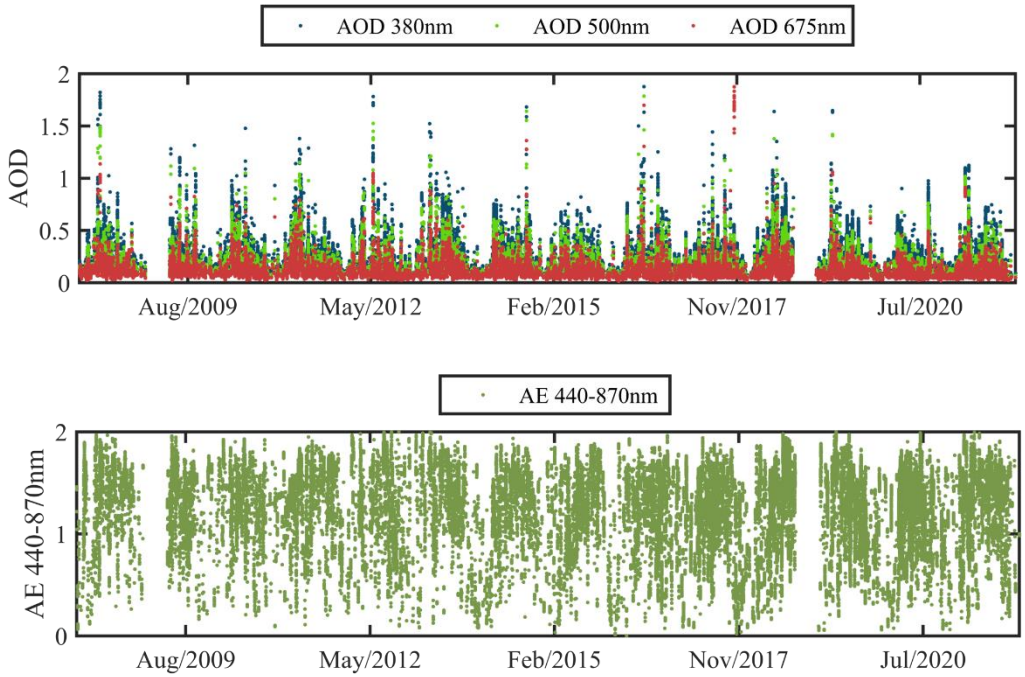

Figure 3.12 Time series of aerosol optical properties from the photometer AERONET data at the ATOLL platform from 2008 – 2021. a) Aerosol Optical Depth at 380 nm, 500 nm, and 675 nm. b) Ångstrom Exponent in the pair of wavelengths of 440 – 870 nm. Time-frequency used: 1 hour.

A previous study (Mortier, 2013) analyzed the ATOLL remote sensing aerosol observations for the 2008-2012 period, reporting Lille as a moderately particle-laden site, compared to other sites under anthropogenic influence: Mexico City (AOD of 0.34), Beijing (0.76), New York City (0.18) and close to some European cities like Munich (0.17), Rome (0.19), Kyiv (0.20) and Paris (0.19). For the same pair of wavelengths (440-870 nm) Mortier, (2013) shows an AE smaller than Mexico City (1.48) and New York (1.45) whereas for Europe he observed comparable mean AE values (Munich 1.42, Rome 1.30, Kyiv 1.39 and Paris 1.26). Through the AE we can estimate the size of the particle, larger values being associated to coarse particles while smaller ones to fine particles (Xu et al. 2020).

Regarding the seasonality, the average value of AOD_{500nm} is high during spring (0.21) and low during winter (0.12), showing an agreement with the reported AOD_{532nm} values by Mortier (2013). The average $AE_{440-880nm}$ is low during winter (1.06) and high during summer (1.32) as Mortier (2013) stated for Lille. Figure 3.13 shows the diel cycle of AOD at 500 nm and $AE_{440-880nm}$ by season. The AOD values exhibit a smooth diel variation, with higher values during spring and summer in comparison to winter and fall, this might be linked to differences in the meteorological conditions between seasons. The AE remains constant, generally above 1, indicating a predominance of fine mode particles (e.g. traffic emissions). Smirnov et al. (2002) analyzed five specific land sites with a multi-year record (1993-2001) representing regionally distributed aerosol types i.e. urban, dust, marine, smoke, and background. They observed a clear diel AOD cycle during the whole period where local pollutants along with atmospheric convection likely played a major role in the slight diurnal increase of the AOD. The diel pattern is consistent each year and the average diurnal increase of 16% corresponds to a 0.04 change in AOD at 500 nm. Kazadzis et al. (2007) also relates the AOD seasonality to processes such as enhanced evaporation and high temperatures in summer, increased turbidity in the boundary layer, which in conjunction with stagnant weather systems over the area help in the built-up of aerosols.

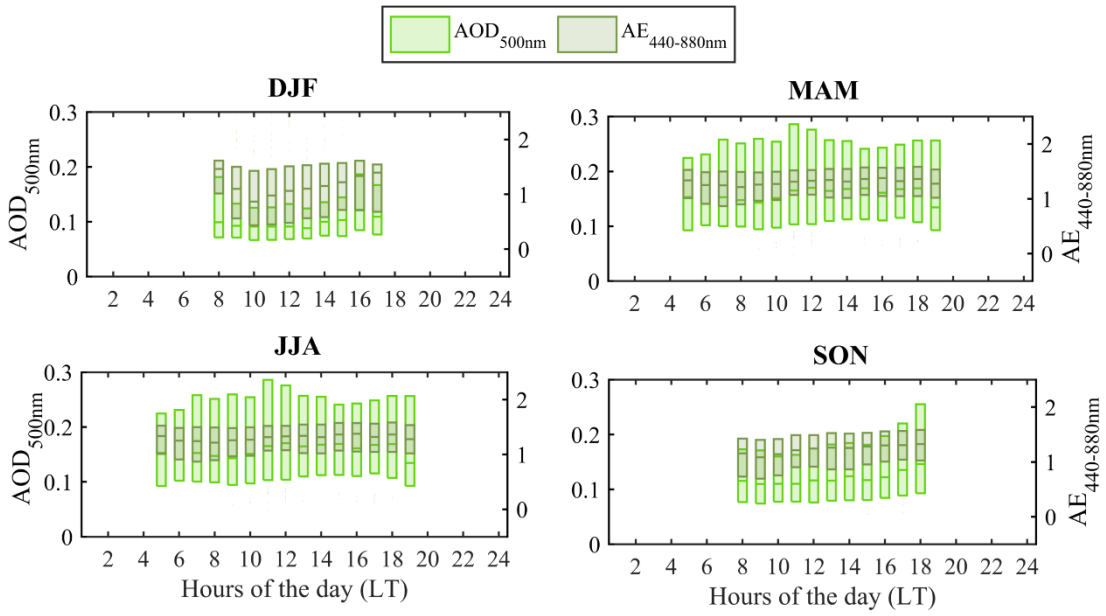

Figure 3.13 Seasonal diel cycle of Aerosol Optical Depth at 500 nm and Ångstrom Exponent for the pair of wavelengths of 440 – 870 nm from the photometer AERONET data at the ATOLL platform from 2008 – 2021. Time-frequency used: 1hr average.

Figure 3.14 shows the seasonal trends in AOD at 3 wavelengths (380 nm, 500 nm, and 675 nm) and the $AE_{440-870nm}$ for the period 2008 to 2021. Overall, one can observe a mostly smooth tendency for all seasons. By applying the trend analysis described on section 3.2 to the data series, the AOD values show a comparable trend (-0.004 to -0.002 yr^{-1}) at the three wavelengths. In the same way, the trends for the $AE_{440-870nm}$ exhibit a flat tendency (-0.02 to -0.01 yr^{-1}). Indeed, various authors report in various world regions a gradual decrease in aerosol loadings. For instance, a study carried out in South Africa (Kumar et al. 2014) demonstrates negative AOD trends for the period 2003–2013 with a decrease of -0.003 (Pretoria), -0.0009 (Bloemfontein) and -0.0001 (Cape Town) over the decade. Over different regions of North China in the period 2001–2016, it can be observed a negative trend of -0.015 (Qinghai Tibet),

-0.059 (Northwest China) and -0.007 (the North China Plain) per decade (Wang et al. 2017). Additionally, in the English Channel (Yang et al. 2020), from the early 2000s to about 2016, the AOD decreased by an overall average of nearly -0.04 per decade. On the contrary, AOD increase was also observed in the area of the Indo-Gangetic Plain for the period 2006–2015, the increasing tendency per decade were 0.0181 (Dhaka), 0.0019 (Kanpur), and 0.0200 (Kolkata) (Kumar et al. 2018).

A study with 90 selected stations (ATOLL included) from the AERONET network during the 2000 to 2013 period (Li et al. 2014) yielded, for the majority of sites, negative trends in AOD, including most stations in North America and Europe. The largest decreases are found over western Europe, reaching ~0.1 decade^{-1}. Strong positive trends are found in Kanpur, in North India, and Solar Village in the Arabian Peninsula. In general, the trends are most prominent during spring and summer seasons, which usually correspond to the seasons with the highest aerosol loading for locations in the Northern Hemisphere, although some stations exhibit significant trends for certain seasons, with frequently missing data, which affects or even precludes the detection of trends.

In the same global study (Li et al. 2014), it is interesting to note that, while AOD decreased uniformly for both North America and Europe, AE trends are opposite there. North America generally exhibits positive trends, while negative trends are found in Europe which suggests a change in aerosol composition. The AOD reduction in Europe might be due to the reduced fine-mode anthropogenic emissions, while in North America it might be related to a reduction in natural sources emissions. Like AOD, the trends for the four seasons are also consistent with annual trends. However, note that different from AOD, which exhibits the most prominent trends in the spring and summer, most AE trends are found during the winter season. Yet winter usually has the minimum aerosol loading for many Northern Hemisphere locations. Overall, the long-term decrease in aerosol loading is more consistent with the reductions in anthropogenic emissions. (Yang et al. 2020).

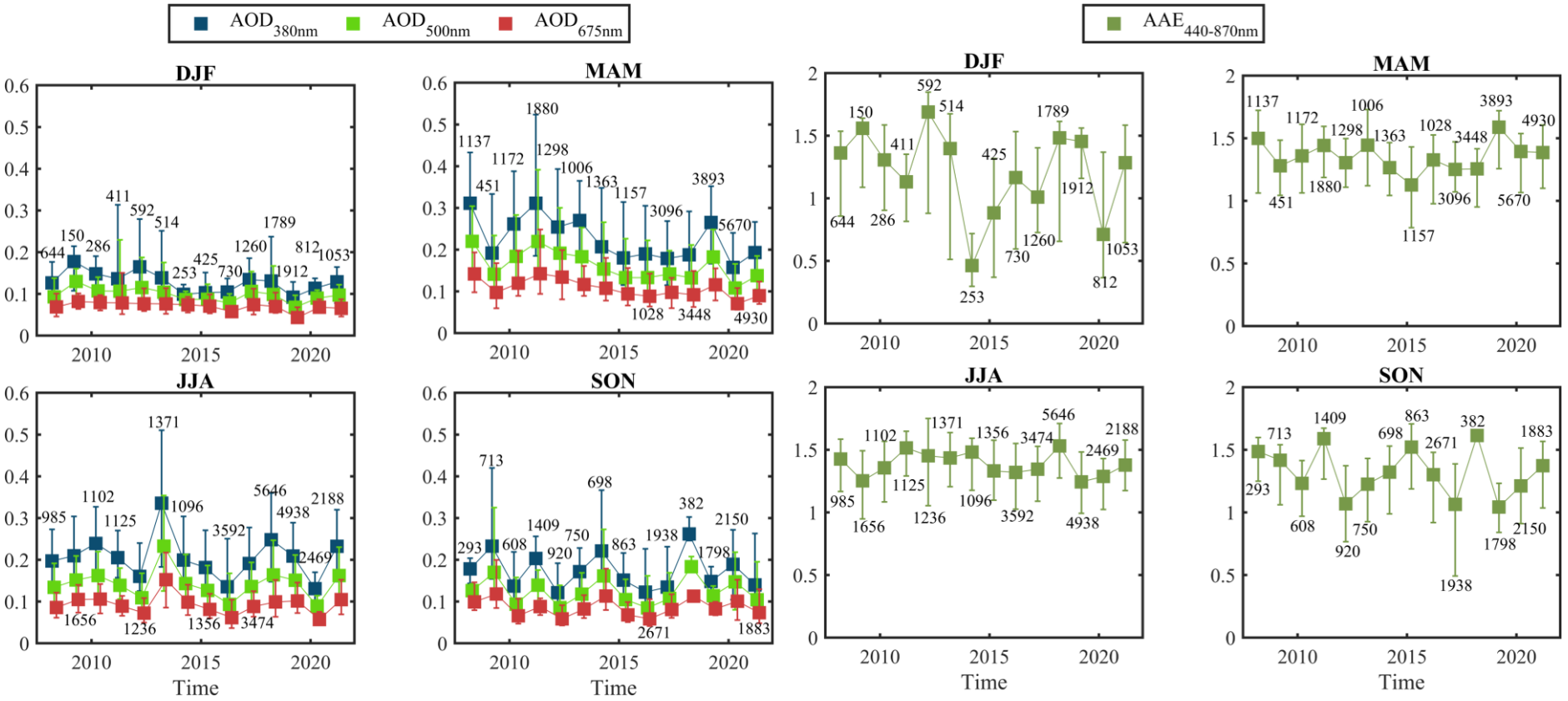

Figure 3.14 Seasonal averages of AERONET data from 2008 – 2021.a) Aerosol Optical Depth at 380 nm, 500 nm and 675 nm. b) Ångstrom Exponent (AE) in the pair of wavelengths of 440 – 870 nm. Time-frequency used: 1 hour.

3.4.2 In-situ analysis

Temporal variations of in situ aerosol optical observations at the ATOLL site are illustrated in Figure 3.15. This extended duration highlights the robustness of online observations of the scattering and absorption coefficients, and the calculation of key parameters such as AAE, SSA, and SAE. For July 2017 till December 2020, the average and standard of the scattering coefficient at 525 nm deviation (34.9 ± 34.4 Mm^{-1}) are comparable with other urban ACTRIS sites in Europe (Pandolfi et al. 2018), although the cut-off size is smaller (PM_1) than at most of the sites (PM_{10} and $PM_{2.5}$). For instance, observations in $PM_{2.5}$ in the visible range performed in Madrid, Spain report a σ_{scat} average value fairly lower than in our study (25.30 ± 22.91 Mm^{-1}) contrary, in Granada, Spain (total particles) and Athens, Greece (PM_{10}), σ_{scat} is significant higher (55.21 ± 44.43 and 55.16 ± 37.93 Mm^{-1}, respectively) than the one observed at ATOLL. In France, only remote sites (SIRTA, Observatoire Pérenne de l'Environnement and Puy de Dôme) are included in the study performed by Pandolfi et al. (2018) where they report an average value lower than 20 Mm^{-1}. On the other hand, the average absorption coefficient (Figure 3.15b) at 880 nm (3.6 ± 3.8 Mm^{-1}) for the Dec. 2016 – Dec. 2021 period is in the same range as the average value (3.82 ± 1.56 Mm^{-1}) reported by Zanatta et al. (2016) for Herwell, UK. The σ_{abs} at the urban site in Ispra, Italy (10.7 ± 1.84 Mm^{-1}) and the average value reported for a remote site in Melpitz, Germany (4.93 ± 1.73 Mm^{-1}) exhibit higher average values than the one observed at the ATOLL platform.

Figure 3.15c shows the intensive optical properties. The SSA at 525 nm shows high variability during the period, indicating high variability of fractions of absorbing or scattering particles. The average value (0.75 ± 0.16) at ATOLL for the Jul. 2017 – Dec. 2020 period has been also observed at urban sites in PM_{10} or $PM_{2.5}$ among the GAW network sites (Laj et al. 2020), UK (McMeeking et al. 2011), the Netherlands (Aouizerats et al. 2010) and Spain (Segura et al. 2014). In a comparable study, Kaskaoutis et al. (2021) observed in PM_1, a slightly lower SSA average value (0.60 ± 0.13) for urban Athens, Greece. Indeed, the observed range of SSA (0.7 – 0.8) for most urban sites in Europe (Laj et al. 2020) points out the frequent presence of high-absorbing aerosols at ground level. Here, it is important to mention that ATOLL is considered a sub-urban site, representative of a large area, and not strongly impacted by local traffic such as in a street canyon or very busy streets.

The average Absorption Ångström Exponent (Figure 3.15d) calculated between 370-880 nm ($AAE_{370\text{-}800nm}$ - 1.36 ± 0.14) for ATOLL is comparable to the average $AAE_{370\text{-}880nm}$ (1.32 ± 0.21) reported by Kaskaoutis et al. (2021) for long-term PM_1 observations (Oct 2016 – Sep 2019) in Athens, Greece. Luoma (2021) also with a size cut-off in PM_1, observed an $AAE_{370\text{-}950nm}$ average value of 1.03 for a suburban site in Hyytiala, Finland. On a bigger size cut-off (PM_{10}), Segura et al. (2016, 2014) show $AAE_{370\text{-}940nm\ values}$ for two urban sites in Spanish cities (Granada: 1.42 ± 0.08 and Valencia: 1.1 ± 0.3) comparable to the one observed at ATOLL as well as for Rome, Italy ($AAE_{450\text{-}635nm}$, 1.3 ; Valentini et al. (2020)) and Toulon, France ($AAE_{440\text{-}870nm}$, >1.2 ; Saha et al. (2008)). It is important to remember that the AAE for externally mixed BC is predicted to be wavelength-independent (AAE = 1), however, the AAE for ambient particles (measured between a short and a long visible wavelength) has often been observed larger than 1. Factors can contribute to these observations, including enhanced absorption by BC internally mixed with non-absorbing material, and/or absorption by BrC or dust. Theoretical calculations have bounded the range of AAE for internally mixed BC, showing that the AAE can vary from a baseline of 1 to an upper limit of ~1.7, depending on the size and optical

properties of the core, the non-absorbing coating and the wavelength pairs used (Lack and Cappa 2010). It should be noted that values of AAE for BrC up to 9.5 have been observed (wavelength pairs: 400-700 nm) (Andreae and Gelencsér 2006) while AAEs for desert dust range from 2.5 to 6.0 (wavelength pairs: 467-600 nm) (Weinzierl et al. 2011). Hence, we can infer that the standard conditions for BC at urban sites over Europe suggest an enhanced absorption by BC internally mixed with non-absorbing material, and/or absorption by BrC.

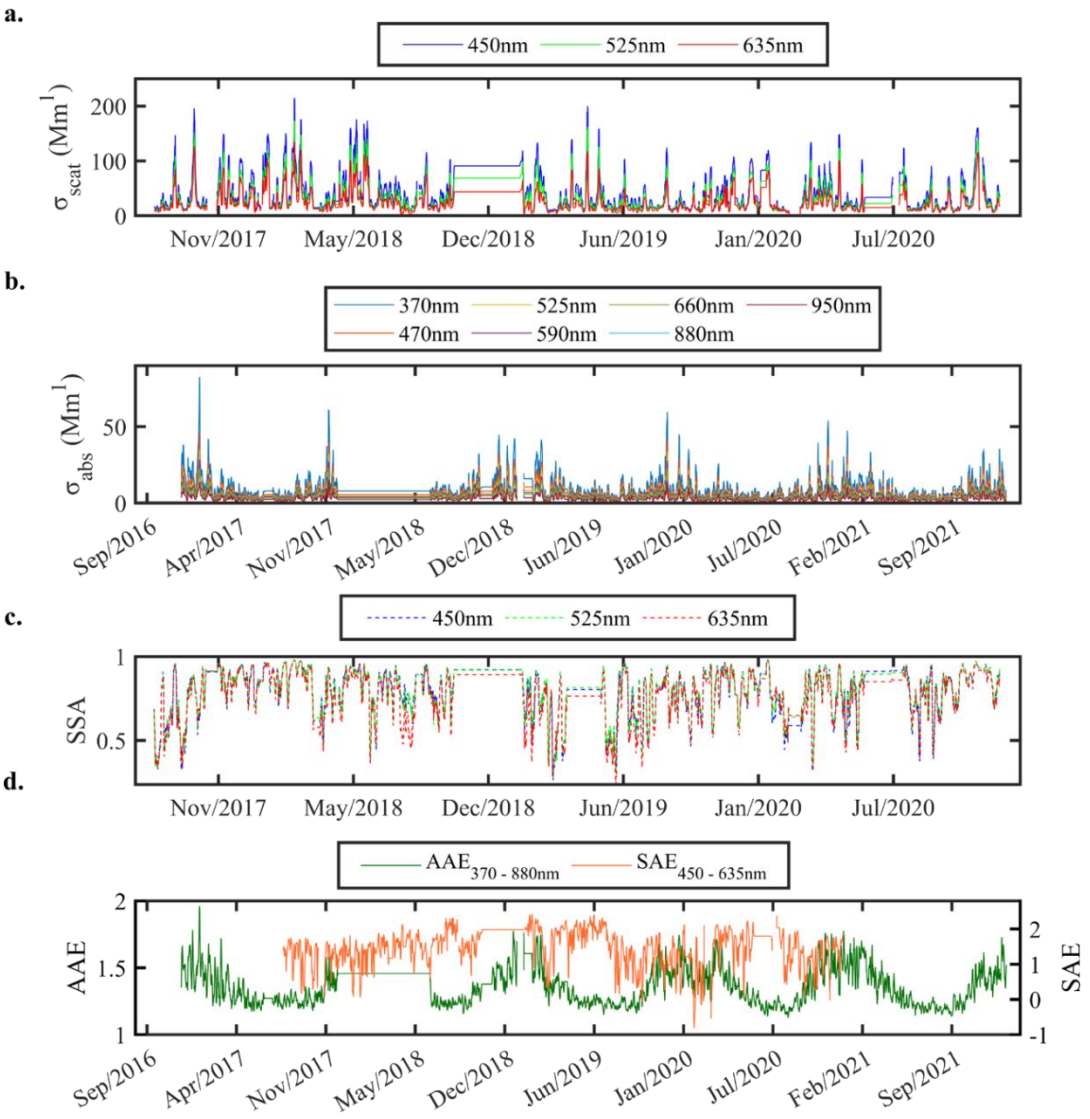

Figure 3.15 Time series of Aerosol Optical properties measured in situ (aethalometer and nephelometer) at ATOLL from 2016 - 2021. a) Scattering coefficient (σ_{Scat} in Mm^{-1}) at 450 nm, 525 nm and 635 nm. b) Absorption coefficient (σ_{Abs} in Mm^{-1}) at 7 wavelengths (370 – 950 nm). c) Single Scattering Albedo at 450 nm, 525 nm and 635 nm. d) Absorption Ångstrom Exponent in the pair of wavelengths of 470–880 nm (left y axis) and Scattering Ångstrom Exponent in the pair of wavelengths of 450–635 nm (right y axis). Time-frequency used: 1 min.

The average SAE (Figure 3.15d) calculated for the pair of wavelengths 450–635nm ($SAE_{450-635nm}$) for the whole period (1.45 ± 0.68) is comparable to the SAE values reported for other urban/suburban ACTRIS sites by Pandolfi et al. (2018). In Madrid, the SAE value reported is highly similar (1.43 ± 0.54) whereas Granada (1.62 ± 0.41) and Germany (1.51 ± 0.72) exhibit slightly higher values. In fact, in central and eastern Europe, independently of the station

location, the SAE is among the highest observed across the network, indicating a large predominance of fine particles. In these regions, the SAE is even higher in summer compared to winter, suggesting a shift toward the small end of the aerosol particle size distribution that is likely linked to new particle formation events during the warmest months (Crumeyrolle et al. 2022).

The optical properties at the site exhibit a marked seasonality; overall, both coefficients, scattering at 525 nm (41.70 ± 36.60 Mm^{-1}) and absorption (4.6 ± 4.8 Mm^{-1}) at 880 nm are higher during winter, while during summer, the coefficient values decrease by 26% and 45%, respectively. For the SSA at 525 nm, we noticed that spring is the season within a higher range of variability (0.60 – 25th percentile and 0.85 – 75th percentile) whereas, summer has the most stable conditions (0.73 – 5th percentile and 0.88 – 95th percentile). The SSA seasonal variability can be linked to the increase in ammonia emissions by agricultural activities in spring leading to strong AN formation (see chapter 4), these species can be internally mixed with BC, thus enhancing the absorption (SSA ~ 0.60) (Yuan et al. 2020). Furthermore, the $AAE_{470\text{-}800nm}$ highlights the differences in the composition of aerosols between winter and summer. For instance, during winter the range of values for the $AAE_{370\text{-}800nm}$ are 1.35 (25th percentile) and 1.66 (75th percentile) differing from summer with a range of values much lower than those observed in winter (1.16, 25th percentile, and 1.31, 95th percentile). This difference between seasons highlights the increase in wood combustion during the cold season, with a significantly higher AAE than fossil fuel emissions.

Figure 3.16 displays the seasonal diel cycle of hourly averaged optical properties (scattering, absorption, SSA, $SAE_{450\text{-}635nm,}$ and $AAE_{470\text{-}880nm}$). In general, the scattering and absorption diel cycles are comparable to aerosol parameters described previously (Figure 1.11 and Figure 1.12), driven by source strength, dilution, and BLH. The absorption coefficient peaks during the rush traffic hours of morning and afternoon and the scattering coefficient reach mostly its maximum value during the early morning. The diel cycle of the SSA highlights the presence of highly absorbing material during the traffic peaks in the morning and afternoon, whereas, in the middle of the day and the evening, SSA reaches higher values suggesting the reduction of light-absorbing aerosols emissions and advection/formation of more scattering material. Previous studies in Athens have shown that SSA decreased with increasing BC/PM_1 and higher values around noon to afternoon ascribed to SOA formation which may increase the SSA (Kaskaoutis et al. 2021; Liu et al. 2020).

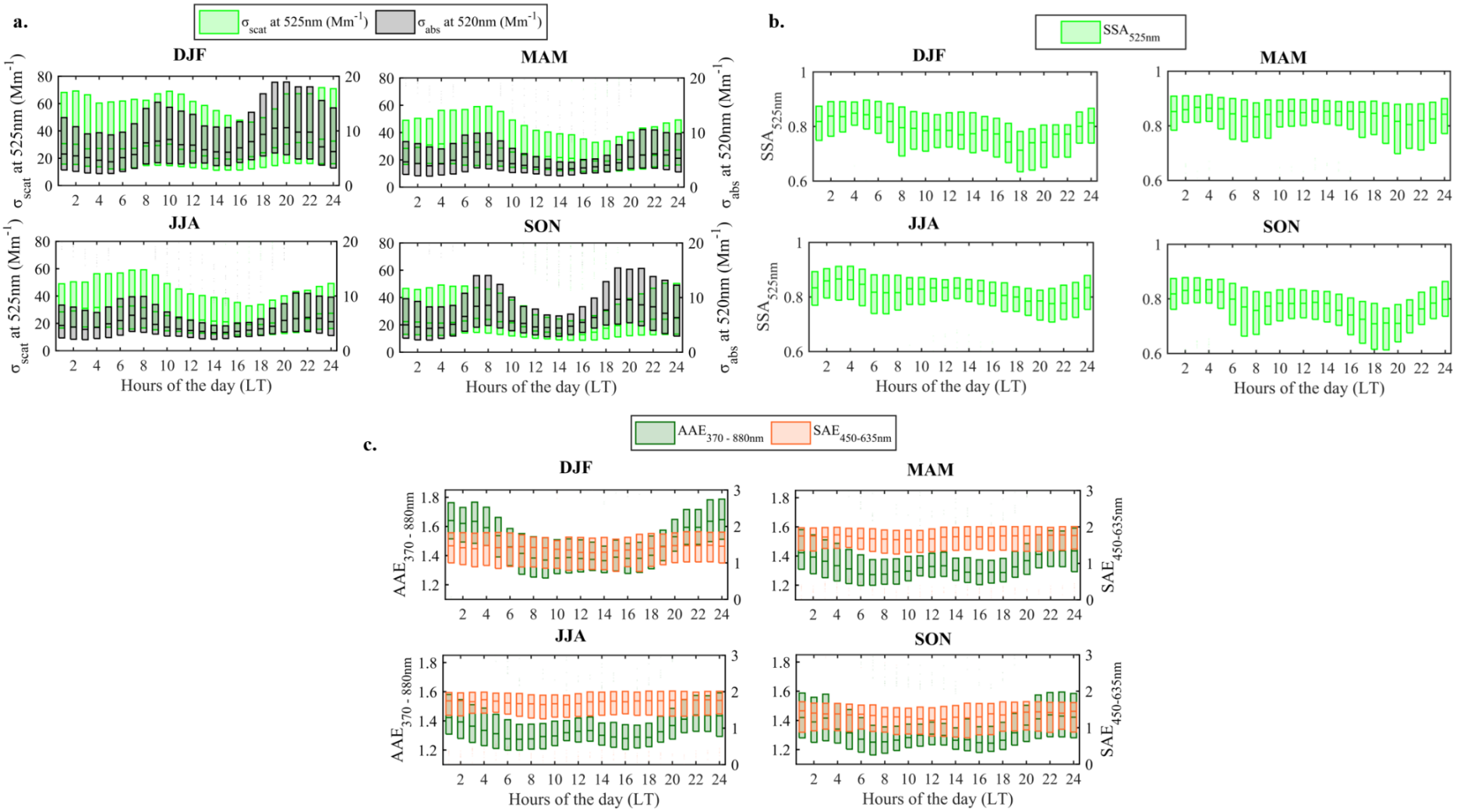

Figure 3.16 Diel cycles of aerosol optical properties at ATOLL for the period 2016 – 2021. a) Scattering coefficient (left y axis) at 525 nm (in Mm^{-1}) and Absorption coefficient (right y axis) at 520 nm (in Mm^{-1}). b) Single Scattering Albedo calculated at 525 nm. c) Absorption Ångstrom Exponent in the pair of wavelengths of 370 – 880 nm (left y axis) and Scattering Ångstrom Exponent in the pair of wavelengths of 450 – 635 nm (right y axis). Time-frequency used: 1 hour average.

The diel cycle of the $AAE_{370\text{-}880nm}$ is consistent with previous studies (Chang et al. 2021; Du et al. 2022; Romano et al. 2019; Zhu et al. 2015). Indeed, the $AAE_{370\text{-}880nm}$ diel profile is dominated by the rates in primary emissions and atmospheric processes. The lowest values occur during the traffic rush hours while the largest values take place during the evening to late night (from 20h00 till 05:00). The latest may be explained by the emission rates of primary sources such as residential heating emissions, especially during the cold season, combined with shallow boundary layer height, and the aging processes of carbonaceous aerosols. For instance, in Rome and Athens (Costabile et al. 2017; Kaskaoutis et al. 2021) the increase in organic aerosol fraction has been associated with larger values of AAE. Figure 3.16c shows the seasonal $SAE_{450\text{-}635nm}$ diel cycles, with, in general, higher values observed in summer (1.69 ± 0.72) compared to winter (1.31 ± 0.76), suggesting a shift toward the small end of the aerosol particle size distribution that is likely linked to new particle formation events during the warmest months (Crumeyrolle et al. 2022). As a common feature, all seasons present a fairly flat pattern of SAE, underlying the constant presence of fine particles at the site.

Finally, we also analyzed the seasonal medians and interquartile ranges in the aerosol optical properties measured at the ATOLL platform (Figure 3.17). Globally the last years show values lower than the earlier years which suggests an agreement with trend analyses for the optical properties in Europe (Collaud Coen et al. 2020; Li et al. 2014; Pandolfi et al. 2018; Yang et al. 2020). However, larger statistics are required to confirm if such a trend is valid for ATOLL. Indeed, Collaud Coen et al. (2020) show statistically significant decreasing trends for aerosol optical properties (scattering and absorption coefficients) for most of European sites for a long-term trend analysis (10 and 15 years) in 37 and 33 datasets of the Global Atmospheric Watch (GAW) network, suggesting that decreasing emissions over the last decades of primary particles and gaseous precursors such as SO_2 would have led to significant decreases of both aerosol absorption and scattering coefficients. In addition, Mortier et al. (2020) suggested for both variables, significant decreases over North America and Europe using AeroCom and CMIP6 models that have simulated the historical evolution of aerosol properties. Still, there are some discrepancies between the work of Collaud Coen et al. (2020) and Mortier et al. (2020), in particular regarding trends derived for specific regions. This may result from different methods used to aggregate measurements to long time series or to differences in the time period (2000 – 2018 vs. 2009–2018) but, overall, they both confirm the shift of polluting activities from the developed countries to the developing countries during the last two decades and may also demonstrate the relatively higher reduction of BC-rich emissions in some regions, which will affect aerosol forcing estimates.

The SSA depends directly on the magnitude of the absorption and scattering coefficients; here, we do not show an analysis of the SSA as the statistics remain poor, and more observations are needed to reach robust conclusions. However, Collaud Coen et al. (2020) report observations across all GAW stations. The SSA is decreasing at three stations in North America whereas in Portugal the SSA increased, mostly related to the increase in Saharan dust load. In Europe, stations exhibiting increasing SSA trends are the urban station in Granada, Spain and most eastern and Scandinavian stations (Hungary, Finland), as well as mid-altitude stations in Germany, contrary to central Europe (Czech Republic, Italy) presenting negative trends. It appears that the historical abatement

policies for gaseous species and primary aerosol particles (e.g., in western Europe in the 1980s) have resulted in present-day decreasing SSA trends in the Western countries, whereas more recent regulations are leading to increasing SSA trends. This suggests it is necessary to consider how regulatory policies designed to improve health and environmental outcomes impact efforts on climate and vice versa.

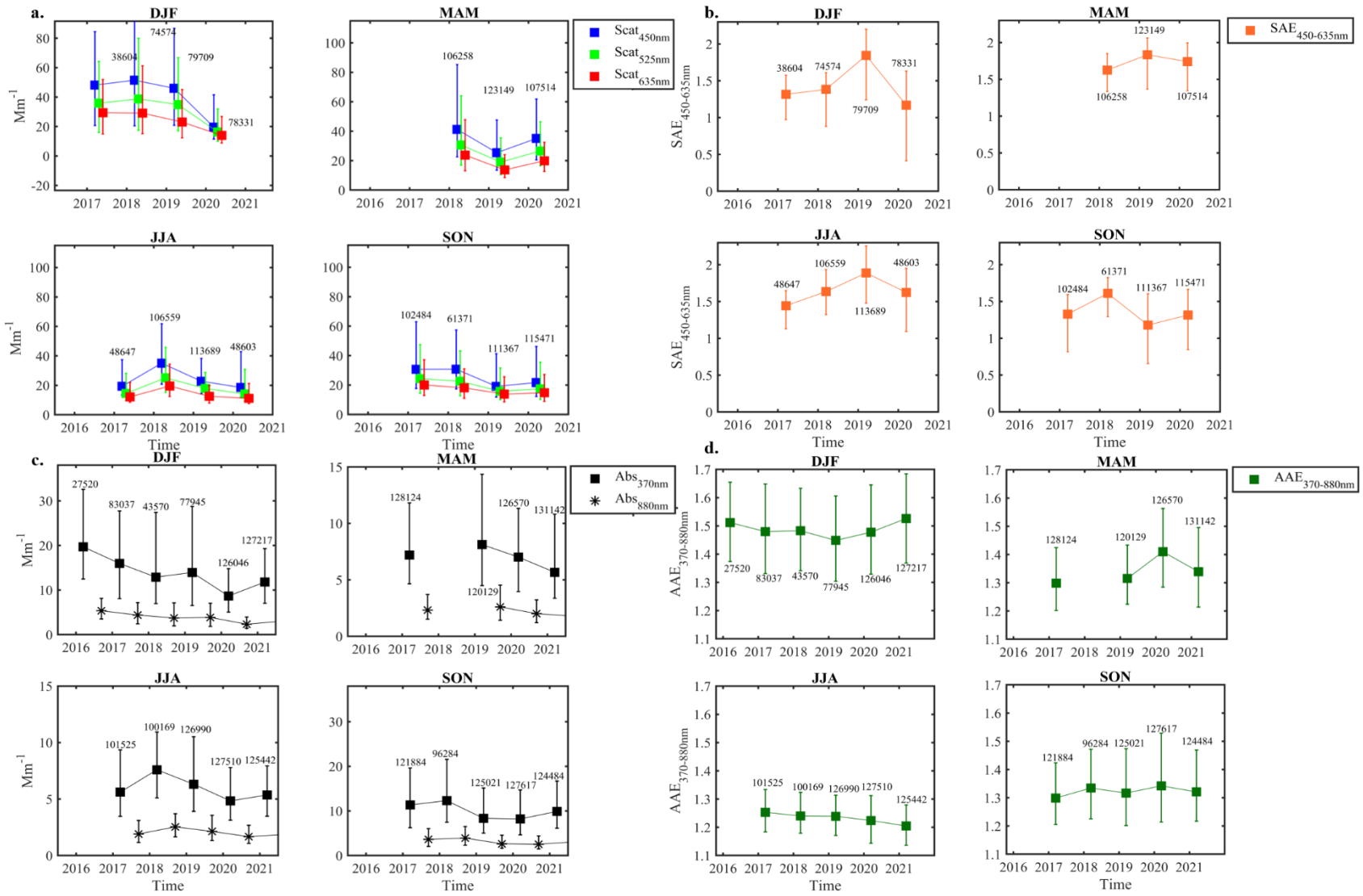

Figure 3.17 Seasonal medians and interquartile ranges of parameters derived from optical in situ observations for the period July 2017 – Dec. 2020 at ATOLL. a) Scattering coefficient, b) Scattering Ångstrom Exponent in 450-635 nm, c) Absorption coefficient, d) Absorption Ångstrom Exponent in 370-880 nm. Time-frequency used: 1 min.

3.5 Conclusions and perspectives

In this chapter, we described the particulate pollution events and variability by analyzing multi-annual observations of PM concentration, PM_1 chemical speciation and optical properties at the ATOLL platform in Northern France. This was achieved by combining the hourly observations from the regional air quality monitoring station (Atmo Hauts-de-France) located in Lille Fives, 4 km apart from ATOLL, and real-time measurements with ACSM, aethalometer, nephelometer and remote sensing observations from the AERONET network.

The ATOLL site is surrounded by many anthropogenic sources of particulate. Our results showed 187 (PM_{10}) and 263 ($PM_{2.5}$) events exceeding the latest World Health Organization – Air Quality Guidelines for the protection of human health in 2021, where nitrate shows higher contribution (29%) in comparison with days of "clear conditions", for which carbonaceous aerosol strongly dominate.

Regarding the ~4-year dataset (Oct. 2016 – Dec. 2020) of PM_1 chemical composition measurements at the site, the main contributor to the total PM_1 mass is organics (40%), followed by nitrate (28%), ammonium (15%), sulfate (8%) and equivalent black carbon (8%). PM_1 presents a seasonal trend, showing strong nitrate contribution during spring (37%), explained by the increased agricultural activities including the spreading of fertilizers and favorable meteorological conditions. Regarding the diel cycles of the chemical composition, the most commonly observed patterns are characterized by maxima in organic aerosol contribution in the afternoon or in the evening, concomitant to an eBC peak in the diel profiles, pointing out to the traffic exhaust. Ammonium and nitrate diel variations are more related to the formation mechanisms and the semi-volatile nature of AN, its concentration in ambient air notably depends on meteorological conditions (e.g. strength of (photo-)chemical atmospheric processes) and the availability of its gaseous precursors.

Concerning the optical properties, we analyzed two different types of observation (remote sensing and in situ) at the ATOLL platform. The AERONET network provides the AOD at 380 nm – 1020 nm and the AE can be calculated for the pair of wavelengths 440 – 870 nm over 13 years (2008–2021) while the in-situ optical measurements provided scattering, and absorption coefficients with their respective key optical properties (SAE, AAE, and SSA) since ~2016. Comparing variables between in-situ and remote sensing does not yield always the same trends, however, to accurately compare the two observations, further analysis regarding the contribution of BLH to the AOD is necessary.

Concerning the changes across the years, PM_{10} and $PM_{2.5}$ concentrations have decreased by 28% and 27%, respectively, between 2013– and 2021, in line with the general trend reported by the EEA (European Environment Agency 2020). By looking year to year, we see the effect that other variables might have in the decrease of concentrations. For instance, in 2020 during spring and summer, as described in section 1.3.1, the COVID lockdowns have somehow impacted the emissions, with a decrease in pollutants related to traffic emissions (Evangeliou et al. 2021; Kaskaoutis et al. 2021; Petit et al. 2021). Also, potential uncommon meteorological conditions can impact the decrease in concentrations and thereby their optical properties. Concerning the temperatures during winter in the latest years 2020 and 2019 were milder than 2017, 2018, and

2021, leading to a possible decrease in emissions from the residential sector. In addition, maximum record temperatures during summer can result in periods of droughts causing wildfires, which also translate into impacts in concentrations and optical properties related to BB (e.g. AOD, AAE).

This study underlines the importance and supports the long-term observations at high-time resolution in order to evaluate the variation and trends of aerosol concentration, chemical and optical properties over the years, which will help to assess the progress in air quality and track changes in the atmosphere which are highly relevant for climate change studies.

Finally, this chapter provided a detailed description of the ATOLL platform background and a comparison of the long-term observations with previous studies in Northern France and other European sites. The following chapter focuses on the link between aerosol optical and chemical properties aiming at investigating the main chemical species and their contribution to optical properties in the region.

CHAPTER 4

4. Linking aerosol chemical composition and optical properties

The scattering and absorption of atmospheric gases are quite well understood, yet, the effect of PM is more complicated to assess since its properties evolved continuously throughout their residence time (Masson-Delmotte et al. 2021). This is further complicated via complex composition leading to high uncertainty of radiative forcing due to ari (RFari) by species (Figure 1.5) (Myhre et al. 2013; Stocker et al. 2013).

Among many physical and optical parameters that characterize aerosol properties, composition-dependent mass efficiencies are the most important to (i) better understand aerosol optical properties and (ii) connect radiation models (Seinfeld and Pandis 2012). The MEE/MAE/MSE (section 1.2.3) can be determined using concurrent measurements of the aerosol optical properties and particle mass. Moreover, many previous derivations were limited to sulfate only to represent particle mass (Bryant et al. 2006; Vrekoussis et al. 2005) and other components, such as mineral dust, nitrate, or organic aerosols, were not considered. This assumption is not valid and it is clear that other aerosol species play an important role (Andreae et al. 2002; Cheng et al. 2008; Crumeyrolle et al. 2022; Hand and Malm 2007).

The present chapter investigates the aerosol optical properties and their relation to fine ($D_p < 1$ µm) particle chemical composition in Lille, based on the multi-annual in situ datasets at the ATOLL platform. We use three years of online submicron aerosol measurements at the surface to derive MSE, MAE, and MEE at different wavelengths and thus assess the contribution of each of the main species on optical properties in northern France. Here, we aim to capture their variability via the highly time-resolved chemical information, thus capturing fast processes of aerosol dynamics over a long period of measurements. To the best of our knowledge, the relation between aerosol chemical composition and their optical properties has not yet been investigated in the polluted urban background environments of northwestern European countries.

4.1 Bibliography

According to different studies (Cheng et al. 2008; Hand and Malm 2007; Titos et al. 2012; Valentini et al. 2018; Wang et al. 2015), α_i, defined in section 1.2.3, can be derived either from measurements of aerosol optical and physicochemical properties (e.g. IMPROVE method) or through theoretical methods (e.g. Mie theory). The first method obtains α_i from the relation between measured mass concentrations and scattering and absorption coefficients (Sciare et al. 2005; Titos et al. 2012; Wang et al. 2015, 2015), whereas the second method uses values of refractive index from the literature and the measured size distribution (Adam 2004; Cheng et al. 2008; Cheng et al. 2014; Jiang et al. 2021; Jung et al. 2020; Quinn et al. 2004; Saide et al. 2022; Valentini et al. 2018).

Different methods have been applied for the computation of scattering and absorption efficiencies, some of them consider the bulk aerosol mass while others try to offer some discrimination using chemical speciation and size segregation (Andreae et al. 2002; Formenti et al. 2001; Hand and Malm 2007; Vrekoussis et al. 2005). Table A4 - 1 presents literature values of MEEs, MAEs, and

MSEs for different aerosol species. The values are generally found to be within a range comparable to those previously reported by either theoretical (Cheng et al. 2008; Pitchford et al. 2007; Valentini et al. 2018) or experimental (Wang et al. 2015; Yao et al. 2010; Yuan et al. 2006) methods, albeit significant variations can be observed depending on the method, size fraction, and type of aerosol analyzed. Whereas values generally tend to agree between them, differences can be highlighted including different aerosol population types, size fractions, wavelengths, calculation approaches, seasons, and temporal coverages. Furthermore, the number of chemical species considered for the optical closure can be significantly larger than those considered here for the submicron fraction. All those parameters can influence the derived optical parameters and need to be carefully considered (Hand and Malm 2007).

Usually, each species contribution to total scattering, absorption, and extinction can be estimated using the volume average mixing (VAM) model and a priori aerosol mass extinction, scattering, or absorption efficiency values for each species (Hand and Malm 2007). More fundamentally, an assumption inherent to VAM is that the aerosol population is externally mixed (independent contribution to extinction), and its MEE is constant despite changes in aerosol size distribution. Despite those assumptions, VAM has successfully provided similar and more stable results than complex mixing rules (e.g. Maxwell Garnett, Bruggeman theory, core-shell model) for retrieving aerosol components (Li et al. 2019; Wang et al. 2021).

An early review by White et al. (1994) reported MSE for individual species but derived them using mass apportionment schemes with measured mass and scattering to compute MSE. Charlson et al. (1999) discussed methods for deriving MSE and briefly reviewed estimates for sulfate species. They did not account for differences in monitoring conditions (e.g. RH) and the estimates they report vary by a factor of two. Hand and Malm, (2007) have done an extensive review of MSE, performing a survey of approximately 60 studies reporting MSE for various aerosol species that were carried out under a variety of monitoring conditions, from pristine environments to urban regions around the globe. Their review distinguishes MSE values based on the particular method used to derive them. They also normalize, where possible, efficiencies to the same mass type and RH, removing some of the inherent uncertainty that exists from different monitoring conditions. Hand and Malm (2007) highlight that, while microphysical and chemical differences undoubtedly exist between aerosols, it is more likely that the methods to retrieve MSE contribute to the large range of variability in the value as seen in the literature. They report average values within the different monitoring sites; for instance, an MSE of 2.5 m^2 g^{-1} is appropriate for fine mode AS for average conditions, however, they observed lower values (~2 m^2 g^{-1}) in dry, more pristine environments compared to higher values (~3 m^2 g^{-1}) in more polluted environments. Hand and Malm (2007) recommend performing measurements over an extended period to obtain representative estimates of MSE.

In the literature, MAE can be also referred to as MAC (Mass Absorption Cross-section), a term proposed by Bond and Bergstrom (2006) which indicates that the absorption cross-section is referenced or normalized to the mass of the particle. For Bond and Bergstrom, (2006), the term "efficiency" is more appropriate to identify the ratio between optical and geometric cross sections, when the results are properly dimensionless. In this thesis, the term MAE is preferred, to facilitate

the consistency with MSE and MEE. In recent years (i.e. after the publication of Bond and Bergstrom, (2006)), Liu et al., (2020) reviewed the light absorption properties of BC. Their goal was to assess whether recent direct measurements are consistent with the value of 7.5 ± 1.2 m^2 g^{-1} at 550 nm recommended by Bond and Bergstrom, (2006). They found MAE values to be somewhat higher (8.0 ± 0.7 m^2 g^{-1}), albeit within the uncertainty. They also report that modeling studies employing numerically accurate methods have consistently underpredicted (by 30%) the MAC of BC aggregates when using a refractive index of $m = 1.95 \pm 0.79i$ (or equivalent values on the void fraction line) as recommended by Bond and Bergstrom, (2006) and the well-established mass density for aged soot.

To assess the contributions of the uncertainties in the different factors needed to estimate direct forcing as the MSE and MAE, the IPCC (Cooper et al. 2002) derived values for rough geographical locations and aerosol types (e.g. continental anthropogenic, biomass burning, etc). using theoretical methods (Mie calculations) by employing size distribution and a constant index of refraction for the accumulation mode. They report that, for fossil fuel BC, the MAE is one of the most important uncertainties ranging between 2.3-4.7 m^2 g^{-1}. Yet, this summary does not reflect the range of observed values and does not report α_i for individual species, nor is it clear whether variations in monitoring conditions (e.g. relative humidity) have been considered.

Given that BC is the most important light-absorbing particle in the atmosphere, its MAE has been extensively studied in the literature (Bond et al. 2013; Pandolfi et al. 2014; Reche et al. 2011). In some cases, the MAE of BC has been observed to vary depending on the degree of the internal mixing of BC with non-absorbing material, such as sulfate and organic compounds (Jacobson 2001; Moffet and Prather 2009; Ramana et al. 2010; Zanatta et al. 2016). The potential for organic to absorb UV and visible light (i.e. brown carbon), has been also studied (Lu et al. 2015; Updyke et al. 2012; Kasthuriarachchi et al. 2020; Ponczek et al. 2021; Qin et al. 2018; de Sá et al. 2019; Wang et al. 2015; Washenfelder et al. 2015). For instance, de Sá et al. (2019) carried out observations and analysis of PM_1 chemical composition and optical properties using a high-resolution time-of-flight aerosol mass spectrometer (AMS) and aethalometer near Manaus, Brazil. They separated organic PM_1 into six different classes by positive matrix factorization (Ulbrich et al., 2009), and they estimated the MAE associated with each factor through multivariate linear regression of BrC absorption at 370 nm on each factor. They found the largest MAE values associated with urban (2.04 ± 0.14 m^2 g^{-1}) and biomass burning (0.82 ± 0.04 to 1.50 ± 0.07 m^2 g^{-1}) sources. In another similar study (Kasthuriarachchi et al. 2020) in Singapore, by using a co-located soot particle-aerosol mass spectrometer (SP-AMS) and aethalometer, the authors retrieved BrC absorption MAE values for organic aerosol components: HOA (0.97-1.6), oxidized-HOA (0.50 – 0.85), COA (0.06 – 0.10) and, LO-OOA (0.67 to 1.13), contributing up to ~ 36-58% of the BrC absorption.

The factor that influences visibility is the light extinction of atmospheric components. Visibility can be perceptible by human eyes and influence urban skyline, land, and air transportation. Thus, studies focusing on aerosol particles historically linked MEE with visibility. Studies estimated that 75 – 95% of the total light extinction is contributed by particles (Sloane and Wolff 1985; Yao et al. 2010; Yuan et al. 2006) and the contribution to extinction from submicron particles is larger

than that from coarse particles with larger size (Watson 2002). The most popular project studying the relationship between particulate chemical composition and light extinction coefficients is IMPROVE (Interagency Monitoring of Protected Visual Environments) which established formulas to investigate the cause of the visibility impairment on the light extinction data and chemical composition measured in different national parks and wilderness areas. The method is described in detail in the next section (4.2). In Asia, the IMPROVE method has been more extensively applied to urban megacities facing serious air pollution problems and haze like Beijing, China (Wang et al. 2015). Yao et al. (2010)., as an example, used online instruments (AMS, aethalometer, and nephelometer) to retrieve MEE values via multiple linear regressions in Shenzhen, China. They showed an increase in the contribution of the organic fraction, BC and AN to the light extinction with increasing pollution levels.

In Europe, studies focusing on MAE, MSE, and MEE have been mostly conducted in southern Europe in field campaigns or during specific periods over the PM_{10} and $PM_{2.5}$ fractions. For example, Sciare et al. (2005) performed an aerosol mass closure reconstruction of the light scattering coefficient over the Eastern Mediterranean Sea. They used ambient aerosol samples to analyze the chemical composition of PM_{10} and a nephelometer to measure the scattering coefficient. Their calculations indicated that one-third of the reconstructed scattering was due to water uptake by ammonium sulfate aerosols, demonstrating its major role in the radiative aerosol properties in the eastern Mediterranean. Titos et al. (2012) investigated the same parameters for the PM_{10} range in Granada, Spain, with sulfate being the most efficient component in terms of scattering, while the least efficient was the mineral matter. Finally, Valentini et al. (2018) developed MEE site-specific coefficients for AS, AN, and Org aiming to reduce uncertainties and assumptions in assessing light extinction at polluted urban sites. For filters collected in a measurement campaign during winter in Milan (Italy), they calculated MEE using theoretical methods (e.g. discrete dipole approximation, Chao et al. (2021) and aerosol size distributions measurements) and site-specific water growth functions for each $PM_{2.5}$ chemical component. They obtained AN and Org as the main contributors to light extinction at 550 nm and a visual range from 4.8 to 21.9 km, for which typical values are about 100-200 km for clean air (Chang et al. 2009).

4.2 The IMPROVE method

Several studies have estimated MSE/MAE/MEE in the last decade but most of them were limited to specific periods of the year (field campaigns) and/or carried out through offline methods (i.e. filter collection) as discussed previously. Instrumentation capable of measuring aerosol chemical composition with high time resolution allows a detailed view of the variability of physical and chemical coupling over a time scale of minutes, while still providing multi-annual observations. Precise estimates of composition-dependent MEEs would therefore significantly improve estimates of the role of different aerosol compounds on visibility. This is particularly relevant for places identified as pollution hotspots such as Northern France.

As previously discussed, VAM assumes light extinction to be associated with mass contribution (C) of individual species (j) of a given aerosol component, thus a mathematical expression is proposed by the U.S. IMPROVE program. The formula also includes a water growth factor as a

function of relative humidity (f(RH)) for hygroscopic species and the gaseous components (NO_2, Rayleigh Scattering -RS) that would only be used at sites with available measurement data. Thus, the extinction coefficient can be calculated by:

$$\sigma_{ext,\lambda} = \sum_j MEE_{j,\lambda} \times f(RH)_j \times C_j + RS_\lambda + \sigma_{NO_2,\lambda} \quad \text{eq. 4.1}$$

IMPROVE, based on filter analysis, suggested fixed MEE values for six major chemical species of $PM_{2.5}$ including AS, AN, Org, BC, fine soil and sea salt. Yet, MEE values vary depending on site (Hand and Malm 2007), season (Tao et al. 2014) and particle morphology (Cheng et al. 2008). Therefore, the application of such coefficients at different sites with no local tailoring can lead to significant uncertainties (Valentini et al. 2018). Contrasting IMPROVE, in this analysis we employed online measurements performed under dry conditions, thus the water growth factor is set to be equal to 1. Besides, this work does not consider the contribution of gases to optical properties, only for aerosol particles. Indeed, the nephelometer is calibrated daily for a zero adjustment. This calibration is performed by sampling particle free air (filtered using HEPA filter) so that only gases can enter the instrument. The remaining signal is then corresponding to the Rayleigh scattering and is set to zero automatically. Assuming that the Rayleigh signal remains constant for the whole day, the signal acquired by the nephelometer is thus only corresponding to the particle scattering. On the other hand, the attenuation measured over time by the aethalometer can be only influenced by particles. This attenuation in time is then converted by a corresponding light-absorbing aerosol concentration in the atmosphere Thus, the equation employed here is expressed as:

$$\sigma_{ext,\lambda} = \sum_j MEE_{j,\lambda} \times C_j \quad \text{eq. 4.2}$$

This method can be extended and applied to retrieve the scattering and absorption coefficients:

$$\sigma_{scat,\lambda} = \sum_j MSE_{j,\lambda} \times C_j \quad \text{eq. 4.3}$$

$$\sigma_{abs,\lambda} = \sum_j MAE_{j,\lambda} \times C_j \quad \text{eq. 4.4}$$

For this study, we use three years of surface measurements to derive composition-dependent MEE at different wavelengths through a Multiple Linear Regression (MLR). The optical properties measured (σ_{scat}, σ_{abs}) work as independent variables, and the species mass concentrations (C_j) as dependent variables. Calculations were performed, through the least-square method, using data as mentioned in Table 4.1, considering at least 75% of data coverage. Coefficients were constrained to be positive to retain their physical meaning, and the linear intercept was fixed to zero to force PM_1 species to explain all scattering and absorption. The MLR analysis (RMSE:15.2; bias: 1.4) was performed under MATLAB 2020a on about 18,000 points of ~30-min averaged PM_1 chemical composition (NR-PM_1 and eBC) and optical coefficients (σ_{scat}, σ_{abs}) during the whole period of interest. With this method, MEEs have been estimated for each species over the whole period, encompassing clean and polluted conditions. The equation of MLR employed in this work is written in eq. 4.5:

$$y = \sum_i b_i x_i + \epsilon \quad \text{eq. 4.5}$$

where:

y is the output data to be predicted by the model (here extinction, absorption or scattering coefficients), x_i are independent input variables (here the mass concentration of particulate chemical species), b_i, the linear regression constants (here MEE, MAE and MSE), and ϵ the residual.

To evaluate the robustness of the MLR method used in this study, the residuals (Appendix A4 - *4* to A4 - 6) as well as the fractional bias (Appendix A4 - 7) were introduced. During 3 full years of measurements corresponding to more than 18,000 data points, 94% of the standardized residuals are obtained within an interval of 2σ around zero while only 6% are highlighted as outliers.

The proposed analysis presents several advantages, including highly time-resolved chemical information, thus capturing fast processes of aerosol dynamics. However, it is important to note that aerosol species such as dust or sea salt are not considered here. Days flagged as impacted by desert dust events using LIDAR measurements at the ATOLL platform were removed from the dataset to avoid possible errors, leading to the exclusion of 3% of data, mostly around March 2019. The presence of sea salt cannot be distinguished at the ATOLL station (no sodium measurements) but sea salt aerosols are generally observed within the PM_{10} fraction (Koçak, Mihalopoulos, and Kubilay 2007) while our measurements focus on the PM_1 fraction.

Table 4.1 List of in situ instrumentation within the PM_1 fraction and additional measurements at the ATOLL platform used for this section of the thesis.

Instrument	**Parameters measured**	**Time resolution (minutes)**	**# of points**		
			Raw data	**30 min-averaged data⁺**	**Data in common**
ACSM	Org, NH_4, SO_4, NO_3, Cl (NR-PM_1)	~30	24 469	26 469	18 065
Nephelometer 3 λ	σ_{scat}	1	966 412	18 994	
Aethalometer 7 λ	σ_{abs} & eBC*		858 753	24 486	

4.3 Composition-dependent mass efficiencies

The composition- and wavelength-dependent MSE, MAE and MEE parameters retrieved through the MLR approach applied to PM_1 measurements at the ATOLL site are summarized in Table 4.2. In general, values are comparable with mass efficiencies retrieved among the literature sites (Appendix A4 - 1) and differences can be attributed to changes in mass concentrations, sources, and aerosol properties (e.g. aerosol particles in the fine mode present higher mass scattering and absorption efficiencies compared to those in the coarse mode, extinguishing light more efficiently). For all components, the 370-470 nm wavelengths are characterized by the largest mass extinction, scattering, and absorption efficiencies, which decrease at higher wavelengths.

The values retrieved in northern France are compared to a comprehensive list of composition-dependent mass efficiencies found in the literature (Appendix A4 - 1) focusing on similar methods (MLR for species in PM_1). Despite the similarities in the method employed such as online instrumentation for both optical and chemical observations, differences in the MSE values can be explained by the period of analysis. To give an instance, while MSE values retrieved at 525 nm at ATOLL are 5.7 $m^2 g^{-1}$ and 3.6 $m^2 g^{-1}$ for AS and AN respectively, for wintertime, Wang et al. (2015) retrieved in Bejing (China) MSE values at 550 nm for AS and AN of 6.5 $m^2 g^{-1}$ and 2.2 $m^2 g^{-1}$, respectively.

In southern Europe, values of MSE have been retrieved focusing on bigger sizes ($PM_{2.5}$ and PM_{10}). During the MINOS campaign in the Eastern Mediterranean Sea, MSE for AS was retrieved at 2.7 $m^2 g^{-1}$ (Sciare et al. 2005) which is slightly lower than at ATOLL at 525 nm (5.7 $m^2 g^{-1}$). This variation is expected since smaller particles scatter light more efficiently. Hand and Malm (2007) performed a survey of 60 studies that report MSE under a variety of monitoring conditions. They observed elevated MSE values for fine particulates at sites under the strong influence of industrial and biomass combustion sources (e.g. Bejing, China; Atlanta, Dallas, New-England, South Africa). These conditions are different on the ATOLL platform. The contribution of sulfate to PM_1 is low (8%) and the influence of wood burning has been seen only during the cold season (section 3.3). This underlies the low effect of industrial emissions at the site and an influence of wood burning only at specific periods of the year, similar to what previous studies have reported (Bressi et al. 2021; Chen et al. 2022; Favez et al. 2009, 2021; Zhang et al. 2020). Overall, our study shows the variability in MSE due to the differences in emission sources between sites, and the contrast between studies conducted during one season of the year (e.g. Wang et al., 2015) and the pooling of 3-year observations.

As expected, BC is recognized as the most important warming agent among aerosol particles. This species is considered stable (i.e. not particularly reactive in the atmosphere) and has a well-established light absorption in the ultraviolet, visible, and infrared ranges. In Rio Branco (Brazil) Ponczek et al.(2022) focusing on PM_1, found a MAE_{BC} of 7.3 $m^2 g^{-1}$ at 520 nm, close to 7.5 $m^2 g^{-1}$ as suggested by Bond and Bergstrom (2006), and 12.0 $m^2 g^{-1}$ at 370 nm. The MAE_{BC} retrieved at ATOLL at 520 nm (7.5 $m^2 g^{-1}$) and 370 nm (11.6 $m^2 g^{-1}$) are consistent with those results. In Milan (Italy), (Gilardoni et al. 2020) retrieved the MAE_{BC} value at 880 nm during winter (9.8 $m^2 g^{-1}$) and summer (9.5 $m^2 g^{-1}$). These values were 6 times higher than the ones obtained at ATOLL (3.9 $m^2 g^{-1}$) and Rio Branco (3.9 $m^2 g^{-1}$), explained by the difference in size range (PM_{10} vs PM_1). Focusing on a bigger cut-size ($PM_{2.5}$), a recent study in Granada, Spain (Yus-Díez et al. 2022), reports a MAE_{BC} at 370 nm of 22.7 $m^2 g^{-1}$, 6 times higher than the reported value at ATOLL. The variability of reported MAE values can be attributed to the mixing of BC with other aerosol particles. Based on a simple configuration of concentric spheres core-shell morphology (Bohren and Huffman 1998), if a BC particle is coated with non-absorbing species, more light is focused towards the BC core, enhancing the amount of light it absorbs (E_{abs}) and thereby increasing its MAC_{BC} value. This is known as the *lensing effect* (Van de Huslt 1957). Thus, the BC radiative effect is highly dependent on the availability of materials mixing with BC, and therefore creating regional variations (Yus-Díez et al. 2022).

In recent decades, Brown Carbon, the absorbing component of Organics, has been receiving particular attention, because of its significant effects on atmospheric radiative impacts (Lu et al. 2015). The chemical composition of Organics is very complex, and its optical properties vary greatly depending on sources and wavelengths (Chen and Bond 2010; Fan et al. 2016). Thus, as mentioned in Appendix A4 - 1, the MAE for Organics can be retrieved both, as total mass (Chen et al. 2020; Cheng et al. 2008; Gilardoni et al. 2020; Tao et al. 2020), or, for the factors given by the source apportionment with Positive Matrix Factorization (Kasthuriarachchi et al. 2020; Li et al. 2019; Ponczek et al. 2021a; Qin et al. 2018; de Sá et al. 2019; Washenfelder et al. 2015). Focusing on small size cut-off (PM_1) and total Organic mass, in Rio Branco, Brazil (Ponczek et al. 2021), the MAE obtained is 3.0 m^2 g^{-1} at 370 nm, whereas, for ATOLL, the MAE retrieved is 0.7 m^2 g^{-1}, comparable with the value reported for Milan, Italy (Gilardoni et al. 2020) during summer (0.5 m^2 g^{-1}). It is worth noting that Rio Branco can be subject to intense tropical deforestation fires, and thus in a quite distinct aerosol population as observed in Europe. Furthermore, the radiative properties depend on the type of material burned, fire conditions (flaming vs. smothering) and the process of atmospheric aging. In addition, the absorption of light in the UV-Vis range can be explained by absorbing molecules such as soluble humic-like substances (HULIS), nitroaromatics, polyoxygenated compounds and polyaromatic hydrocarbons, known as chromophores (Moise et al. 2015). Hence, the formation of chromophore compounds in organics has mechanisms common to all types of fuel/fire and exhibits unique properties addressed to local emission characteristics and aging time.

As previously discussed, literature-based MEEs yield strong variability in the reconstructed extinction coefficient. In recent years, MEE estimation via the IMPROVE approach has been used in numerous studies, mainly carried out in heavily polluted urban areas in China, or over US national parks where uniform haze occurred often. In a similar trend as observed for MSE, the MEE at ATOLL for AS at 635nm is 4.5 m^2 g^{-1}, in comparison to the study in Bejing (China) perfomed by in wintertime (Wang et al. 2015). In Shenzhen, China (Yao et al. 2010) the MEE value of AS at 550 nm retrieved is 2.3 m^2 g^{-1}, whereas we obtained 5.0 m^2 g^{-1} at 525 nm. Conversely, their MEE for Organics was 4.5 m^2 g^{-1}, while we obtained 1.8 m^2 g^{-1} at ATOLL. Given that scattering makes a large fraction of extinction, it is expected that MSE and MEE are somehow comparable.

Table 4.2 Retrieved values of Mass Scattering, Absorption and Extinction Efficiencies (MSE, MAE, MEE, respectively) from 370 to 950 nm based on MLR analysis at ATOLL.

	Wavelength (nm)	**Ammonium Sulfate**	**Ammonium Nitrate**	**Organics**	**eBC**
Mass Scattering Efficiency, MSE (m^2 g^{-1})	450	7.1	4.6	3.1	-
	525	5.7	3.6	2.2	-
	635	4.8	2.7	1.5	-
Mass Absorption Efficiency, MAE (m^2 g^{-1})	370	-	-	0.7	11.6
	470	-	-	0.3	8.9
	520	-	-	0.2	7.5
	590	-	-	0.2	6.5
	660	-	-	0.1	5.5
	880	-	-	0.0	3.9
	950	-	-	0.0	3.7
Mass Extinction Efficiency, MEE (m^2 g^{-1})	450	5.8	4.6	2.9	13.5
	525	5.0	3.7	1.8	11.2
	635	4.4	2.7	1.0	10.7

Based on $PM_{2.5}$ filter analysis during wintertime in the Po valley (Italy), Valentini et al. (2018) obtained an MEE at 550 nm for AS comparable to ours (4.4 m^2 g^{-1}), but a value almost 3-fold higher for organics (6.1 m^2 g^{-1}), comparable with the value reported by Gilardoni et al. (2020) in Italy. As previously mentioned, organics are characterized by complex chemical composition and optical properties, determined by their origins (anthropogenic or biogenic, primary emitted or secondary produced) (Laskin, and Nizkorodov 2015). This study in Italy (Valentini et al. 2018) focused on a bigger size fraction (1 µm vs. 2.5µm) during a single season (winter), whereas our study targets the PM_1 fraction on a multi-annual basis. Thus, different MEE for organics could be explained by diverse aerosol origins during the studied period (multi-seasonal vs. wintertime) with different mixing states and size ranges (Hand and Malm 2007), although the roles of possible measurement artifacts (ACSM vs. Thermal Optical Transmittance analysis) and of the method employed to retrieve aerosol mass efficiency (experimental vs. theoretical) cannot be excluded. Indeed, site-specific dry mass extinction efficiencies in the Po valley (Valentini et al. 2018) were retrieved considering additional physical properties (e.g. density, geometric mean radii, the mass fractions of four modes and site-specific water growth factors for individual species). Hence, the discrepancy in MEE calculated for Org is also likely to be ascribed to differences in mass relative

contribution and geometric standard deviations of the modes, as well as the water growth factors detected at the Po Valley compared to the ATOLL site.

In order to estimate the range of variability in optical properties discussed above, Figure 4.1 displays the impact of using literature values for MEEs with ATOLL mass concentration observations for each species to retrieve the extinction coefficients (eq. 4.2). For comparison, we selected six studies focusing on fine aerosol fractions (either PM_1 or $PM_{2.5}$) and the same species as in our work (AN, AS, Org, eBC). For example, using MEE values based on theoretical calculations from Cheng et al. (2008) and Pitchford et al. (2007) could result in respectively a 30% underestimation and 74% overestimation of the total extinction observed at ATOLL. Conversely, experimentally-derived MEEs from field observations (Wang et al. 2015; Yao et al. 2010) are showing better results with 18% difference in comparison to total extinction observed at ATOLL. Nevertheless, even a good agreement for total extinction does not automatically imply an agreement for individual species, as discussed in the next section.

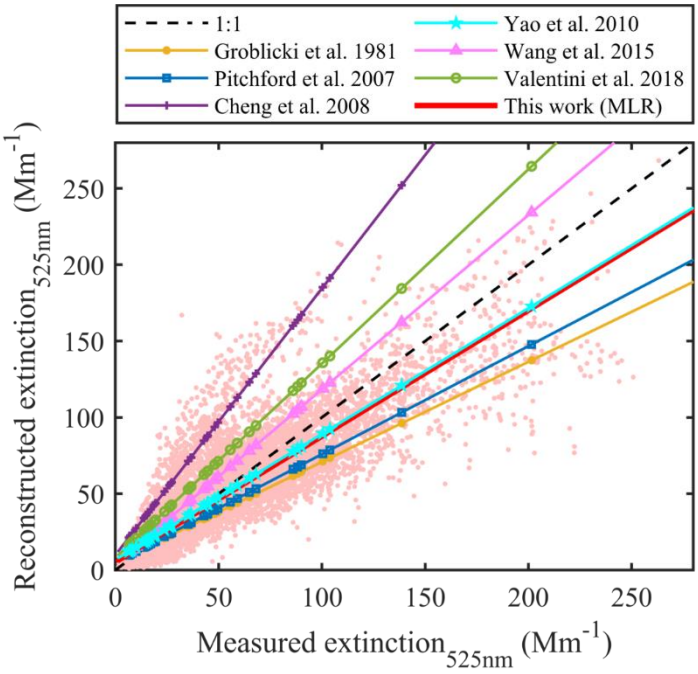

Figure 4.1 Scatter plot of reconstructed versus measured aerosol extinction coefficient at 525 nm for ~ 3-year measurements at the ATOLL platform. Solid lines represent the linear least-square fit through the data where y-values have been calculated using fixed MEE taken from the literature (Cheng et al. 2008; Groblicki, 1981; Pitchford et al. 2007; Valentini et al. 2018; Wang et al. 2015; Yao et al. 2010) combined with ATOLL PM_1 species mass concentrations. Results of the Multiple Linear Regression with ATOLL MEE values are represented by the pink dots and the solid line in red (# of points: 18 065; R^2: 0.80; slope: 0.82).

To explore the seasonality in the masses of extinction at the site, we apply the MLR to retrieve MEE/MAE/MASE values by seasons (Appendix A4 - 2). In general, the model manages to replicate the observed extinction with a good correlation coefficient (R^2 >0.8) for all seasons except spring (R^2 < 0.5), where the model has issues retrieving accurate values of MSE and MEE

at all wavelengths. This might be explained by the limited number of data coverage for spring season across the three years of observation.

4.4 Chemical contribution to aerosol optical properties

By considering the obtained MSE/MAE/MEE and average mass concentration of each species, we calculate their relative contribution to optical properties. SIA, i.e. AN and AS, were the main contributors (66%) to scattering for all three wavelengths: 450, 525 and 635 nm (Figure 4.2a). In general, AN is the main contributor with 35%, followed by the Org (33%) and AS (22%) at 525 nm, the contribution for Org tends to slightly decrease (by ~5%) at 635 nm. This agrees with a comparable study for a heavily polluted urban area in Xi'an, China, (Zhou et al. 2019), where AN and Org are the main contributors to scattering, also responsible for the degradation of visibility (< 5 km) and air quality.

Conversely, light absorption is entirely apportioned to carbonaceous aerosols, with Organics being optically active at the near-ultraviolet and blue wavelengths (370 – 590 nm) accounting for up to 22% of the total absorption at 370 nm, the rest being apportioned to eBC (Figure 4.2b). This is comparable with what is reported for Zürich in Switzerland (Moschos et al. 2021), for which an Organic contribution to the total measured absorption of 30 ± 14% was assessed at 370 nm, decreasing down to 4 ± 2% at 590 nm, while BC contribution was estimated two-thirds of the particle absorption in the near-UV to infrared wavelength range. Notably, for sites highly impacted by combustion sources and gas precursors (VOCs), as Rio Branco, Brazil (Ponczek et al. 2021), the organic species can contribute to approximately 50% of absorption at 370 nm, decreasing to 10% at 630 nm. Several studies (Kasthuriarachchi et al. 2020; Ponczek et al. 2021; Qin et al. 2018; de Sá et al. 2019; Washenfelder et al. 2015) have observed strong absorption of biomass burning organic aerosol within the UV-Visible range. Similarly, at the ATOLL platform, BBOA is the main contributor source to organic absorption at 470 nm (Velazquez Garcia et al. 2022).

Considering aerosol extinction at 525 nm (Figure 4.2c), AN is the dominant species (35%), followed by eBC (29%) and Organics (21%), and finally AS (15%). For other wavelengths, organics has a slightly higher contribution at 450 nm, but a lower contribution at 635 nm, whereas BC show an inverse wavelength dependency, with maximum at 635 nm (Figure 4.2c). While Valentini et al. (2018) have also identified AN as the main contributor to extinction at 550 nm in the Po valley, Yu et al. (2010) identified BC (76%) as the dominant species in urban areas in the Pearl River region (China). All the differences cited above highlight the complex and probably mixed influence of source intensities, topography, and meteorological conditions that drive optical properties at a given site, and more generally reflect the spatial and temporal variability of fine particles in the atmosphere.

Regarding seasonality (Appendix A4 - 12), the contribution of chemical species to extinction and scattering at all wavelengths does not vary, the main dominant chemical species is AN, followed by carbonaceous species and AS. The contribution of absorption by the Org and eBC presents a more marked seasonality at the UV-Visible range. During the cold seasons (winter and fall) the contribution of Org at 370 nm is higher (29% and 21%) in comparison with summer (10%) and spring (8%). This difference is explained by wood combustion from residential heating during those seasons (Qin et al. 2018; Velazquez Garcia et al. 2022; Zhang et al. 2020).

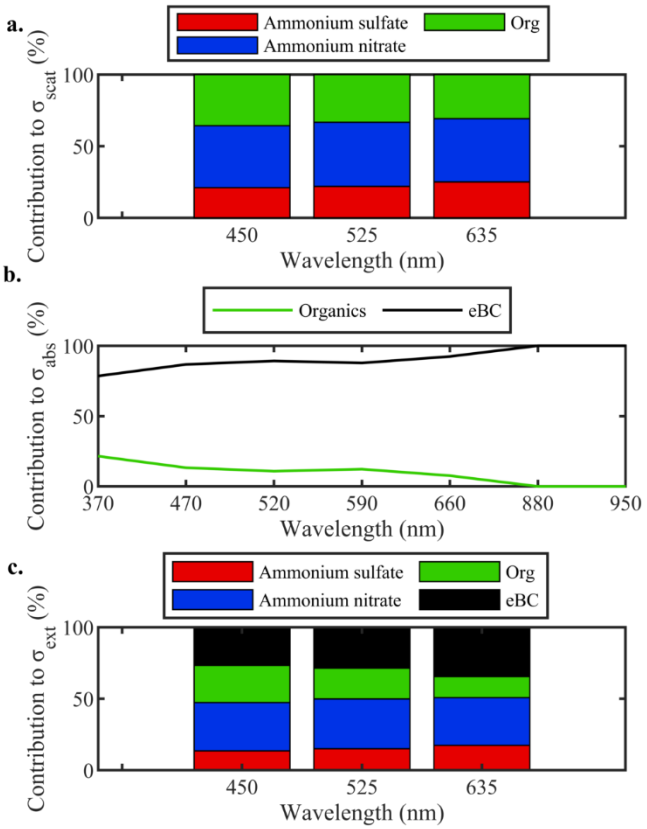

Figure 4.2 Averaged relative contributions of PM_1 chemical species to the aerosol optical properties at ATOLL over the period July 2017 – Dec. 2019: a) Secondary Inorganic Aerosols and Organics to light scattering at 450, 525 and 635 nm; b) carbonaceous aerosols to light absorption from 370 to 940 nm; c) PM_1 species to light extinction at 450, 525 and 635 nm.

Figure 4.3 represents the monthly normalized light extinction broken down according to species contribution, a product of mass efficiency and changes in the mass concentrations. As expected, light extinction is generally higher during the cold months, with three maxima in November, February and April. As explained in chapter , these months are strongly impacted by aerosol emissions related to solid fuel combustion from residential heating (carbonaceous aerosols), and agricultural activities leading to strong AN (5.8 µg m^{-3}) formation (Crenn et al. 2017; Rodelas et al. 2019) during spring. AS (1.2 ± 1.2 µg m^{-3}) has a fairly constant absolute contribution throughout the year peaking at about 25% of extinction during the summer. It is interesting to note the increase in the relative contribution of Org during summertime, likely associated with higher sources of biogenic precursors to the particulate secondary formation (Gómez-González et al. 2012) favored at higher temperatures, also discussed in chapter 3.

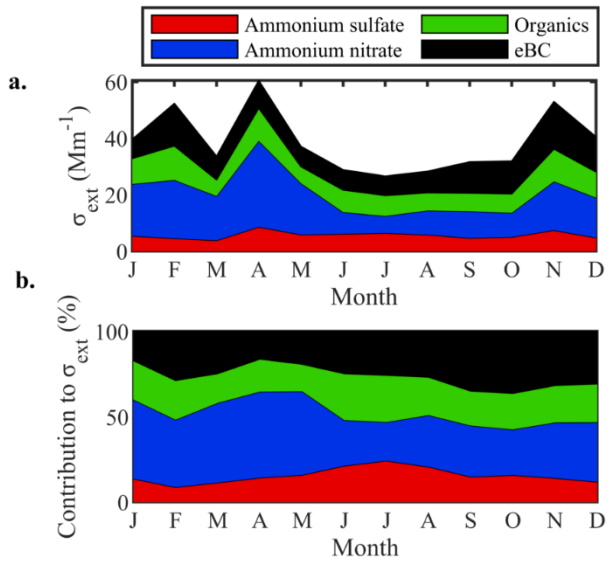

Figure 4.3 Contribution of the main aerosol species to the extinction coefficient at ATOLL over the period July 2017 – Dec. 2019. a) Monthly-averaged variation of the light extinction coefficient at 525 nm (in Mm^{-1}) for each considered species. b) Monthly-averaged relative contributions of each component to the light extinction coefficient at 525 nm.

In Section 4.2, it is discussed how using the literature values of optical properties can lead to significant bias (or not) when estimating light extinction at other sites. However, it is important to consider that even for cases when the total extinction is comparable, large discrepancies can remain on composition-based apportionment (Appendix A4 - 13). For example, applying the MEEs derived from the study of the experimental method in Shenzhen for the PM_1 fraction (Yao et al. 2010) to ATOLL mass concentrations allows to reconstruct the total extinction within 18% of the observed values, however, it overestimates the role of Organics by 50% compared to similar calculations using ATOLL site-specific MEE (Figure 4.4). Conversely, using MEEs based on theoretically-calculated (Mie model) values for National Parks in the USA (Pitchford et al. 2007), would lead to a lower underestimation (about 9%) of the role of AN, while the total reconstructed extinction would be 30% larger than the light extinction observed. Finally, using a fairly comparable sampling site in Europe, MEE parameters derived through theoretical calculations on a filter analysis for $PM_{2.5}$ in the Po Valley (Valentini et al. 2018), would lead to an underestimation of the AS extinction by 6% which might be driven by the contribution of supermicron aerosols (mainly sulfate and nitrate; Qin et al., 2012) to the PM mass concentration.

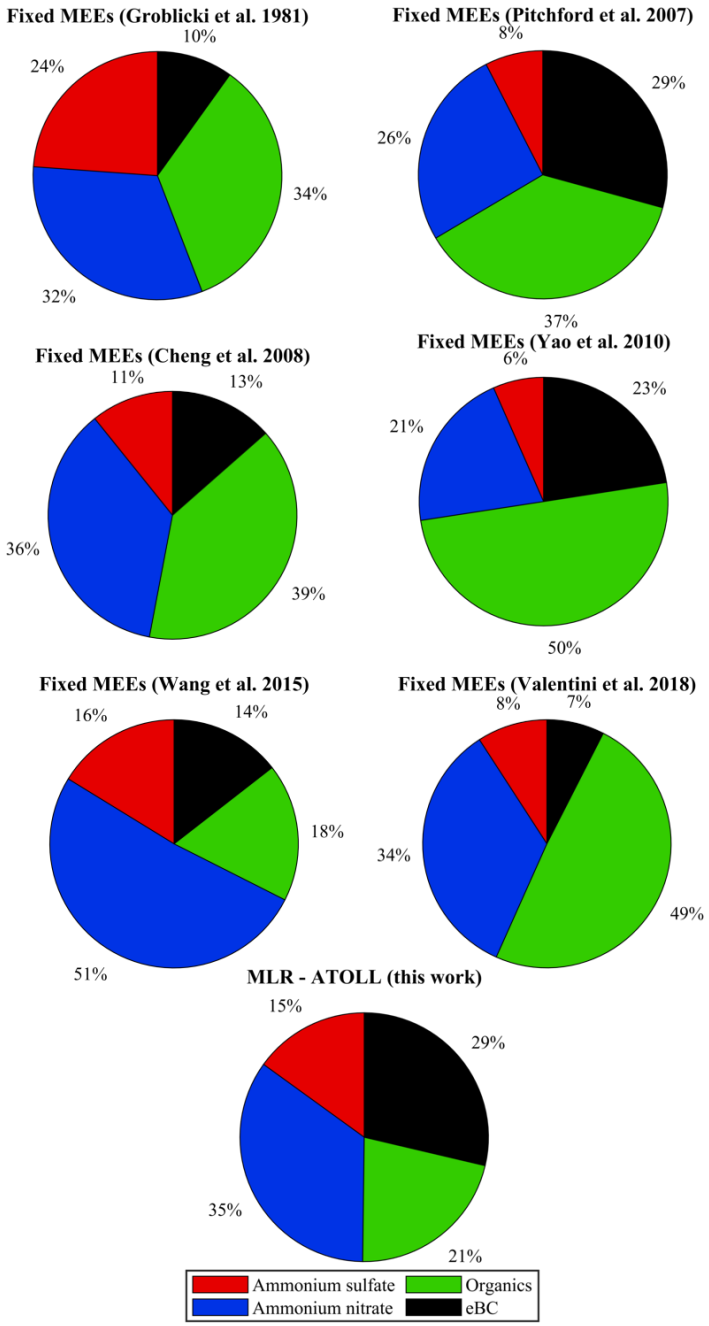

Figure 4.4 Relative contribution to extinction at 525nm calculated from the IMPROVE equation (eq. 4.2) of ammonium sulfate ammonium nitrate, organic fraction, and black carbon using MEEs from the literature (Cheng et al. 2008; Groblicki et al.1981; Pitchford et al. 2007; Valentini et al. 2018; Wang et al. 2015; Yao et al. 2010) and retrieved from MLR (this work) and each species mass concentrations at ATOLL.

4.5 Conclusions and perspectives

The present chapter points out the need for accurate knowledge of the physical, chemical, and optical properties of aerosol particles, essential to reduce current uncertainties associated with their radiative impacts on the Earth's climate. Nevertheless, the complex aerosol (trans)formation

processes and range of sources lead to a strong spatial and temporal variability in aerosol properties. Here, we combined in situ coincident aerosol chemical and physical measurements within the PM_1 fraction via the IMPROVE algorithm, to provide robust estimates of their optical properties relevant for better assessments of their radiative effects. The IMPROVE algorithm uses a single MEE value for each major chemical species of PM (ammonium sulfate, ammonium nitrate, organic fraction, black carbon). This method has been used for estimating the extinction coefficients mostly in the United States and China. Several studies have addressed this topic over Europe, mostly at south European sites, and within the PM_{10} and $PM_{2.5}$ fractions. Hence, for the first time, we retrieved the light extinction and the composition-based apportionment in the PM_1 fraction at a polluted site in northwestern Europe.

First of all, we employed literature-based MEE reported for suburban and urban sites and used it to estimate the light extinction at 525 nm over ~3 years of measurements at ATOLL. where the reconstructed and the composition-based apportionment are retrieved with a range of biases depending on the chosen reference. The results highlight strong over- or underestimation of the total extinction coefficient depending on the literature reference used. As an example, when using MEE derived from Chinese megalopolis (Cheng et al. 2008) the reconstructed extinction can be overestimated by 74%.

The multiannual analysis for ATOLL highlights that AN is the predominant species regarding light extinction at 525 nm (35%), followed by the carbonaceous aerosol species (eBC 29%, Org 21%) and AS (15%). Regarding the absorption at 370 nm, organics are responsible for 22% of light absorption, evidencing a significant contribution of Brown Carbon in the region, associated with BBOA (Velazquez Garcia et al. 2022). The scattering at 525 nm is dominated by AN (44 %) and organics (33 %), species related to poor air quality in polluted urban environments (Cheng et al. 2014; Sciare et al. 2005; Titos et al. 2012). The extinction is shown to be generally higher during winter, strongly impacted by aerosol emissions related to solid fuel combustion from residential heating. Moreover, during spring, agricultural activities combined with traffic emissions (NO_x) lead to strong AN formation.

Overall, this study provides new evidence that not considering aerosol heterogeneity among different sampling sites and seasons can lead to significant biases in estimating their extinction. Our analysis of the long-term ATOLL dataset in Lille highlights the ability to retrieve robust aerosol optical properties from chemical composition measurements, constrained by coincident absorption and scattering measurements. In addition, this work supports the use of site-specific parameters (that reflect various influences, such as aerosol mixing state and size distribution of aerosol components) along with long-term field observations, to derive key aerosol optical properties relevant for climate modeling and air quality assessment.

In this chapter, we highlighted the important contribution to the optical properties of the light-absorption aerosols on the site (Velazquez-Garcia et. al. 2023). Thus, in the next chapter, we investigate their geographical origins and associated optical properties through an innovative approach combining different methods.

CHAPTER 5

5. Light-absorbing aerosol origins

Carbonaceous particles (e.g., BC and Org) suspended in the atmosphere have attracted increasing attention in scientific research because of their multitude of sources, and effect on climate as highlighted in the previous chapter. Due to its strong light absorption, BC is largely responsible for the positive radiative forcing due to aerosol while Org is one of the largest contributors to fine particulate matter mass concentrations. Recently, the scientific community has become interested in brown carbon (BrC), which is a light-absorbing organic compound whose lifetime and impacts remain still uncertain. Understanding the properties and dynamics of carbonaceous particles and the transformation of carbonaceous aerosols in the atmosphere is a complex task that requires extensive research. In this last chapter of the thesis, we analyzed how different anthropogenic sources and their geographical origins affect the optical properties of those carbonaceous aerosols at ATOLL via a novel approach combining multiannual coincident real-time submicron aerosol observations, individual back trajectories and monthly EDGAR emission inventory (Crippa et al. 2020).

5.1 Introduction

Light-absorbing aerosols (LAAs) are an important component of the climate system due to their effect on solar radiation (Aerosol-Radiation Interactions, ari) and the associated impact on cloud properties (Aerosol-Cloud Interactions, aci) (Forster et al. 2021). In addition, LAAs can efficiently reduce snow/ice albedo when deposited, increasing heating and accelerating melting (Pu et al. 2017; Wang et al. 2017). They are mainly composed of mineral dust and BC, both of which absorb solar radiation over a broad spectral range, from UV to infrared. Light-absorbing organic carbon (also called brown carbon, BrC) is characterized by an absorption spectrum at the UV wavelengths. These aerosols can be highly relevant to atmospheric photochemical processes, however, uncertainties remain on what types of molecules or molecular aggregates dictate the optical properties of BrC, and how atmospheric processing forms or destroys those compounds (Laskin, and Nizkorodov 2015; Moise et al. 2015). To date, numerous LAA sources have been identified, including both anthropogenic (e.g. emissions from combustion of fossil fuel and biomass) and biogenic ones (e.g. vegetation emitted terpene/isoprene oxidation and primary biological aerosol particles from plants and fungi) (He et al. 2021; Kanakidou et al. 2005; Ng et al. 2017).

Figure 5.1 shows a range of atmospheric carbonaceous compounds divided by their analytical techniques or their physical properties. At the top of the chart, amorphous carbonaceous materials (BC or EC, depending on the classification method) have the lowest volatility and are characterized by the strongest absorption coefficients. For simplicity, those aerosol types will be referred to as BC hereafter.

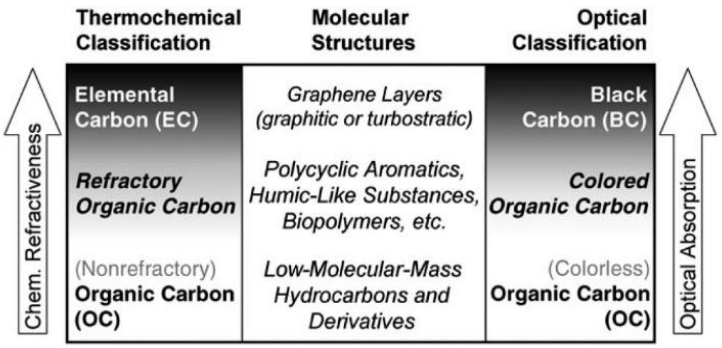

Figure 5.1 Optical and thermochemical classification of atmospheric carbonaceous particulate matter. BrC material is an ensemble of light-absorbing (colored) organic compounds with a variety of molecular structures and molecule-specific optical properties. Source: Pöschl (2005)

Once emitted into the atmosphere, the properties of LAA can evolve over time as a result of changes in their chemical composition, as well as their physical properties (e.g. size distribution, phase state, viscosity) (Laskin, and Nizkorodov 2015; Moise et al. 2015). BC has a typical atmospheric lifetime of 7 to 10 days, observations have shown that it typically ages within a few hours over polluted regions such as urban and biomass-burning areas (Denjean et al. 2020; Kumar et al. 2018; Saturno et al. 2018; Sun et al. 2021), whereas the aging time scale can be days to weeks in remote areas. Conversely, BrC, as organic aerosol, is even more likely to react in the atmosphere, potentially leading to bulk OA formation or loss (e.g. fragmentation), or changes in its optical properties via functionalization or fragmentation leading to absorption enhancement or decrease (also known as bleaching) (Laskin, and Nizkorodov 2015). BrC can be photolyzed and degraded to be less absorbing when directly exposed to solar radiation (i.e. photobleaching) but with different photolysis rates for certain chromophores (Chen et al. 2021; Hems et al. 2021; Liu et al. 2021; Liu et al. 2016). As a consequence, only a few modeling studies tried to include the lifetime of BC and BrC to estimate climate impacts (Saleh 2020). This is further complicated by the significant impact that long-range transport pollution plumes have over large distances while being transformed via atmospheric aging (van Pinxteren et al. 2016; van Pinxteren et al. 2019; Waked et al. 2018; Yttri et al. 2020). Therefore, a broader overview of real-world LAA properties according to sources and age is fundamentally relevant to guide a better representation of the climatic impact of aerosol particles.

5.2 INTERPLAY approach

Typically, the methods used to identify, quantify and characterize pollutant emission sources in the literature can be grouped into two main classes: dispersion and receptor models (DM and RM, respectively). DMs are mathematical simulation approaches used to predict pollutant dispersion in the atmosphere (e.g. Gaussian models, Chemical Transport Models) (Althuwaynee et al. 2021; Holmes and Morawska 2006). RMs are statistical approaches used for the identification and quantification of pollutant sources at a receptor site (e.g. Principal Component Analysis – PCA, Positive Matrix Factorization – PMF, Chemical Mass Balance – CMB) (van Pinxteren et al. 2016; Poulain et al. 2021). They are based on observations, analyzing the temporal co-variability of parameters, and attributing sources based on previously established source signatures. For

example, at the ATOLL site, a 1-year PMF analysis on Organic Aerosols (OA) yielded a source attribution only for traffic and wood combustion (11 and 14% of OA, respectively), leaving the majority (73%) as oxygenated (i.e. aged) compounds, without further source attribution (Chen et al. 2022). DMs, on the other hand, can provide a broad overview of atmospheric sources and processes, however typically with high computational costs making them impractical for integrating source assessments with comparable high-time resolution observation (Thunis et al. 2016). Hence, in this work, we developed an hybrid-method termed INTERPLAY by combining 'IN-siTu obsERvations, hysPLit And emission inventorY'. It is based on computationally inexpensive Lagrangian modeling, and emission inventories, providing a significantly faster calculation time than typical DMs, with complementary information for RM analysis. This method consists of integrating emissions of a given species along individual back-trajectories (BT) in order to quantify the relative contributions (including information such as residence time) to the receptor site. Here, INTERPLAY has been applied to BC, given that it is expected to be conserved in the time frame of BT considered here (72 hours). Furthermore, the INTERPLAY approach aims to help interpret the multi-annual real-time in-situ observations, allowing to the characterization of the corresponding optical properties of LAA measured at ATOLL according to their sources and age since emission.

The BTs used here were calculated for the 2016 – 2019 period with the NOAA Hybrid Single-Particle Lagrangian Integrated Trajectory (HYSPLIT) model (Stein et al. 2015) with an arrival height at half the BLH and 1-hour intervals (24 trajectories per day, UTC), for 72 hours back in time using 1° × 1° resolution Global Data Assimilation System (GDAS). The emission inventory was supplied by the Emissions Database for Global Atmospheric Research (EDGAR[1]) developed by the Joint Research Center (JRC). EDGAR provides independent estimates of global anthropogenic emissions and emission trends, based on publicly available statistics (Crippa et al. 2020). The emission inventory is characterized by a world-historical trend from 1970-2018, including emissions of all greenhouse gases, air pollutants, and aerosols. Data are presented for all countries, with emissions provided per main source category, and gridded on a spatial resolution of 0.1° × 0.1°. The 6.1 version employed in this work is time-dependent, with temporal profiles developed for country/region- and sector-specific to achieve the seasonal trend. Here, we chose monthly sector-specific grid maps for black carbon emissions, where the sectors included in this analysis are non-resuspended traffic and resuspended traffic, shipping, combustion for manufacturing, residential, oil refineries and transformation, agricultural waste burning and power industry (Figure 5.2). The sum of these sectors represents 88% of BC emissions.

[1] EDGAR web site - https://data.jrc.ec.europa.eu/collection/EDGAR

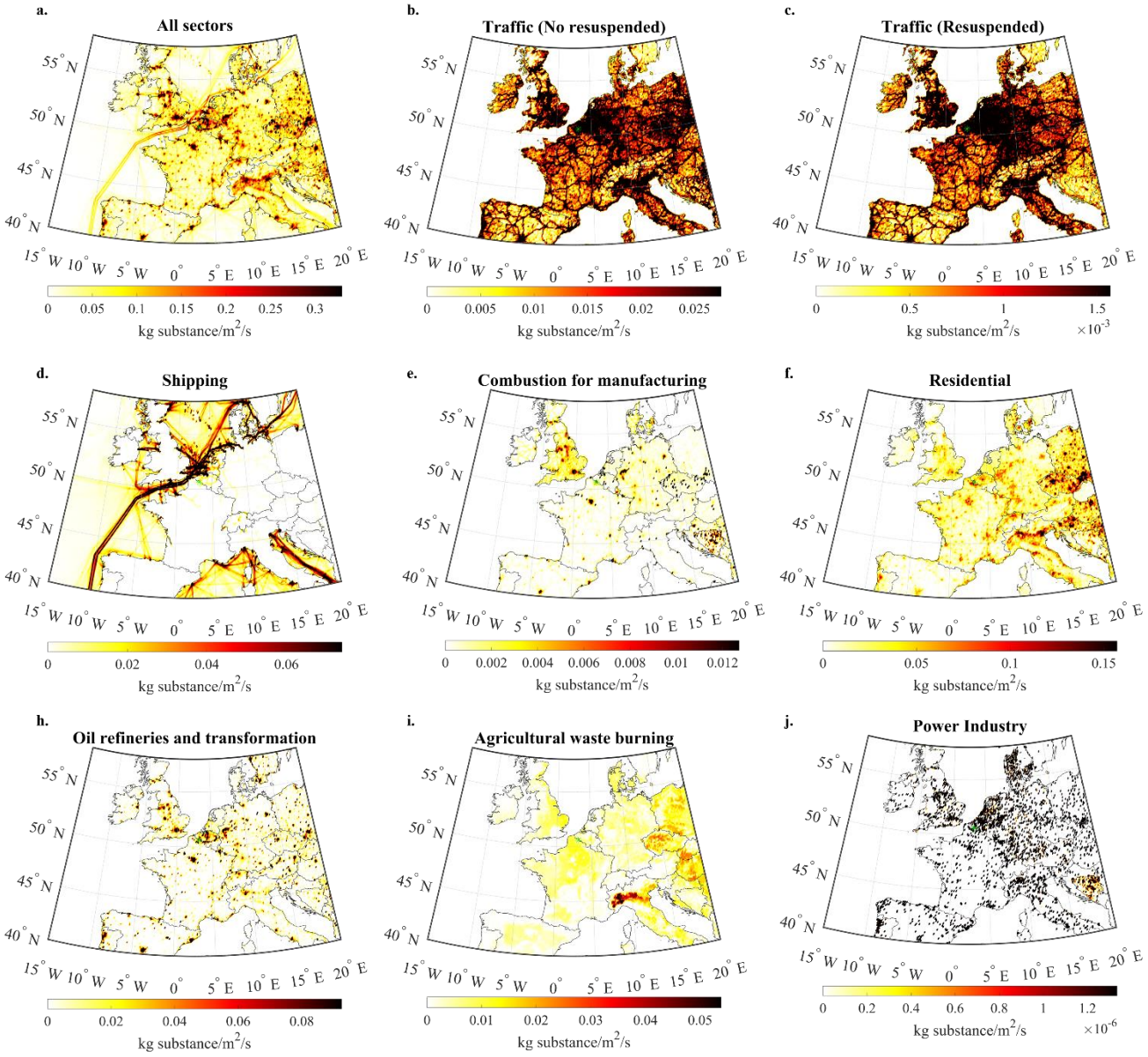

Figure 5.2 Sector-specific grid maps in kg of substance/m^2/s (0-95th percentile) from EDGAR v6.1 (https://edgar.jrc.ec.europa.eu/index.php/dataset_ap61). (a) All sectors combined. (b) Tail-pipe traffic emissions. (c) Resuspended by traffic. (d) Shipping emissions, including on rivers and canals. (e) Industry-manufacturing, generation of electricity and heat for own usage. (f) Residential sector, generation of heat (biomass or liquid fuel). (g) Oil refineries and transformation – refining petroleum products and production of charcoal. (h) Agricultural waste burning. (i) Power industry, producers of electricity generation, heat and power generation.

INTERPLAY firstly interpolates hourly HYSPLIT trajectories into 10-min points for a finer spatial coverage, and, for points more than 40 km from the receptor site, it integrates EDGAR emissions over a square of 35 km × 35 km centered on the BT location. For distances smaller than 40 km, INTERPLAY considers the air mass arrival direction and integrates only the emissions

contained in the wind sector of arrival. This criterion has been defined to better represent the emissions in the vicinity of the site (e.g. not consider emissions from Lille, located in the NW direction from ATOLL, when air masses arrive from the SE) (Appendix A5 - 1).

The method proposed here has also been optimized according to certain criteria. For example, tests were performed to not include ground-level emissions when air masses were located above certain heights (e.g. free troposphere as defined by HYSPLIT), but the best correlation between INTERPLAY and observations was obtained without such filtering, probably from inaccurate identification of boundary layer/free troposphere by the model, and/or mixing between air masses during transport. Furthermore, for the 72h BT, only 19% of points were found to be above the BLH, with a fairly small effect. Another filter considered was to limit the effect of aerosol removal by precipitation (known as wash-out). To address this in INTERPLAY, only BTs with less than 1 mm of integrated rain over the 72h have been used, removing about 41% of the BTs. Indeed, without the BLH criteria and only filtering the rain, we refine the capacity of INTERPLAY to describe the hourly in-situ BC observations (R^2 of 0.153 using BLH and rain filter improves slightly to 0.165 accounting only for rain).

INTERPLAY has been developed using Matlab, and country apportionment has made use of the climate data toolbox (Greene et al. 2019). BC footprints have been calculated considering six different sectors (sum of all, and separately as shown in Figure 5.2). Finally, to minimize the effect of sporadic, local BC sources on our analysis, BTs were aggregated into 12 hour averages, and the median of integrated BC and its corresponding sources and distances were calculated. Those values were then correlated with in-situ observations, however focusing on the 5^{th} percentile of the period, i.e., the baseline values. The objective of such analysis is two-fold: it decreases the relevance of local sporadic sources (making them more regionally-relevant), as well as improving significantly the ability of INTERPLAY to explain in-situ BC observations (R^2 of 0.165 for hourly data up to 0.36, Figure 5.3).

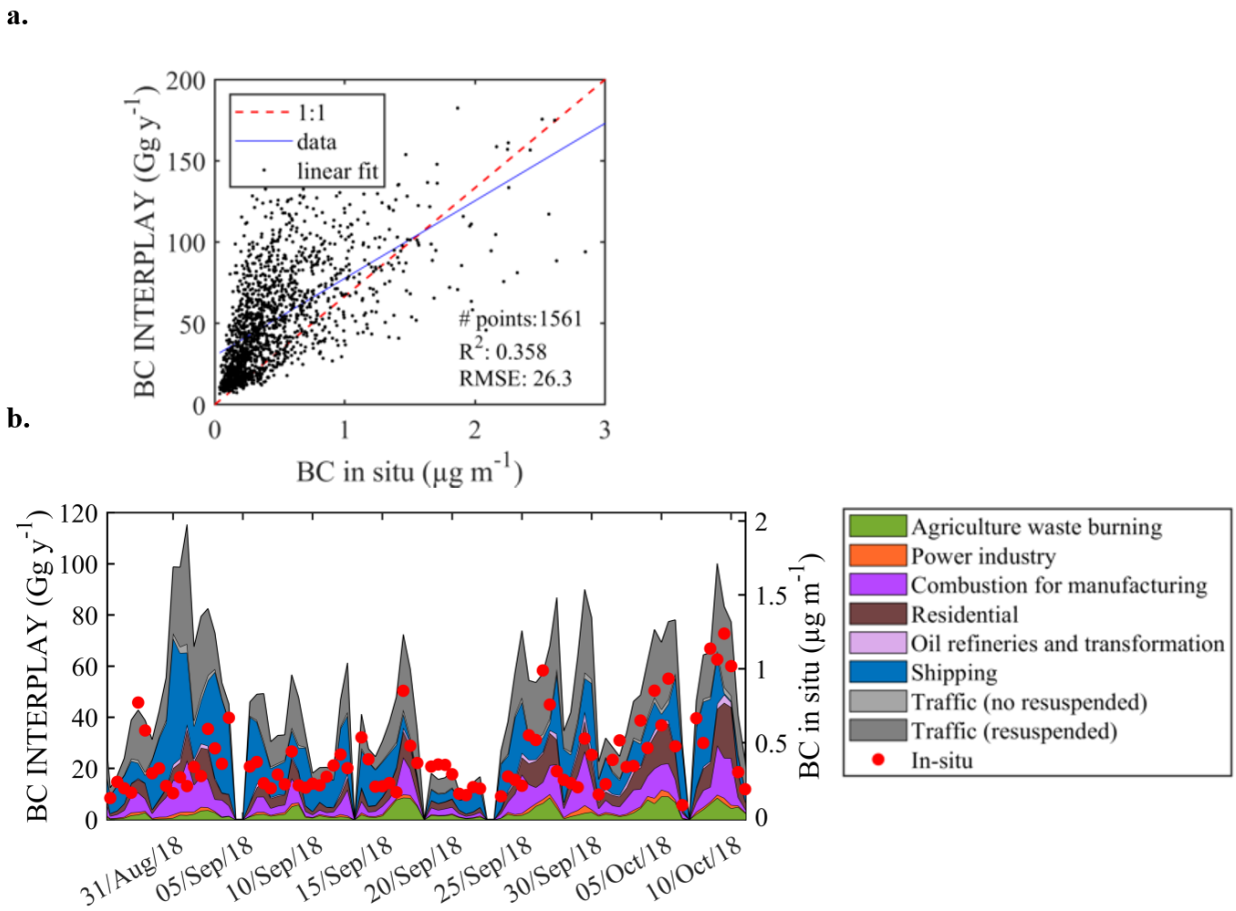

Figure 5.3 (a) Linear correlation and (b) zoom into a sample period showing the INTERPLAY approach and in situ BC observations.

For a seasonal analysis, data are separated into the cold (Sep-Apr, 8 months) and warm (May-Aug, 4 months) seasons. In order to associate a given source or region with an optical property (e.g. AAE, between 370 nm and 880 nm), a minimum contribution of 20% of total BC footprint is applied for individual BTs to be considered in the statistics developed below, disregarding regions and sources with < 70 BT points associated.

Using atmospheric observations and the novel INTERPLAY approach described above, we focused on assessing BrC lifetime, notably from wood combustion. Firstly, BrC absorption (σ_{BrCabs}) at 470 nm was calculated assuming that BC is the only species responsible for light absorption at 880 nm, and extrapolating its contribution (σ_{BCabs}) at 470 nm by assuming an AAE of 1 (Bond et al. 2013). The difference between σ_{BCabs} and the total aerosol absorption coefficient (σ_{abs}) was then attributed to BrC (eq. 5.1):

$$\sigma_{BrC\ abs,\lambda} = \sigma_{abs,\lambda} - \sigma_{BC\ abs,\lambda} \qquad \text{eq. 5.1}$$

The BrC lifetime analysis is then performed using MLR, with in-situ (σ_{BrCabs}) being the explained variable, and the dependent variables (obtained from INTERPLAY), being the BC contributions from traffic and residential sectors, each further separated according to the time since emission as

either “fresh” (less than 24 hours), or “aged” (more than 24 hours). Calculations were performed using the least-square method, coefficients were only constrained to be positive and the linear intercept was set to zero to explain the absorption measured by the in-situ observations. The MLR analysis (R^2:0.64) was performed in MATLAB 2020a on 715 data points of 12-hour averaged integrated mass (BC-traffic and BC-residential). Further details of the data obtained for each analysis are given in Table 5.1.

Table 5.1 List of in situ instrumentation within the PM_1 fraction at ATOLL and additional methods used for the analysis under the period of 10 Dec. 2016 – 31 Dec. 2019

Method		**Parameter used**	**Time resolution**	**Raw data**	**12h integra-tion**	**Cold period (12h)**	**Warm period (12h)**
In situ	Aethalometer	σ_{abs} & eBC*	1 min	1 226 414	1 581	726	685
	Nephelometer	σ_{scat}		966 412	1 408	611	622
HYSPLIT	HYSPLIT 2020v	BT	1 hour.	11 607 864	NA+	NA	NA
		Rain				NA	NA
Emission Inventory	EDGAR 2018v	BC sector-specific grid maps	1 month	6 480 000	NA	NA	NA
INTERPLAY approach		Integrated BC	1 hour	6 144 703	675 913	309 595	293 141

+NA = not applicable. The 12-hour integration applies only for in situ observations and BC footprint from INTERPLAY for comparison.

5.3 BC daily variation and wind direction analysis

As discussed in chapter 3, the decrease or increase in air pollution concentrations is the result of an imbalance between their emission/formation and removal rates, which is strongly modulated by meteorological parameters (e.g., temperature, wind, atmospheric dynamics). Thus, to apportion the sources of LAAs at ATOLL, the concentrations of BC_{ff} (fossil fuel) and BC_{wb} (wood burning) described in section 2.2.3 were analyzed. For this dataset, the main contributor to the BC mass concentration is BC_{ff} with 60%. Whereas in summer the BC_{ff} fraction reaches 76%, in winter BC_{wb} amounts up to 43% of BC, as a result of wood combustion from heating (Favez et al., 2021). The average concentrations of BC_{ff} (0.66 ± 1.02 µg m^{-3}) and BC_{wb} (0.31 ± 0.43 µg m^{-3}) are significantly lower than those (1.22 ± 1.36 and 5.35 ± 4.81) reported for an urban site in Athens, Greece over a similar period of observations and cut-off size (PM_1) (Kaskaoutis et al. 2021)„ due to the density of population, fuel/biomass burned type as well as the type of sources between both cities. Helin et al. (2018) in urban Finland, found higher concentrations for BC_{ff} (1.50 ± 1.48 µg m^{-3}) but lower concentrations for BC_{wb} (0.14 ± 0.21 µg m^{-3}). In the city of Milan, Italy within a bigger size fraction ($PM_{2.5}$), average values of BC_{ff} (1.37 ± 0.10 µg m^{-3}) and BC_{wb} (0.57 ± 0.087 µg m^{-3}) are both significantly higher than the values observed at ATOLL. The concentration over a remote site in

the Czech Republic (Mbengue et al., 2020), shows fairly similar values for BC_{wb} (0.33 ± 0.39 µg m^{-3}) and BC_{ff} (0.48 ± 0.58 µg m^{-3}). Thus, the ATOLL site exhibits mean BC_{ff} and BC_{wb} concentration levels that are in the range of values reported for other urban sites in Europe, for which traffic emissions and the high density of population within the city and surroundings are important source contributors.

Figure 5.4 shows the wind roses (Figure 5.4a) and the contour plots of average concentrations (Figure 5.4b) according to the wind sector and hour of the day of BC_{ff} and BC_{wb} for the warm and cold seasons. During the cold period, the highest wind frequency comes from the southwest sector with a median wind speed of 1.5 m s^{-1}. During the warm period, despite a predominance again from the southwest sector, with wind velocities comparable to the cold season, winds were also observed to arise from the north and northeast sectors with moderate speed (2 – 4 m s^{-1}).

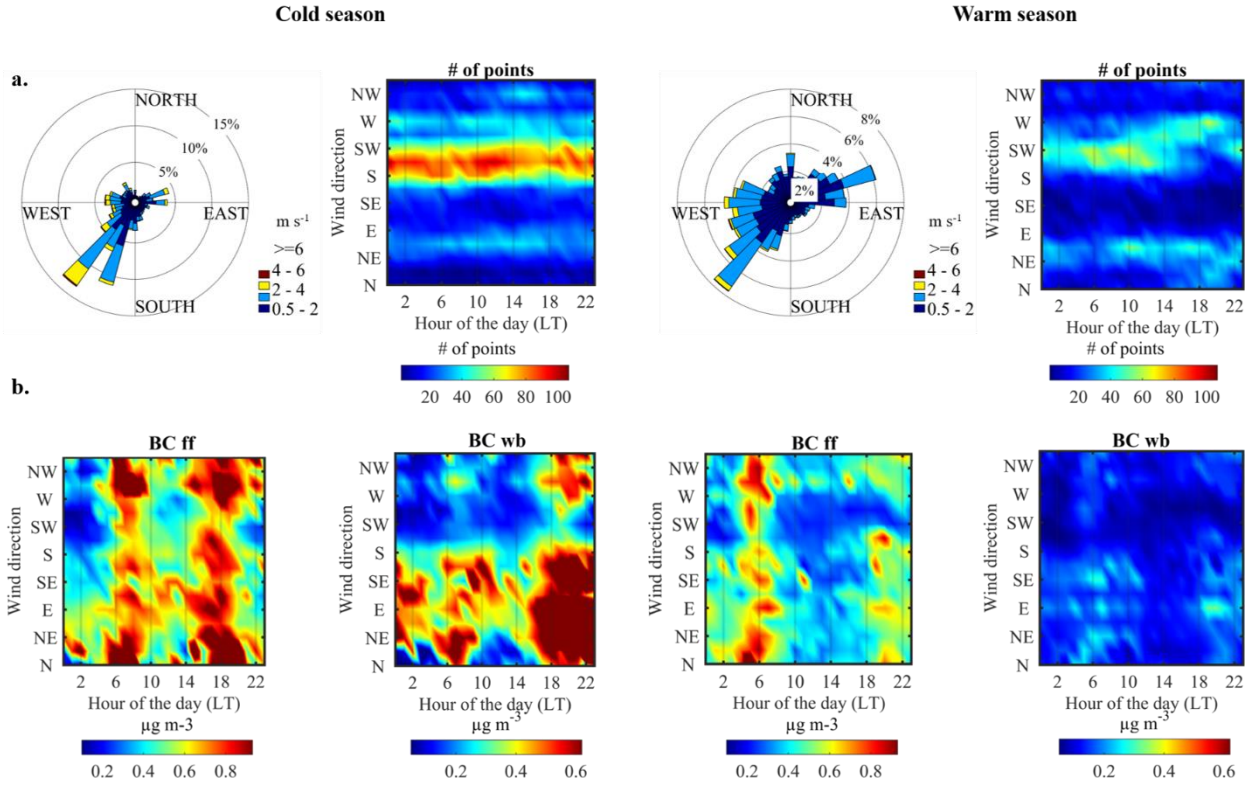

Figure 5.4 Wind analysis and BC_{ff} and BC_{wb} levels at the ATOLL site during cold (left) and warm (right) seasons. a) Wind roses and wind frequency by the hour of the day (minimum wind speed of 0.5 m s^{-1}). b) Contour plots of BC component loadings according to wind sector and hour of the day. The color scale is based on the 5th and 75th percentiles for both seasons.

Using daily-averaged concentrations in chapter 3 we described the daily variability of eBC. Similarly, here we observe BC_{ff} to peak (> 0.7 µg m^{-3}) during the morning rush hours for the cold and warm periods among all wind sectors, highlighting the role of local emissions, overlaid on a background of about 0.2-0.5 µg m^{-3} throughout the day. In contrast, the evening peak is less clear during the warm period, probably due to the effect of higher boundary layer height and enhanced

dispersion associated with warmer temperatures in the afternoon, combined with a less well-defined evening peak due to summer holidays over the 4-month period. Conversely, BC_{wb} depicts higher concentrations over the eastern sector and is attributed to continental air masses loaded with wood combustion particles. As expected, BC_{wb} levels are significantly higher during the cold season compared to the warm season, due to the widespread combustion of wood for residential heating as dicussed in chapter 3. It is interesting to note that despite the proximity of ATOLL to Lille, the wind direction associated with the city (NW) does not show particularly high BC_{ff} or BC_{wb} levels, indicating a more regional contribution from the well-populated region, as well as Long Range Transport leading to a typically high background level.

We further used the INTERPLAY approach to study the different origins of BC, allowing deeper analysis of in-situ observations, thus complementing previous studies carried out in the region (Potier et al. 2019; Rodelas et al. 2019).

5.4 Geographical origins and associated properties

In the previous section, we discussed the influence of the road traffic and residential sectors as identified via the AAE, however, real-world sources are far more complex, including industrial and agricultural activities, maritime transport, and waste treatment, among others (Alleman et al. 2010; Crenn et al. 2017; Espina Martin 2020; Ledoux et al. 2018). For instance; Ledoux et al. (2018) estimated the influence of maritime transport in the North Sea harbor of Calais in France, reporting in-port ship enhancement of 32.5 µg m^{-3} on PM_1 concentration, correlated with SO_2 and NO_x peaks associated with ferry departures and arrivals. INTERPLAY allows an analysis of the shipping emissions not at the source (e.g. harbor), but in the vicinity of Lille, over 60 km farther from the coast. Thus, focusing on BC, INTERPLAY provides further insights into LAA sources and age at the ATOLL site.

Figure 5.5 represents the integrated spatial origins of BC observed at the ATOLL platform (source strengths multiplied by back trajectory frequency at a given grid point). Results from Figure 5.5a show most of BC impacting ATOLL has its origins in the Benelux region, western Germany, south UK (and London), Paris, and shipping lanes in the Channel between the North Sea and the Atlantic Ocean. The pie chart presented in Figure 5.5b gives estimates of BC origins with about 35% of national origin (8% from the Lille metropolitan area, and 27% from the rest of the country). It is interesting to note that the combined shipping lanes over the Channel and North Sea show also a significant contribution of 15%, followed by Belgium at 13%, Germany at 8%, the UK at 7%, and others (i.e. European countries and seas in the vicinity) at 23%. Analyzing INTERPLAY according to different BC emission sectors (Figure 5.5c), traffic appears as a major source (31%), followed by shipping (25%, including also canals and rivers), residential (21%), and industry-manufacturing (17%). Agricultural waste burning (4%) and the power industry (2%) are minor contributors to BC at ATOLL.

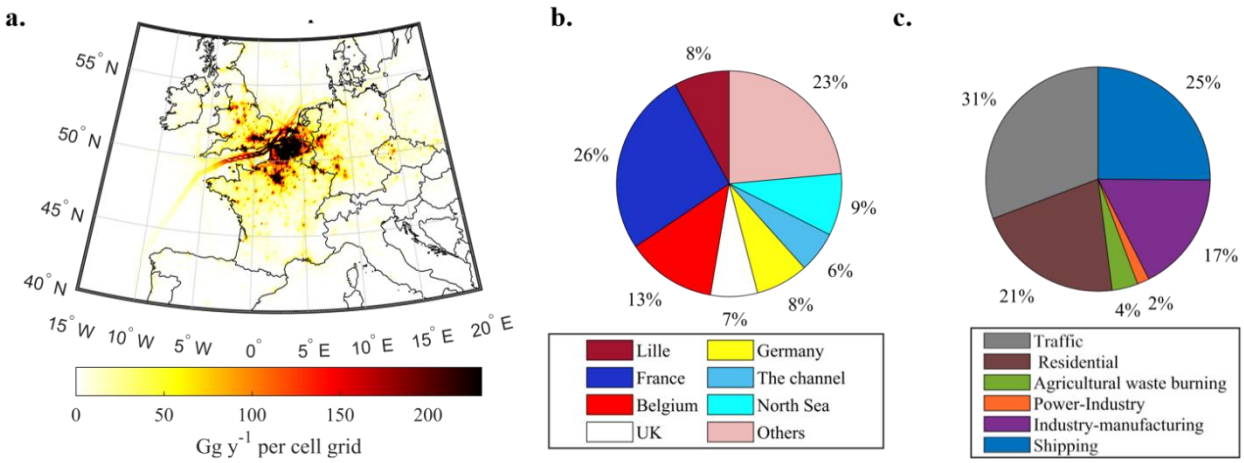

Figure 5.5 (a) Accumulated contribution of BC to ATOLL in Gg yr^{-1} per cell grid and its regional (b) and sectorial (c) distribution over the period Dec. 2016 – Dec. 2019.

Figure 5.6 shows separately the spatial distribution of each of the six sectors. Indeed, the traffic (Figure 5.6a) and residential (Figure 5.6b) sectors depict comparable contributions for the Lille area and the rest of the country (roughly 10% and 30% each for both sectors). Furthermore, Belgium and the UK have a prominent contribution to traffic BC (12-18%), whereas Germany stands out for the power industry sector (16%). Furthermore, Figure 5.6c highlights the importance of the shipping lanes contributing to BC at ATOLL. The North Sea is the main contributor with 34%, followed by the Channel with 22%. It should be noted that the southern North Sea with large harbors in Calais, Dunkirk, Zeebruge, Antwerp, Rotterdam, and Hamburg is a region with one of the highest ship traffic density in the world (Environmental European Agency 2013; European Commission 2019). Some strong restrictions currently apply, notably on the sulfur content when approaching coastal areas, yet shipping emissions are still considered to be able to significantly affect the atmospheric chemistry and air quality in the continental areas surrounding harbors and traffic lanes (Ledoux et al. 2018; Yang et al. 2020). In fact, PM emissions have been observed to depend on the engine operation and fuel type (Cooper 2001, 2003; Moldanová et al. 2013; Petzold et al. 2010; Sippula et al. 2014). Carbonaceous compounds are some of the major fractions of the PM emitted by shipping (Agrawal et al. 2008; Healy et al. 2009; Moldanová et al. 2009; Viana et al. 2009). For instance, Helin et al. (2021) studied the exhaust emissions for different marine fuels and engine loads using an aethalometer, showing that organics and BC emissions were generally higher at an engine load of 25% (near-harbor) than at 75% load (open sea) for different fuels tested. The BC emissions were the highest when heavy fuel oil (HFO) and intermediate fuel oil (IFO) were used, yet the emissions also contained the highest amounts of metal, PAHs, and low volatility organic compounds.

Regarding the contribution to BC of the industry-manufacturing sector (Figure 5.6d), 38% is domestic (Lille metropolitan area 10%, and the rest of the territory 28%), whereas, 62% is transboundary (with Belgium 22%, Germany 10%, the UK 9% and the rest of Europe 16%). Additionally, for the agricultural waste burning sector (Figure 5.6b), the French territory contributes 55% to BC, of which only 5% is attributed to the Lille area and the rest to the

surroundings. Finally, 46% of BC from the power industry sector is domestic and 54% is transboundary, with Germany being an important contributor (16%) (Figure 5.6f).

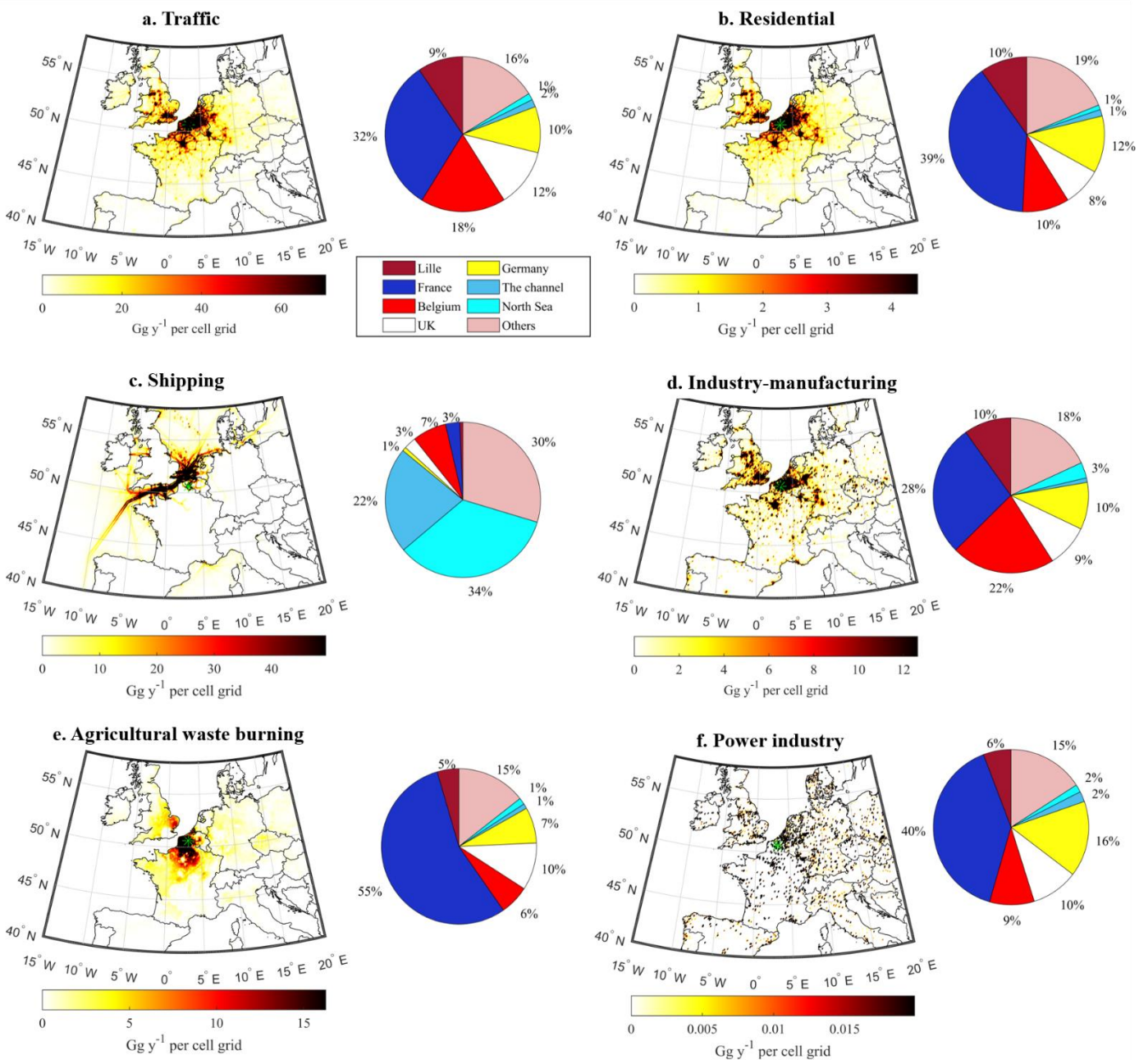

Figure 5.6 Accumulated contribution of BC to ATOLL in Gg y^{-1} per cell grid and relative distribution for (a) traffic, (b) residential sector, (c) shipping emissions, (d) industry-manufacturing counting oil refineries and transformation as well as combustion for manufacturing, (e) agricultural waste burning, (f) power industry over the period Dec 2016 – Dec 2019.

Figure 5.7 shows the seasonality of BC spatial distribution and the relative distribution of the sectors. The relative contribution of the traffic sector remains important across all seasons, contributing typically to about one-third of BC at ATOLL. Residential emissions, conversely, shows a stark seasonality, as expected, peaking in winter (30%), down to a minimum of 8% in summer. During the latter, shipping is the major contributor (38%), likely due to enhanced shipping activities and a decrease in both traffic and residential sources, combined with favorable wind conditions. For the other sectors, the relative contribution shows fairly small seasonality, dominated by industry-manufacturing (16-20%), agricultural waste burning (6%-2%), and finally the power industry (2%).

The changes in geographical origins also shown in Figure 5.7 are the result of different emission patterns, combined with varying air mass origins across seasons (Appendix A5 - 2) For example, the contribution of transboundary BC (i.e. all minus Lille and the rest of France) ranges from 56% in winter up to 74% in spring. Studies based on back-trajectories and in-situ concentrations, namely trajectory-based statistical models (TMs) found for example that Central Europe (e.g Germany, Hungary, Romania, Croatia and Slovenia) were important contributors to PM_{10} pollution during winter in Lille, while nitrate-rich and sulfate-rich sources were brought to the area by northern winds during the spring season (Waked et al. 2018). Another comparable study combining different methods (TMs, chemical transport models, in-situ observations) (Potier et al. 2019), showed that some long-range emissions could have a strong but infrequent impact on PM_{10} levels in Northern France, while some nearer countries had a frequent and predominant impact.

In addition to estimating geographical and source contributions to LAA observed at ATOLL, one of the main objectives of INTERPLAY is to be able to link in-situ aerosol properties with BC sources and time since emission, i.e. its age. Figure 5.9 and Figure 5.9 show the $AAE_{370\text{-}880nm}$ and concentrations of BC_{ff}, BC_{wb}, when the incident air masses have at least 20% BC originating from a given region or source. Figure 5.9 associates the AAE of four sectors employed in this analysis. By applying the INTERPLAY approach, we obtained an $AAE_{370\text{-}880nm}$ ~ 1.5 from the residential sector (with values up to 1.6), whereas industry-manufacturing, traffic, and shipping emissions have a lower $AAE_{370\text{-}880nm}$ of ~1.3 on average. The higher AAE from residential (wood combustion) agrees with the literature. For example, diesel bus exhaust emissions have an $AAE_{470\text{-}950nm}$ in the order of 0.8-1.2 (Helin et al.; 2021). The AAE for fresh wood-burning derived aerosols is highly dependent on the combustion appliance, the material burned, the phase of the burn cycle and the time of emissions (Helin et al. 2021; Martinsson et al. 2015), but is generally assumed to be around 2 (Sandradewi et al. 2008). The AAE for shipping emissions is variable. Helin et al., (2021) observed the highest $AAE_{370\text{-}950nm}$ (up to 2.0 ± 0.1) when high-sulfur content heavy fuel oil was used, whereas low sulfur content fuels had the lowest $AAE_{470\text{-}950nm}$ (0.9 - 1.1). The data from ATOLL agrees with a low AAE range, suggesting a dominance of low sulfur content fuels.

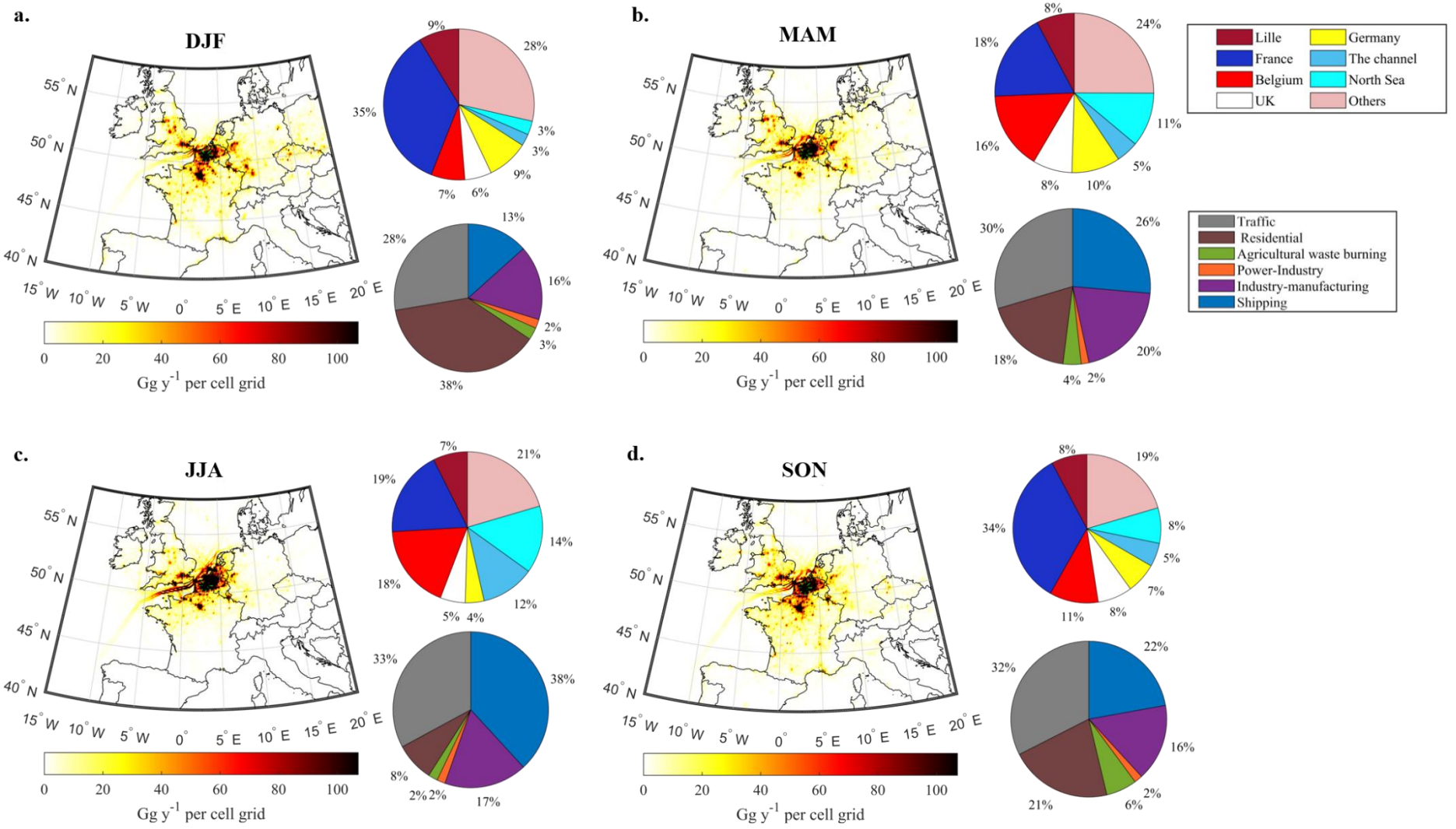

Figure 5.7 Accumulated contribution of BC to ATOLL in Gg yr^{-1} per cell grid and its regional and sectorial distribution for (a) DJF – Winter, (b) MAM – Spring, (c) JJA -Summer, and (d) SON – Fall

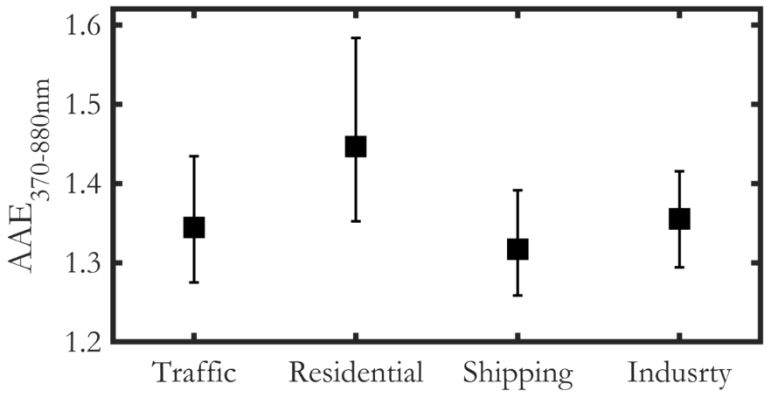

Figure 5.8 Statistics of BC in-situ data associated with different sectors using INTERPLAY method. Absorption Ångström Exponent calculated for the pair of wavelengths 370-880 nm ($AAE_{370\text{-}880nm}$).

Figure 5.9 shows the in-situ aerosol properties for a given region. The concentration of BC_{ff} is higher during the cold season when originating from different regions, probably as a result of a shallow boundary layer and reduced dispersion. Furthermore, as expected, BC_{wb} concentration is significantly higher during that period, which can be explained by residential heating, compounded with the same processes as for BC_{ff}. When air masses originate from the east (e.g. Germany), we observe the highest concentration of both BC_{ff} and BC_{wb} during the cold season. This is in line with previous findings, which in addition to coming from BC hotspots (due to e.g. transport, intensive agriculture, heavy industry, metallurgy, and exploitation of open mines), air masses are generally drier and colder, with lower dispersion favoring air pollutant accumulation (Asmi et al. 2011; Barnaba et al. 2011; Bovchaliuk et al. 2013; Giles et al. 2012). During the warm period, BC_{ff} concentration at ATOLL when receiving air masses dominated by domestic emissions (i.e. France) is comparable to air masses from the east, linked to the high density of population in Central Europe and the intensity of road traffic over the area (Eurostat 2022). Furthermore, the AAE is used to apportion BC_{wb} and BC_{ff} sources. While the AAE for BC_{ff} is low (0.9 - 1.1), the AAE or BC_{wb} is higher (>1.68 – 3.5) (Petit et al. 2021; Zhang et al. 2019; Zotter et al. 2017). Thus, although the AAE value is expected to be 1 given the regional sources associated with traffic emissions during the summer (Favez et al. 2021), the observed AAE values do not show this number, suggesting a secondary process leading to BrC formation and/or different mixing state (BC with non-absorbing coatings) (Chylek et al. 2019; Moise et al. 2015; Saleh et al. 2013; Zhang et al. 2020).

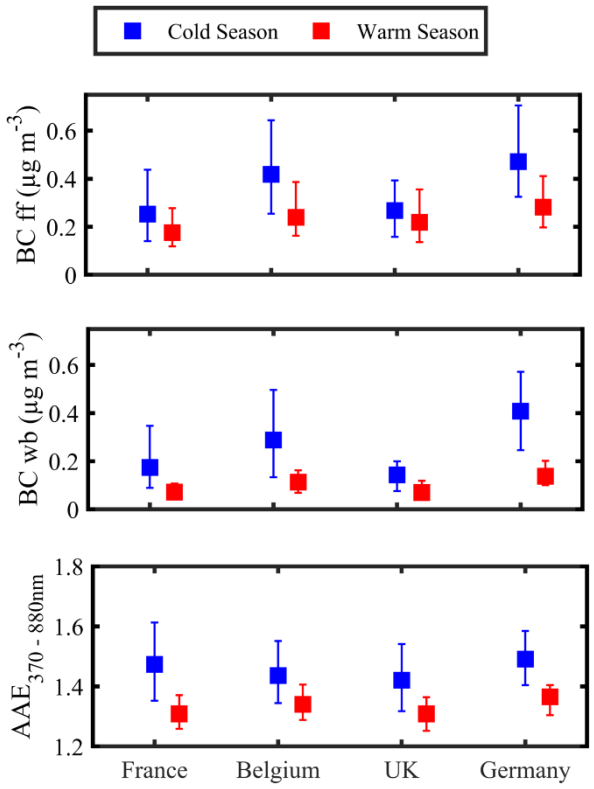

Figure 5.9 Statistics of BC in-situ data associated with different regions using INTERPLAY method. From top to bottom: BC_{ff} concentration; BC_{wb} concentration; Absorption Ångström Exponent calculated in the pair of wavelengths 370-880nm.

5.5 Brown carbon origins and lifetime

Figure 5.10 shows the apportionment of light absorption by BC and BrC from 370 to 950 nm for the ATOLL site. The mean of BrC calculated at 370 nm for ATOLL is 5.1 Mm^{-1}, which is somewhat lower than reported in Athens (15.9 Mm^{-1}), but larger than the Czech Republic (2.1 Mm^{-1}). On average, BrC contribution to absorption at 370 nm was 29.0%, which is somewhat higher than identified by Liakakou et al. (2020) in Athens (23.7%). It is important to note that ATOLL sampling was performed in PM_1, a similar size range as the Liakakou et al. (2020) study, which can lead to some underestimation of aged, internally mixed BC-containing aerosols, however less prone to be affected by artifacts at higher sizes as typically deployed ($PM_{2.5}$ or PM_{10}). Thus, the difference observed here could be explained by a higher usage of wood burning in northern France compared to Athens. Another study (Mbengue et al. 2021) at a rural background site in the Czech Republic reported an averaged BrC contribution at 370 nm lower than ATOLL and Athens (16%) for the period from March 2013 – December 2017, albeit with a different instrument model (AE31). Conversely, other sites have reported comparable or higher BrC contribution to aerosol light absorption, such as the southeastern margin of the Tibetan Plateau (20% to 40%) (Wang et al. 2019), Central Amazon (17% - 26%) (Saturno et al. 2018), at the northern peninsular Southeast Asia (46%) (Pani et al. 2021), and in Xi'an, China (41%) (Zhu et al. 2021). This large difference (> 40%) may be explained by active fires over the region, displaying substantial open biomass burning activities in and around the sampling location (Pani et al. 2021) as well as some contribution of secondary BrC (Wang et al. 2019).

At the ATOLL site, the total absorption at 370 nm presents varies markedly by season, being higher during winter (18.6 Mm^{-1}) compared to summer (7.5 Mm^{-1}), where the BrC relative contribution represents 38% and 18%, respectively. As discussed in previous sections, the difference between seasons is explained by the increase in emissions from biomass burning during the cold season (Velazquez Garcia et al. 2022). Comparing our winter results with other studies in France, Zhang et al. (2020) calculated the BrC absorption and its contribution using online measurements on a bigger size fraction ($PM_{2.5}$ size cut-off) at different urban and suburban areas during the winter season 2014 – 2015. In this work, results reported the highest mean contributions in Northeastern regions while the lowest is in the Southeast (e.g. Marseille), both contributions explained by the increase of biomass burning emissions. Indeed, residential wood burning is now recognized as the predominant wintertime organic source in Western Europe (van der Gon et al. 2015) and it has been assessed as a major source of BrC in various urban (Favez et al. 2009; Moschos et al. 2018; Zhang et al. 2020) and rural (Golly et al. 2019) environments.

Figure 5.11 exhibits the seasonal diel cycle of BrC absorption at 370 nm and the ratio between BC and BrC absorption. The displayed diel profiles are consistent with those generally observed for residential wood burning aerosols described in previous sections and preceding works (Favez et al. 2010; Sciare et al. 2011; Zhang et al. 2019, 2020), with higher values during the late evening to early morning hours. The BrC absorption decreased by 44% as the day progressed, which may be explained by the rising boundary layer height and the photobleaching/volatilization, as temperature reaches its maximum during this time (section 3.1). Zhao et al. (2015) documented that the presence of oxidants like O_3 and OH radicals (abundant during the daytime may degrade BrC into smaller and more volatile organic compounds). Higher absorption during the evening into the night is attributable to the emission rates of primary sources, in addition to shallow boundary layer height, and the absence of volatilization and photobleaching processes (Satish et al. 2017). Several studies in urban areas (Liakakou et al. 2020; Satish et al. 2017; Stanaway et al. 2018; Wang et al. 2018; Zhang et al. 2019; Zhang et al. 2020) showed a similar trend with higher values usually observed at night. According to the authors, the enhanced NO_3 oxidation at night may lead to more BrC formation than during the daytime. Other authors (Gao et al. 2022; Wang et al. 2019) show an opposite trend at remote sites, where values higher during the day than at other times are observed, attributed to the influence of photooxidation processes forming BrC through photochemical oxidation during the daytime. Indeed, different types of chromophores can be emitted from various sources and/or formed in the atmosphere. Budisulistiorini et al. (2017) have shown that the direct burning of several types of biomass can produce primary BrC. Laboratory studies (Lin et al. 2015; Moise et al. 2015; Teich et al. 2017) have found that anthropogenic VOCs (benzene, toluene, phenols, and polycyclic aromatics hydrocarbons – PAHs) react with nitrogen oxides and produce nitro aromatics, identified as light-absorbing compounds.

BrC levels in the atmosphere are a complex result of primary sources and secondary processes (condensation, volatilization), mixing with other aerosol types (core-shell mixing), and effects from local meteorology and boundary-layer dynamics (Lambe et al. 2013; Li et al. 2018; Romonosky et al. 2016). It is interesting to note that the contribution of BrC to absorption observed at the ATOLL platform is comparable with other European cities discussed (Athens), despite some differences in weather regime and fuel for heating. It is also noteworthy to mention that the methods to retrieve BrC absorption also impact its estimates. For instance, Zhang et al., (2020) applied a sensitivity test using three different values of AAE for pure BC (AAE_{BC}) to

calculate BrC absorption, choosing 0.9 as a reference. Furthermore, de Sá et al. (2019) estimated BrC absorption by calculating for every point in time the AAE_{BC} at the wavelengths 700 and 880 nm instead of using a fixed value. To look at the impact of the AAE_{BC} values in the BrC calculations at ATOLL, we performed a sensitivity test as Zhang et al., (2020) carried out. Here, we applied three different AAE_{BC} values of three distinctive BC states in the atmosphere, i.e., fresh (1.05), compact (0.95), and coated ones (0.90), derived from a numerical computation study constrained with variables (e.g. size) that may impact the AAE_{BC} (Liu et al. 2018). Results show an effect in the estimated BrC as expected, for which the lowest value (0.90) increased by 9% the BrC contribution at 370 nm in comparison with the largest value (1.05) (Appendix A5 - 10).

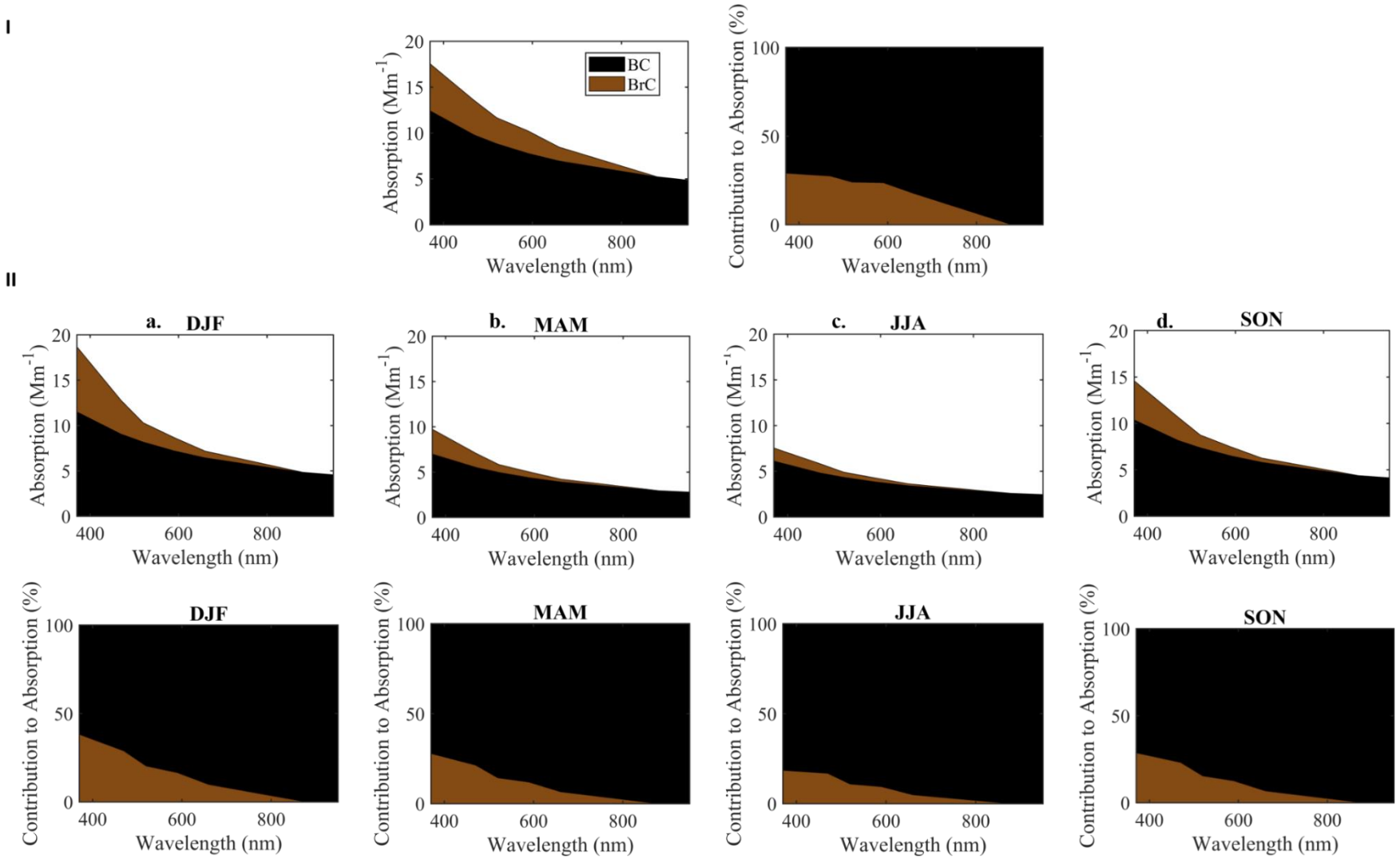

Figure 5.10 BC and BrC apportionment at the ATOLL site. Top: Site average (in Mm^{-1}) and contribution to absorption (in percentage). Middle and bottom: same as the top plot however separated by seasons.

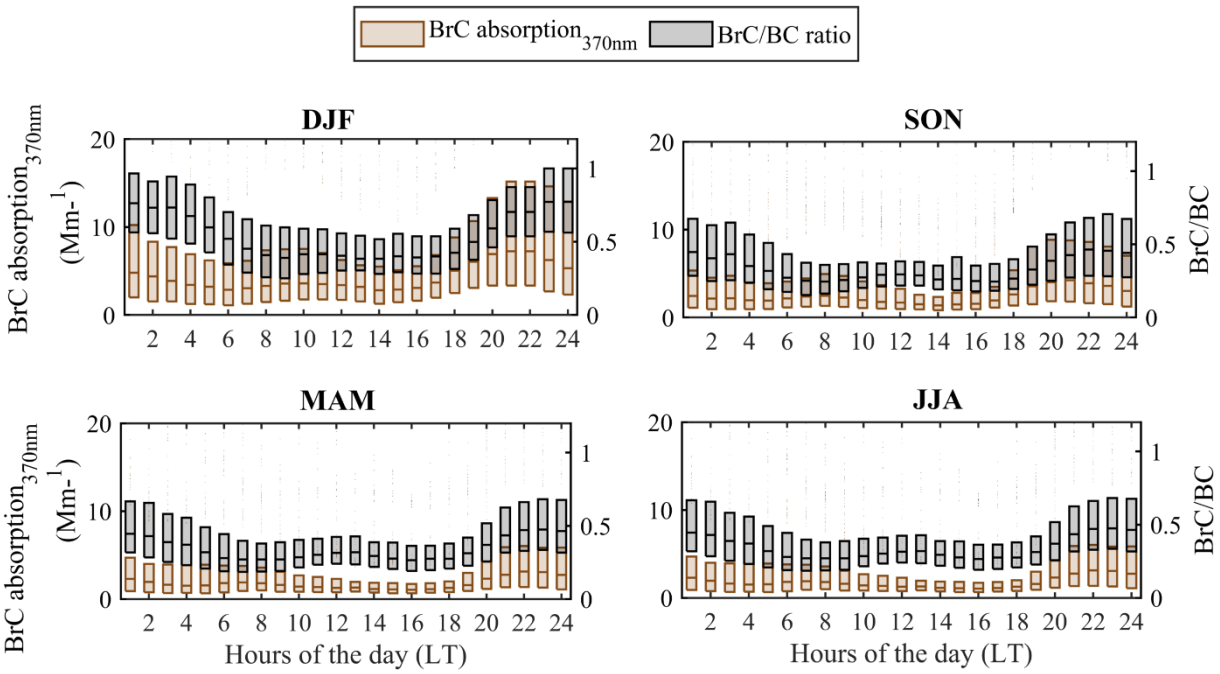

Figure 5.11 Diel cycles of BrC absorption (in Mm^{-1}) calculated at 370 nm (y-axis left) and BrC/BC ratio (y-axis right) at the ATOLL platform. The line is the median, whereas the box shows the interquartile range.

Further analysis between INTERPLAY and in-situ observations has focused on the effect of BC aging on BrC intensity. This analysis has focused only on the cold season, given the widespread use of wood combustion as residential heating source during that period. As described in section 5.2, we separated traffic and residential into fresh (BC emitted less than 24h ago) and aged (more than 24h ago). It is important to note that this analysis includes the two main sources during the cold period (in Sep-Apr, traffic and residential correspond to 66% of BC according to INTERPLAY), however neglecting shipping and industrial emissions. Here, we do not find strong evidence that those could be categorized as BC_{ff} (AAE ≈ 1) or BC_{wb} (AAE ≈ 2), given that INTERPLAY has identified an AAE of roughly 1.3 for both of them. Therefore, they were not included in the MLR, which would increase the number of independent variables without a clear role in BrC loadings.

Figure 5.12a shows the relative contribution of fresh and aged BC from traffic and residential, showing a relatively balanced contribution among the four categories (fresh BC being slightly higher with 28% for both sectors, whereas aged BC is higher for residential than traffic with 24% and 20%, respectively). Once applying the MLR method, the dominating component for BrC is identified as fresh residential (72%), followed by aged residential (16%) and aged traffic (12%), and no contribution from fresh traffic. This analysis suggests that, after 24h of atmospheric aging, the BrC components associated with residential heating strongly decreased, i.e. suffered including photobleaching (loss of chromophores). Thus, the majority of the impact in the UV range happens in the first 24h for wood combustion used in regions that impact ATOLL. For comparison, some studies on the evolution of biomass combustion BrC paint a qualitatively similar picture to laboratory measurements: BrC absorption typically decays, but the decay eventually levels out. Nevertheless, atmospheric observations have reported longer BrC absorption lifetimes (~1 day) (Forrister et al. 2015; Wang et al. 2016; Wong et al. 2019) than laboratory experiments (hours) (Saleh 2020).

The FireLab from Missoula, Montana in the USA (Fleming et al. 2020) collected biomass burning organic aerosol particles onto Teflon filters and analyzed them offline. Aiming to study the stability of the observed BrC compounds concerning photodegradation, BBOA particle samples were irradiated directly on filters with near UV (300–400 nm) radiation, followed by extraction and analysis. They found that the lifetimes of individual BrC chromophores depended on the fuel type and the corresponding combustion conditions. Lignin-derived and flavonoid classes of BrC generally had the longest lifetimes concerning UV photodegradation. Lifetimes for the same type of BrC chromophores varied depending on biomass fuel and combustion conditions. While individual BrC chromophores disappeared on a timescale of several days, the overall light absorption by the sample persisted longer, presumably because the condensed-phase photochemical processes converted one set of chromophores into another without complete photobleaching or from undetected BrC chromophores that photobleached more slowly. Browne et al. (2019) and Sumlin et al. (2018) suggest that the photobleaching observed for smoldering biomass-combustion BrC in the aerosol phase differ from secondary BrC in three ways: 1) combustion BrC exhibits a photo-enhancement period before photobleaching (Wong et al. 2019; Wong et al. 2017; Zhong and Jang 2014); 2) the decay of absorption occurs at longer timescales than secondary BrC (Wong et al. 2017); and 3) a fraction of combustion BrC is resistant to photobleaching.

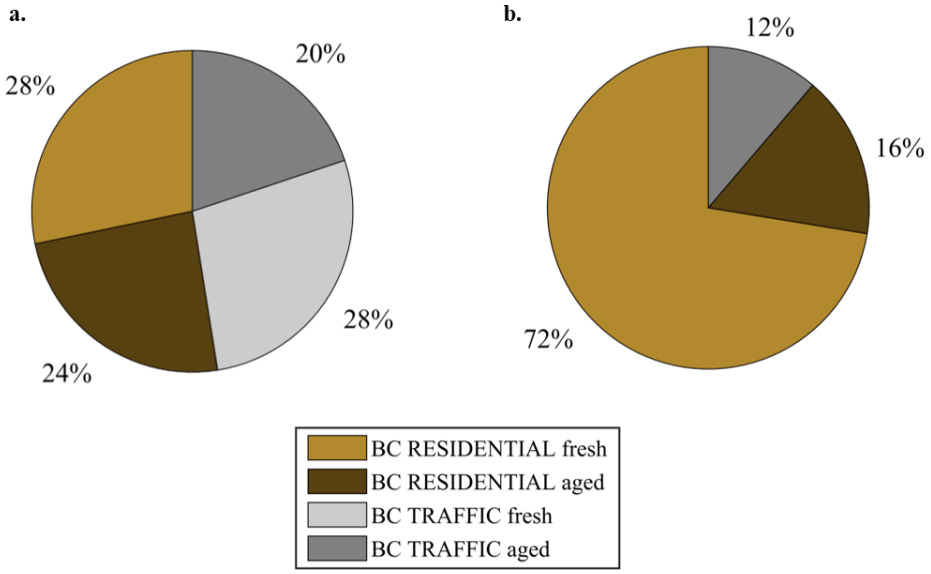

Figure 5.12 Brow carbon lifetime. a) Relative contribution to the mass of different BC sources (residential, traffic) emitted <24hrs (fresh) and >24hrs (aged). b) Relative contribution to light BrC absorption calculated at 470 nm explained by the mass of different BC sources (residential, traffic) emitted <24hrs (fresh) and >24hrs (aged).

Some field studies (Forrister et al. 2015; Selimovic et al. 2019) observed a substantial decay in aerosol UV light absorption in biomass-burning plumes, corresponding to a half-life of 9 to 15 h. Similarly, Lin et al. (2017) reported the rapid evolution of both the BBOA composition and optical properties during a nationwide biomass-burning event in Israel. However, there is a refractory fraction of BrC that persists even after long aging times. Di Lorenzo et al. (2017) found that the fraction of higher-molecular-weight chromophores (>500 Da) relative to lower-molecular-weight chromophores (<500 Da) increased with plume transport time, on the order of hours to days. These changes in BBOA properties are supported by laboratory studies of photochemical aging of BBOA or relevant surrogates via heterogeneous photooxidation

(exposure of particles to gaseous OH and other oxidants), aqueous photooxidation (exposure of BBOA compounds to OH within cloud/fog water droplets), direct photolysis (exposure of particles or their aqueous extracts to actinic UV radiation), and indirect photolysis (photosensitized reactions between BBOA molecules and electronically excited triplet states of photosensitizers). Saleh et al., (2013) burned pocosin pine and oak, and the diluted smoke was irradiated with UV lights in a smog chamber. Aerosol optical properties were monitored with an aethalometer at seven wavelengths. They found that aged emissions were more absorbing than fresh emissions at 370 and 470 nm after 1 h. Zhong and Jang, (2014) tracked the absorption coefficients of BBOA during solar exposure in a smog chamber and observed an increase of 11 %–54 % in the integrated MAC (280–600 nm) in the first half of the day, followed by a decrease in the afternoon.

As previously discussed, the time of day that smoke is formed may impact BrC, since during the daytime, OH reactions and photolysis dominate the aging, while the NO_3 and O_3 oxidation account for the nighttime aging (Li et al. 2020; Sumlin et al. 2018; Zhao et al. 2015). For instance, Benedict et al. (2017) further observed that smoke impacts from a nearby wildfire had a much higher smoldering-to-flaming ratio at night than during the day, which then suggests the potential for increased BrC formation at night (Saide et al. 2015). It is also known that smoldering combustion of biomass emits many precursors, including monoterpene furans, and cresol (Stockwell et al. 2015), which can react quickly with the major nighttime oxidant, NO_3, and ostensibly form UV-absorbing organic nitrates that could augment BrC. Once daytime starts, other studies show that some types of BrC, depending on the precursor, can experience rapid photochemical degradation or formation via both direct photolysis and oxidation (Lee et al. 2014; Sareen et al. 2010; Zhao et al. 2015; Zhong and Jang 2014).

The literature summary above evidences that much work has been done in terms of characterizing the optical properties of photochemically-aged BBOA and surrogates. Yet, a consensus on what drives the photobleaching and photo-enhancement of chromophores in BBOA, as well as the relative importance of these processes on atmospherically relevant timescales, has not yet been reached. Photobleaching of BrC chromophores upon atmospheric aging is an important phenomenon that should be accounted for in climate calculations. There is evidence that susceptibility to photobleaching decreases with increasing molecular size (correlated with absorption). It is noteworthy to mention that, climate models representing BrC absorption, account for BrC emissions from biomass and biofuel combustion, and some account for secondary BrC from aromatic VOCs. However, recent observations indicate that low-efficiency coal combustion and ship engines utilizing heavy-fuel oil are important BrC sources that should also be accounted for in models (Fleming et al. 2020; Saleh 2020).

5.6 Conclusions and perspectives

In France, the annual WHO AQG for PM concentration levels (15 µg m^{-3} and 5 µg m^{-3}, for PM_{10} and $PM_{2.5}$, respectively) are frequently exceeded, as in many European countries. The main origins of PM are residential wood burning (during the cold period), road transport (exhaust and non-exhaust) throughout the year, and other sources distributed more heterogeneously across regions, such as shipping and industrial emissions (Favez et al. 2021). Thus, in the present chapter, we analyzed the local, national, and transboundary origins and associated optical properties of LAAs influencing the ATOLL platform by developing an innovative approach combining in-situ observations, back-trajectories and emission inventories (INTERPLAY).

The in-situ aerosol absorption measurements performed by the aethalometer at ATOLL can be used to derive a simple BC source apportionment into fossil fuel and wood burning, the latter being assumed to have strong absorption in the UV and blue parts of the light spectrum from polycyclic aromatic hydrocarbons and humic-like substances (Sandradewi et al. 2008). Results of this approach exhibit differences in sources during the cold and warm seasons. For instance, during the cold season, peaks of BC_{ff} (0.98 µg m^{-1} -75^{th} percentile) are associated with all wind sectors during rush traffic hours while BC_{wb} peaks (0.83 µg m^{-1} - 75^{th} percentile) are mostly associated with easterly winds, as a consequence of meteorology and arrival of continental air masses. During the warm season, increased dispersion and higher boundary layer height, combined with the holiday period, lead to an average decrease of BC_{ff} by about 37%, whereas a strong reduction in residential heating (combined with the reasons above) is mostly associated with an 82% decrease in BC_{wb}.

In this analysis, we applied INTERPLAY to ~3 years (2016-2019) of coincident in-situ measurements performed at the ATOLL platform. The latest monthly EDGAR emission inventory (Crippa et al. 2020) for BC was used. The monthly sector-specific grid maps include traffic (resuspended and no-resuspended), residential, shipping, industrial-manufacturing (combustion for manufacturing as well as oil refineries and transformation) agriculture waste burning and power industry. Results of the BC-footprint obtained with INTERPLAY show a reasonably good agreement with in-situ BC (R^2:0.36 with 12h integration). The multiannual analysis of the spatial and relative contribution applying INTERPLAY implies an 8% local contribution from the Lille area, 27% domestic (rest of the French territory), and 65% of transboundary (with Belgium 13%, North Sea 9%, Germany 8%, the UK 7%, the Channel 6%, and others sea and countries making up the remainder). The main sectors contributing to BC levels at ATOLL are traffic (31%), followed by shipping (25%), residential (21%), industry-manufacturing (17%) sectors. Agricultural waste burning (4%) and the power industry (2%) sectors contribute less.

Concerning the seasonality of both spatial and sector contributors, the local (from the Lille area) and domestic contributions increase during winter in comparison with summer (7% and 19%, respectively). The highest transboundary contribution (74%) occurs during spring and summer; while the important contributors during summer are Belgium (18%), the North Sea (14%) and the Channel (12%). Germany (10%) is also an important contributor in spring, with higher contribution than the Channel (5%). It should be noted that, during summer, the shipping sector is responsible for 38% of the contribution to BC at ATOLL, highlighting the importance of this sector in Northern France. In addition, during this season, an additional key sector to the contribution of BC is the traffic sector (33%), which also remains the main contributor during spring (30%) and fall (32%). The residential sector is the main contributor to BC during winter, increasing its contribution up to 30% in comparison to summer. Remarkable differences are seen for agricultural waste burning increasing during fall and spring whereas, for industry manufacturing the highest contribution (20%) to BC occurs during spring.

The INTERPLAY approach enriched the in-situ observations, allowing to identify and compare the associated BC source apportionment (BC_{ff}, BC_{wb}) and the respective optical properties ($AAE_{370\text{-}880nm}$) to the air masses reaching the site from different regions during the cold (Sep-Apr) and warm seasons (May-Aug), with at least a 20% increase of the total BC-footprint. Results regarding the regions showed an average BC_{wb} concentration higher during the cold season for all regions, although differences between cold and warm seasons remains small.

INTERPLAY identified a high average concentration of BC_{ff} and BC_{wb} coming from Germany during the cold and warm seasons. Moreover, during the cold season, the $AAE_{370\text{-}880nm}$ for air masses related to traffic emissions at the ATOLL platform is higher (1.3) than the expected reported by different authors (0.9 – 1.1) (Petit et al. 2021; Sandradewi et al. 2008; Zhang et al. 2019, 2020; Zotter et al. 2017).

In this chapter, we also analyzed the contribution and diel profiles of BrC absorption in the UV range. The average contribution to absorption (29.0%) at the site is comparable with other European sites (e.g. Athens), increasing during winter by 9%. The BrC diel profile shows higher values during late evening to early morning hours, reduced by 44% as the day progressed. This pattern is the result of primary sources and secondary processes (condensation, volatilization), mixing with other aerosol types (core-shell mixing), and effects from local meteorology and boundary-layer dynamics. It is important to note that the BrC levels may be impacted by the method applied to retrieve its absorption. For instance, assuming a constant value of AAE =1 for pure BC may be incorrect in our case, as was suggested above from the average AAE value obtained for air masses associated to traffic sources and further analysis is therefore needed.

Finally, we used the INTERPLAY approach to explore the lifetime and origins of BrC during the cold season. To do so, we separated air masses emitted less than 24 hours (fresh aerosols) before reaching ATOLL from those emitted more than 24 hours (aged aerosols) for the traffic and residential sectors. In general, the highest contribution to BC are from the fresh emissions for both the residential and traffic sectors, while aged emissions represent for the residential and traffic sector 24% and 20%, respectively. The BrC absorption was calculated at 470 nm from the in-situ observations and used to calculate the contribution to BrC absorption of fresh and aged aerosols from the residential and traffic sectors. By applying a multiple linear regression, we determined that 72% of the contribution to BrC absorption at 470 nm was from fresh air masses from the residential sector, whereas only 16% of the contribution is attributed to aged air masses from the residential sector and 12% by aged traffic BrC. These results highlight the bleaching effect after 24 hours of atmospheric transport and oxidation.

Overall, this study offers the possibility to exploit the in-situ observations on a larger scale via the INTERPLAY approach. This work supports the evidence of high contribution to carbonaceous aerosols emitted by the traffic, shipping, and residential sectors in the region, where the residential sector shows a strong seasonality. Furthermore, this chapter draws attention to the precautions needed when performing aerosol characterization and source apportionment based on AAE values. Based on INTERPLAY results, the source apportionment of light-absorbing carbonaceous matter into fossil fuel and wood burning fractions may be biased since the value of AAE not only depends on the class of combustion, type of fuel, and kind of wood burned (e.g. high AAE by using high sulfur content as fuel in shipping emissions), but it also depends on the atmospheric transport giving relatively low, yet highly variable, AAE values from wood combustion emissions. In addition, it points out the lack of studies of atmospheric aging based on atmospheric observations, relevant to the quantification of the radiative impact of organic species to be accounted for in climate calculations. This study opens the possibility to explore the aging of LAAs employing atmospheric long-term in situ observations, it also recommends analyzing the aging by daytime and it encourages the investigation of BrC aging during nighttime at ATOLL, where secondary reactions with precursors (e.g. NO_3) can lead to the formation of BrC.

General conclusions and perspectives

Aerosols influence the Earth's climate directly through scattering and absorption of solar radiation and indirectly by affecting cloud properties. In order to quantify the effects of aerosols on air quality and climatic impacts, it is important to provide robust analyses of their nature and to interpret their optical properties on the ground and/or along the atmospheric column. Since 2008, remote sensing observations are performed continuously at the ATOLL platform, in parallel with near real-time in-situ measurements since 2016. The site, and more generally Northern France, is strongly affected by many anthropogenic sources (e.g. road traffic, residential sector, agriculture, industries and maritime transport), and oceanic emissions. Depending on the meteorological conditions, continental air masses reaching the site also cause numerous particle pollution episodes. Hence, this thesis aims to investigate particulate pollution in the region by linking observations of high temporal resolution chemical composition in the submicron fraction and their optical properties.

To achieve this objective, we first analyzed the particle pollution events occurring in Lille. Observations from 8 years (2013 -2021) of the PM_{10} and $PM_{2.5}$ concentrations performed by the regional air quality monitoring station located in Fives (4 km apart from ATOLL), were investigated to calculate the number of exceedance days of PM concentrations following the latest WHO recommendations. Results showed 187 and 263 events in 2021 for PM_{10} and $PM_{2.5}$ mass concentrations, respectively. Furthermore, the PM_1 chemical speciation measured at ATOLL during the exceedance days, exhibits a high fraction of nitrate in comparison with normal site conditions, in which a higher fraction of light-absorbing aerosols was observed. Indeed, over the ~ 4 years (2016 – 2020) of PM_1 chemical composition measurements at the site, the main contributor to the total PM_1 mass (13.9 ± 10.5 µg m^{-3}) is Organics (40%), followed by nitrate (28%), ammonium (15%), sulfate (8%) and equivalent black carbon (8%). The PM_1 composition presents a marked seasonal shift during spring, showing nitrate (37%) as the main contributor to PM_1, explained by the changes in the wind direction sector and the growth in agricultural activities including the spreading of fertilizers.

The 13 years (2008 – 2021) of remote sensing observations at the site allowed to determine the average AOD at 500 nm and AE for the pair of wavelengths 440 – 870 nm, values were comparable with other sites in the region and smaller than previous values reported for large cities like Mexico-city or Beijing. Measured over a shorter period of time, the optical in-situ measurements at high time resolution, that is to say, scattering (2017–2020) and absorption coefficients (2016–2021) are slightly lower in comparison with other urban/suburban sites in southern Europe (Italy, Greece, Spain). The intensive key aerosol optical properties exhibit values comparable to most sub- and urban sites in Europe. For instance, the SSA at 525 nm of 0.75 is comparable with the Ispra site, in Italy. The SAE at 450-635 nm shows values of fine particles typical from combustion sources. The AAE in the wavelengths 370 – 880 nm is comparable with values reported for the UK, Greece, and other parts of France, increasing 21% during winter compared to summer, highlighting the differences in aerosol composition, during the cold season more related to the residential heating emissions and during the warm season to traffic emissions.

To assess the sources responsible for the chemical species concentrations and optical properties, a more detailed analysis of diel profiles was performed on a seasonal basis. In general, the boundary layer height tends to be lower during winter compared with summer, combined with low ambient air temperatures, concentrating all pollutants in a shallow mixing layer. Overall,

two important peaks are observed during the traffic rush hours in the morning and afternoon across the seasons for the carbonaceous aerosols and some optical properties (absorption, scattering). Moreover, the photobleaching and volatilization are important processes as the day progresses, impacting the reactivity for some chemical species (e.g. organics, nitrate, sulfate) and some other optical properties, for example, SOA growth may increase the SSA and the AAE.

We also explored the trends in time of PM concentration and the optical parameters previously discussed. The PM mass concentration in Fives between 2013 to 2021 has decreased by 28% and 27% for PM_{10} and $PM_{2.5}$, respectively. Similarly, the AOD reported by AERONET in Lille, showed a decreasing trend comparable to other sites. Albeit on an even shorter period, PM_1 at ATOLL suggests also a decrease in concentration between 2016 to 2020.

By combining ~3 years of in situ coincident aerosol chemical and optical measurements via the IMPROVE algorithm, we provide robust estimates of MEE, MSE and MAE at different wavelengths, relevant for better assessments of their radiative effects. At the ATOLL site, the scattering at 525 nm is dominated by AN (44 %) and Org (33 %), species linked to poor air quality in polluted urban environments. Regarding the absorption at 370 nm, organics are responsible for 22% of light absorption, evidencing a significant contribution of Brown Carbon in the region, associated with BBOA. Looking at the light extinction at 525 nm, AN is also the predominant species (35%), followed by the carbonaceous aerosol species (eBC 29%, Org 21%) and ammonium sulfate (15%). Furthermore, as expected, the extinction is generally higher during winter and spring, seasons which are strongly impacted by anthropogenic emissions (solid fuel combustion from residential heating and agricultural activities combined with traffic emissions). For comparison to our retrievals, we employed literature-based MEE reported for suburban and urban sites and used them to estimate the light extinction at 525 nm over the measurements at ATOLL. The results of the comparison highlight strong over- or underestimation of the individual species and total extinction coefficient depending on the MEE dataset used, which advocates for the use of site-specific MEE values.

The analysis of 3 years of optical measurements identified the presence of large light-absorbing particles at the ATOLL site. This is attributed not only to road traffic and residential sectors but also to industrial and agricultural waste-burning activities, maritime transport, and waste treatment, among others. Besides, according to previous work, the region is highly impacted by air masses from Eastern Europe, loaded with PM, especially SIA and carbonaceous aerosols. Thus, in this thesis, we explored the sectorial and regional contributions to black carbon levels observed at ATOLL and its associated optical properties. To do so, we developed a hybrid method termed INTERPLAY, based on Lagrangian modeling and emission inventories, providing a significantly faster calculation time than typical dispersion models, with complementary information for receptor model analysis.

In this study, results of the black carbon footprint obtained with INTERPLAY demonstrate a reasonably good agreement with in-situ equivalent black carbon (R^2: 0.36 within 12h integration). Notably, the main sectors contributing to the BC levels at the ATOLL platform are from traffic, shipping and residential. The relative spatial contribution to BC fom the Lille area is relatively small (8%) compared to the transboundary contribution (65%), for which Belgium and the North Sea are important spatial contributors. The approach proposed in this work follows the studies previously reported by other authors, highlighting an important

transboundary contribution in the region. Thus, it would be interesting to further apply INTERPLAY to other air pollutants with important contribution at the site, aiming to evaluate and improve the applicability of the tool to other chemical species. The analysis showed a marked seasonality of both the spatial and sector contributors. For instance, during winter, the local contribution from the Lille and domestic areas increases in comparison with summer, whereas the highest transboundary contributions occur during spring and summer. The shipping sector is responsible for 38% of the contribution to black carbon at ATOLL, highlighting the importance of this sector in the region. The agricultural waste burning increase during fall and spring whereas the industry manufacturing highest contribution (20%) occurs also during spring.

The INTERPLAY approach allowed us to identify and compare the associated black carbon source apportionment (BC_{ff}, BC_{wb}) and the $AAE_{370\text{-}880nm}$ to the air masses reaching the site from different sectors and regions. Overall, INTERPLAY showed a high average concentration of BC_{ff} and BC_{wb} from Germany during the cold season and warm seasons. Moreover, despite the dominance of air masses related to traffic emissions during the warm season, the $AAE_{370\text{-}880nm}$ is higher (1.3) than the value expected (1), suggesting a different value of $AAE_{370\text{-}880nm}$ for air masses related to traffic emissions at the ATOLL platform. Similarly, regarding the $AAE_{370\text{-}880nm}$ by sectors, the value associated with traffic is higher than the one typically reported in the literature.

Finally, we also explored the contribution, diel cycle, origins, and lifetime of Brown Carbon at the site. For the most part, the average contribution to absorption (29%) at the site is comparable with other European sites (e.g. Athens), increasing during winter by 9%. The diel cycle of BrC absorption showed a drop of 44% during the day while higher values were seen during the night, underlying important atmospheric effects (enhancement, photobleaching) in BrC. Furthermore, we analyzed the impact of BC aging on BrC absorption intensity using INTERPLAY. Results show that aged BC from house heating is systematically underestimated by current methods due to the limited lifetime of Brown Carbon. Thus, our results clearly support the importance of the atmospheric aging in optical properties, and encourages to the quantification of BrC lifetime impact within the observations.

In recent years, the automation of ground-based measurements, and their deployment in the form of regional or global networks have made it possible to characterize aerosol optical and chemical properties at the scale of many regions of the world. However, although in situ measurements allow more precise characterizations (especially online chemical), they remain more punctual, and their cost (investment and operation) also limit their deployment at such a scale. The establishment of robust links between the chemical composition and the optical properties of the particles could make possible a chemical characterization on a large scale, from the ground and/or satellite remote sensing measurements. Such an approach could also improve the model estimation of aerosol radiative impacts, which would reduce the current uncertainties associated with direct and indirect aerosol effects. A first perspective appears therefore in the need to collect a longer-term dataset (> 10 years), in order to be able to identify statistically robust trends and observe more contrasting situations.

This study emphasizes the importance of considering the heterogeneity of aerosols and supports the use of site-specific parameters reflecting their influences, such as aerosol mixing state and size distribution of aerosol components to derive key aerosol optical properties. Therefore, the

second perspective of this thesis emerges, as we strongly recommend to explore the optical properties through Mie modelling at the ATOLL platform.

Regarding organic compounds, additional studies in the region are strongly recommended including secondary formation and absorption in the UV range. Here, we showed that the time of day impact the optical properties of Brown Carbon. According to the authors (Liakakou et al. 2020; Satish et al. 2017, and references therein), during the daytime, OH reactions and photolysis dominate the aging, while the NO_3 and O_3 oxidations account for the nighttime aging. Thus, supplementary analyses looking at the aging of organics at night would be highly appreciated, especially, concerning the reaction between anthropogenic VOCs with nitrogen oxides, producing nitro-aromatics, which are identified as light-absorbing compounds (Moise et al. 2015). To give an example of the type of analysis that could be carried out, we cite here the work done by de Sà et al. (2019), which, by employing an aerosol mass spectrometer (AMS), estimated the organic and inorganic nitrate concentrations based on the ratio of the signal intensity of NO_2^+ to that of NO, then compared it with the BrC absorption derived from an aethalometer (AE-31). Other authors (Kang et al. 2011; Ortega et al. 2016) have also explored the SOA in real time by combining an oxidation flow reactor (OFR, Kang et al. 2007) coupled with mass spectrometer (AMS), MPSS and O_3 monitor, sampling both ambient air, and ambient air aged in the OFR by systematically changing the OH exposure.

Finally, research into different combustion sources and their effect on AAE lifetime is encouraged. Indeed, the analysis of long-term observations performed here suggests a higher value of AAE associated with air masses from traffic emissions. Therefore, more work is needed regarding the accurate determination of the source-specific AAE values and the applicability of the Aethalometer model at ATOLL. In this thesis, we also highlight the lack of atmospheric observations that relate to the different AAE values of various types of sources and how these AAE values evolve with residence time (fresh vs. aged). Consequently, we support further research on this topic.

References

Adam, Mariana. 2004. "Aerosol Optical Characterization by Nephelometer and Lidar: The Baltimore Supersite Experiment during the Canadian Forest Fire Smoke Intrusion." *Journal of Geophysical Research* 109(D16). https://www.academia.edu/51577669/Aerosol_optical_characterization_by_nephelometer_and_lidar_The_Baltimore_Supersite_experiment_during_the_Canadian_forest_fire_smoke_intrusion (October 10, 2022).

Adam, Max G., Phuong T. M. Tran, Nanthi Bolan, and Rajasekhar Balasubramanian. 2021. "Biomass Burning-Derived Airborne Particulate Matter in Southeast Asia: A Critical Review." *Journal of Hazardous Materials* 407: 124760.

Agrawal, Harshit, William A. Welch, J. Wayne Miller, and David R. Cocker. 2008. "Emission Measurements from a Crude Oil Tanker at Sea." *Environmental Science & Technology* 42(19): 7098–7103.

Aiken, Allison C. et al. 2008. "O/C and OM/OC Ratios of Primary, Secondary, and Ambient Organic Aerosols with High-Resolution Time-of-Flight Aerosol Mass Spectrometry." *Environmental Science & Technology* 42(12): 4478–85.

Allan, James D et al. 2004. "A Generalised Method for the Extraction of Chemically Resolved Mass Spectra from Aerodyne Aerosol Mass Spectrometer Data." *Journal of Aerosol Science* 35(7): 909–22.

Alleman, L. et al. 2010. "PM10 Metal Concentrations and Source Identification Using Positive Matrix Factorization and Wind Sectoring in a French Industrial Zone."

Althuwaynee, Omar F. et al. 2021. "Spatial Identification and Temporal Prediction of Air Pollution Sources Using Conditional Bivariate Probability Function and Time Series Signature." *Journal of Exposure Science & Environmental Epidemiology* 31(4): 709–26.

Amato, P. et al. 2017. "Main Biological Aerosols, Specificities, Abundance, and Diversity." In *Microbiology of Aerosols*, John Wiley & Sons, Ltd, 1–21. https://onlinelibrary.wiley.com/doi/abs/10.1002/9781119132318.ch1a (August 3, 2022).

Anderson, Jonathan O., Josef G. Thundiyil, and Andrew Stolbach. 2012. "Clearing the Air: A Review of the Effects of Particulate Matter Air Pollution on Human Health." *Journal of Medical Toxicology* 8(2): 166–75.

Anderson, Theodore L., and John A. Ogren. 1998. "Determining Aerosol Radiative Properties Using the TSI 3563 Integrating Nephelometer." *Aerosol Science and Technology* 29(1): 57–69.

Andreae, M. O., and A. Gelencsér. 2006. "Black Carbon or Brown Carbon? The Nature of Light-Absorbing Carbonaceous Aerosols." *Atmospheric Chemistry and Physics* 6(10): 3131–48.

Andreae, Meinrat O. et al. 1986. "Internal Mixture of Sea Salt, Silicates, and Excess Sulfate in Marine Aerosols." *Science* 232(4758): 1620–23.

Andreae, Meinrat O., Chris D. Jones, and Peter M. Cox. 2005. “Strong Present-Day Aerosol Cooling Implies a Hot Future.” *Nature* 435(7046): 1187–90.

Andreae, Tracey W. et al. 2002. “Light Scattering by Dust and Anthropogenic Aerosol at a Remote Site in the Negev Desert, Israel.” *Journal of Geophysical Research: Atmospheres* 107(D2): AAC 3-1-AAC 33-18.

Andrews, Elisabeth et al. 2019. “Overview of the NOAA/ESRL Federated Aerosol Network.” *Bulletin of the American Meteorological Society* 100(1): 123–35.

Aouizerats, B. et al. 2010. “Development of an Online Radiative Module for the Computation of Aerosol Optical Properties in 3-D Atmospheric Models: Validation during the EUCAARI Campaign.” *Geoscientific Model Development* 3(2): 553–64.

Araujo, Jesus A. 2011. “Particulate Air Pollution, Systemic Oxidative Stress, Inflammation, and Atherosclerosis.” *Air Quality, Atmosphere & Health* 4(1): 79–93.

Asmi, A. et al. 2011. “Number Size Distributions and Seasonality of Submicron Particles in Europe 2008–2009.” *Atmospheric Chemistry and Physics* 11(11): 5505–38.

Barnaba, F., F. Angelini, G. Curci, and G. P. Gobbi. 2011. “An Important Fingerprint of Wildfires on the European Aerosol Load.” *Atmospheric Chemistry and Physics* 11(20): 10487–501.

Barros de Oliveira, Diogo Miguel. 2017. “Identification of the Main Sources and Geographical Origins of PM10 in the Northern Part of France.” These de doctorat. Lille 1. http://www.theses.fr/2017LIL10007 (June 13, 2022).

Bellouin, N. et al. 2020. “Bounding Global Aerosol Radiative Forcing of Climate Change.” *Reviews of Geophysics* 58(1): e2019RG000660.

Benedict, Katherine B. et al. 2017. “Enhanced Concentrations of Reactive Nitrogen Species in Wildfire Smoke.” *Atmospheric Environment* 148: 8–15.

Bian, Qijing et al. 2017. “Secondary Organic Aerosol Formation in Biomass-Burning Plumes: Theoretical Analysis of Lab Studies and Ambient Plumes.” *Atmospheric Chemistry and Physics* 17(8): 5459–75.

Bohren, Graig F., and Donald R. Huffman. 1998. “Absorption and Scattering of Light by Small Particles | Wiley.” *Wiley.com*. https://www.wiley.com/en-us/Absorption+and+Scattering+of+Light+by+Small+Particles-p-9780471293408 (June 13, 2022).

Bond, T. C. et al. 2013. “Bounding the Role of Black Carbon in the Climate System: A Scientific Assessment.” *Journal of Geophysical Research: Atmospheres* 118(11): 5380–5552.

Bond, Tami C., and Robert W. Bergstrom. 2006. “Light Absorption by Carbonaceous Particles: An Investigative Review.” *Aerosol Science and Technology* 40(1): 27–67.

Boucher, Olivier. 2016. *Atmospheric Aerosols: Properties and Climate Impacts*. Softcover Reprint of the Original 1st 2015 ed. édition. Dordrecht u.a: Springer.

Bovchaliuk, A. et al. 2013. “Variability of Aerosol Properties over Eastern Europe Observed from Ground and Satellites in the Period from 2003 to 2011.” *Atmospheric Chemistry and Physics* 13(13): 6587–6602.

Bowman, William D. et al. 2008. “Negative Impact of Nitrogen Deposition on Soil Buffering Capacity.” *Nature Geoscience* 1(11): 767–70.

Bressi, M. et al. 2021. “A European Aerosol Phenomenology - 7: High-Time Resolution Chemical Characteristics of Submicron Particulate Matter across Europe.” *Atmospheric Environment: X* 10: 100108.

Brown, Hunter et al. 2021. “Biomass Burning Aerosols in Most Climate Models Are Too Absorbing.” *Nature Communications* 12(1): 277.

Brown, R. J., C. Bonadonna, and A. J. Durant. 2012. “A Review of Volcanic Ash Aggregation.” *Physics and Chemistry of the Earth, Parts A/B/C* 45–46: 65–78.

Browne, Eleanor C. et al. 2019. “Effect of Heterogeneous Oxidative Aging on Light Absorption by Biomass Burning Organic Aerosol.” *Aerosol Science and Technology* 53(6): 663–74.

Bryant, C. et al. 2006. “Optical Properties of Aerosols over the Eastern Mediterranean.” *Atmospheric Environment* 40(32): 6229–44.

Budisulistiorini, Sri Hapsari et al. 2017. “Light-Absorbing Brown Carbon Aerosol Constituents from Combustion of Indonesian Peat and Biomass.” *Environmental Science & Technology* 51(8): 4415–23.

Bui, Thi Hieu, Duc Luong Nguyen, and Hoang Hiep Nguyen. 2022. “Study of Aerosol Optical Properties at Two Urban Areas in the North of Vietnam with the Implication for Biomass Burning Impacts.” *Environmental Science and Pollution Research* 29(28): 41923–40.

Burrows, S. M. et al. 2009. “Bacteria in the Global Atmosphere – Part 2: Modeling of Emissions and Transport between Different Ecosystems.” *Atmospheric Chemistry and Physics* 9(23): 9281–97.

Burt, P. J. A. 2012. “M. A. Sutton, C. M. Howard, J. W. Erisman, G. Billen, A. Bleeker, P. Grennfelt, H. Van Grinsven and B. Grizzetti (Eds), 2011. The European Nitrogen Assessment: Sources, Effects and Policy Perspectives, Cambridge University Press, UK. ISBN: 978-1-107-00612-6. LI + 612 PP.” *Meteorological Applications* 19(1): E2–E2.

Buseck, Peter R., and Kouji Adachi. 2008. “Nanoparticles in the Atmosphere.” *Elements* 4(6): 389–94.

Calderón-Garcidueñas, Lilian, and Rodolfo Villarreal-Ríos. 2017. “Living Close to Heavy Traffic Roads, Air Pollution, and Dementia.” *The Lancet* 389(10070): 675–77.

Calvo, A. I. et al. 2008. “Chemical Composition of Urban Aerosols in Toulouse, France during CAPITOUL Experiment.” *Meteorology and Atmospheric Physics* 102(3): 307–23.

Canagaratna, M.r. et al. 2007. “Chemical and Microphysical Characterization of Ambient Aerosols with the Aerodyne Aerosol Mass Spectrometer.” *Mass Spectrometry Reviews* 26(2): 185–222.

Canonaco, F. et al. 2013. “SoFi, an IGOR-Based Interface for the Efficient Use of the Generalized Multilinear Engine (ME-2) for the Source Apportionment: ME-2 Application to Aerosol Mass Spectrometer Data.” *Atmospheric Measurement Techniques* 6(12): 3649–61.

Cao, Jing et al. 2022. “Enhanced Summertime Ozone and SOA from Biogenic Volatile Organic Compound (BVOC) Emissions Due to Vegetation Biomass Variability during 1981–2018 in China.” *Atmospheric Chemistry and Physics* 22(4): 2351–64.

Carn, S. A. et al. 2011. “In Situ Measurements of Tropospheric Volcanic Plumes in Ecuador and Colombia during TC4.” *Journal of Geophysical Research* 116. https://www.academia.edu/23464868/In_situ_measurements_of_tropospheric_volcanic_plumes_in_Ecuador_and_Colombia_during_TC_4 (July 8, 2022).

Chang, Di, Yu Song, and Bing Liu. 2009. “Visibility Trends in Six Megacities in China 1973–2007.” *Atmospheric Research* 94(2): 161–67.

Chang, Liang et al. 2021. “Variability of Surface Aerosol Properties at an Urban Site in Beijing Based on Two Years of In-Situ Measurements.” *Atmospheric Research* 256: 105562.

Chao, Luomeng et al. 2021. “Evaluation of the Optical Properties of Various-Shaped and Core-Shell-Structured Lanthanum Hexaboride Nanoparticles Based on Discrete Dipole Approximation.” *Journal of Quantitative Spectroscopy and Radiative Transfer* 272: 107806.

Charlson, R. J., T. L. Anderson, and H. Rodhe. 1999. “Direct Climate Forcing by Anthropogenic Aerosols: Quantifying the Link between Atmospheric Sulfate and Radiation.” *Contributions to Atmospheric Physics* 72. https://www.osti.gov/etdeweb/biblio/333002 (October 12, 2022).

Chen, Cheng et al. 2018. “Retrieval of Desert Dust and Carbonaceous Aerosol Emissions over Africa from POLDER/PARASOL Products Generated by the GRASP Algorithm.” *Atmospheric Chemistry and Physics* 18(16): 12551–80.

Chen, Gang et al. 2022. “European Aerosol Phenomenology − 8: Harmonised Source Apportionment of Organic Aerosol Using 22 Year-Long ACSM/AMS Datasets.” *Environment International* 166: 107325.

Chen, Lung-Wen Antony et al. 2021. “Brownness of Organic Aerosol over the United States: Evidence for Seasonal Biomass Burning and Photobleaching Effects.” *Environmental Science & Technology* 55(13): 8561–72.

Chen, Pengfei et al. 2020. “Seasonality of Carbonaceous Aerosol Composition and Light Absorption Properties in Karachi, Pakistan.” *Journal of Environmental Sciences* 90: 286–96.

Chen, Y., and T. C. Bond. 2010. “Light Absorption by Organic Carbon from Wood Combustion.” *Atmospheric Chemistry and Physics* 10(4): 1773–87.

Cheng, Y. F. et al. 2008. “Aerosol Optical Properties and Related Chemical Apportionment at Xinken in Pearl River Delta of China.” *Atmospheric Environment* 42(25): 6351–72.

Cheng, Zhen et al. 2014. “Estimation of Aerosol Mass Scattering Efficiencies under High Mass Loading: Case Study for the Megacity of Shanghai, China.” *ACS Publications*. https://pubs.acs.org/doi/pdf/10.1021/es504567q (March 1, 2022).

Chu, Biwu et al. 2022. “Application of Smog Chambers in Atmospheric Process Studies.” *National Science Review* 9(2): nwab103.

Chylek, Petr et al. 2019. “Mie Scattering Captures Observed Optical Properties of Ambient Biomass Burning Plumes Assuming Uniform Black, Brown, and Organic Carbon Mixtures.” *Journal of Geophysical Research: Atmospheres* 124(21): 11406–27.

Citepa. 2021. “Inventaire des émissions de polluants atmosphériques et de gaz à effet de serre en France.” *Citepa*. https://www.citepa.org/fr/secten/ (September 27, 2022).

Collaud Coen, Martine et al. 2020. “Multidecadal Trend Analysis of in Situ Aerosol Radiative Properties around the World.” *Atmospheric Chemistry and Physics* 20(14): 8867–8908.

Cooper, D. A. 2001. “Exhaust Emissions from High Speed Passenger Ferries.” *Atmospheric Environment* 35(24): 4189–4200.

Cooper, D. A. 2003. “Exhaust Emissions from Ships at Berth.” *Atmospheric Environment* 37(27): 3817–30.

Cooper, Richard N., J. T. Houghton, James J. McCarthy, and Bert Metz. 2002. “Climate Change 2001: The Scientific Basis.” *Foreign Affairs* 81(1): 208.

Costabile, Francesca et al. 2017. “First Results of the ‘Carbonaceous Aerosol in Rome and Environs (CARE)’ Experiment: Beyond Current Standards for PM10.” *Atmosphere* 8(12): 249.

Crenn, V. et al. 2015. “ACTRIS ACSM Intercomparison – Part 1: Reproducibility of Concentration and Fragment Results from 13 Individual Quadrupole Aerosol Chemical Speciation Monitors (Q-ACSM) and Consistency with Co-Located Instruments.” *Atmospheric Measurement Techniques* 8(12): 5063–87.

Crenn, V. et al. 2018. “Fine Particles Sampled at an Urban Background Site and an Industrialized Coastal Site in Northern France—Part 2: Comparison of Offline and Online Analyses for Carbonaceous Aerosols.” *Aerosol Science and Technology* 52(3): 287–99.

Crenn, V., I. Fronval, D. Petitprez, and V. Riffault. 2017a. “Fine Particles Sampled at an Urban Background Site and an Industrialized Coastal Site in Northern France — Part 1: Seasonal Variations and Chemical Characterization.” *Science of The Total Environment* 578: 203–18.

Crenn, V. et al. 2017. “Fine Particles Sampled at an Urban Background Site and an Industrialized Coastal Site in Northern France — Part 1: Seasonal Variations and Chemical Characterization.” *Science of The Total Environment* 578: 203–18.

Crippa, Monica et al. 2020. “High Resolution Temporal Profiles in the Emissions Database for Global Atmospheric Research.” *Scientific Data* 7(1): 121.

Crumeyrolle, S. et al. 2008. “Increase of the Aerosol Hygroscopicity by Cloud Processing in a Mesoscale Convective System: A Case Study from the AMMA Campaign.” *Atmospheric Chemistry and Physics* 8(23): 6907–24.

Crumeyrolle, Suzanne et al. 2022. “Measurement Report: Atmopsheric New Particle Formation in a Peri-Urban Site in Lille, Northern France.” *Atmospheric Chemistry and Physics Discussions*: 1–35.

Cuesta-Mosquera, Andrea et al. 2021. “Intercomparison and Characterization of 23 Aethalometers under Laboratory and Ambient Air Conditions: Procedures and Unit-to-Unit Variabilities.” *Atmospheric Measurement Techniques* 14(4): 3195–3216.

De Mazière, Martine et al. 2018. “The Network for the Detection of Atmospheric Composition Change (NDACC): History, Status and Perspectives.” *Atmospheric Chemistry and Physics* 18(7): 4935–64.

Delmas, Rodert, Gérard Mégie, and Vincent-Henri Peuch. 2015. “Physique et chimie de l’atmosphère.” *Unithèque*. https://www.unitheque.com/physique-chimie-atmosphere/echelles/belin/Livre/9318 (July 8, 2022).

Denier van der Gon, H. a. C. et al. 2015. “Particulate Emissions from Residential Wood Combustion in Europe – Revised Estimates and an Evaluation.” *Atmospheric Chemistry and Physics* 15(11): 6503–19.

Denjean, Cyrielle et al. 2020. “Unexpected Biomass Burning Aerosol Absorption Enhancement Explained by Black Carbon Mixing State.” *Geophysical Research Letters* 47(19): e2020GL089055.

Dentener, F. et al. 2006. “Emissions of Primary Aerosol and Precursor Gases in the Years 2000 and 1750 Prescribed Data-Sets for AeroCom.” *Atmospheric Chemistry and Physics* 6(12): 4321–44.

Di Lorenzo, Robert A. et al. 2017. “Molecular-Size-Separated Brown Carbon Absorption for Biomass-Burning Aerosol at Multiple Field Sites.” *Environmental Science & Technology* 51(6): 3128–37.

Drinovec, L. et al. 2015. “The ‘Dual-Spot’ Aethalometer: An Improved Measurement of Aerosol Black Carbon with Real-Time Loading Compensation.” https://oa.tib.eu/renate/handle/123456789/765 (March 8, 2022).

Drosatou, Anthoula D., Ksakousti Skyllakou, Georgia N. Theodoritsi, and Spyros N. Pandis. 2019. “Positive Matrix Factorization of Organic Aerosol: Insights from a Chemical Transport Model.” *Atmospheric Chemistry and Physics* 19(2): 973–86.

Du, Aodong et al. 2022. “Rapid Transition of Aerosol Optical Properties and Water-Soluble Organic Aerosols in Cold Season in Fenwei Plain.” *Science of The Total Environment* 829: 154661.

Dubovik, O. et al. 2011. “Statistically Optimized Inversion Algorithm for Enhanced Retrieval of Aerosol Properties from Spectral Multi-Angle Polarimetric Satellite Observations.” *Atmospheric Measurement Techniques* 4(5): 975–1018.

Dubovik, Oleg et al. 2002. “Variability of Absorption and Optical Properties of Key Aerosol Types Observed in Worldwide Locations.” *Journal of the Atmospheric Sciences* 59(3): 590–608.

Dubovik, Oleg, and Michael D. King. 2000. “A Flexible Inversion Algorithm for Retrieval of Aerosol Optical Properties from Sun and Sky Radiance Measurements.” *Journal of Geophysical Research: Atmospheres* 105(D16): 20673–96.

Ealo, Marina et al. 2018. “Impact of Aerosol Particle Sources on Optical Properties in Urban, Regional and Remote Areas in the North-Western Mediterranean.” *Atmospheric Chemistry and Physics* 18(2): 1149–69.

European Environment Agency. 2013. “The Impact of International Shipping on European Air Quality and Climate Forcing — European Environment Agency.” https://www.eea.europa.eu/publications/the-impact-of-international-shipping (August 18, 2022).

European Environment Agency. 2021. “Health Impacts of Air Pollution in Europe, 2021 — European Environment Agency.” https://www.eea.europa.eu/publications/air-quality-in-europe-2021/health-impacts-of-air-pollution (July 8, 2022).

Espina Martin, Pablo. 2020. “Determinants and sources of secondary inorganic aerosols in a rural area in Northern France.” Thèse de doctorat. IMT Nord Europe.

European Center for Aerosol Calibration and Characterization. 2022. “PMC Non-Refractory Organics and Inorganics.” *ECAC*. https://www.actris-ecac.eu/pmc-non-refractory-organics-and-inorganics.html (October 8, 2022).

European Commission, European Commission. 2019. “Top Cargo Ports in 2017.” https://ec.europa.eu/eurostat/web/products-eurostat-news/-/DDN-20190711-1 (August 18, 2022).

European Environment Agency. 2020. “Emissions and Energy Use in Large Combustion Plants in Europe.” https://www.eea.europa.eu/ims/emissions-and-energy-use-in (October 2, 2022).

European Environment Agency. 2022. “Europe’s Air Quality Status 2022 — European Environment Agency.” https://www.eea.europa.eu//publications/status-of-air-quality-in-Europe-2022 (September 26, 2022).

Eurostat. 2016. “Urban Europe — Statistics on Cities, Towns and Suburbs.” https://ec.europa.eu/eurostat/web/products-statistical-books/-/ks-01-16-691 (September 26, 2022).

Eurostat. 2022. “Population Statistics at Regional Level.” https://ec.europa.eu/eurostat/statistics-explained/index.php?title=Population_statistics_at_regional_level (October 14, 2022).

Evangeliou, Nikolaos et al. 2021. “Changes in Black Carbon Emissions over Europe Due to COVID-19 Lockdowns.” *Atmospheric Chemistry and Physics* 21(4): 2675–92.

Facchini, Maria Cristina et al. 2008. “Primary Submicron Marine Aerosol Dominated by Insoluble Organic Colloids and Aggregates.” *Geophysical Research Letters* 35(17). https://onlinelibrary.wiley.com/doi/abs/10.1029/2008GL034210 (June 10, 2022).

Fan, Hao, Chuanfeng Zhao, and Yikun Yang. 2020. “A Comprehensive Analysis of the Spatio-Temporal Variation of Urban Air Pollution in China during 2014–2018.” *Atmospheric Environment* 220: 117066.

Fan, Xingjun et al. 2016. “Comprehensive Characterization of Humic-like Substances in Smoke $PM_{2.5}$ Emitted from the Combustion of Biomass Materials and Fossil Fuels.” *Atmospheric Chemistry and Physics* 16(20): 13321–40.

Favez, O. et al. 2010. “Inter-Comparison of Source Apportionment Models for the Estimation of Wood Burning Aerosols during Wintertime in an Alpine City (Grenoble, France).” *Atmospheric Chemistry and Physics* 10(12): 5295–5314.

Favez, O. et al. 2009. “Evidence for a Significant Contribution of Wood Burning Aerosols to PM2.5 during the Winter Season in Paris, France.” *Atmospheric Environment* 43(22): 3640–44.

Favez, O. et al. 2021. “Overview of the French Operational Network for In Situ Observation of PM Chemical Composition and Sources in Urban Environments (CARA Program).” *Atmosphere* 12(2): 207.

Finlayson-Pitts, Barbara J., and James N. Pitts Jr. 1999. *Chemistry of the Upper and Lower Atmosphere: Theory, Experiments, and Applications*. San Diego.

Fitzgerald, James W. 1991. “Marine Aerosols: A Review.” *Atmospheric Environment. Part A. General Topics* 25(3): 533–45.

Fleming, Lauren T. et al. 2020. “Molecular Composition and Photochemical Lifetimes of Brown Carbon Chromophores in Biomass Burning Organic Aerosol.” *Atmospheric Chemistry and Physics* 20(2): 1105–29.

Font, A., K. Ciupek, D. Butterfield, and G. W. Fuller. 2022. “Long-Term Trends in Particulate Matter from Wood Burning in the United Kingdom: Dependence on Weather and Social Factors.” *Environmental Pollution* 314: 120105.

Formenti, P. et al. 2001. “Physical and Chemical Characteristics of Aerosols over the Negev Desert (Israel) during Summer 1996.” *Journal of Geophysical Research: Atmospheres* 106(D5): 4871–90.

Forrister, Haviland et al. 2015. “Evolution of Brown Carbon in Wildfire Plumes.” *Geophysical Research Letters* 42(11): 4623–30.

Forster, Piers et al. 2021. “The Earth’s Energy Budget, Climate Feedbacks, and Climate Sensitivity.” In *Climate Change 2021: The Physical Science Basis. Contribution of Working Group I to the Sixth Assessment Report of the Intergovernmental Panel on Climate Change,* eds. Valérie Masson-Delmotte et al. Cambridge University Press.

Frogner Kockum, Paul C., Roger B. Herbert, and Sigurdur R. Gislason. 2006. "A Diverse Ecosystem Response to Volcanic Aerosols." *Chemical Geology* 231(1): 57–66.

Fröhlich-Nowoisky, Janine et al. 2016. "Bioaerosols in the Earth System: Climate, Health, and Ecosystem Interactions." *Atmospheric Research* 182: 346–76.

Gao, Yuan et al. 2022. "Optical Properties of Mountain Primary and Secondary Brown Carbon Aerosols in Summertime." *Science of The Total Environment* 806: 150570.

Gilardoni, Stefania et al. 2020. "Spatial and Temporal Variability of Carbonaceous Aerosol Absorption in the Po Valley." *Aerosol and Air Quality Research* 20(12): 2624–39.

Giles, D. M. et al. 2012. "An Analysis of AERONET Aerosol Absorption Properties and Classifications Representative of Aerosol Source Regions." *Journal of Geophysical Research: Atmospheres* 117(D17). https://onlinelibrary.wiley.com/doi/abs/10.1029/2012JD018127 (August 18, 2022).

Golly, B. et al. 2019. "Organic Markers and OC Source Apportionment for Seasonal Variations of PM2.5 at 5 Rural Sites in France." *Atmospheric Environment* 198: 142–57.

Gómez-González, Y. et al. 2012. "Chemical Characterisation of Atmospheric Aerosols during a 2007 Summer Field Campaign at Brasschaat, Belgium: Sources and Source Processes of Biogenic Secondary Organic Aerosol." *Atmospheric Chemistry and Physics* 12(1): 125–38.

Gomišček, B, H Hauck, S Stopper, and O Preining. 2004. "Spatial and Temporal Variations of PM1, PM2.5, PM10 and Particle Number Concentration during the AUPHEP—Project." *Atmospheric Environment* 38(24): 3917–34.

Greene, Chad A. et al. 2019. "The Climate Data Toolbox for MATLAB." *Geochemistry, Geophysics, Geosystems* 20(7): 3774–81.

Groblicki, Peter J., George T. Wolff, and Richard J. Countess. 1981. "Visibility-Reducing Species in the Denver 'Brown Cloud'—I. Relationships between Extinction and Chemical Composition." *Atmospheric Environment (1967)* 15(12): 2473–84.

Groot Zwaaftink, Christine D. et al. 2022. "What Caused a Record High PM_{10} Episode in Northern Europe in October 2020?" *Atmospheric Chemistry and Physics* 22(6): 3789–3810.

Guarnieri, Michael, and John R. Balmes. 2014. "Outdoor Air Pollution and Asthma." *The Lancet* 383(9928): 1581–92.

Guenther, Alex et al. 1995. "A Global Model of Natural Volatile Organic Compound Emissions." *Journal of geophysical research* 100: 8873–92.

Guerreiro, Cristina B. B., Valentin Foltescu, and Frank de Leeuw. 2014. "Air Quality Status and Trends in Europe." *Atmospheric Environment* 98: 376–84.

Hama, Sarkawt et al. 2022. "Carbonaceous Aerosols in Five European Cities: Insights into Primary Emissions and Secondary Particle Formation." *Atmospheric Research* 274: 106180.

Han, Lihui et al. 2021. “Characteristics, Evolution, and Potential Source Regions of Submicron Aerosol in Beijing, China.” *Atmospheric Environment* 246: 118061.

Hand, J. L., and W. C. Malm. 2007. “Review of Aerosol Mass Scattering Efficiencies from Ground-Based Measurements since 1990.” *Journal of Geophysical Research: Atmospheres* 112(D16). https://agupubs.onlinelibrary.wiley.com/doi/abs/10.1029/2007JD008484 (May 14, 2020).

Handler, Paul. 1989. “The Effect of Volcanic Aerosols on Global Climate.” *Journal of Volcanology and Geothermal Research* 37(3): 233–49.

Hauglustaine, D. A., Y. Balkanski, and M. Schulz. 2014. “A Global Model Simulation of Present and Future Nitrate Aerosols and Their Direct Radiative Forcing of Climate.” *Atmospheric Chemistry and Physics* 14(20): 11031–63.

Haywood, James, and Olivier Boucher. 2000. “Estimates of the Direct and Indirect Radiative Forcing Due to Tropospheric Aerosols: A Review.” *Reviews of Geophysics* 38(4): 513–43.

Haywood, Jim, and Michael Schulz. 2007. “Causes of the Reduction in Uncertainty in the Anthropogenic Radiative Forcing of Climate between IPCC (2001) and IPCC (2007).” *Geophysical Research Letters* 34(20). https://hal.archives-ouvertes.fr/hal-03191249 (June 13, 2022).

He, Quanfu et al. 2021. “Optical Properties of Secondary Organic Aerosol Produced by Nitrate Radical Oxidation of Biogenic Volatile Organic Compounds.” *Environmental Science & Technology* 55(5): 2878–89.

Heald, Colette L., and Dominick V. Spracklen. 2009. “Atmospheric Budget of Primary Biological Aerosol Particles from Fungal Spores.” *Geophysical Research Letters* 36(9). https://onlinelibrary.wiley.com/doi/abs/10.1029/2009GL037493 (June 10, 2022).

Healy, Robert M. et al. 2009. “Characterisation of Single Particles from In-Port Ship Emissions.” *Atmospheric Environment* 43(40): 6408–14.

Heintzenberg, J., D. C. Covert, and R. Van Dingenen. 2000. “Size Distribution and Chemical Composition of Marine Aerosols: A Compilation and Review.” *Tellus B: Chemical and Physical Meteorology* 52(4): 1104–22.

Helin, A. et al. 2021. “Variation of Absorption Ångström Exponent in Aerosols From Different Emission Sources.” *Journal of Geophysical Research: Atmospheres* 126(10): e2020JD034094.

Helin, Aku et al. 2018. “Characteristics and Source Apportionment of Black Carbon in the Helsinki Metropolitan Area, Finland.” *Atmospheric Environment* 190: 87–98.

Hems, Rachel F. et al. 2021. “Aging of Atmospheric Brown Carbon Aerosol.” *ACS Earth and Space Chemistry* 5(4): 722–48.

Hoffmann, Erik Hans et al. 2016. “An Advanced Modeling Study on the Impacts and Atmospheric Implications of Multiphase Dimethyl Sulfide Chemistry.” *Proceedings of the National Academy of Sciences* 113(42): 11776–81.

Hofman, J. et al. 2016. “Ultrafine Particles in Four European Urban Environments: Results from a New Continuous Long-Term Monitoring Network.” *Atmospheric Environment* 136: 68–81.

Hofmann, D. J., and J. M. Rosen. 1980. “Stratospheric Sulfuric Acid Layer: Evidence for an Anthropogenic Component.” *Science* 208(4450): 1368–70.

Holben, B. N. et al. 1998. “AERONET—A Federated Instrument Network and Data Archive for Aerosol Characterization.” *Remote Sensing of Environment* 66(1): 1–16.

Holben, B. N. et al. 2006. “Aeronet’s Version 2.0 Quality Assurance Criteria.” In eds. Si-Chee Tsay, Teruyuki Nakajima, Ramesh P. Singh, and R. Sridharan. Goa, India, 64080Q. http://proceedings.spiedigitallibrary.org/proceeding.aspx?doi=10.1117/12.706524 (July 7, 2022).

Holmes, Nicholas, and Lidia Morawska. 2006. “A Review of Dispersion Modelling and Its Application to the Dispersion of Particles: An Overview of Different Dispersion Models Available.” *Atmospheric Environment* 40(30): 5902–28.

Hussein, T., L. Sogacheva, and T. Petäjä. 2018. “Accumulation and Coarse Modes Particle Concentrations during Dew Formation and Precipitation.” *Aerosol and Air Quality Research* 18(12): 2929–38.

Islam, Rajib et al. 2021. “A Molecular Modeling Approach to Identify Effective Antiviral Phytochemicals against the Main Protease of SARS-CoV-2.” *Journal of Biomolecular Structure and Dynamics* 39(9): 3213–24.

Jacobson, M. C., H. -C. Hansson, K. J. Noone, and R. J. Charlson. 2000. “Organic Atmospheric Aerosols: Review and State of the Science.” *Reviews of Geophysics* 38(2): 267–94.

Jacobson, Mark Z. 2001. “Strong Radiative Heating Due to the Mixing State of Black Carbon in Atmospheric Aerosols.” *Nature* 409(6821): 695–97.

Jaenicke, Ruprecht. 2005. “Abundance of Cellular Material and Proteins in the Atmosphere.” *Science (New York, N.Y.)* 308(5718): 73.

Jahl, Lydia G. et al. 2021. “Atmospheric Aging Enhances the Ice Nucleation Ability of Biomass-Burning Aerosol.” *Science Advances* 7(9): eabd3440.

Jiang, Meng et al. 2021. “Influence of Particle Properties on Measuring a Low-Particulate-Mass Concentration by Light Extinction Method.” *Fuel* 286: 119460.

Jung, Chang Hoon, JiYi Lee, Junshik Um, and Yong Pyo Kim. 2020. “Reconstructed Expression for Aerosol Extinction Coefficient by Considering Mass Extinction Efficiency and Hygroscopic Growth for Polydipersed Aerosol.” : 7475.

Kanakidou, M. et al. 2005. “Organic Aerosol and Global Climate Modelling: A Review.” *Atmospheric Chemistry and Physics* 5(4): 1053–1123.

Kang, E., M. J. Root, D. W. Toohey, and W. H. Brune. 2007. “Introducing the Concept of Potential Aerosol Mass (PAM).” *Atmospheric Chemistry and Physics* 7(22): 5727–44.

Kang, E., D. W. Toohey, and W. H. Brune. 2011. “Dependence of SOA Oxidation on Organic Aerosol Mass Concentration and OH Exposure: Experimental PAM Chamber Studies.” *Atmospheric Chemistry and Physics* 11(4): 1837–52.

Karanasiou, Angeliki et al. 2021. “Short-Term Health Effects from Outdoor Exposure to Biomass Burning Emissions: A Review.” *Science of The Total Environment* 781: 146739.

Kaskaoutis, D. G. et al. 2021. “In Situ Identification of Aerosol Types in Athens, Greece, Based on Long-Term Optical and on Online Chemical Characterization.” *Atmospheric Environment* 246: 118070.

Kaskaoutis, Dimitris G. et al. 2021. “Assessment of the COVID-19 Lockdown Effects on Spectral Aerosol Scattering and Absorption Properties in Athens, Greece.” *Atmosphere* 12(2): 231.

Kasthuriarachchi, Nethmi Y., Laura-Hélèna Rivellini, Max G. Adam, and Alex K. Y. Lee. 2020. “Light Absorbing Properties of Primary and Secondary Brown Carbon in a Tropical Urban Environment.” *Environmental Science & Technology* 54(17): 10808–19.

Kazadzis, S. et al. 2007. “Nine Years of UV Aerosol Optical Depth Measurements at Thessaloniki, Greece.” *Atmospheric Chemistry and Physics* 7(8): 2091–2101.

Kerker, Milton. 1969. “The Scattering of Light and Other Electromagnetic Radiation - 1st Edition.” https://www.elsevier.com/books/the-scattering-of-light-and-other-electromagnetic-radiation/kerker/978-1-4832-0021-7 (June 13, 2022).

Khomenko, Sasha et al. 2021. “Premature Mortality Due to Air Pollution in European Cities: A Health Impact Assessment.” *The Lancet Planetary Health* 5(3): e121–34.

Kiebel, Stefan J. et al. 1999. “Robust Smoothness Estimation in Statistical Parametric Maps Using Standardized Residuals from the General Linear Model.” *NeuroImage* 10(6): 756–66.

Kim, Ki-Hyun, Ehsanul Kabir, and Shamin Kabir. 2015. “A Review on the Human Health Impact of Airborne Particulate Matter.” *Environment International* 74: 136–43.

Knippertz, Peter, and Martin C. Todd. 2012. “Mineral Dust Aerosols over the Sahara: Meteorological Controls on Emission and Transport and Implications for Modeling.” *Reviews of Geophysics* 50(1). https://onlinelibrary.wiley.com/doi/abs/10.1029/2011RG000362 (July 8, 2022).

Koçak, Mustafa, Nikos Mihalopoulos, and Nilgün Kubilay. 2007. “Contributions of Natural Sources to High PM10 and PM2.5 Events in the Eastern Mediterranean.” *Atmospheric Environment* 41(18): 3806–18.

Kok, Jasper F. et al. 2021. “Contribution of the World’s Main Dust Source Regions to the Global Cycle of Desert Dust.” *Atmospheric Chemistry and Physics* 21(10): 8169–93.

Koulouri, E. et al. 2013. “Study of Size-Segregated Particle (PM1, PM2,5, PM10) Concentrations over Greece.” https://journal.gnest.org/publication/554 (November 3, 2022).

Kumar, K. Raghavendra et al. 2014. “Long-Term (2003–2013) Climatological Trends and Variations in Aerosol Optical Parameters Retrieved from MODIS over Three Stations in South Africa.” *Atmospheric Environment* 95: 400–408.

Kumar, M. et al. 2018. “Long-Term Aerosol Climatology over Indo-Gangetic Plain: Trend, Prediction and Potential Source Fields.” *Atmospheric Environment* 180: 37–50.

Kumar, Nivedita K. et al. 2018. “Production of Particulate Brown Carbon during Atmospheric Aging of Residential Wood-Burning Emissions.” *Atmospheric Chemistry and Physics* 18(24): 17843–61.

Kürten, Andreas et al. 2018. “New Particle Formation in the Sulfuric Acid–Dimethylamine–Water System: Reevaluation of CLOUD Chamber Measurements and Comparison to an Aerosol Nucleation and Growth Model.” *Atmospheric Chemistry and Physics* 18(2): 845–63.

Laborde, M. et al. 2013. “Black Carbon Physical Properties and Mixing State in the European Megacity Paris.” *Atmospheric Chemistry and Physics* 13(11): 5831–56.

Lack, D. A., and C. D. Cappa. 2010. “Impact of Brown and Clear Carbon on Light Absorption Enhancement, Single Scatter Albedo and Absorption Wavelength Dependence of Black Carbon.” *Atmospheric Chemistry and Physics* 10(9): 4207–20.

Laj, Paolo et al. 2020. “A Global Analysis of Climate-Relevant Aerosol Properties Retrieved from the Network of Global Atmosphere Watch (GAW) near-Surface Observatories.” *Atmospheric Measurement Techniques* 13(8): 4353–92.

Lambe, Andrew T. et al. 2013. “Relationship between Oxidation Level and Optical Properties of Secondary Organic Aerosol.” *Environmental Science & Technology* 47(12): 6349–57.

Lanz, V. A. et al. 2007. “Source Apportionment of Submicron Organic Aerosols at an Urban Site by Factor Analytical Modelling of Aerosol Mass Spectra.” *Atmospheric Chemistry and Physics* 7(6): 1503–22.

Lanz, Valentin A. et al. 2008. “Source Attribution of Submicron Organic Aerosols during Wintertime Inversions by Advanced Factor Analysis of Aerosol Mass Spectra.” *Environmental Science & Technology* 42(1): 214–20.

Lanzafame, G. M. et al. 2021. “One-Year Measurements of Secondary Organic Aerosol (SOA) Markers in the Paris Region (France): Concentrations, Gas/Particle Partitioning and SOA Source Apportionment.” *Science of The Total Environment* 757: 143921.

Laskin, Alexander, Julia Laskin, and Sergey A. Nizkorodov. 2015. “Chemistry of Atmospheric Brown Carbon.” *Chemical Reviews* 115(10): 4335–82.

Leck, Caroline, and E. Keith Bigg. 2008. “Comparison of Sources and Nature of the Tropical Aerosol with the Summer High Arctic Aerosol.” *Tellus B* 60(1): 118–26.

Ledoux, Frédéric et al. 2018. “Influence of Ship Emissions on NOx, SO2, O3 and PM Concentrations in a North-Sea Harbor in France.” *Journal of Environmental Sciences* 71: 56–66.

Lee, Hyun Ji (Julie) et al. 2014. “Effect of Solar Radiation on the Optical Properties and Molecular Composition of Laboratory Proxies of Atmospheric Brown Carbon.” *Environmental Science & Technology* 48(17): 10217–26.

Levy, R. C. et al. 2010. “Global Evaluation of the Collection 5 MODIS Dark-Target Aerosol Products over Land.” *Atmospheric Chemistry and Physics* 10(21): 10399–420.

Li, Chih-Shan, and Chia-Ho Lin. 2002. “PM 1 /PM 2.5 /PM 10 Characteristics in the Urban Atmosphere of Taipei.” *Aerosol Science and Technology* 36(4): 469–73.

Li, Chunlin et al. 2020. “Formation of Secondary Brown Carbon in Biomass Burning Aerosol Proxies through NO3 Radical Reactions.” *Environmental Science & Technology* 54(3): 1395–1405.

Li, J., B. E. Carlson, O. Dubovik, and A. A. Lacis. 2014. “Recent Trends in Aerosol Optical Properties Derived from AERONET Measurements.” *Atmospheric Chemistry and Physics* 14(22): 12271–89.

Li, Lei et al. 2019. “Retrieval of Aerosol Components Directly from Satellite and Ground-Based Measurements.” *Atmospheric Chemistry and Physics* 19(21): 13409–43.

Li, Meiju et al. 2019. “Abundance and Light Absorption Properties of Brown Carbon Emitted from Residential Coal Combustion in China.” *Environmental Science & Technology* 53(2): 595–603.

Li, Sheng et al. 2018. “Filter-Based Measurement of Light Absorption by Brown Carbon in PM2.5 in a Megacity in South China.” *Science of The Total Environment* 633: 1360–69.

Liakakou, E. et al. 2020. “Long-Term Brown Carbon Spectral Characteristics in a Mediterranean City (Athens).” *Science of The Total Environment* 708: 135019.

Lin, Peng et al. 2017. “Molecular Chemistry of Atmospheric Brown Carbon Inferred from a Nationwide Biomass Burning Event.” *Environmental Science & Technology* 51(20): 11561–70.

Lin, Peng, Julia Laskin, Sergey A. Nizkorodov, and Alexander Laskin. 2015. “Revealing Brown Carbon Chromophores Produced in Reactions of Methylglyoxal with Ammonium Sulfate.” *Environmental Science & Technology* 49(24): 14257–66.

Liu, Chao, Chul Eddy Chung, Yan Yin, and Martin Schnaiter. 2018. “The Absorption Ångström Exponent of Black Carbon: From Numerical Aspects.” *Atmospheric Chemistry and Physics* 18(9): 6259–73.

Liu, Dantong et al. 2021. “Evolution of Aerosol Optical Properties from Wood Smoke in Real Atmosphere Influenced by Burning Phase and Solar Radiation.” *Environmental Science & Technology* 55(9): 5677–88.

Liu, Dantong, Cenlin He, Joshua P. Schwarz, and Xuan Wang. 2020. “Lifecycle of Light-Absorbing Carbonaceous Aerosols in the Atmosphere.” *npj Climate and Atmospheric Science* 3(1): 1–18.

Liu, Fengshan et al. 2020. “Review of Recent Literature on the Light Absorption Properties of Black Carbon: Refractive Index, Mass Absorption Cross Section, and Absorption Function.” *Aerosol Science and Technology* 54(1): 33–51.

Liu, Jiumeng et al. 2016. “Optical Properties and Aging of Light-Absorbing Secondary Organic Aerosol.” *Atmospheric Chemistry and Physics* 16(19): 12815–27.

Lohmann, U., and J. Feichter. 2005. “Global Indirect Aerosol Effects: A Review.” *Atmospheric Chemistry and Physics* 5(3): 715–37.

Lohmann, Ulrike, and Johann Feichter. 2001. “Can the Direct and Semi-Direct Aerosol Effect Compete with the Indirect Effect on a Global Scale?” *Geophysical Research Letters* 28(1): 159–61.

Lovett, Gary M. et al. 2009. “Effects of Air Pollution on Ecosystems and Biological Diversity in the Eastern United States.” *Annals of the New York Academy of Sciences* 1162(1): 99–135.

Lu, Zifeng et al. 2015. “Light Absorption Properties and Radiative Effects of Primary Organic Aerosol Emissions.” *Environmental Science & Technology* 49(8): 4868–77.

Lundgren, Dale A., Daniel N. Hlaing, Thomas A. Rich, and Virgil A. Marple. 1996. “PM10/PM2.5/PM1 Data from a Trichotomous Sampler.” *Aerosol Science and Technology* 25(3): 353–57.

Luoma, Krista. 2021. “Aerosol Optical Properties, Black Carbon and Their Spatio-Temporal Variation.” https://helda.helsinki.fi/handle/10138/325857 (May 2, 2022).

Lyamani, H., F. J. Olmo, and L. Alados-Arboledas. 2010. “Physical and Optical Properties of Aerosols over an Urban Location in Spain: Seasonal and Diurnal Variability.” *Atmospheric Chemistry and Physics* 10(1): 239–54.

Mäkelä, J. M. et al. 1997. “Observations of Ultrafine Aerosol Particle Formation and Growth in Boreal Forest.” *Geophysical Research Letters* 24(10): 1219–22.

Maring, H. et al. 2000. “Aerosol Physical and Optical Properties and Their Relationship to Aerosol Composition in the Free Troposphere at Izaña, Tenerife, Canary Islands, during July 1995.” *Journal of Geophysical Research: Atmospheres* 105(D11): 14677–700.

Maring, H. et al. 2003. “Mineral Dust Aerosol Size Distribution Change during Atmospheric Transport.” *Journal of Geophysical Research: Atmospheres* 108(D19). https://onlinelibrary.wiley.com/doi/abs/10.1029/2002JD002536 (August 3, 2022).

Martinsson, J. et al. 2015. “Impacts of Combustion Conditions and Photochemical Processing on the Light Absorption of Biomass Combustion Aerosol.” *Environmental Science & Technology* 49(24): 14663–71.

Masson-Delmotte, Valérie et al., eds. 2021. *Climate Change 2021: The Physical Science Basis. Contribution of Working Group I to the Sixth Assessment Report of the Intergovernmental Panel on Climate Change*. Cambridge University Press.

Mbengue, Saliou et al. 2020. "Characterization of Equivalent Black Carbon at a Regional Background Site in Central Europe: Variability and Source Apportionment☆." *Environmental Pollution* 260: 113771.

Mbengue, Saliou et al. 2021. "Mass Absorption Cross-Section and Absorption Enhancement from Long Term Black and Elemental Carbon Measurements: A Rural Background Station in Central Europe." *Science of The Total Environment* 794: 148365.

McMeeking, G. R. et al. 2011. "Black Carbon Aerosol Mixing State, Organic Aerosols and Aerosol Optical Properties over the United Kingdom." *Atmospheric Chemistry and Physics* 11(17): 9037–52.

Medina, Sylvia et al. 2021. "Impact de pollution de l'air ambiant sur la mortalité en France métropolitaine. Réduction en lien avec le confinement du printemps 2020 et nouvelles données sur le poids total pour la période 2016-2019." https://www.santepubliquefrance.fr/import/impact-de-pollution-de-l-air-ambiant-sur-la-mortalite-en-france-metropolitaine.-reduction-en-lien-avec-le-confinement-du-printemps-2020-et-nouvelle (September 26, 2022).

Météo-France. 2020. "Le Changement Climatique En France | Météo-France." https://meteofrance.com/changement-climatique/observer/le-changement-climatique-en-france (September 29, 2022).

Middlebrook, Ann M., Roya Bahreini, Jose L. Jimenez, and Manjula R. Canagaratna. 2012. "Evaluation of Composition-Dependent Collection Efficiencies for the Aerodyne Aerosol Mass Spectrometer Using Field Data." *Aerosol Science and Technology* 46(3): 258–71.

Mills, Michael J. et al. 2016. "Global Volcanic Aerosol Properties Derived from Emissions, 1990–2014, Using CESM1(WACCM)." *Journal of Geophysical Research: Atmospheres* 121(5): 2332–48.

Ministère de la Transition Ecologique. 2021. "La pollution de l'air par l'ozone (O3)." *Données et études statistiques pour le changement climatique, l'énergie, l'environnement, le logement, et les transports*. https://statistiques.developpement-durable.gouv.fr/la-pollution-de-lair-par-lozone-o3 (October 2, 2022).

Moffet, Ryan, and Kim Prather. 2009. "In-Situ Measurements of the Mixing State and Optical Properties of Soot with Implications for Radiative Forcing Estimates." *Proceedings of the National Academy of Sciences of the United States of America* 106: 11872–77.

Moise, Tamar, J. Michel Flores, and Yinon Rudich. 2015. "Optical Properties of Secondary Organic Aerosols and Their Changes by Chemical Processes." *Chemical Reviews* 115(10): 4400–4439.

Moldanová, J. et al. 2013. "Physical and Chemical Characterisation of PM Emissions from Two Ships Operating in European Emission Control Areas." *Atmospheric Measurement Techniques* 6(12): 3577–96.

Moldanová, Jana et al. 2009. “Characterisation of Particulate Matter and Gaseous Emissions from a Large Ship Diesel Engine.” *Atmospheric Environment* 43(16): 2632–41.

Mortier, Augustin. 2013. “Tendances et Variabilités de l’aérosol Atmosphérique à l’aide Du Couplage Lidar/Photomètre Sur Les Sites de Lille et Dakar.” These de doctorat. Lille 1. https://www.theses.fr/2013LIL10164 (October 3, 2022).

Mortier, Augustin. 2020. “Evaluation of Climate Model Aerosol Trends with Ground-Based Observations over the Last 2 Decades – an AeroCom and CMIP6 Analysis.” *Atmospheric Chemistry and Physics* 20(21): 13355–78.

Moschos, Vaios et al. 2018. “Source Apportionment of Brown Carbon Absorption by Coupling Ultraviolet–Visible Spectroscopy with Aerosol Mass Spectrometry.” *Environmental Science & Technology Letters* 5(6): 302–8.

Moschos, Vaios et al. 2021. “Source-Specific Light Absorption by Carbonaceous Components in the Complex Aerosol Matrix from Yearly Filter-Based Measurements.” *Atmospheric Chemistry and Physics* 21(17): 12809–33.

Müller, T., M. Laborde, G. Kassell, and A. Wiedensohler. 2011. “Design and Performance of a Three-Wavelength LED-Based Total Scatter and Backscatter Integrating Nephelometer.” *Atmospheric Measurement Techniques* 4(6): 1291–1303.

Myhre, G. et al. 2013. “Radiative Forcing of the Direct Aerosol Effect from AeroCom Phase II Simulations.” *Atmospheric Chemistry and Physics* 13(4): 1853–77.

Nee, Jan-Bai et al. 2021. “Optical Properties of Volcanic Aerosols from Eruptions of Nishinoshima Island Observed in Southern Taiwan.” *Applied Optics* 60(15): C8–11.

Ng, N. L. et al. 2011. “An Aerosol Chemical Speciation Monitor (ACSM) for Routine Monitoring of the Composition and Mass Concentrations of Ambient Aerosol.” *Aerosol Science and Technology* 45(7): 780–94.

Ng, Nga Lee et al. 2017. “Nitrate Radicals and Biogenic Volatile Organic Compounds: Oxidation, Mechanisms, and Organic Aerosol.” *Atmospheric Chemistry and Physics* 17(3): 2103–62.

Nøjgaard, Jacob K., Quynh T. Nguyen, Marianne Glasius, and Lise L. Sørensen. 2012. “Nucleation and Aitken Mode Atmospheric Particles in Relation to O3 and NOX at Semirural Background in Denmark.” *Atmospheric Environment* 49: 275–83.

Ortega, Amber M. et al. 2016. “Real-Time Measurements of Secondary Organic Aerosol Formation and Aging from Ambient Air in an Oxidation Flow Reactor in the Los Angeles Area.” *Atmospheric Chemistry and Physics* 16(11): 7411–33.

Paatero, Pentti. 1999. “The Multilinear Engine—A Table-Driven, Least Squares Program for Solving Multilinear Problems, Including the n-Way Parallel Factor Analysis Model.” *Journal of Computational and Graphical Statistics* 8(4): 854–88.

Paatero, Pentti, and Unto Tapper. 1994. “Positive Matrix Factorization: A Non-Negative Factor Model with Optimal Utilization of Error Estimates of Data Values.” *Environmetrics* 5(2): 111–26.

Pandolfi, M., A. Ripoll, X. Querol, and A. Alastuey. 2014. “Climatology of Aerosol Optical Properties and Black Carbon Mass Absorption Cross Section at a Remote High-Altitude Site in the Western Mediterranean Basin.” *Atmospheric Chemistry and Physics* 14(12): 6443–60.

Pandolfi, Marco et al. 2018. “A European Aerosol Phenomenology – 6: Scattering Properties of Atmospheric Aerosol Particles from 28 ACTRIS Sites.” *Atmospheric Chemistry and Physics* 18(11): 7877–7911.

Pani, Shantanu Kumar et al. 2021. “Brown Carbon Light Absorption over an Urban Environment in Northern Peninsular Southeast Asia.” *Environmental Pollution* 276: 116735.

Pappalardo, G. et al. 2014. “EARLINET: Towards an Advanced Sustainable European Aerosol Lidar Network.” *Atmospheric Measurement Techniques* 7(8): 2389–2409.

Penner, Joyce et al. 2001. “Aerosols, Their Direct and Indirect Effects.” *Climate Change 2001: The Scientific Basis. Contribution of Working Group I to the Third Assessment Report of the Intergovernmental Panel on Climate Change, 289-348 (2001).*

Petit, J.-E. et al. 2015. “Two Years of near Real-Time Chemical Composition of Submicron Aerosols in the Region of Paris Using an Aerosol Chemical Speciation Monitor (ACSM) and a Multi-Wavelength Aethalometer.” *Atmospheric Chemistry and Physics* 15(6): 2985–3005.

Petit, Jean-Eudes et al. 2021. “Response of Atmospheric Composition to COVID-19 Lockdown Measures during Spring in the Paris Region (France).” *Atmospheric Chemistry and Physics* 21(22): 17167–83.

Pettersson, Anders et al. 2004. “Measurement of Aerosol Optical Extinction at 532nm with Pulsed Cavity Ring down Spectroscopy.” *Journal of Aerosol Science* 35(8): 995–1011.

Petzold, A. et al. 2010. “Physical Properties, Chemical Composition, and Cloud Forming Potential of Particulate Emissions from a Marine Diesel Engine at Various Load Conditions.” *Environmental Science & Technology* 44(10): 3800–3805.

Pey Betrán, Jorge. 2008. TDX (Tesis Doctorals en Xarxa) “Caracterización fisico-química de los aerosoles atmosféricos en el Mediterráneo Occidental.” Ph.D. Thesis. Universitat Politècnica de Catalunya. http://www.tdx.cat/handle/10803/6992 (October 3, 2022).

Pinxteren, D. van et al. 2016. “Regional Air Quality in Leipzig, Germany: Detailed Source Apportionment of Size-Resolved Aerosol Particles and Comparison with the Year 2000.” *Faraday Discussions* 189(0): 291–315.

van Pinxteren, Dominik et al. 2019. “Trans-Boundary PM10: Quantifying Impact and Sources during Winter 2016/17 in Eastern Germany.” *Atmospheric Environment* 200: 119–30.

Pitchford, Marc et al. 2007. “Revised Algorithm for Estimating Light Extinction from IMPROVE Particle Speciation Data.” *Journal of the Air & Waste Management Association* 57(11): 1326–36.

Ponczek, Milena et al. 2021. “Linking Chemical Composition and Optical Properties of Biomass Burning Aerosols in Amazonia.” *Environmental Science: Atmospheres*. https://pubs.rsc.org/en/content/articlelanding/2022/ea/d1ea00055a (January 18, 2022).

Pöschl, Ulrich. 2005. “Atmospheric Aerosols: Composition, Transformation, Climate and Health Effects.” *Angewandte Chemie International Edition* 44(46): 7520–40.

Potier, E. et al. 2019. “Characterizing the Regional Contribution to PM10 Pollution over Northern France Using Two Complementary Approaches: Chemistry Transport and Trajectory-Based Receptor Models.” *Atmospheric Research* 223: 1–14.

Poulain, Laurent et al. 2021. “Source Apportionment and Impact of Long-Range Transport on Carbonaceous Aerosol Particles in Central Germany during HCCT-2010.” *Atmospheric Chemistry and Physics* 21(5): 3667–84.

Pratt, Kerri A., and Kimberly A. Prather. 2012. “Mass Spectrometry of Atmospheric Aerosols—Recent Developments and Applications. Part I: Off-Line Mass Spectrometry Techniques.” *Mass Spectrometry Reviews* 31(1): 1–16.

Pratt, Kerri A., and Kimberly A. Prather. 2012. “Mass Spectrometry of Atmospheric Aerosols—Recent Developments and Applications. Part II: On-Line Mass Spectrometry Techniques.” *Mass Spectrometry Reviews* 31(1): 17–48.

Pu, Wei et al. 2017. “Properties of Black Carbon and Other Insoluble Light-Absorbing Particles in Seasonal Snow of Northwestern China.” *The Cryosphere* 11(3): 1213–33.

Putaud, J. -P. et al. 2010. “A European Aerosol Phenomenology – 3: Physical and Chemical Characteristics of Particulate Matter from 60 Rural, Urban, and Kerbside Sites across Europe.” *Atmospheric Environment* 44(10): 1308–20.

Putaud, Jean-P et al. 2004. “A European Aerosol Phenomenology—2: Chemical Characteristics of Particulate Matter at Kerbside, Urban, Rural and Background Sites in Europe.” *Atmospheric Environment* 38(16): 2579–95.

Qin, Xueying et al. 2012. “Seasonal Comparisons of Single-Particle Chemical Mixing State in Riverside, CA.” *Atmospheric Environment* 59: 587–96.

Qin, Yi Ming et al. 2018. “Chemical Characteristics of Brown Carbon in Atmospheric Particles at a Suburban Site near Guangzhou, China.” *Atmospheric Chemistry and Physics* 18(22): 16409–18.

Quinn, P. K. et al. 2004. “Aerosol Optical Properties Measured on Board the Ronald H. Brown during ACE-Asia as a Function of Aerosol Chemical Composition and Source Region.” *Journal of Geophysical Research: Atmospheres* 109(D19). https://onlinelibrary.wiley.com/doi/abs/10.1029/2003JD004010 (October 10, 2022).

Ramana, M. V. et al. 2010. “Warming Influenced by the Ratio of Black Carbon to Sulphate and the Black-Carbon Source.” *Nature Geoscience* 3(8): 542–45.

Rao, Xiaoquan, Priti Patel, Robin Puett, and Sanjay Rajagopalan. 2015. “Air Pollution as a Risk Factor for Type 2 Diabetes.” *Toxicological Sciences* 143(2): 231–41.

Reche, C. et al. 2011. “New Considerations for PM, Black Carbon and Particle Number Concentration for Air Quality Monitoring across Different European Cities.” *Atmospheric Chemistry and Physics* 11(13): 6207–27.

Rega, Carlo, Chris Short, Marta Pérez-Soba, and Maria Luisa Paracchini. 2020. “A Classification of European Agricultural Land Using an Energy-Based Intensity Indicator and Detailed Crop Description.” *Landscape and Urban Planning* 198: 103793.

Rind, D., N. K. Balachandran, and R. Suozzo. 1992. “Climate Change and the Middle Atmosphere. Part II: The Impact of Volcanic Aerosols.” *Journal of Climate* 5(3): 189–208.

Roig Rodelas, Roger, Abhishek Chakraborty, et al. 2019. “Real-Time Assessment of Wintertime Organic Aerosol Characteristics and Sources at a Suburban Site in Northern France.” *Atmospheric Environment* 203: 48–61.

Roig Rodelas, Roger, Esperanza Perdrix, Benoît Herbin, and Véronique Riffault. 2019. “Characterization and Variability of Inorganic Aerosols and Their Gaseous Precursors at a Suburban Site in Northern France over One Year (2015–2016).” *Atmospheric Environment* 200: 142–57.

Romano, Salvatore et al. 2019. “Optical Properties of PM2.5 Particles: Results from a Monitoring Campaign in Southeastern Italy.” *Atmospheric Environment* 203: 35–47.

Romonosky, Dian E. et al. 2016. “Effective Absorption Cross Sections and Photolysis Rates of Anthropogenic and Biogenic Secondary Organic Aerosols.” *Atmospheric Environment* C(130): 172–79.

Ryan, Patrick A., Doug Lowenthal, and Naresh Kumar. 2005. “Improved Light Extinction Reconstruction in Interagency Monitoring of Protected Visual Environments.” *Journal of the Air & Waste Management Association* 55(11): 1751–59.

de Sá, Suzane S. et al. 2019. “Contributions of Biomass-Burning, Urban, and Biogenic Emissions to the Concentrations and Light-Absorbing Properties of Particulate Matter in Central Amazonia during the Dry Season.” *Atmospheric Chemistry and Physics* 19(12): 7973–8001.

Saha, Auromeet et al. 2008. “One Year Measurements of Aerosol Optical Properties over an Urban Coastal Site: Effect on Local Direct Radiative Forcing.” *Atmospheric Research* 90(2–4): 195–202.

Saide, Pablo E. et al. 2015. “Revealing Important Nocturnal and Day-to-Day Variations in Fire Smoke Emissions through a Multiplatform Inversion.” *Geophysical Research Letters* 42(9): 3609–18.

Saide, Pablo E. et al. 2022. “Understanding the Evolution of Smoke Mass Extinction Efficiency Using Field Campaign Measurements.” *Geophysical Research Letters* 49(18): e2022GL099175.

Saleh, R. et al. 2013. “Absorptivity of Brown Carbon in Fresh and Photo-Chemically Aged Biomass-Burning Emissions.” *Atmospheric Chemistry and Physics* 13(15): 7683–93.

Saleh, Rawad. 2020. “From Measurements to Models: Toward Accurate Representation of Brown Carbon in Climate Calculations.” *Current Pollution Reports* 6(2): 90–104.

Sandradewi, Jisca et al. 2008. “Using Aerosol Light Absorption Measurements for the Quantitative Determination of Wood Burning and Traffic Emission Contributions to Particulate Matter.” *Environmental Science & Technology* 42(9): 3316–23.

Sareen, N. et al. 2010. “Secondary Organic Material Formed by Methylglyoxal in Aqueous Aerosol Mimics.” *Atmospheric Chemistry and Physics* 10(3): 997–1016.

Satish, Rangu et al. 2017. “Temporal Characteristics of Brown Carbon over the Central Indo-Gangetic Plain.” *Environmental Science & Technology* 51(12): 6765–72.

Saturno, Jorge et al. 2018. “Black and Brown Carbon over Central Amazonia: Long-Term Aerosol Measurements at the ATTO Site.” *Atmospheric Chemistry and Physics* 18(17): 12817–43.

Schagen, Ian. 2006. “The Use of Standardized Residuals to Derive Value-added Measures of School Performance.” *Educational Studies* 32(2): 119–32.

Sciare, J. et al. 2005. “Aerosol Mass Closure and Reconstruction of the Light Scattering Coefficient over the Eastern Mediterranean Sea during the MINOS Campaign.” *Atmospheric Chemistry and Physics* 5(8): 2253–65.

Sciare, Jean et al. 2011. “Large Contribution of Water-Insoluble Secondary Organic Aerosols in the Region of Paris (France) during Wintertime.” *Journal of Geophysical Research: Atmospheres* 116(D22). https://onlinelibrary.wiley.com/doi/abs/10.1029/2011JD015756 (October 21, 2022).

Segura, S. et al. 2014. “Determination and Analysis of in Situ Spectral Aerosol Optical Properties by a Multi-Instrumental Approach.” *Atmospheric Measurement Techniques* 7(8): 2373–87.

Segura, S. et al. 2016. “Multiyear In-Situ Measurements of Atmospheric Aerosol Absorption Properties at an Urban Coastal Site in Western Mediterranean.” *Atmospheric Environment* 129: 18–26.

Seinfeld, John H., and Spyros N. Pandis. 2012. *Atmospheric Chemistry and Physics: From Air Pollution to Climate Change*. John Wiley & Sons.

Selimovic, Vanessa, Robert J. Yokelson, Gavin R. McMeeking, and Sarah Coefield. 2019. “In Situ Measurements of Trace Gases, PM, and Aerosol Optical Properties during the 2017 NW US Wildfire Smoke Event.” *Atmospheric Chemistry and Physics* 19(6): 3905–26.

Sellitto, Pasquale et al. 2020. “Small-Scale Volcanic Aerosols Variability, Processes and Direct Radiative Impact at Mount Etna during the EPL-RADIO Campaigns.” *Scientific Reports* 10(1): 15224.

Shah, Viral et al. 2020. “Effect of Changing NO_x Lifetime on the Seasonality and Long-Term Trends of Satellite-Observed Tropospheric NO_2 Columns over China.” *Atmospheric Chemistry and Physics* 20(3): 1483–95.

Sicard, Pierre. 2021. “Ground-Level Ozone over Time: An Observation-Based Global Overview.” *Current Opinion in Environmental Science & Health* 19: 100226.

Sipilä, Mikko et al. 2010. “The Role of Sulfuric Acid in Atmospheric Nucleation.” *Science* 327(5970): 1243–46.

Sippula, O. et al. 2014. “Particle Emissions from a Marine Engine: Chemical Composition and Aromatic Emission Profiles under Various Operating Conditions.” *Environmental Science & Technology* 48(19): 11721–29.

Sloane, Christine S., and George T. Wolff. 1985. “Prediction of Ambient Light Scattering Using a Physical Model Responsive to Relative Humidity: Validation with Measurements from Detroit.” *Atmospheric Environment (1967)* 19(4): 669–80.

Smirnov, A. et al. 2000. “Cloud-Screening and Quality Control Algorithms for the AERONET Database.” *Remote Sensing of Environment* 73(3): 337–49.

Smirnov, A. et al. 2002. “Diurnal Variability of Aerosol Optical Depth Observed at AERONET (Aerosol Robotic Network) Sites.” *Geophysical Research Letters* 29(23): 30-1-30–34.

Solomon, S., D et al. 2007. “Contribution of Working Group I to the Fourth Assessment Report of the Intergovernmental Panel on Climate Change, 2007.” https://www.ipcc.ch/report/ar4/wg1/ (June 15, 2022).

Stanaway, Jeffrey D. et al. 2018. “Global, Regional, and National Comparative Risk Assessment of 84 Behavioural, Environmental and Occupational, and Metabolic Risks or Clusters of Risks for 195 Countries and Territories, 1990–2017: A Systematic Analysis for the Global Burden of Disease Study 2017.” *The Lancet* 392(10159): 1923–94.

Stein, A. F. et al. 2015. “NOAA’s HYSPLIT Atmospheric Transport and Dispersion Modeling System.” *Bulletin of the American Meteorological Society* 96(12): 2059–77.

Stocker, T.F. et al. 2013. “IPCC, 2013: Climate Change 2013: The Physical Science Basis. Contribution of Working Group I to the Fifth Assessment Report of the Intergovernmental Panel on Climate Change.” https://www.ipcc.ch/report/ar5/wg1/ (September 30, 2021).

Stockwell, C. E., P. R. Veres, J. Williams, and R. J. Yokelson. 2015. “Characterization of Biomass Burning Emissions from Cooking Fires, Peat, Crop Residue, and Other Fuels with High-Resolution Proton-Transfer-Reaction Time-of-Flight Mass Spectrometry.” *Atmospheric Chemistry and Physics* 15(2): 845–65.

Sumlin, Benjamin J. et al. 2018. “Correction to Atmospheric Photooxidation Diminishes Light Absorption by Primary Brown Carbon Aerosol from Biomass Burning.” *Environmental Science & Technology Letters* 5(3): 193–193.

Sun, Jiaxing et al. 2021. “Light Absorption of Black Carbon and Brown Carbon in Winter in North China Plain: Comparisons between Urban and Rural Sites.” *Science of The Total Environment* 770: 144821.

Swietlicki, E. et al. 2008. “Hygroscopic Properties of Submicrometer Atmospheric Aerosol Particles Measured with H-TDMA Instruments in Various Environments—a Review.” *Tellus B: Chemical and Physical Meteorology* 60(3): 432–69.

Tao, Jun, Leiming Zhang, Junji Cao, et al. 2014. “Characterization and Source Apportionment of Aerosol Light Extinction in Chengdu, Southwest China.” *Atmospheric Environment* Complete(95): 552–62.

Tao, Jun, Leiming Zhang, Kinfai Ho, et al. 2014. “Impact of PM2.5 Chemical Compositions on Aerosol Light Scattering in Guangzhou — the Largest Megacity in South China.” *Atmospheric Research* 135–136: 48–58.

Tao, Jun et al. 2020. “High Mass Absorption Efficiency of Carbonaceous Aerosols during the Biomass Burning Season in Chiang Mai of Northern Thailand.” *Atmospheric Environment* 240: 117821.

Tarín-Carrasco, Patricia et al. 2021. “Contribution of Fine Particulate Matter to Present and Future Premature Mortality over Europe: A Non-Linear Response.” *Environment International* 153: 106517.

Tasoglou, Antonios, Georges Saliba, R. Subramanian, and Spyros N. Pandis. 2017. “Absorption of Chemically Aged Biomass Burning Carbonaceous Aerosol.” *Journal of Aerosol Science* 113: 141–52.

Taylor, Jonathan W. et al. 2020. “Absorption Closure in Highly Aged Biomass Burning Smoke.” *Atmospheric Chemistry and Physics* 20(19): 11201–21.

Teich, Monique et al. 2017. “Contributions of Nitrated Aromatic Compounds to the Light Absorption of Water-Soluble and Particulate Brown Carbon in Different Atmospheric Environments in Germany and China.” *Atmospheric Chemistry and Physics* 17(3): 1653–72.

Textor, Christiane, Hans-F. Graf, Michael Herzog, and J. M. Oberhuber. 2003. “Injection of Gases into the Stratosphere by Explosive Volcanic Eruptions.” *Journal of Geophysical Research: Atmospheres* 108(D19). https://onlinelibrary.wiley.com/doi/abs/10.1029/2002JD002987 (August 3, 2022).

Thunis, P. et al. 2016. “On the Design and Assessment of Regional Air Quality Plans: The SHERPA Approach.” *Journal of Environmental Management* 183: 952–58.

Tian, Pengfei et al. 2018. “Radiative Absorption Enhancement of Dust Mixed with Anthropogenic Pollution over East Asia.” *Atmospheric Chemistry and Physics* 18(11): 7815–25.

Titos, G. et al. 2012. “Optical Properties and Chemical Composition of Aerosol Particles at an Urban Location: An Estimation of the Aerosol Mass Scattering and Absorption Efficiencies.” *Journal of Geophysical Research: Atmospheres* 117(D4). https://onlinelibrary.wiley.com/doi/abs/10.1029/2011JD016671 (January 19, 2022).

Toledano, C. et al. 2007. “Aerosol optical depth and Ångström exponent climatology at El Arenosillo AERONET site (Huelva, Spain).” *Quarterly Journal of the Royal Meteorological Society* 133(624): 795–807.

Tröstl, Jasmin et al. 2016. “The Role of Low-Volatility Organic Compounds in Initial Particle Growth in the Atmosphere.” *Nature* 533(7604): 527–31.

Ulbrich, I. M. et al. 2009. “Interpretation of Organic Components from Positive Matrix Factorization of Aerosol Mass Spectrometric Data.” *Atmospheric Chemistry and Physics* 9(9): 2891–2918.

Updyke, Katelyn M., Tran B. Nguyen, and Sergey A. Nizkorodov. 2012. “Formation of Brown Carbon via Reactions of Ammonia with Secondary Organic Aerosols from Biogenic and Anthropogenic Precursors.” *Atmospheric Environment* 63: 22–31.

Valentini, S. et al. 2018. “Tailored Coefficients in the Algorithm to Assess Reconstructed Light Extinction at Urban Sites: A Comparison with the IMPROVE Revised Approach.” *Atmospheric Environment* 172: 168–76.

Valentini, S. et al. 2020. “Classifying Aerosol Particles through the Combination of Optical and Physical-Chemical Properties: Results from a Wintertime Campaign in Rome (Italy).” *Atmospheric Research* 235: 104799.

Vallius, Marko J., Juhani Ruuskanen, Aadu Mirme, and Juha Pekkanen. 2000. “Concentrations and Estimated Soot Content of PM1, PM2.5, and PM10 in a Subarctic Urban Atmosphere.” *Environmental Science & Technology* 34(10): 1919–25.

Van de Huslt, H.C. 1957. “Light Scattering by Small Particles par Van de Hulst, H.C.: Hardcover (1957) | Second Story Books, ABAA.” https://www.abebooks.fr/Light-Scattering-Small-Particles-Hulst-H.C/31086362817/bd (October 11, 2022).

Velazquez Garcia, Alejandra et al. 2022. “Proceedings of Abstracts 13th International Conference on Air Quality: Science and Application.” : 104.

Vestreng, V. et al. 2007. “Twenty-Five Years of Continuous Sulphur Dioxide Emission Reduction in Europe.” *Atmospheric Chemistry and Physics Discussions* 7(2): 5099–5143.

Viana, Mar et al. 2009. “Chemical Tracers of Particulate Emissions from Commercial Shipping.” *Environmental Science & Technology* 43(19): 7472–77.

Vrekoussis, M. et al. 2005. “Seasonal Variability of Optical Properties of Aerosols in the Eastern Mediterranean.” *Atmospheric Environment* 39(37): 7083–94.

Waked, A. et al. 2014. “Source Apportionment of PM_{10} in a North-Western Europe Regional Urban Background Site (Lens, France) Using Positive Matrix Factorization and Including Primary Biogenic Emissions.” *Atmospheric Chemistry and Physics* 14(7): 3325–46.

Waked, Antoine et al. 2018. “Investigation of the Geographical Origins of PM10 Based on Long, Medium and Short-Range Air Mass Back-Trajectories Impacting Northern France during the Period 2009–2013.” *Atmospheric Environment* 193: 143–52.

Wang, Peng et al. 2017. “Trends and Variability in Aerosol Optical Depth over North China from MODIS C6 Aerosol Products during 2001–2016.” *Atmosphere* 8(11): 223.

Wang, Qingqing et al. 2015. “Chemical Composition of Aerosol Particles and Light Extinction Apportionment before and during the Heating Season in Beijing, China.” *Journal of Geophysical Research: Atmospheres* 120(24): 12708–22.

Wang, Qiyuan et al. 2018. “Sources and Physicochemical Characteristics of Black Carbon Aerosol from the Southeastern Tibetan Plateau: Internal Mixing Enhances Light Absorption.” *Atmospheric Chemistry and Physics* 18(7): 4639–56.

Wang, Qiyuan et al. 2019. “High Contribution of Secondary Brown Carbon to Aerosol Light Absorption in the Southeastern Margin of Tibetan Plateau.” *Geophysical Research Letters* 46(9): 4962–70.

Wang, Shuo et al. 2021. “Real-Time Retrieval of Aerosol Chemical Composition Using Effective Density and the Imaginary Part of Complex Refractive Index.” *Atmospheric Environment* 245: 117959.

Wang, Xiaofei et al. 2017. “The Role of Jet and Film Drops in Controlling the Mixing State of Submicron Sea Spray Aerosol Particles.” *Proceedings of the National Academy of Sciences* 114(27): 6978–83.

Wang, Xin et al. 2017. “Observations and Model Simulations of Snow Albedo Reduction in Seasonal Snow Due to Insoluble Light-Absorbing Particles during 2014 Chinese Survey.” *Atmospheric Chemistry and Physics* 17(3): 2279–96.

Wang, Xuan et al. 2016. “Deriving Brown Carbon from Multiwavelength Absorption Measurements: Method and Application to AERONET and Aethalometer Observations.” *Atmospheric Chemistry and Physics* 16(19): 12733–52.

Washenfelder, R. A. et al. 2015. “Biomass Burning Dominates Brown Carbon Absorption in the Rural Southeastern United States.” *Geophysical Research Letters* 42(2): 653–64.

Watson, John G. 2002. “Visibility: Science and Regulation.” *Journal of the Air & Waste Management Association* 52(6): 628–713.

von der Weiden, S.-L., F. Drewnick, and S. Borrmann. 2009. “Particle Loss Calculator – a New Software Tool for the Assessment of the Performance of Aerosol Inlet Systems.” *Atmospheric Measurement Techniques* 2(2): 479–94.

Weingartner, E. et al. 2003. “Absorption of Light by Soot Particles: Determination of the Absorption Coefficient by Means of Aethalometers.” *Journal of Aerosol Science* 34(10): 1445–63.

Weinzierl, Bernadett et al. 2011. “Microphysical and Optical Properties of Dust and Tropical Biomass Burning Aerosol Layers in the Cape Verde Region—an Overview of the Airborne in Situ and Lidar Measurements during SAMUM-2.” *Tellus B: Chemical and Physical Meteorology* 63(4): 589–618.

White, Warren H., Edward S. Macias, Robert C. Nininger, and David Schorran. 1994. “Size-Resolved Measurements of Light Scattering by Ambient Particles in the Southwestern U.S.A.” *Atmospheric Environment* 28(5): 909–21.

Wiedensohler, A. et al. 2012. “Mobility Particle Size Spectrometers: Harmonization of Technical Standards and Data Structure to Facilitate High Quality Long-Term Observations of Atmospheric Particle Number Size Distributions.” *Atmospheric Measurement Techniques* 5(3): 657–85.

Wong, Jenny P. S. et al. 2019. “Atmospheric Evolution of Molecular-Weight-Separated Brown Carbon from Biomass Burning.” *Atmospheric Chemistry and Physics* 19(11): 7319–34.

Wong, Jenny P. S., Athanasios Nenes, and Rodney J. Weber. 2017. “Changes in Light Absorptivity of Molecular Weight Separated Brown Carbon Due to Photolytic Aging.” *Environmental Science & Technology* 51(15): 8414–21.

Woolf, David K., Peter A. Bowyer, and Edward C. Monahan. 1987. “Discriminating between the Film Drops and Jet Drops Produced by a Simulated Whitecap.” *Journal of Geophysical Research: Oceans* 92(C5): 5142–50.

World Health Organization. 2021. *COP26 Special Report on Climate Change and Health: The Health Argument for Climate Action*. Geneva: World Health Organization. https://apps.who.int/iris/handle/10665/346168 (September 26, 2022).

World Health Organization. 2022. “Exposure & Health Impacts of Air Pollution.” https://www.who.int/teams/environment-climate-change-and-health/air-quality-and-health/health-impacts/exposure-air-pollution (September 26, 2022).

World Meteorological Organization, World Meteorological Organization, and Global Atmosphere Watch. 2016. *WMO/GAW Aerosol Measurement Procedures: Guidelines and Recommendations.*

Xu, Ruixin, Mohammed S. Alam, Christopher Stark, and Roy M. Harrison. 2020. “Behaviour of Traffic Emitted Semi-Volatile and Intermediate Volatility Organic Compounds within the Urban Atmosphere.” *Science of The Total Environment* 720: 137470.

Xu, Xiaofeng et al. 2020. “Aerosol Optical Properties at Seven AERONET Sites over Middle East and Eastern Mediterranean Sea.” *Atmospheric Environment* 243: 117884.

Xu, Zhenzhu, Yanling Jiang, and Guangsheng Zhou. 2016. “Nitrogen Cycles in Terrestrial Ecosystems: Climate Change Impacts and Mitigation.” *Environmental Reviews* 24(2): 132–43.

Yang, Mingxi et al. 2020. “Temporal and Spatial Trends in Aerosols near the English Channel – An Air Quality Success Story?” *Atmospheric Environment: X* 6: 100074.

Yang, Yang et al. 2020. “Trends and Source Apportionment of Aerosols in Europe during 1980–2018.” *Atmospheric Chemistry and Physics* 20(4): 2579–90.

Yao, TingTing et al. 2010. “High Time Resolution Observation and Statistical Analysis of Atmospheric Light Extinction Properties and the Chemical Speciation of Fine Particulates.” *Science China Chemistry* 53(8): 1801–8.

Yttri, Karl Espen et al. 2020. “1 Trends, Composition, and Sources of Carbonaceous Aerosol in 2 the Last 18 Years at the Birkenes Observatory, Northern Europe.” : 45.

Yu, H., C. Wu, D. Wu, and J. Z. Yu. 2010. “Size Distributions of Elemental Carbon and Its Contribution to Light Extinction in Urban and Rural Locations in the Pearl River Delta Region, China.” *Atmospheric Chemistry and Physics* 10(11): 5107–19.

Yuan, Cheng et al. 2020. “Significant Restructuring and Light Absorption Enhancement of Black Carbon Particles by Ammonium Nitrate Coating.” *Environmental Pollution* 262: 114172.

Yuan, Chung-Shin et al. 2006. “Correlation of Atmospheric Visibility with Chemical Composition of Kaohsiung Aerosols.” *Atmospheric Research* 82(3): 663–79.

Yue, Wei et al. 2008. “Source Apportionment of Ambient Fine Particle Size Distribution Using Positive Matrix Factorization in Erfurt, Germany.” *Science of The Total Environment* 398(1): 133–44.

Yus-Díez, Jesús et al. 2022. “Absorption Enhancement of Black Carbon Particles in a Mediterranean City and Countryside: Effect of Particulate Matter Chemistry, Ageing and Trend Analysis.” *Atmospheric Chemistry and Physics* 22(13): 8439–56.

Zanatta, M. et al. 2016. “A European Aerosol Phenomenology-5: Climatology of Black Carbon Optical Properties at 9 Regional Background Sites across Europe.” *Atmospheric Environment* 145: 346–64.

Zhan, Junlei et al. 2021. “Ozone and SOA Formation Potential Based on Photochemical Loss of VOCs during the Beijing Summer.” *Environmental Pollution* 285: 117444.

Zhang, Q. et al. 2007. “Ubiquity and Dominance of Oxygenated Species in Organic Aerosols in Anthropogenically-Influenced Northern Hemisphere Midlatitudes.” *Geophysical Research Letters* 34(13). https://onlinelibrary.wiley.com/doi/abs/10.1029/2007GL029979 (October 8, 2022).

Zhang, Qi et al. 2005. “Deconvolution and Quantification of Hydrocarbon-like and Oxygenated Organic Aerosols Based on Aerosol Mass Spectrometry.” *Environmental Science & Technology* 39(13): 4938–52.

Zhang, Qi et al. 2011. “Understanding Atmospheric Organic Aerosols via Factor Analysis of Aerosol Mass Spectrometry: A Review.” *Analytical and Bioanalytical Chemistry* 401(10): 3045–67.

Zhang, Qian et al. 2019. “Optical Properties and Source Identification of Black Carbon and Brown Carbon: Comparison of Winter and Summer Haze Episodes in Xi’an, Northwest China.” *Environmental Science: Processes & Impacts* 21(12): 2058–69.

Zhang, Shouwen. 2016. “Analyse Dynamique, En Champ Proche et à Résolution Temporelle Fine, de l’aérosol Submicronique En Situation Urbaine Sous Influence Industrielle.” These de doctorat. Littoral. https://www.theses.fr/2016DUNK0436 (October 1, 2022).

Zhang, Shouwen. 2021. “Near Real-Time PM1 Chemical Composition Measurements at a French Urban Background and Coastal Site under Industrial Influence over More than a Year: Temporal Variability and Assessment of Sulfur-Containing Emissions.” *Atmospheric Environment* 244: 117960.

Zhang, Xiaolin et al. 2021. “Lensing Effect of Black Carbon With Brown Coatings: Dominant Microphysics and Parameterization.” *Journal of Geophysical Research: Atmospheres* 126(3): e2020JD033549.

Zhang, Xiaolin, Mao Mao, Yan Yin, and Shihao Tang. 2020. “The Absorption Ångstrom Exponent of Black Carbon with Brown Coatings: Effects of Aerosol Microphysics and Parameterization.” *Atmospheric Chemistry and Physics* 20(16): 9701–11.

Zhang, Yunjiang et al. 2019. “Six-Year Source Apportionment of Submicron Organic Aerosols from near-Continuous Highly Time-Resolved Measurements at SIRTA (Paris Area, France).” *Atmospheric Chemistry and Physics* 19(23): 14755–76.

Zhang, Yunjiang et al. 2020. “Substantial Brown Carbon Emissions from Wintertime Residential Wood Burning over France.” *Science of The Total Environment* 743: 140752.

Zhao, Chuanfeng et al. 2019. “Estimating the Contribution of Local Primary Emissions to Particulate Pollution Using High-Density Station Observations.” *Journal of Geophysical Research: Atmospheres* 124(3): 1648–61.

Zhao, R. et al. 2015. “Photochemical Processing of Aqueous Atmospheric Brown Carbon.” *Atmospheric Chemistry and Physics* 15(11): 6087–6100.

Zhao, Xiaoxi, Kan Huang, Joshua S. Fu, and Sabur F. Abdullaev. 2022. “Long-Range Transport of Asian Dust to the Arctic: Identification of Transport Pathways, Evolution of Aerosol Optical Properties, and Impact Assessment on Surface Albedo Changes.” *Atmospheric Chemistry and Physics* 22(15): 10389–407.

Zhong, M., and M. Jang. 2014. “Dynamic Light Absorption of Biomass-Burning Organic Carbon Photochemically Aged under Natural Sunlight.” *Atmospheric Chemistry and Physics* 14(3): 1517–25.

Zhou, Yaqing et al. 2019. “Exploring the Impact of Chemical Composition on Aerosol Light Extinction during Winter in a Heavily Polluted Urban Area of China.” *Journal of Environmental Management* 247: 766–75.

Zhu, Chong-Shu et al. 2015. “The Optical Properties of Urban Aerosol in Northern China: A Case Study at Xi’an.” *Atmospheric Research* 160: 59–67.

Zhu, Chong-Shu et al. 2021. “High Light Absorption and Radiative Forcing Contributions of Primary Brown Carbon and Black Carbon to Urban Aerosol.” *Gondwana Research* 90: 159–64.

Zhuang, Goushan, Zhen Yi, Robert A. Duce, and Phyllis R. Brown. 1992. “Chemistry of Iron in Marine Aerosols.” *Global Biogeochemical Cycles* 6(2): 161–73.

Zotter, Peter et al. 2017. “Evaluation of the Absorption Ångström Exponents for Traffic and Wood Burning in the Aethalometer-Based Source Apportionment Using Radiocarbon Measurements of Ambient Aerosol.” *Atmospheric Chemistry and Physics* 17(6): 4229–49.

Annex 0: Scientific valorization

Articles in peer-reviewed journals

1. S. CRUMEYROLLE, J. KONTKANEN, C. ROSE, E. BOURRIANNE, V. RIFFAULT, E. TISON, J. BRITO, **A. VELAZQUEZ-GARCIA**, M. CATALFAMO, N. FERLAY, F. AURIOL, I. CHIAPELLO, Measurement report: Atmospheric new particle formation in a peri-urban site in Lille, Northern France, Atmos. Chem. Phys., 23, 183–201. https://doi.org/10.5194/acp-23-183-2023, 2023.
2. **VELAZQUEZ-GARCIA A**., CRUMEYROLLE S., F. DE BRITO J., TISON E., BOURRIANNE E., CHIAPELLO I., RIFFAULT V., Deriving composition-dependent aerosol absorption, scattering and extinction mass efficiencies from multi-annual observations in Northern France, Atmospheric Environment, 298: 119613. https://doi.org/10.1016/j.atmosenv.2023.119613, 2023.
3. **VELAZQUEZ-GARCIA A**., F. DE BRITO J., CRUMEYROLLE S., CHIAPELLO I., RIFFAULT V., Studying light-absorbing aerosols properties in Northern France through combined in-situ observations, emission inventory, and individual back-trajectory analyses, *in preparation*.

International conferences

1. **VELAZQUEZ-GARCIA A.**, CRUMEYROLLE S., F. DE BRITO J., TISON E., BOURRIANNE E., CHIAPELLO I., RIFFAULT V., Deriving composition-dependent absorption, scattering and extinction mass efficiencies at the ATOLL platform in Northern France, Oral presentation, European Aerosol Conference, Online, 30-3 September 2021.
2. **VELAZQUEZ-GARCIA A.**, CRUMEYROLLE S., F. DE BRITO J., TISON E., BOURRIANNE E., CHIAPELLO I., RIFFAULT V., Linking long-term aerosol chemical composition and optical properties measured at the ATOLL platform in Lille, Northern France, Oral presentation, 1st ACTRIS Science Conference, Online, 11-13 May 2022.
3. S. CRUMEYROLLE, J. KONTKANEN, C. ROSE, E. BOURRIANNE, V. RIFFAULT, E. TISON, J. DE BRITO, **A. VELAZQUEZ-GARCIA**, M. CATALFAMO, N. FERLAY, F. AURIOL, I. CHIAPELLO, New Particle Formation observed in the close vicinity of a French megalopolis, Poster, 1st ACTRIS Science Conference, Online, 11-13 May 2022.
4. **VELAZQUEZ-GARCIA A**., CHEBAICHEB H., F. DE BRITO J., TISON E., CRUMEYROLLE S., FAVEZ O., CHIAPELLO I., RIFFAULT V., Multi-annual source apportionment and absorbing properties of organic aerosols in Northern France, Oral presentation, 13th International Conference on Air Quality, Thessaloniki, Greece, 27 June-1 July 2022.
5. **VELAZQUEZ-GARCIA A.**, F. DE BRITO J., CRUMEYROLLE S., TISON E., BOURRIANNE E., CHIAPELLO I., RIFFAULT V., Studying light-absorbing aerosols properties in Northern France through combined in-situ observations, emission inventory, and individual back-trajectory analyses, Poster, International Aerosol Conference, Athens, Greece, 4-9 September 2022.

Other communications

1. V. RIFFAULT, S. CRUMEYROLLE, **A. VELAZQUEZ-GARCIA**, E. TISON, J. BRITO, I. CHIAPELLO, Lille observations Spatial representativeness of the site and physical, chemical and optical properties of the PM_1 fraction, Oral presentation, Workshop virtuel des acteurs et utilisateurs d'ACTRIS-FR, 10-13 November 2020.
2. **VELAZQUEZ-GARCIA A.**, CRUMEYROLLE S., F. DE BRITO J., TISON E., BOURRIANNE E., CHIAPELLO I., RIFFAULT V., Study of particle pollution in the Lille area by combining chemical and optical observations, Oral presentation, Journée des doctorants du Laboratoire d'Optique Atmosphérique, Villeneuve d'Ascq, France, 14 December 2020.
3. **VELAZQUEZ-GARCIA A.,** CRUMEYROLLE S., F. DE BRITO J., TISON E., BOURRIANNE E., CHIAPELLO I., RIFFAULT V., Deriving composition-dependent absorption, scattering and extinction mass efficiencies from multi-annual observations in Northern France, Oral presentation, Demi-journée doctorant.e.s CaPPA, Villeneuve d'Ascq, France, 7-9 September 2021.
4. **VELAZQUEZ-GARCIA A.,** CRUMEYROLLE S., F. DE BRITO J., TISON E., BOURRIANNE E., CHIAPELLO I., RIFFAULT V., Aerosol optical properties and chemical properties at the ATOLL site, Oral presentation, Journée scientifique du Labex CaPPA, Villeneuve d'Ascq, France, 10 March 2022.
5. **VELAZQUEZ-GARCIA A**., CRUMEYROLLE S., F. DE BRITO J., TISON E., BOURRIANNE E., CHIAPELLO I., RIFFAULT V., Studying light-absorbing aerosols properties in Northern France through combined in-situ observations, emission inventory, and individual back-trajectory analyses, Poster, Workshop ACTRIS-FR, Autrans, France, 10-13 October 2022.

Atmospheric Environment 298 (2023) 119613

Contents lists available at ScienceDirect

Atmospheric Environment

journal homepage: www.elsevier.com/locate/atmosenv

Deriving composition-dependent aerosol absorption, scattering and extinction mass efficiencies from multi-annual high time resolution observations in Northern France

A. Velazquez-Garcia [a,b,**], S. Crumeyrolle [b,*], J.F. de Brito [a], E. Tison [a], E. Bourrianne [b], I. Chiapello [b], V. Riffault [a]

[a] *IMT Nord Europe, Institut Mines-T´el´ecom, Universit´e de Lille, Centre for Energy and Environment, 59000, Lille, France*

[b] *LOA-Laboratoire d'Optique Atmosph´erique, CNRS, UMR 8518, Univ. Lille, 59000, Lille, France*

HIGHLIGHTS

- High time resolution in situ measurements from a French suburban ACTRIS site.
- Ammonium nitrate dominates the PM_1 fraction during spring.
- Low average value of the Single Scattering Albedo in PM_1 at 0.77
- Carbonaceous aerosols dominate (50%) the extinction in the visible range.
- Organics contribute 22% to absorption in the near UV-range.

ARTICLE INFO

Keywords:
PM_1
Urban sites
Optical properties
Chemical properties
Aerosol mass efficiencies
Brown carbon

ABSTRACT

The wide range of sources and complex (trans)formation processes of aerosol particles lead to strong spatial and temporal variability in their physical, chemical and optical properties. Their accurate representation is essential to assess their impacts, notably on climate. Here, we investigate for the first time the aerosol optical propeérties and their relation to fine particle chemical composition in Northern France, based on a multi-annual in situ dataset. Real-time submicron aerosol measurements at the ATOLL (ATmospheric Observations in liLLe) site have shown that ammonium nitrate contributes about 36% of the total mass, being the predominant species regarding the extinction at 525 nm (35%). Yet, organics are responsible for 22% of the absorption in the UV range (370 nm), pointing at a significant contribution of Brown Carbon. Furthermore, our study highlights the need for site- specific values to correctly assess the impact of different aerosol species on extinction. It also sheds a light on the relevancy of widespread combined aerosol chemical and physical

observations to better estimate their role on climate, particularly reducing uncertainties on future scenarios based on mitigation strategies.

1. Introduction

Aerosol particles can influence the Earth's climate through scattering and absorption of solar radiation (Aerosol-Radiation Interactions, ari), as well as affecting cloud formation and lifetime (Aerosol-Cloud Interactions, aci) (Forster et al., 2021; Myhre et al., 2013; Wilcox, 2012). Both the magnitude and sign of these impacts depend mainly on their optical, chemical and microphysical properties (Seinfeld and Pandis, 2012). Light-absorbing carbon and some minerals are the most common particle components that absorb light while all particles scatter light, which contributes the most to extinction. According to estimations of radiative forcing due to ari (RFari) from AeroCom Phase II (Myhre et al., 2013), there is a higher uncertainty on the RFari species breakdown than considering total RFari, e.g. calculations probably underestimate the positive RFari from Black Carbon (BC) and the negative forcing from organic aerosols (OA), and currently there is no evidence that one of these opposing biases dominates over the other.

Total aerosol light extinction, and the contribution for each species

* Corresponding author.
** Corresponding author. IMT Nord Europe, Institut Mines-T´elecom, Universit´e de Lille, Centre for Energy and Environment, 59000, Lille, France.
E-mail addresses: ale-vg13@hotmail.com (A. Velazquez-Garcia), suzanne.crumeyrolle@univ-lille.fr (S. Crumeyrolle).

https://doi.org/10.1016/j.atmosenv.2023.119613
Received 29 April 2022; Received in revised form 21 December 2022; Accepted 23 January 2023
Available online 26 January 2023

can be assessed using the volume average mixing (VAM) model and a priori Mass Extinction Efficiency (MEE) values for different species (Hand and Malm, 2007). MEE can be derived whether theoretically (calculations using refractive index from literature and measured size distribution) (Cheng et al., 2008) or experimentally (Wang, 2015a) for each chemical compound. Such methods have originally been proposed within the Interagency Monitoring of Protected Visual Environments (IMPROVE) program, applied for long-term measurements and at first on measurements performed over the USA national parks (Malm et al., 1994; Pitchford et al., 2007). Subsequently, the method has been applied in other parts of the world, including China (Chen et al., 2016; Cheng et al., 2008; Z. Cheng et al., 2015; Qu et al., 2015; Tao et al., 2020; Wang et al., 2015a,b; Wang et al., 2015a,b; Xia et al., 2017; Yao et al., 2010; Zhou et al., 2019) and, to a lesser extent, some south European sites mainly in Italy, Spain, and Greece (Sciare et al., 2005; Titos et al., 2012; Valentini et al., 2018; Vecchi et al., 2018). However, to the best of our best knowledge, the IMPROVE approach, although most useful to reduce uncertainties associated to the relation between aerosol chemical composition and their optical properties, has not been investigated in the polluted urban background environments of northwestern European countries. Besides, instrumentation capable of measuring aerosol chemical composition with high time resolution allows nowadays for a detailed view of the variability of physical and chemical coupling over a time scale of minutes, while still providing multi-annual observations. Precise estimates of composition-dependent MEEs would therefore significantly improve estimates of the role of different aerosol compounds on visibility, which is particularly relevant for places identified as pollution hotspots.

The north of France suffers from significant particulate pollution events, arising from a combination of heavily populated urban areas, industrial/agricultural/shipping emissions and transport of polluted atmospheric plumes from the UK, Belgium, Germany and Eastern Europe (Crumeyrolle et al., 2021; Rodelas et al., 2019; Waked et al., 2018). Here, we use three years of online submicron aerosol (PM_1) surface measurements at a suburban site in Lille to derive composition-dependent Mass Scattering Efficiencies (MSE), Mass Absorption Efficiency (MAE), and Mass Extinction Efficiency (MEE) at different wavelengths, and thus assess the contribution of each of the main species on optical properties in the region. The proposed analysis presents several advantages, including a highly time-resolved chemical information capturing fast processes of aerosol dynamics. However, it is important to note that aerosol species such as dust or sea salt are not considered here. This is partly overcome by focusing on PM_1 fraction, and by removing periods of identified influence of those species, nonetheless limitations remain. More fundamentally, an assumption inherent to VAM is that aerosol population is externally mixed (independent contribution to extinction), and its MEE is constant despite changes on aerosol size distribution. Despite those assumptions, VAM has successfully provided similar and more stable results than complex mixing rules (e.g. Maxwell Garnett, Bruggeman theory, core-shell model) for retrieving aerosol components (Li et al., 2019; Wang et al., 2021).

2. Material and methods

Sampling site. Since October 2014 near real-time in situ measurements are performed routinely on the ATOLL (ATmospheric Observations in liLLe) platform located on the rooftop of a University of Lille building (50.6111 °N, 3.1404 °E, 70 m a.s.l.), 6 km south east of Lille downtown area, without significant local aerosol sources (Riffault et al. *in preparation*). With more than 1.1 million inhabitants, the metropolitan area of Lille is characterized by a high population density (1765 inhabitants km^{-2}). As part of North of France, bounded on the north by the Benelux countries, the sampling site is under the influence of various anthropogenic regional and trans-boundary emission sources that cause relatively frequent particulate pollution episodes exceeding the WHO threshold values (Waked et al., 2018). The

ATOLL site is part of the CARA program (Favez et al., 2021) and a French National Facility of the European 'Aerosols, Clouds, and Trace gases Research Infrastructure' (ACTRIS) network focusing on high-quality long-term atmospheric data.

The chemical composition of non-refractory submicron particles (NR-PM_1) has been continuously monitored using an Aerosol Chemical Speciation Monitor (ACSM, Aerodyne Research Inc.) providing mass concentrations of particulate organics (Org), nitrate (NO_3^-), sulfate ($SO^2{}_4^-$), ammonium (NH_4^+) and chloride (Cl^-) (Ng et al., 2011). Equivalent Black carbon (eBC) concentrations and the absorption coefficients (σ_{abs}) are continuously measured with a seven-wavelength aethalometer (AE33, Magee Scientific Inc.) (Cuesta-Mosquera et al., 2021; Drinovec et al., 2015). According to ACTRIS current guidelines (https://actris -ecac.eu/particle-light-absorption.html), σ_{abs} coefficients at each wavelength have been recalculated by multiplying eBC by the mass-specific absorption coefficient (MAC) then dividing by the suitable harmonization factor to account for the filter multiple scattering effect, 2.21 (M8020 filter tape) in 2017 and 1.76 (M8060 filter tape) for 2018 and 2019. These two instruments have independent sampling lines. The ACSM is downstream a $PM_{2.5}$ cyclone (URG-2000-30ED, URG Corp.) at 3 L min^{-1} and a Nafion dryer with stainless steel tubing (2.3 m) all along. The Aethalometer is working at 5 L min^{-1} downstream a PM_1 cyclone (BGI SCC1.197, Mesa Labs) with a stainless-steel line (2.6 m) and flexible tubing (1.85 m) designed to limit the aerosol electrostatic losses.

Dry scattering coefficient (σ_{scat}) measurements are performed using two Aurora (ECOTECH) nephelometers (4000 and 3000) operating at 450, 525, and 635 nm. Both nephelometers are running in series, with a Nafion dryer upstream of both instruments (<40% RH), and a PM_1 cyclone prior the Aurora 3000. Therefore, dry scattering coefficients are measured first within the total suspended particle (A-4000) then within the PM_1 (A-3000) fractions. Both nephelometers are calibrated daily using filtered air and weekly using CO_2. Both scattering coefficients have been corrected from angular truncation errors and illumination intensity non-idealities based on Müller et al. (2011).

All the data have been averaged to the ACSM time stamp (i.e. about 30 min), and cover the period from July 2017 to December 2019. The optical properties, that is to say the extinction coefficient (σ_{ext}) – explained later on in this section – and the Single Scattering Albedo (SSA_{PM1}) defined in eq. (1) below, were estimated at the three nephelometer wavelengths. Therefore, the absorption coefficient at wavelength λ ($\sigma_{abs,\lambda}$) was interpolated using the Ångstrom ¨ Absorption Exponents (AAE) calculated every 30 min (for each data point) using the nearest wavelengths (AAE370-470 for σabs,450 calculations; AAE520-590 for σabs,525 calculations; AAE590-660 for σabs,635 calculations).

$$SSA_\lambda = \frac{\sigma_{scat,\lambda}}{\sigma_{abs,\lambda} + \sigma_{scat,\lambda}} \quad \text{eq. 1}$$

Further technical details of the sampling are given in Table S1, and data coverage on Fig. S1.

Light extinction retrieval. The extinction coefficient at a given wavelength λ can be expressed as the sum of scattering and absorption coefficients of particles and gases in the atmosphere:

$$\sigma_{ext,\lambda} = \sigma_{ap,\lambda} + \sigma_{sp,\lambda} + \sigma_{ag,\lambda} + \sigma_{sg,\lambda} \quad \text{eq. 2}$$

where subscripts "s" and "a" indicate scattering and absorption, and "p" and "g" denote particles and gases, respectively. NO_2 is the main absorbing gas within the visible range and its absorption can be directly estimated by multiplying its concentration by its absorption efficiency (0.33) (Pitchford et al., 2007). Scattering by gases is described by the Rayleigh scattering (RS) theory, which can be estimated using local meteorological conditions (T and RH) (Bodhaine et al., 1999).

Regarding particles, the U.S. IMPROVE program proposed a mathematical expression which allows the individual particle component contributions to the extinction coefficient to be separately estimated by multiplying the concentrations (C) of six major

components (j) with typical component- and site-specific mass extinction efficiencies (MEE). The formula also includes a water growth factor as a function of relative humidity (f(RH)) for hygroscopic species. Thus, the extinction coefficient can be calculated by:

$$\sigma_{ext,\lambda} = \sum_j MEE_{j,\lambda} \times f(RH)_j \times C_j + RS_\lambda + \sigma_{NO_2,\lambda} \quad \text{eq. 3}$$

IMPROVE, based on filter analysis, suggested fixed MEE values for six major chemical species of $PM_{2.5}$ including ammonium sulfate (AS), ammonium nitrate (AN), organics (Org), black carbon (BC), fine soil (FS) and sea salt (SS). Yet, MEE values vary depending on site (Hand and Malm, 2007), season (Tao et al., 2014) and particle morphology (Cheng et al., 2008). Therefore, the application of such coefficients at different sites with no local tailoring can lead to significant uncertainties (Valentini et al., 2018). Contrasting IMPROVE, in this analysis we employed online measurements performed under dry conditions, thus the water growth factor is set to be equal to 1. Besides, this work does not consider the contribution of gases to optical properties, only for aerosol particles. Indeed, the nephelometer is calibrated daily for a zero adjustment. This calibration is performed by sampling particle free air (filtered using HEPA filter) so that only gases can enter the instrument. The remaining signal is then corresponding to the Rayleigh scattering and is set to zero automatically. Assuming that the Rayleigh signal remains constant for the whole day, the signal acquired by the nephelometer is thus only corresponding to the particle scattering. On the other hand, the attenuation measured over time by the aethalometer can be only influenced by particles. This attenuation in time is then converted by a corresponding light-absorbing aerosol concentration in the atmosphere Thus, the equation employed here is expressed as:

$$\sigma_{ext,\lambda} = \sum_j MEE_{j,\lambda} \times C_j \quad \text{eq. 4}$$

In this work, we retrieved local composition-dependent MSE, MAE, and MEE values through Multiple Linear Regression (MLR) taking the optical properties measured (σ_{scat}, σ_{abs}) as independent variables and, the species mass concentrations (C_j) as dependent variables. Calculations were performed using the least square method, coefficients were constrained to be positive to retain their physical meaning, and the linear intercept was fixed to zero to force PM_1 species to explain all PM_1 scattering and absorption coefficients. With this method, MEEs have been estimated for each species over the whole period of three years, encompassing clean and polluted conditions. The equation of MLR employed in this work is written in eq. (5):

$$y = \sum_i b_i x_i + \epsilon \quad \text{eq. 5}$$

where y is the output data to be predicted by the model (here extinction, absorption or scattering coefficients), x_i are independent input variables (here the mass concentration of particulate chemical species), b_i, the linear regression constants (here MEE, MAE and MSE), and ε the residuals.

The MLR analysis (RMSE:15.2; bias: 1.5) was performed in MATLAB 2020a on almost 18,000 points of ~30-min averaged PM_1 chemical composition (NR-PM_1 and eBC) and optical coefficients (σ_{scat}, σ_{abs}) during the whole period of interest. Days flagged as impacted by desert dust events at the ATOLL platform were removed from the dataset to avoid possible errors, leading to the exclusion of 3% of data, mostly around March 2019. To evaluate the robustness of the MLR method used in this study, the residuals as well as the fractional bias were introduced (see Supplementary material). During 3 full years of measurements corresponding to more than 18,000 data points, 94% of the standardized residuals are obtained within an interval of 2σ around zero while only 6% are highlighted as outliers. Therefore, the MLR analysis developed here is robust and the results will be interpreted in the next section.

3. Results & discussion

Aerosol properties. At the ATOLL site, the 3-year averaged PM_1 concentration (calculated as the sum of ACSM species and BC concentrations) and its

standard deviation is 14.2 ± 9.7 μg m^{-3}, with seasonal averages of 16.4 ± 9.5, 15.5 ± 10.6, 14.0 ± 9.3 and 11.3 ± 8.8 μg m^{-3} for winter, spring, fall and summer, respectively. Fig. 1 shows the monthly averages of the PM_1 species concentrations. Although PM_1 changes significantly throughout the year, individual species exhibit varied behaviors. Sulfate evolution did not show a marked seasonality, with averaged monthly values varying between 0.7 ± 0.7 μg m^{-3}

(winter - DJF) and 0.9 ± 0.6 μg m^{-3} (summer - JJA). Concentrations of particulate sulfate could be directly emitted via some natural (volcanoes, oceanic phytoplankton) and anthropogenic (coal and oil combustion) sources or secondarily formed through the oxidation of its gaseous precursor sulfur dioxide (SO_2). In France emissions of SO_2 are mainly attributed to energy transformation, manufacturing, industry and residential or tertiary emissions, therefore concentrations can be highly variable at a given site, depending on the presence of local emitters and air mass origins (Rodelas et al., 2019). Moreover, non-refractory Cl^- is found typically below the detection limit, representing a minor fraction of PM_1 (<1%), with concentrations close to zero over the entire observation period.

Ammonium (NH_4^+), nitrate (NO_3^-) and carbonaceous aerosols (Org, BC) variations are more season-dependent (Fig. 1). Carbonaceous aerosols showed a higher concentration in winter (5.3 ± 4.9 and 1.2 ± 1.2 μg m^{-3} for Org and BC, respectively) compared to summer (3.7 ±3.4 to and 0.7 ± 0.5 μg m^{-3}). The increase in carbonaceous aerosols during winter could be explained by residential heating emissions combined with stagnant conditions, also favorable for semi-Volatile Organic Compounds (VOCs) species to be in particle-phase. On the other hand, during summer, Org concentrations are significantly impacted by secondary formation (SOA) (Laskin et al., 2015; Zhang et al., 2020). The concentrations of NH_4^+ and NO_3^- exhibit a marked seasonal variation showing maximum during spring with average peaks around 2.2 ± 1.8 μg m^{-3} and 4.5 ± 4.8 μg m^{-3}. The seasonality of those species arises from the widespread use of fertilizers (rich in ammonia) in the agricultural sector in spring, associated with combustion processes from traffic or industry (main source of NOx at urban sites) (Rodelas et al., 2019), compounded with favorable meteorological conditions. The

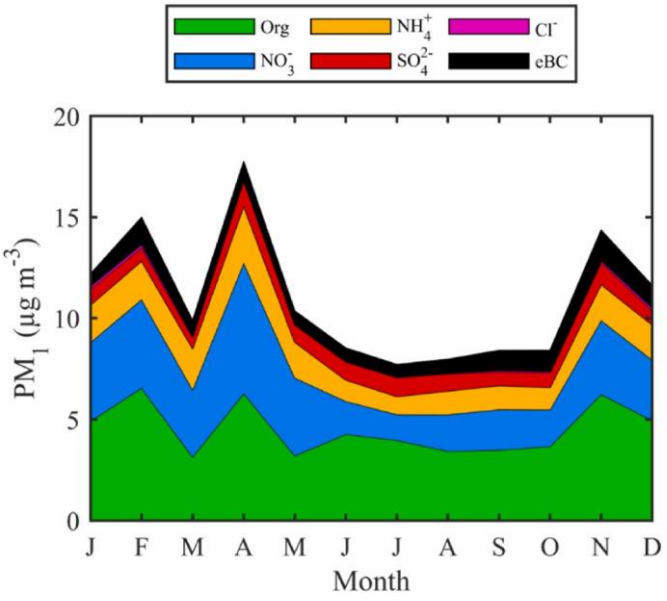

Fig. 1. Monthly averages of PM_1 species measured at ATOLL from July 2017 to December 2019.

levels of AN in the HdF region are related to both local and regional origins. Previous studies (Rodelas et al., 2019; Rodelas et al., 2019; Zhang et al., 2021) identified significant contributions of AN and organic aerosols from air masses that passed over Belgium, the Netherlands and Germany (North to North-East sectors) associated to high wind speeds and increased farming activities in those areas, suggesting the transport of neutralized and aged aerosols.

Regarding optical properties in ATOLL, the average light extinction of PM_1 at 525 nm ($\sigma_{ext,525nm}$) is 38.0 ± 34.9 Mm^{-1} consistent with the recent analysis (Laj et al., 2020) performed within the Global Atmosphere Watch (GAW) aerosol network for urban and suburban sites in Europe. For instance, in the urban Ispra, Italy (IPR), the total extinction value of the $PM_{2.5}$ fraction (44.8 Mm^{-1}) is comparable to the extinction observed here, although it is important to note differences in cut-off sizes (1 μm vs 2.5 μm). Seasonal variations of extinction coefficient show a

marked increase during winter (55.5 ± 39.9 Mm^{-1}) compared to summer (28.2 ± 27.0 Mm^{-1}), a trend that was also seen in Italy.

Fig. 2 depicts the PM_1 chemical composition as a function of SSA_{PM1}, i.e., the ratio of scattering to extinction coefficients, at 525 nm. In general, periods dominated by highly absorbing aerosols, corresponding to low SSA_{PM1} values (<0.60) where carbonaceous aerosols dominate the chemical composition with over 75% of the mass concentration. Conversely, SSA_{PM1} increases correspond to significant increases of the relative contribution of Secondary Inorganic Aerosols (AS and AN, particularly the latter). The mean SSA_{PM1} observed at ATOLL is 0.77 ± 0.11, exhibiting values comparable to most urban sites in Europe including Ispra, and lower than most remote sites (Laj et al., 2020).

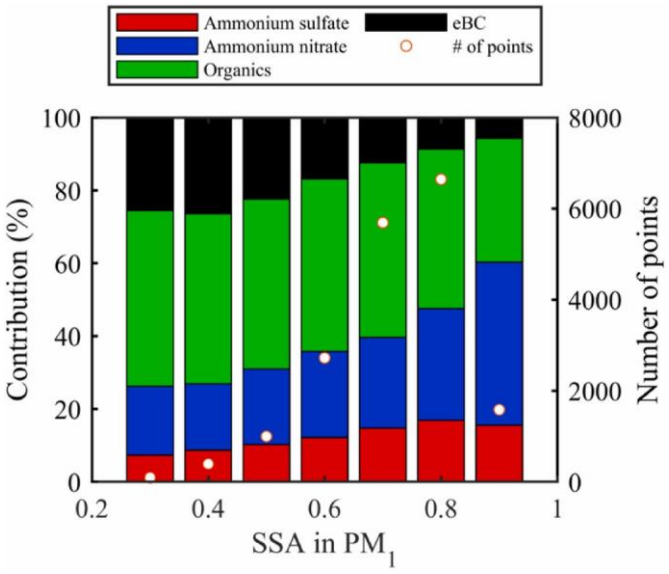

Fig. 2. PM_1 fractional composition (left axis) and number of observations (dots, right axis) according to SSA_{PM1} bins at 525 nm at ATOLL.

Composition-dependent optical properties. The composition- and wavelength-dependent MSE, MAE and MEE parameters retrieved through the MLR approach applied to PM_1 measurements at the ATOLL site are summarized in Table 1. For all components, the UV and blue ranges are characterized by the largest mass extinction, scattering and absorption efficiencies, which decrease at higher wavelengths. MEE values retrieved in northern France are compared to a comprehensive list of composition-dependent MEEs found in the literature (Table S2). Focusing on results from comparable approaches (MLR for species in PM_1), in Shenzhen, China (Yao et al., 2010) the MEE value of AS at 550 nm retrieved is 2.3 $m^2\ g^{-1}$, whereas we obtained 5.0 $m^2\ g^{-1}$ at 525 nm. Conversely, their MEE for Organics was 4.5 $m^2\ g^{-1}$, while we obtained 1.8 $m^2\ g^{-1}$ at ATOLL. Another study (Wang et al., 2015a,b) also applied MLR to PM_1 measurements performed in Beijing (China), and obtained values of MEE at 630 nm for AS slightly higher (5–2.7 $m^2\ g^{-1}$) than the value of 4.5 $m^2\ g^{-1}$ at ATOLL (Table 1). Considering the results above were obtained focusing on the same aerosol size fraction, and through similar methodology, those variations can be attributed to difference in aerosol populations, notably their mixing state and species size distributions, ultimately influencing their optical properties (Cheng et al., 2008; Hand and Malm, 2007; Pitchford et al., 2007; Valentini et al., 2018).

Based on $PM_{2.5}$ filter analysis during wintertime in the Po valley, Italy (Valentini et al., 2018), obtained an MEE at 550 nm for AS comparable to ours (4.4 $m^2\ g^{-1}$), but a value almost 3-fold higher for Organics (6.1 $m^2\ g^{-1}$). It is important to mention that organics are characterized by complex chemical composition and optical properties, determined by their origins (anthropogenic or biogenic, primary emitted or secondary produced) (Laskin et al., 2015). The study in Italy (Valentini et al., 2018) focused on a bigger size fraction (1 µm vs 2.5 µm) during a single season (winter), whereas our study targets the PM_1 fraction on a multi-annual basis. Thus, different MEE for organics could be explained by diverse aerosol origins during the studied period (multi-seasonal vs wintertime) with different mixing states and size

ranges (Hand and Malm, 2007), although the roles of possible measurement artifacts (ACSM vs Thermal Optical Transmittance analysis) and of the method employed to retrieve aerosol mass efficiency (experimental vs theoretical) cannot be excluded. Indeed, site-specific dry mass extinction efficiencies in the Po valley (Valentini et al., 2018) were retrieved considering additional physical properties (e.g. density, geometric mean radii and the mass fractions of four modes). For organics, the average ambient dry mass size distribution used (Bernardoni et al., 2017) also contemplates hygroscopicity for water-soluble organics, which represents 25% of fine organic carbon concentration. Hence, the discrepancy in MEE calculated for Org is also likely to be ascribed to differences in mass relative contribution and in geometric standard deviations of the modes, as well as the water growth factors detected at the Po Valley compared to ATOLL site.

Fig. 3 displays the impact of using literature values for MEEs with ATOLL mass concentration observations for each species to retrieve the extinction coefficients (eq. (4)). For comparison, we selected six studies focusing on fine aerosol fractions (either 1 or 2.5 μm) and on the same species as in our work (AN, AS, Org, eBC). Using literature values instead of site-specific MEE leads to a large range of reconstructed extinction coefficients at 525 nm. For example, using MEE values based on theoretical calculations (Cheng et al., 2008; Pitchford et al., 2007), could result in a 30% underestimation and 74% overestimation of the total extinction, respectively. Conversely, experimentally-derived MEEs from field observations (Wang et al., 2015a,b; Yao et al., 2010) were within 18% of the total extinction observed here. Nevertheless, even a good agreement for total extinction coefficient does not automatically imply a similar agreement for individual species, as discussed in the next section.

Chemical contribution to the Aerosol Optical Properties (AOPs). By considering the obtained MEEs and average mass concentration of each species, we could calculate their relative contribution to optical properties. Secondary Inorganic Aerosols (SIA), i.e. AN and AS, were the main contributors (67%) to the light scattering for all three wavelengths: 450, 525 and 635 nm (Fig. 4a). Conversely, light absorption is entirely apportioned to carbonaceous aerosols, with Organics being optically active at the near-ultraviolet and blue wavelengths (370–590 nm) accounting up to 22% of the total absorption, the rest being apportioned to eBC (Fig. 4b). This is comparable with what is reported for Zurich in Switzerland (Moschos et al., 2020), for which an Organics contribution to the total measured absorption of 30 ± 14% was assessed at 370 nm, decreasing down to 4 ± 2% at 590 nm, while BC contribution was estimated two-thirds of the particle absorption in the near-UV to infrared wavelength range. Considering aerosol light extinction at 525 nm (Fig. 4c), AN is the dominant species (35%), followed by eBC (29%) and Organics (21%), and finally AS (15%). For other wavelengths, Organics and eBC exhibit a slightly higher contribution at 450 and 635 nm,

Table 1
Retrieved values of Mass Scattering, Absorption and Extinction Efficiencies (MSE, MAE, MEE, respectively) from 370 to 930 nm based on MLR analysis at ATOLL.

	Wavelength (nm)	Ammonium Sulfate	Ammonium Nitrate	Organics	eBC
Mass Scattering Efficiency, MSE ($m^2\ g^{-1}$)	450	7.1	4.6	3.1	–
	525	5.7	3.6	2.2	–

Mass Absorption Efficiency, MAE ($m^2 g^{-1}$)	635	4.8	2.7	1.5	–
	370	–	–	0.7	11.6
	470	–	–	0.3	8.9
	520	–	–	0.2	7.5
	590	–	–	0.2	6.5
	660	–	–	0.1	5.5
	880	–	–	0.0	3.9
Mass Extinction Efficiency, MEE ($m^2 g^{-1}$)	950	–	–	0.0	3.7
	450	5.8	4.6	2.9	13.5
	525	5.0	3.7	1.8	11.2
	635	4.5	2.7	1.0	10.3

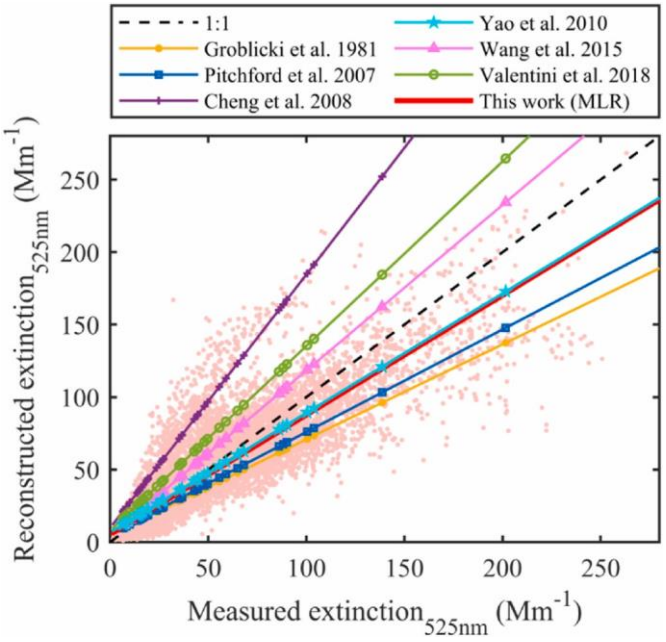

Fig. 3. Scatter plot of reconstructed versus measured aerosol extinction coefficient at 525 nm for ~ 3-year measurements at the ATOLL platform. Solid lines represent the linear least-square fit through the data where y-values have been calculated using fixed MEE taken from the literature (Cheng et al., 2008; Groblicki et al., 1981; Pitchford et al., 2007; Valentini et al., 2018; Wang et al., 2015a,b; Yao et al., 2010) combined with ATOLL PM_1 species mass concentrations. Results of the Multiple Linear Regression with ATOLL MEE values are represented by the pink dots and the solid line in red (# of points: 18,065; R^2: 0.80; slope: 0.82) (For interpretation of the references to colour in this figure legend, the reader is referred to the web version of this article).

respectively (Fig. 4c). While (Valentini et al., 2018) have also identified AN as the main contributor to extinction at 550 nm in the Po valley (Yu et al., 2010), identified BC (76%) as the dominant species in urban areas in the Pearl River region (China). This highlights the complex and probably mixed influence of source intensities, topography and meteorological conditions that drive light extinction at a given site, and more generally reflects the spatial and temporal variability of fine particles in the atmosphere.

Fig. 5a represents the monthly light extinction broken down according to species contribution, a product of mass efficiency and changes in the mass concentrations. As expected, light extinction is generally higher during the cold months, with three maxima in November, February and April. These

months are strongly impacted by aerosol emissions related to solid fuel combustion from residential heating (carbonaceous aerosols), and agricultural activities leading to

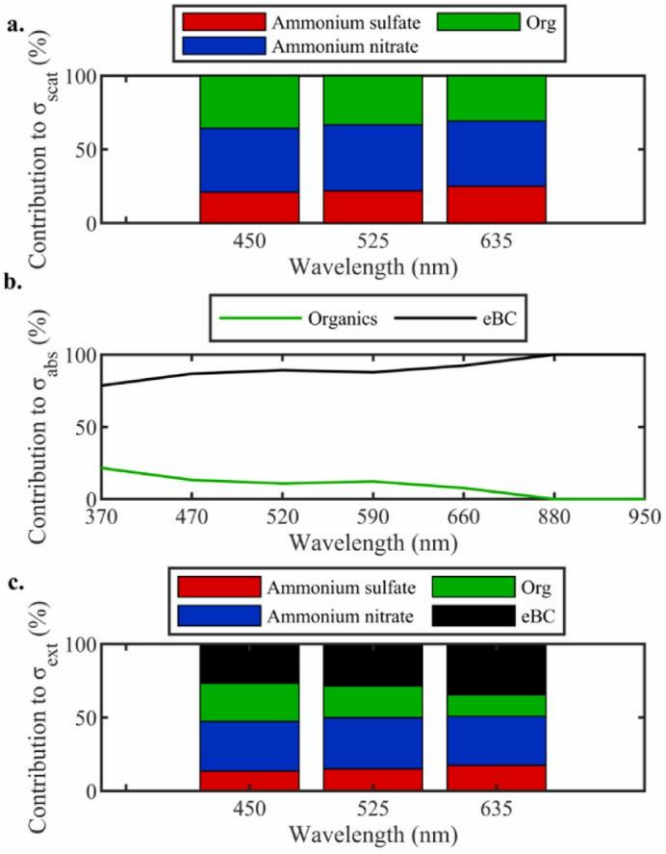

Fig. 4. Averaged relative contributions of PM_1 chemical species to the Aerosol Optical Properties at ATOLL over the period July/2017–December/2019: a) Secondary Inorganic Aerosols and Organics to light scattering at 450, 525 and 635 nm; b) carbonaceous aerosols to light absorption from 370 to 940 nm; c) PM_1 species to light extinction at 450, 525 and 635 nm.

strong AN (5.8 ± 6.2 μg/m^{-3}) formation (Crenn et al., 2017; Rodelas et al., 2019; Rodelas et al. 2019) during spring. Fig. 5b shows the monthly evolution of the normalized extinction, highlighting the highest contribution of eBC and AN in October and April respectively. AS (1.2 ± 1.2 μg/m^{-3}) has a fairly constant absolute contribution throughout the year peaking at about 25% of extinction during the summer. It is interesting to notice the increase in Organics relative contribution during summertime, likely associated with biogenic particulate secondary formation (Gomez-Gonz´ alez ´ et al., 2012) favored at higher temperatures.

As previously discussed, literature-based MEEs yield to strong variability in the reconstructed extinction coefficient. In recent years, MEE

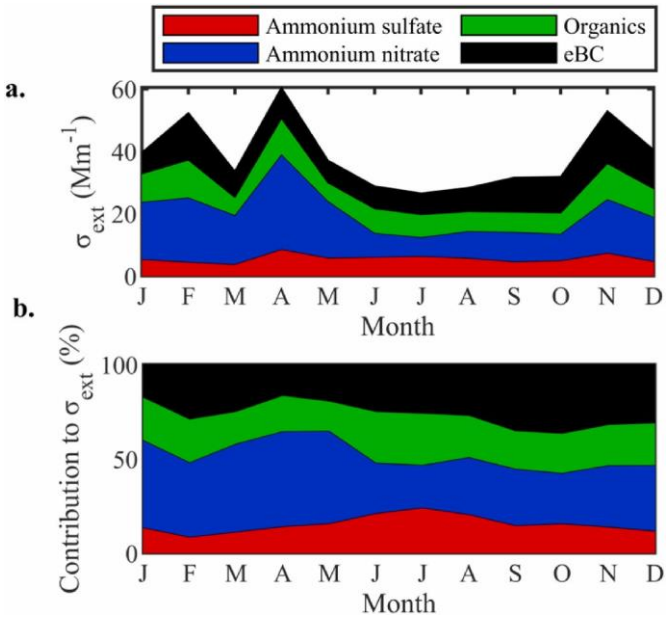

Fig. 5. Contribution of the main aerosol species to the extinction coefficient at ATOLL over the period July 2017–December 2019. a) Monthly-averaged variation of the light extinction coefficient at 525 nm (in Mm^{-1}) for each considered species. b) Monthly-averaged relative contributions of each particulate component to the light extinction coefficient at 525 nm.

estimation via the IMPROVE approach has been applied in numerous studies, mainly carried out at heavily polluted urban areas in China, or over US national parks where uniform haze occurred often. Over Europe, the IMPROVE approach has only been used over south Europe (Sciare et al., 2005; Titos et al., 2012; Valentini et al., 2018; Vecchi et al., 2018). Although the cut-off sizes (1 vs 2.5 μm) and method to derive site-specific MEE are slightly different from this work, we used the only available study for a hotspot of pollution at a European urban site in the Po Valley, Italy (Valentini et al., 2018).

It is important to consider that even for cases when the total extinction is comparable, large discrepancies can remain on composition-based apportionment. For example, applying the MEEs derived from the study of experimental method in Shenzhen for the PM_1 fraction (Yao et al., 2010) to ATOLL mass concentrations reconstructs the total extinction within 18% of the observed values, however it overestimates the role of Organics by 50% compared to similar calculations using ATOLL site-specific MEE (Fig. S2). Conversely, using MEEs, based on theoretically-calculated (Mie model) values for national parks in USA (Pitchford et al., 2007), would lead to large underestimation (9%) of the role of AN, while the total reconstructed extinction would be 30% of the light extinction observed. Finally, using a fairly comparable sampling site in Europe, MEE parameters derived through theoretical calculations on a filter analysis for $PM_{2.5}$ in the Po Valley (Valentini et al., 2018), would lead to an underestimation of the AS extinction by 6% which might be driven by the contribution of super micron aerosols (mainly sulfate and nitrate) to the PM mass concentration (for more details, please refer to Fig. S2 in the Supplementary Information).

4. Conclusion

Accurate knowledge of the physical, chemical and optical properties of aerosol particles is essential to reduce current uncertainties associated to their radiative impacts on Earth's climate. Nevertheless, the complex aerosol (trans)formation processes and range of sources lead to a strong spatial and temporal variability in aerosol properties. In this study, we combined in situ coincident aerosol chemical and physical measurements in PM_1 via the IMPROVE algorithm, to provide robust estimates of their optical properties relevant for better assessments on their role on climate.

The IMPROVE algorithm uses fixed MEE values for six major chemical species of PM. This method has been used for estimating the extinction coefficients mostly in the United States and China, whereas only a few studies have addressed this topic at south European sites in PM_{10} and $PM_{2.5}$, lacking information in polluted urban hotspots of northwestern European countries. Hence, in this study for the first time, we retrieved the light extinction and the composition-based apportionment in the smallest fraction of one of the most polluted northwestern Europe cities (Lille). First of all, we employed literature-based MEE reported for suburban and urban sites over ~3 years of measurements at ATOLL, where the light extinction reconstructed at 525 nm and the composition-based apportionment are retrieved with a range of biases depending on the chosen reference (e. g. overestimation of 70% reconstructed extinction using Cheng et al., 2008). Therefore, we used a multiple linear regression to derive specific multi-annual MEEs for ATOLL.

The multiannual analysis, using MEE derived from the multiple linear regression, highlights ammonium nitrate as the predominant species regarding the extinction at 525 nm (35%), followed by the carbonaceous aerosol species (eBC 29%, Org 21%) and ammonium sulfate (15%). Regarding the absorption at 370 nm, organics are responsible for 22% of the absorption, evidencing a significant contribution of Brown Carbon in the region. The extinction is shown to be generally higher during winter, strongly impacted by aerosol emissions related to solid fuel combustion from residential heating, and during spring, in which agricultural activities combined with traffic emissions (NOx) lead to strong ammonium nitrate formation.

Overall, this study provides new evidences that not considering aerosol heterogeneity among different sampling sites and seasons, can lead to significant biases in estimating their extinction. Our analysis of the long-term ATOLL dataset in Lille highlights the ability of retrieving robust aerosol optical properties from chemical composition measurements, constrained by coincident absorption and scattering measurements. In addition, this work supports the use of site-specific parameters (that reflect various influences, as mixing state, size distribution of aerosol components) along with long-term field observations, to derive key aerosol optical properties

relevant for climate modelling and air quality assessment.

Author contributions

Conceptualization: JFB, SC, IC, VR; Data Curation: AVG, SC, VR; Formal analysis: AVG, JFB, SC; Funding acquisition: AVG, IC, VR; Investigation: AVG, JFB, SC, VR; Methodology: JFB, SC; Project administration: IC, VR; Resources: ET, EB, VR; Software: AVG, JFB, SC; Supervision: IC, VR; Validation: JFB, SC, ET, EB, VR; Visualization: AVG; Writing – Original Draft: AVG, JFB; Writing – Review & Editing: SC, IC, VR.

Funding sources

A. Velazquez Garcia's PhD grant is supported by CONACyT PhD grant (2019-000004-01EXTF-00001) and the Hauts-de-France Regional Council. IMT Nord Europe and LOA acknowledge financial support from the Labex CaPPA project, which is funded by the French National Research Agency (ANR) through the PIA (Programme d'Investissement d'Avenir) under contract ANR-11-LABX-0005-01, and the CLIMIBIO project, both financed by the Regional Council "Hauts-de-France" and the European Regional Development Fund (ERDF). IMT Nord Europe participated in the COST COLOSSAL Action CA16109. The ATOLL site is one of the French ACTRIS National Facilities and contributes to the CARA program of the LCSQA funded by the French Ministry of Environment.

Declaration of competing interest

The authors declare that they have no known competing financial interests or personal relationships that could have appeared to influence the work reported in this paper.

Data availability

Data will be made available on request.

Acknowledgment

The authors are really grateful to the staff at LOA, in particular Prof. P. Goloub, F. Auriol and R. De Filippi, for supporting the technical and logistical implementation of the instruments, and to Dr. L.-H. Rivellini (now at Singapore National University) for her early involvement. We thank T. Podvin (LOA) for providing the weather data at ATOLL, and the air quality monitoring network Atmo Hauts-de-France for providing NO_2 concentrations at the Lille Fives monitoring station. **Appendix A. Supplementary data**

Supplementary data to this article can be found online at https://doi.org/10.1016/j.atmosenv.2023.119613.

ABBREVIATIONS

ATOLL- ATmospheric Observations in liLLe
MEE- Mass Extinction Efficiency
MSE- Mass Scattering Efficiency
MAE- Mass Absorption Efficiency
IMPROVE- Interagency Monitoring of Protected Visual Environments
ACTRIS- The Aerosol, Clouds and Trace Gases Research Infrastructure
ACSM- Aerosol Chemical Speciation Monitor
AAE- Absorption Ångstrom exponent ¨
SSA- Single Scattering Albedo
RS- Rayleigh scattering
T-Temperature
RH-Relative Humidity
C_j- Mass concentration of species
f(RH)- Water growth function
AS- Ammonium Sulfate
AN- Ammonium Nitrate
Org- Organic fraction
BC- Black Carbon
FS- Fine Soil
SS- Sea Salt
MLR- Multiple Linear Regression
PM_1- Fine particles with an aerodynamic diameter less than 1 μm
NR- PM_1- Non-Refractory PM_1
eBC- equivalent Black carbon (for data derived from optical absorption methods)
σ_{scat}- Scattering Coefficient
σ_{abs}- Absorption Coefficient
σ_{ext}- Extinction Coefficient
SIA- Secondary Inorganic Aerosols
GAW- Global Atmosphere Watch
IPR- Ispra, Po Valley, Italy (GAW site)

References

Bernardoni, V., et al., 2017. Size-segregated aerosol in a hot-spot pollution urban area: chemical composition and three-way source apportionment. Environ. Pollut. 231, 601–611.

Bodhaine, Barry A., Wood, Norman B., Dutton, Ellsworth G., Slusser, James R., 1999. On Rayleigh optical depth calculations. J. Atmos. Ocean. Technol. 16 (11), 1854–1861.

Chen, Xiaojia, et al., 2016. Reconstructed light extinction coefficients of fine particulate matter in rural guangzhou, southern China. Aerosol Air Qual. Res. 16 (8), 1981–1990.

Cheng, Y.F., et al., 2008. Aerosol optical properties and related chemical apportionment at xinken in Pearl River delta of China. Atmos. Environ. 42 (25), 6351–6372.

Cheng, Zhen, et al., 2015. Estimation of aerosol mass scattering efficiencies under high mass loading: case study for the megacity of shanghai, China. Environ. Sci. Technol. 49 (2), 831–838.

Crenn, V., Fronval, I., Petitprez, D., Riffault, V., 2017. Fine particles sampled at an urban background site and an industrialized coastal site in northern France — Part 1: seasonal variations and chemical characterization. Sci. Total Environ. 578, 203–218.

Crumeyrolle, Suzanne, et al., 2021. On the importance of nitrate for the droplet concentration in stratocumulus in the north-sea region. Atmos. Environ. 252, 118278.

Cuesta-Mosquera, Andrea, et al., 2021. Intercomparison and characterization of 23 aethalometers under laboratory and ambient air conditions: procedures and unit-to- unit variabilities. Atmos. Meas. Tech. 14 (4), 3195–3216.

Drinovec, L., et al., 2015. The 'Dual-Spot' Aethalometer: an Improved Measurement of Aerosol Black Carbon with Real-Time Loading Compensation. https://oar.tib.eu/jspui/handle/123456789/765. (Accessed 22 October 2020).

Favez, Olivier, et al., 2021. Overview of the French operational network for in situ observation of PM chemical composition and sources in urban environments (CARA program). Atmosphere 12 (2), 207.

Forster, Piers, et al., 2021. The Earth's energy budget, climate feedbacks, and climate sensitivity. In: Masson-Delmotte, Val´erie, et al. (Eds.), Climate Change 2021: the Physical Science Basis. Contribution of Working Group I to the Sixth Assessment Report of the

Intergovernmental Panel on Climate Change. Cambridge University Press.
Gomez-Gon´ zalez, Y., et al., 2012. Chemical characterisation of atmospheric aerosols´ during a 2007 summer field campaign at brasschaat, Belgium: sources and source processes of biogenic secondary organic aerosol. Atmos. Chem. Phys. 12 (1), 125–138.
Groblicki, Peter J., Wolff, George T., Countess, Richard J., 1981. Visibility-reducing species in the denver 'Brown cloud'—I. Relationships between extinction and chemical composition. Atmos. Environ. 15 (12), 2473–2484, 1967.
Hand, J.L., Malm, W.C., 2007. Review of aerosol mass scattering efficiencies from ground-based measurements since 1990. J. Geophys. Res. Atmos. 112 (D16). https://agupubs.onlinelibrary.wiley.com/doi/abs/10.1029/2007JD008484. (Accessed 14 May 2020).
Laj, Paolo, et al., 2020. A global analysis of climate-relevant aerosol properties retrieved from the network of global atmosphere Watch (GAW) near-surface observatories. Atmos. Meas. Tech. 13 (8), 4353–4392.
Laskin, Alexander, Laskin, Julia, Sergey, A., Nizkorodov, 2015. Chemistry of atmospheric Brown carbon. Chem. Rev. 115 (10), 4335–4382.
Li, Lei, et al., 2019. Retrieval of aerosol components directly from satellite and ground- based measurements. Atmos. Chem. Phys. 19 (21), 13409–13443.
Malm, William C., et al., 1994. Spatial and seasonal trends in particle concentration and optical extinction in the United States. J. Geophys. Res. 99 (D1), 1347–1370.
Moschos, Vaios, et al., 2020. Source-specific light absorption by carbonaceous components in the complex aerosol matrix from yearly filter-based measurements. Atmos. Chem. Phys. Discuss. 1–44.
Müller, T., Laborde, M., Kassell, G., Wiedensohler, A., 2011. Design and performance of a three-wavelength LED-based total scatter and backscatter integrating nephelometer. Atmos. Meas. Tech. 4 (6), 1291–1303.
Myhre, G., et al., 2013. Radiative forcing of the direct aerosol effect from AeroCom Phase II simulations. Atmos. Chem. Phys. 13 (4), 1853–1877.
Ng, N.L., et al., 2011. Real-time methods for estimating organic component mass concentrations from aerosol mass spectrometer data. Environ. Sci. Technol. 45 (3), 910–916.
Pitchford, Marc, et al., 2007. Revised algorithm for estimating light extinction from IMPROVE particle speciation data. J. Air Waste Manag. Assoc. 57 (11), 1326–1336.
Qu, W.J., et al., 2015. Influence of relative humidity on aerosol composition: impacts on light extinction and visibility impairment at two sites in coastal area of China. Atmos. Res. 153, 500–511.
Rodelas, Roig, Roger, Esperanza Perdrix, Herbin, Benoît, Riffault, Veronique, 2019.´ Characterization and variability of inorganic aerosols and their gaseous precursors at a suburban site in northern France over one year (2015–2016). Atmos. Environ. 200, 142–157.
Sciare, J., et al., 2005. Aerosol mass closure and reconstruction of the light scattering coefficient over the eastern mediterranean sea during the MINOS campaign. Atmos. Chem. Phys. 5 (8), 2253–2265.
Seinfeld, John H., Pandis, Spyros N., 2012. Atmospheric Chemistry and Physics: from Air Pollution to Climate Change. John Wiley & Sons.
Tao, Jun, et al., 2014. Impact of PM2.5 chemical compositions on aerosol light scattering in guangzhou — the largest megacity in south China. Atmos. Res. 135–136, 48–58. Tao, Jun, Zhang, Leiming, Wu, Yunfei, Zhang, Zhisheng, 2020. Evaluation of the IMPROVE formulas based on mie model in the calculation of particle scattering coefficient in an urban atmosphere. Atmos. Environ. 222, 117116.
Titos, G., et al., 2012. Optical properties and chemical composition of aerosol particles at an urban location: an estimation of the aerosol mass scattering and absorption efficiencies. J. Geophys. Res. Atmos. 117 (D4). https://agupubs.onlinelibrary.wiley.com/doi/abs/10.1029/2011JD016671. (Accessed 23 October 2020).
Valentini, S., et al., 2018. Tailored coefficients in the algorithm to assess reconstructed light extinction at urban sites: a comparison with the improve revised approach. Atmos. Environ. 172, 168–176.
Vecchi, R., et al., 2018. Assessment of light extinction at a European polluted urban area during wintertime: impact of PM1 composition and sources. Environ. Pollut. 233, 679–689.
Waked, Antoine, et al., 2018. Investigation of the geographical origins of PM10 based on long, medium and short-range air mass back-trajectories impacting northern France during the period 2009–2013. Atmos. Environ. 193, 143–152.
Wang, Huanbo, et al., 2015a. Chemical composition and light extinction contribution of PM2.5 in urban beijing for a 1-year period. Aerosol Air Qual. Res. 15 (6),

2200–2211.
Wang, Qingqing, et al., 2015b. Chemical composition of aerosol particles and light extinction apportionment before and during the heating season in beijing, China. J. Geophys. Res. Atmos. 120 (24), 12708–12722.
Wang, Shuo, et al., 2021. Real-time retrieval of aerosol chemical composition using effective density and the imaginary part of complex refractive index. Atmos. Environ. 245, 117959.
Wilcox, E.M., 2012. Direct and semi-direct radiative forcing of smoke aerosols over clouds. Atmos. Chem. Phys. 12 (1), 139–149.
Xia, Yunjie, et al., 2017. Impact of size distributions of major chemical components in fine particles on light extinction in urban guangzhou. Sci. Total Environ. 587–588, 240–247.
Yao, TingTing, et al., 2010. High time resolution observation and statistical analysis of atmospheric light extinction properties and the chemical speciation of fine particulates. Sci. China Chem. 53 (8), 1801–1808.
Yu, H., Wu, C., Wu, D., Yu, J.Z., 2010. Size distributions of elemental carbon and its contribution to light extinction in urban and rural locations in the Pearl River delta region, China. Atmos. Chem. Phys. 10 (11), 5107–5119.
Zhang, Shouwen, et al., 2021. Near real-time PM1 chemical composition measurements at a French urban background and coastal site under industrial influence over more than a year: temporal variability and assessment of sulfur-containing emissions. Atmos. Environ. 244, 117960.
Zhang, Yunjiang, et al., 2020. Substantial Brown carbon emissions from wintertime residential wood burning over France. Sci. Total Environ. 743, 140752.
Zhou, Yaqing, et al., 2019. Exploring the impact of chemical composition on aerosol light extinction during winter in a heavily polluted urban area of China. J. Environ. Manag. 247, 766–775.

Manuscript in preparation

Black and brown carbon sources at the ATOLL site in Northern France

Alejandra Velazquez-Garcia[1-2], Joel F. de Brito[1], Suzanne Crumeyrolle[2], Isabelle Chiapello[2], Véronique Riffault[1]

[1]Centre for Energy and Environment, IMT Nord Europe, Institut Mine-Télécom, Université de Lille, Lille, 59000, France

[2]LOA, UMR, University of Lille, Lille, 59000, France

Correspondence to: Joel F. de Brito (joel.brito@imt-nord-europe.fr) & Alejandra Velazquez-Garcia (ale-vg13@hotmail.com)

Key words: Black Carbon, Brown Carbon, optical properties, in situ observations, global emission inventories, and Back trajectories

Abstract. Aerosols influence the Earth's climate directly through scattering and absorption of solar radiation and indirectly by affecting cloud properties. The brown carbon (BrC) contribution to light absorption is estimated by global models around ~30−70% of the one for black carbon (BC) in several regions of the world. Thus, it is important to understand BrC sources and characteristics on temporal and spatial scales. In this study, light-absorbing aerosol observations were complemented by integration with hourly 72h Hysplit back-trajectories and the latest version of the EDGAR (Emissions Database for Global Atmospheric Research) emission inventory. This so-called INTERPLAY (combIning iN-siTu obsERvations hysPLit And emissions-inventorY) approach allows estimating emission source type (shipping/vehicular/residential heating, etc.) and atmospheric age of BC observed over ATOLL (Atmospheric Observations in liLLe) platform. Results showed a significant contribution of traffic (31%) and residential (21%) to BC concentration, as expected, however a quite large fraction from shipping (25%), despite the distance between ATOLL and the North Sea (60 km). Outside France, countries such as Belgium (13%), Germany (8%), the UK (7%), and important shipping lanes in the Channel (6%) and North Sea (9%) are important contributors to BC over ATOLL. By focusing only on residential and traffic emissions from INTERPLAY, one can further separate fresh (<24h sampling since emission) from aged (>24h) aerosol. Results yield that BrC at ATOLL is dominated by fresh residential (72%), followed by aged residential (16%) and aged traffic (12%), and negligible contribution from fresh traffic. Given that, in terms of mass, fresh residential accounts for only 28%, the result obtained here suggests that BrC concentration issued from residential heating in Central Europe tends to decrease already after 24h since emission (so-called photobleaching), and confirms that no BrC is associated with fresh traffic emission. Furthermore, secondary processes and source mixing could explain the mild contribution of aged traffic to BrC observed here (12%). Given that BrC has one of the largest uncertainties on the aerosol-radiation interactions, this result has important consequences on the climatic impact of wood combustion for residential heating. Furthermore, given that current BC source apportionment techniques rely on the presence of BrC, our results suggest that long-range transported house heating (>24h) is systematically underestimated by current methods.

1 Introduction

Light-absorbing carbonaceous aerosols (LACs) are an important component of the climate system due to their effect on solar radiation (Aerosol-Radiation Interactions, ari) and on cloud properties (Aerosol-Cloud Interactions, aci) (Forster et al. 2021). In addition, LACs can efficiently reduce snow/ice albedo when deposited, increasing heating and accelerating melting (Pu et al. 2017; Wang et al. 2017). They are mainly composed of brown and black carbon (BrC and BC, respectively). Whereas BC absorbs over a broad spectral range, from UV to infrared, and is widely recognized as an important climatic agent, BrC absorbs mostly in the UV and its impacts suffer from large uncertainties due to the complex variety of molecules or molecular aggregates dictating its optical properties, and how atmospheric processing forms or destroys those compounds (Laskin, and Nizkorodov 2015; Moise, Flores, and Rudich 2015).

To date, numerous LAC sources have been identified, including both anthropogenic (e.g. emissions from combustion of fossil fuel and biomass) and biogenic ones (e.g. vegetation emitted terpene/isoprene oxidation and primary biological aerosol particles from plants and fungi) (He et al. 2021; Kanakidou et al. 2005; Ng et al. 2017). Biomass burning (BB), including forest fires and the burning of crop residues, is considered to be the main source of BrC (Lin et al. 2017; Teich et al. 2017). Yet, field observations and laboratory studies show BrC from secondary formation through multiple phase reactions occurring in or between the gas phase, particle phase, and cloud droplets (Laskin and Nizkorodov, 2015). For instance, the nitrification of aromatic compounds (Harrison et al. 2005; Lu et al. 2011), oligomers of acid-catalyzed condensation of hydroxyl aldehyde (Haan et al. 2009; Shapiro et al. 2009), and the reaction of ammonia (NH_3) or amino acids with carbonyls (De Haan et al. 2011; Flores et al. 2014; Nguyen et al. 2013) can all produce BrC. Corbin et al. (2019) found that the BrC in the form of highly absorbing tar balls may dominate total aerosol light absorption of ship emissions in the open ocean and Arctic, associated with heavy-fuel oil. At the global scale, emissions from shipping represent only a minor contribution to LAC mass (Bond et al. 2013) but occur in remote regions that are climatically sensitive.

Once emitted into the atmosphere, the properties of LAC can evolve as a result of changes in their chemical composition, as well as their physical properties (e.g. size distribution, phase state, viscosity) (Laskin, and Nizkorodov 2015; Moise, Flores, and Rudich 2015). BC has a typical atmospheric lifetime of 7 to 10 days, observations have shown that it typically ages within a few hours over polluted regions such as urban and biomass-burning areas (Denjean et al. 2020; Kumar et al. 2018; Saturno et al. 2018; Sun et al. 2021), whereas the aging time scale can be days to weeks in remote areas. Conversely, BrC, as organic aerosol (OA), is even more likely to react in the atmosphere, via atmospheric processing such as oligomerization, functionalization, or fragmentation leading to absorption enhancement or decrease (also known as bleaching) (Laskin, and Nizkorodov 2015). BrC can be photolyzed and degraded into a less absorbing compound when directly exposed to solar radiation (i.e. photobleaching) but with different photolysis rates for certain chromophores (Chen et al. 2021; Hems et al. 2021; Liu et al. 2021; Liu et al. 2016). Only a few modeling studies tried to include the BC and BrC lifetime to estimate climate impacts (Saleh 2020). Therefore, a broader overview of real-world LAC properties according to sources and age is fundamentally relevant to guide a better representation of the climatic impact of aerosol particles. Here, we analyze how different sources and geographical origins affect the optical properties of carbonaceous aerosols via a novel approach combining multiannual submicron aerosol (PM_1) observations, back trajectories (BTs), and emission inventories. The study is centered at the sub-urban site ATOLL (ATmospheric Observations in liLLe) in Northern France. The region is a heavily populated pollution hotspot in Europe, with a significant fraction of

secondary aerosols (Chen at al. 2022), and strongly impacted by LAC, having a major role in aerosol light extinction at the site (Velazquez-Garcia et al., 2023).

2 Materials and Methods

2.1 Sampling site

Real-time in situ aerosol measurements are performed routinely since October 2016 on the ATOLL platform, located on the rooftop of a University of Lille building (50.6111 °N, 3.1404 °E, 70 m a.s.l.), 6 km southeast of Lille downtown area. The ATOLL site is part of the CARA program (Favez et al. 2021) and of the French ACTRIS (Aerosols, Clouds, and Traces gases Research InfraStructure) National Facilities, aiming at continuous, long-term and high quality atmospheric data. Dry scattering coefficient (σ_{scat}) measurements are performed using two nephelometers (Aurora, ECOTECH, 4000 and 3000) operating at 450, 525, and 635 nm. Both nephelometers are running in series, with a Nafion dryer upstream of both instruments (<40% RH), and a PM_1 cyclone upstream of the Aurora 3000. Consequently, dry scattering coefficients are measured within the total suspended particle (A-4000) and within the PM_1 (A-3000) fractions. They are daily calibrated using filtered air and weekly calibrated using span gaz (CO_2), else, scattering coefficients have been corrected from angular truncation errors and illumination intensity non-idealities (Müller et al. 2011). Black carbon (eBC) concentrations and the absorption coefficients (σ_{abs}) are continually measured with a seven-wavelength aethalometer (AE33, Magee Scientific Inc., Drinovec et al., 2015; Cuesta-Mosquera et al., 2021). According to ACTRIS current guidelines (https://actris-ecac.eu/particle-light-absorption.html), σ_{abs} coefficients at each wavelength have been recalculated by multiplying eBC by the mass-specific absorption coefficient (MAC) then dividing by the suitable harmonization factor by account for the filter multiple scattering effects, 2.21 (M8020 filter tape) in 2017 and 1.76 (M8060 filter tape) for 2018 and 2019. The aethalometer is working at 5 L min^{-1} downstream a PM_1 cyclone (BGI SCC1.197, Mesa Labs) with a stainless-steel line (3.5 m) and flexible tubing (0.50 m) designed to limit the aerosol electrostatic losses.

2.2 Aerosol Optical Properties

Absorption Ångström Exponent (AAE) and Single Scattering Albedo (SSA) are derived from σ_{abs}, and σ_{scatt}. The AAE is a widely used parameter that described the wavelength (λ) dependence of aerosol light absorption, also employed in aerosol characterization and apportionment studies (Liu et al. 2018). Here we approximate the AAE between two wavelengths (λ_1 = 370nm and λ_2 = 880nm) by:

$$AAE\left(\frac{\sigma_{abs,\lambda1}}{\sigma_{abs,\lambda2}}\right) = -\frac{\log\left(\frac{\sigma_{abs,\lambda1}}{\sigma_{abs,\lambda2}}\right)}{log\left(\frac{\lambda1}{\lambda2}\right)} = -\frac{\log(\sigma_{abs,\lambda1})-\log(\sigma_{abs,\lambda2})}{\log(\lambda1)-log(\lambda2)} \quad \text{eq. 1}$$

The Single Scattering Albedo is often used to evaluate the total effect of aerosol on atmospheric radiative transfer, a low value is associated with the dominance of light-absorbing aerosols, while a value near 1 indicates purely scattering components. The SSA is evaluated based on aerosol light absorption and scattering both retrieved at 525nm as follows:

$$SSA = \frac{\sigma_{scat}}{\sigma_{scat}+\sigma_{abs}} \quad \text{eq. 2}$$

In addition, the wavelength dependence of the BrC absorption coefficient ($\sigma_{BrC\ abs}$) at 470nm was calculated assuming that BC is the only species responsible for light absorption at 880nm. The spectral dependence of BC absorption ($\sigma_{BC\ abs}$) can be derived based on the measured total aerosol absorption coefficients (σ_{abs}) using eq. 1. The AAE for BC usually ranges between 0.9 and 1.2 (Bond et al. 2013; Lu et al. 2015), thus we applied an AAE of 1 in our analysis and calculated BrC absorption as:

$$\sigma_{BrC\ abs,\lambda} = \sigma_{abs,\lambda} - \sigma_{BC\ abs,\lambda} \quad \text{eq. 3}$$

Furthermore, we used the well-known "Aethalometer model" approach (Sandradewi et al. 2008), for the estimation of the black carbon from fossil fuel (BC ff) and black carbon from wood burning (BC wb) sources, using AAE_{ff} = 1.0 and AAE_{wb} = 2. The equation relating the wavelengths (i.e. 370 and 880 nm) and the absorption coefficient for the fossil fuel and wood burning are:

$$\frac{\sigma_{abs,ff}(\lambda 1)}{\sigma_{abs,ff}(\lambda 2)} = \frac{\lambda 1}{\lambda 2}^{-AAE_{ff}} \quad \text{eq. 4}$$

$$\frac{\sigma_{abs,wb}(\lambda 1)}{\sigma_{abs,wb}(\lambda 2)} = \frac{\lambda 1}{\lambda 2}^{-AAE_{wb}} \quad \text{eq. 5}$$

2.3 Individual back trajectory analysis

The BTs used here were calculated for the 2016 – 2019 period with the NOAA Hybrid Single-Particle Lagrangian Integrated Trajectory (HYSPLIT) model (Stein et al. 2015). Arrival height of half the PBL at 1-hour intervals (24 trajectories per day, UTC), for 72 hours back in time using 1° x 1° resolution Global Data Assimilations System (GDAS).

2.4 Emission inventory

The emission inventory was supplied by the Emissions Database for Global Atmospheric Research (EDGAR) developed by the Joint Research Center (JRC). EDGAR provides independent estimates of global anthropogenic emissions and emission trends, based on publicly available statistics (Crippa et al. 2020). The emission inventory is characterized by a world-historical trend from 1970-2018, including emissions of all greenhouse gases, air pollutants, and aerosols. Data are presented for all countries, with emissions provided per main source category, and gridded on a spatial resolution of 0.1° × 0.1°. The version employed in this work is 6.1. This version is time-dependent, with temporal profiles developed for country/region- and sector-specific to achieve the seasonal trend. Here, we choose monthly sector-specific grid maps for black carbon emission, the sectors included in this analysis are no-resuspended traffic and resuspended traffic, shipping, combustion for manufacturing, residential, oil refineries and transformation, agricultural waste burning, and power industry. For further details please refer to the supplementary information and Crippa et al. (2020).

2.5 INTERPLAY approach

The INTERPLAY (iN-siTu obsERvations, hysPLit, And emission inventorY) approach derives from the footprint analysis (e.g. Pöhlker et al. 2019). The method combines back-trajectories and land information to explore air mass history and better interpret the atmospheric composition and its properties. The main advantage is that it is based on computationally inexpensive Lagrangian modeling, being able to gain important insights from large datasets, such as multi-annual observations. The method consists of integrating emissions of a given species along individual BTs to quantify the relative contributions (including information such as distance, and traveled time) to the receptor site. Here, INTERPLAY has been applied to BC, given that it is expected to be relatively stable in the atmosphere within the time frame of BT considered here (72 hours). INTERPLAY firstly interpolates hourly HYSPLIT trajectories into 10-min points for a finer spatial coverage. At distances larger than 40km from the receptor site, it integrates EDGAR emissions over a square of 0.5 × 0.5° centered on the BT latitude and longitude. For distances smaller than 40km, INTERPLAY considers the air mass arrival direction and integrates only the emissions contained in the wind sector of arrival. This criterion has been defined to better represent the emissions in the vicinity of the site (e.g. not consider emissions from Lille if air masses arrive from the opposite direction, Figure S2).

The method proposed here has also been optimized according to certain criteria. For example, tests were performed to not include ground-level emissions when air masses were located above certain heights (e.g. free troposphere as defined by HYSPLIT), but the best correlation between INTERPLAY and observations was obtained without such filtering, probably from inaccurate identification of boundary layer/free troposphere by hysplit, as well as mixing between atmospheric layers during transport. Another filter considered was to limit the effect of aerosol removal by precipitation (known as wash-out). Thus, only BTs with less than 1 mm of integrated rain over the 72h have been used, removing about 41% of the BTs. Despite the simplistic approach (e.g. not accounting for dilution, dry deposition, and inaccuracies in both BT and emission inventories), the method has been observed to correlate fairly well with BC hourly in-situ data (Pearson of 0.41). Finally, to minimize the effect of sporadic, local BC sources on our analysis, INTERPLAY was aggregated into 12h data, and the median of BC information (age, distance, relative sources) was calculated. Those values were then compared with 12h aggregated in-situ observations, however focusing on the 5^{th} percentile of the period, i.e., the baseline values. By decreasing the relevance of local sporadic sources, the ability of INTERPLAY to explain in-situ BC observations further improves (Pearson of 0.60, fig. S3). Further description of the method and effect of different choices made here is given in the supplementary information.

For a seasonal analysis, data are separated into the cold (Sep-Apr) and warm (May-Aug) seasons. Analysis associating in-situ observations with a given source region or sector was performed by applying a minimum contribution of 20% in the integrated BC for each BT (e.g. a point in time is associated with traffic emissions if the corresponding INTERPLAY analysis yields a contribution higher than 20% for that source). Statistics are only shown if more than 70 points are obtained. The BrC lifetime analysis is performed through Multiple Linear Regression (MLR), with in-situ (σ_{BrCabs}) being the explained variable, and the dependent variables obtained from INTERPLAY, namely the BC contribution from traffic and residence sectors, further separated according to the time since emission as "fresh", less than 24h, and "aged", more than 24h. Calculations were performed using the least square method, coefficients were only constrained to be positive and the linear intercept was fixed to zero to explain the absorption measured by the in-situ observations. The analysis on 715 data points of 12h averaged integrated mass (BC-traffic and BC-residential) yielded a Pearson coefficient of 0.8. Further details of the data obtained in every analysis are given in Table 1Table *5.1* List of in situ instrumentation within the PM1 fraction at ATOLL and additional methods used for the analysis under the period of 10 Dec. 2016 – 31 Dec. 2019.

Table 1 List of in situ instrumentation within the PM_1 fraction at the ATOLL platform and additional methods used for the analysis under the period of 10/Dec/2016 – 31/Dec/2019

Method		**Parameter used**	**Time resolution**	**Raw data**	**12h baseline**	**Cold period (12h)**	**Warm period (12h)**
In situ	Aethalometer	σ_{abs} & eBC*	1 min	1 226 414	1 703	726	685
	Nephelometer	σ_{scat}		966 412	1 342	611	622
Hysplit	Hysplit 2020v	Back trajectories	1 hr.	11 607 864	NA+	NA	NA
		Rain				NA	NA

Emission Inventory	EDGAR 2018v	Black Carbon sector-specific grid maps	Monthly	64 800 00	NA	NA	NA
INTERPLAY approach		Integrated BC	1hr	6 144 703	512 058	364 256	147 802

[+]NA = not applicable. The 12-baseline applies only for in situ observations and BC footprint from INTERPLAY for comparison.

INTERPLAY has been developed using Matlab 2020a, and country apportionment has made use of the climate data toolbox (Greene et al. 2019).

3. Results and Discussion

3.1 Wind direction and BC analysis

Figure 1 shows the wind roses (Figure 1a) and the contour plots of average concentration (Figure 1b) according to wind sector and hour of the day of BC_{ff}, BC_{wb}. The data has been separated into warm (May-Aug), and cold seasons (Sep-Apr), following loosely a potential usage of wood combustion as house heating. During the cold period, the highest wind frequency comes from the southwest sector, and the median wind speed of 1.5 m s^{-1}. During the warm period, despite a predominance from the southwest sector, with wind velocities comparable to the cold season, winds were also observed to arise from the north and northeast sectors with moderate speed (2 – 4 m s^{-1}). The average concentration over this multi-annual dataset for BC_{ff} and BC_{wb} are 0.66 and 0.31 µg m^{-3}, respectively. Daily concentration analysis shows BC_{ff} to peak (>0.7 µg m^{-3}) during the morning rush hours during the cold period and warm periods among all wind sectors, highlighting the role of local emissions, overlaid on a background of about 0.2-0.5 µg m^{-3} throughout the day. In contrast, the evening peak is less clear during the warm period, probably due to the effect of higher boundary layer height, combined with a less defined evening peak due to summer holidays in the period. Conversely, BC_{wb} depicts higher concentrations over the eastern sector and is attributed to continental air masses loaded with wood combustion. As expected, BC_{wb} levels are significantly higher during the cold season than the warm season, due to the widespread combustion of wood as house heating (Favez et al. 2021). It is interesting to note that despite the proximity of ATOLL to Lille (~4 km), the wind direction associated with the city (NW) does not show particularly high BC_{ff} or BC_{wb} levels. This corroborates that ATOLL is not dominated by local emissions, but rather regional and Long-Range Transport (LRT). Furthermore, a recent 1-year study at the ATOLL site identified that OA was mainly composed (73%) of oxygenated (i.e. aged) compounds, with only a small fraction related to fresh traffic and wood combustion (11% and 14%, respectively) (Chen et al. 2022). Those results support the use of back-trajectories and emission inventories to explain in-situ data, thus complementing previous studies carried out in the region. For instance, Zhang et al. (2020) show an excellent correlation of BrC absorption at 370nm with levoglucosan across nine air quality monitoring networks in France during winter, suggesting an important contribution of wood burning emissions to ambient BrC aerosol. Specifically, at the suburban site in Paris, the main BrC contributors were found to be the two biomass-burning OA factors; low oxygenated BBOA (40%) and more oxygenated BBOA (30%) followed by oxygenated OA (18%)

and traffic-related OA (8%). At the ATOLL platform, the low average SSA (0.77) underline the important role of LAC in the site. Indeed, at the site organics are found to be responsible for 22% of the absorption in the UV range, whereas, BC and OA contribute 50% of the extinction in the visible range (525nm) (Velazquez-Garcia et al. 2023).

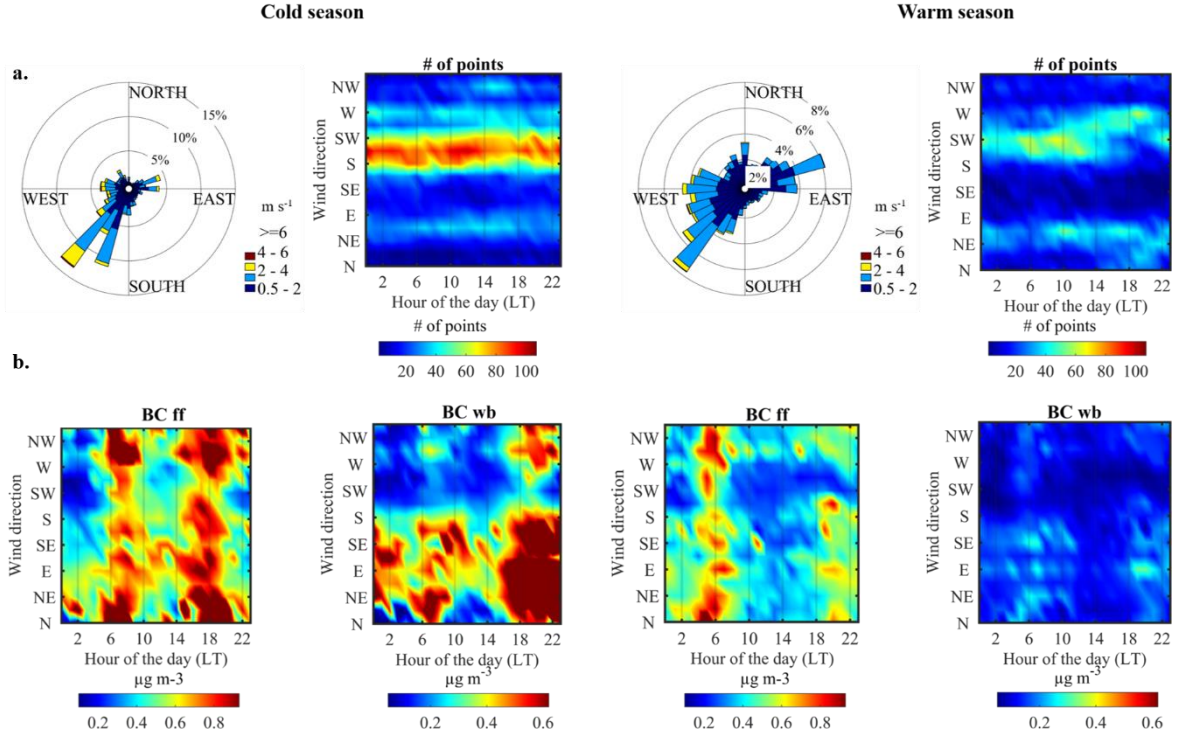

Figure 1: Wind analysis and BC_{ff} and BC_{wb} levels at the ATOLL site during cold (left, Sep-Apr) and warm (right, May-Aug) seasons. a) Wind roses and wind frequency by the hour of the day (minimum wind speed of 0.5 m s^{-1}). b) Contour plots of BC components loadings according to wind sector and hour of the day. The scale of color is based on the 5th and 75th percentile for both seasons.

3.2 Sources of BC at ATOLL

Figure 2 represents the map of BC origins to the ATOLL platform (source strengths multiplied by back trajectory frequency at a given grid point). Results show most of BC impacting ATOLL has its origins in the Benelux (Belgium, Netherlands, Luxemburg) area, including western Germany, south UK (particularly London), Paris, and shipping lanes in the Channel between the North Sea and the Atlantic Ocean. The geographical distribution by sector (traffic, residential, etc.) is further detailed in the SI (Fig. S5). We estimate that most of BC originates from France (8% from the Lille metropolitan area, and 27% from the rest of the country) or nearby Belgium (13%) and the UK (7%). It is interesting to note that the combined shipping lanes over the Channel and North Sea show also a significant contribution with 15%, whereas others sectors (i.e. European countries and seas in the vicinity) with 23%. If separated according to emission sectors, traffic is in the lead (31%), followed by shipping (25%, including also canals and rivers), residential (21%), and industry-manufacturing (17%, Figure 2c). Agricultural waste burning (4%) and the power industry (2%) are minor contributors to BC at ATOLL. It is interesting to note that the so-called aethalometer model is generally interpreted as traffic versus residential, thus neglecting potentially important sources such as shipping or industry-manufacturing. Nonetheless, BC_{wb} has been estimated to be about 32% of BC from in-situ observations, which is not in disagreement with the figures obtained from INTERPLAY (21% from residential) considering that some other sources might be (partially or not) apportioned as BC_{wb}, such as Shipping (e.g. Corbin et al.; 2019) or Agricultural waste burning.

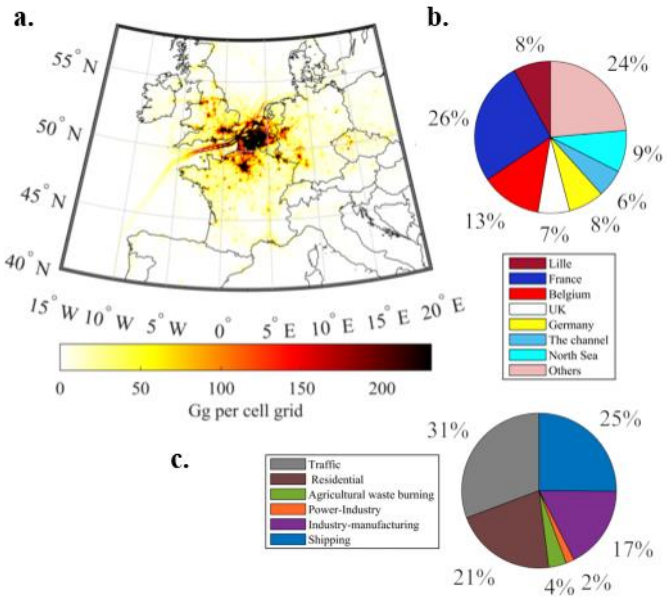

Figure 2: (a) Accumulated contribution of BC to ATOLL in Gg y^{-1} per cell grid and its regional (b) and sectorial (c) distribution over the period Dec 2016 – Dec 2019.

This analysis highlights the importance of the shipping lanes contributing to BC in the region. The North Sea is the main contributor to this sector with 34%, followed by the English Channel with 22% (Fig. S5). It should be noted that the southern North Sea with the large harbors in Calais, Dunkerque, Zeebruge, Antwerp, Rotterdam, and Hamburg is a region with one of the highest ship traffic densities in the world (European Environment Agency 2013; European Commission 2019). As stated previously, the ATOLL platform is roughly 60 km from the Channel coast, and 90 km from Dunkirk harbor. According to the European Environment Agency (2013), it has been estimated that nearly 70% of ship emissions occur within 400 km of coastlines and can contribute to the further inland ambient PM levels between 1 to 7% within the PM_{10} fraction, 1 to 14% within $PM_{2.5}$ fraction and at least 11% for PM_1.

Figure 3 shows the BC spatial distribution and the relative distribution of sources during summer (JJA) and winter (DJF). Spring and fall spatial distribution are showing mixed results between previous extreme seasons and are therefore are shown in the SI. During summertime, the dominating source of BC at ATOLL is shipping (38%) and traffic (33%), showing only a minor contribution of residential (8%), as expected. This significant contribution of shipping arises likely from an intense activity in this sector in the summertime, combined with decreased traffic during the summer holidays. Conversely, during wintertime, residential emission dominates (38%), followed by traffic (28%) and shipping (13%). As for geographical origins, the fraction associated with local emissions (Lille) remains fairly constant across all seasons (7-9%), as well as the fraction associated with French and Belgium emissions corresponding generally to about half of BC. A recent study, although focusing on PM_{10} (Potier et al. 2019), combined chemical transport models and in-situ observations to estimate that long-range emissions could have a strong but infrequent impact on PM_{10} levels in Northern France, while some nearer areas countries (e.g. Benelux region, Germany, Central Europe) had a frequent and predominant impact (30 to 80% of contribution to PM_{10}). Albeit focusing on a specific component of the aerosol population, BC, our results agree with this study, showing that neighboring regions (France, Belgium, the Channel, and the North Sea) dominate light-absorbing aerosols at the ATOLL site.

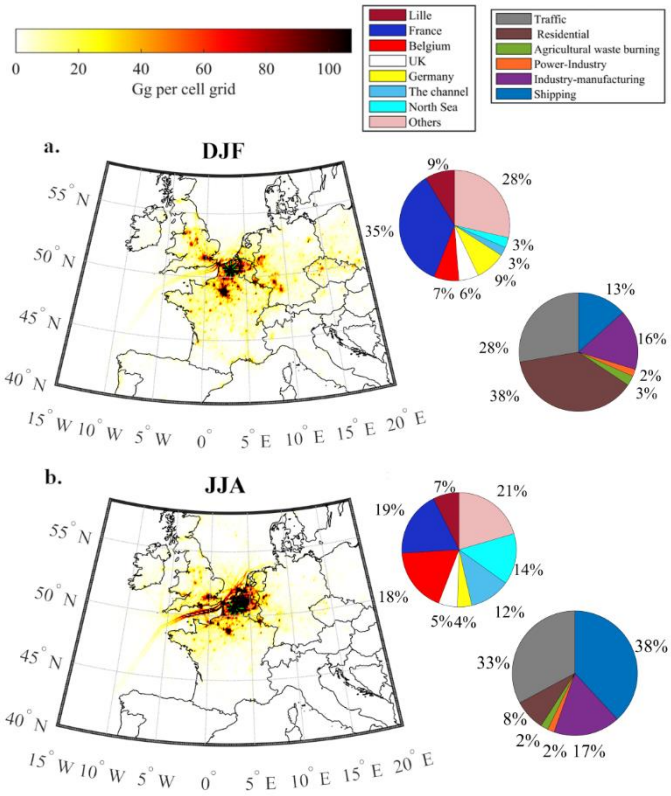

Figure 3: Accumulated contribution of BC to ATOLL in Gg y^{-1} per cell grid and its regional and sectorial distribution for (a) DJF – Winter, (b) JJA -Summer

In addition to estimating geographical and source contributions to LAC observed at ATOLL, one of the main objectives of INTERPLAY is to be able to link in-situ aerosol properties with BC source (e.g. traffic/residential/shipping/etc.) and time since emission, i.e. its age. Figure 4 shows the $AAE_{370\text{-}880nm}$ and concentrations of BC_{ff} and BC_{wb} when the incident air masses have at least 20% BC originating from a given region or source. Figure 4a associates the AAE of the four sectors employed in this analysis. By combining the INTERPLAY approach with in-situ measurements, for the residential sector, we obtained an $AAE_{370\text{-}880nm}$ ~ 1.5 (with values up to 1.6), whereas, for emissions from industry-manufacturing, traffic, and shipping, we found a lower $AAE_{370\text{-}880nm}$ of ~1.3. The trend of AAE from residential (wood combustion) and traffic agree with the literature, while the AAE for BC_{ff} is low (1), the AAE or BC_{wb} is higher (2) (Sandradewi et al. 2008). Nonetheless, it is important to note that notable variations have been observed (Heilin et al. 2021, Petit et al. 2021; Zhang et al. 2019; Zotter et al. 2017). For instance, in the study of Heilin et al. (2021), diesel bus exhaust emissions have an $AAE_{470\text{-}950nm}$ between 0.8-1.2, the $AAE_{470\text{-}950nm}$ from the pellet boiler emissions during normal operation was 1.4 ± 0.1, shipping using high and low sulfur content had an $AAE_{470\text{-}950nm}$ of 2.0±0.1 and 1.0±0.1, respectively. The data from ATOLL agrees with a lower AAE range, suggesting a dominance of low sulfur content fuels in the region. It is important to note that the values of AAE obtained here and associated with different sources include regional atmospheric aerosol processing and complex mixing, in contrast to near-source characterization, further addressed below. Thus, although the AAE value is expected to be 1 given the regional sources associated with traffic emissions during the summer (Favez et al. 2021), the observed AAE values on the shelf do not show this number, suggesting a secondary process leading to BrC formation and/or different mixing state (BC with non-absorbing coatings) (Chylek et al. 2019; Moise, Flores, and Rudich 2015; Saleh et al. 2013; Zhang et al. 2020).

Figure 4b shows the in-situ aerosol properties associated with main regions (France, Belgium, Germany, UK), and separated into cold and warm seasons. The concentration of BC_{ff} is higher during the cold season across all regions, probably as a result of a shallow boundary layer. Furthermore, as expected, BC_{wb} concentration is significantly higher during the cold season, which can be explained by house heating, compounded with the same processes as for BC_{ff}. When air masses originate from the east (e.g. Germany), we observe the highest concentration of both BC_{ff} and BC_{wb} during the cold season. This is in line with previous findings, which in addition to being BC hotspots (e.g. transport, intensive agriculture, heavy industry, metallurgy, and exploitation of open mines), air masses are generally drier and colder, with lower dispersion favoring air pollutant accumulation (Asmi et al. 2011; Barnaba et al. 2011; Bovchaliuk et al. 2013; Giles et al. 2012). During the warm period, BC_{ff} concentration at ATOLL when receiving air masses dominated from domestic emissions (i.e. France) is comparable to air masses from the east, linked to the high density of population in Central Europe and the intensity of road traffic over the area (Eurostat 2022).

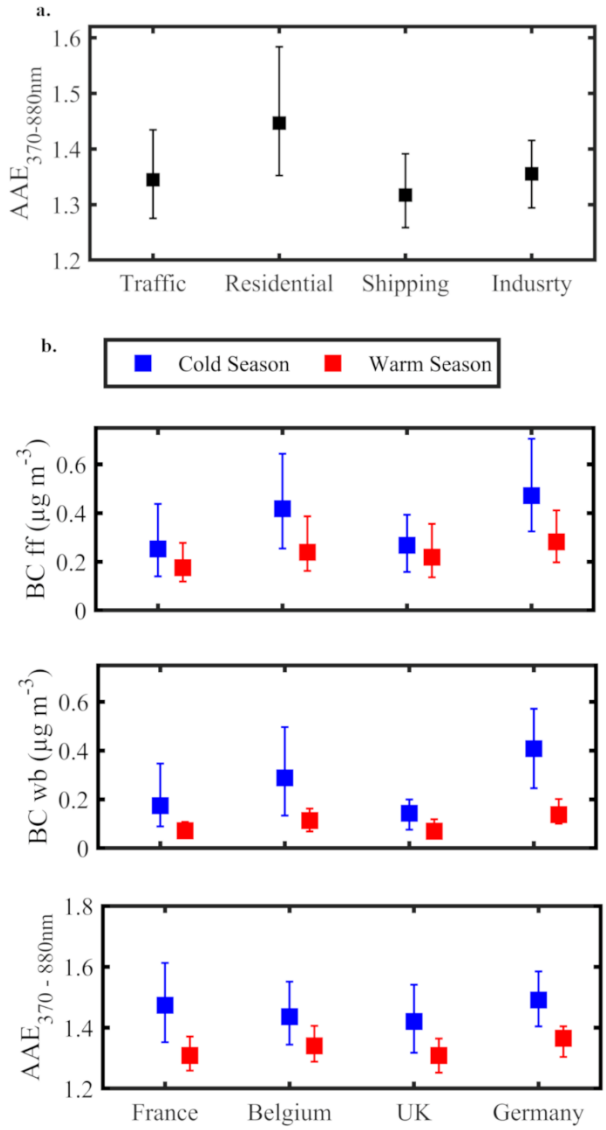

Figure 4: Statistics of BC in-situ data associated with different sectors (a) and regions (b) using the INTERPLAY method. Absorption Ångström Exponent calculated in the pair of wavelengths 370-880nm ($AAE_{370\text{-}880nm}$, y-axis left), BC_{ff} concentration, and BC_{wb} concentration (in µg m^{-3} y-axis left).

3.3 Brown carbon origins and lifetime

On average, BrC absorption at ATOLL was 5.1 Mm^{-1}, its contribution to absorption at 370nm was 29.0% and presents a seasonal trend, being higher during winter (30%) compared to summer (18%), as discussed previously, associated with BC_{wb} during the cold season (Velazquez-Garcia et al., 2023). The average contribution is comparable to Liakakou et al. (2020) in Athens (23.7%), albeit with a different instrument model (AE31). Furthermore, other sites have reported comparable or higher BrC contribution to aerosol light absorption, such as the southeastern margin of the Tibetan Plateau (20% to 40%) (Wang et al. 2019), Central Amazon (17% - 26%) (Saturno et al. 2018), at the northern peninsular Southeast Asia (46%) (Pani et al. 2021), and in Xi'an, China (41%) (Zhu et al. 2021). This large difference (>40%) may be explained by active fires over the region, displaying the substantial open biomass burning activities in and around the sampling location (Pani et al. 2021) as well as some contribution of secondary BrC (Wang et al. 2019). Certainly, residential wood burning has been assessed as a major source of BrC in various urban (Favez et al. 2009; Moschos et al. 2018; Zhang et al. 2020) and rural (Golly et al., 2019) environments. It is interesting to note that the contribution of BrC to absorption observed at the ATOLL platform is comparable with other European cities (e.g. Athens), despite some differences in climate and fuel for heating (Rehfeldt et al. 2020). It is noteworthy to mention that the methods to retrieve BrC absorption also impact its estimates. For instance, Zhang et al., (2020) applied a sensitivity test using three different values of AAE for pure BC (AAE_{BC}) to calculate BrC absorption, choosing 0.9 as a reference. The sensitivity test performed by Zhang et al. (2020) indicated an uncertainty of approximately 11% at 370nm when using these three different AAE values (0.9, 1, 1.1) to calculate BrC. Moreover, de Sá et al. (2019) estimated BrC absorption by calculating for every point in time the AAE_{BC} at the wavelengths 700 and 880 nm instead of using a fixed value.

Figure 5 exhibits the diel cycle of BrC absorption at 370nm and its fraction during winter and summer. The displayed diel profiles show a significant increase in the BrC fraction during nighttime and to less extent during the day. While during winter the diel profiles are consistent with those generally observed for BC_{wb} (Favez et al. 2010; Sciare et al. 2011; Zhang et al. 2019, 2020), during summer, the significant increase of BrC fraction suggests BrC formation (combined undoubtedly with bleaching). Indeed, different types of chromophores can be emitted from various sources and/or formed in the atmosphere. Laboratory studies (Lin et al. 2015; Flores, and Rudich 2015; Teich et al. 2017) have found that anthropogenic VOCs (benzene, toluene, phenols, and polycyclic aromatics hydrocarbons – PAHs) react with nitrogen oxides and produce nitro aromatics, identified as light-absorbing compounds. Zhao et al. (2015) documented that the presence of oxidants like O_3 and OH radicals (abundant during the daytime and may degrade BrC into smaller and more volatile organic compounds). Higher absorption during the evening into the night is attributable to the emission rates of primary sources, in addition to shallow boundary layer height, and the absence of volatilization and photobleaching processes (Satish et al. 2017). Several studies in urban areas (Liakakou et al. 2020; Satish et al. 2017; Stanaway et al. 2018; Wang et al. 2018; Zhang et al. 2019; Zhang et al. 2020) showed a similar trend with higher values usually observed at night. According to the authors, the enhanced NO_3 oxidation at night may lead to more BrC formation than during the daytime. Other authors (Gao et al. 2022; Wang et al. 2019) show an opposite trend in remote sites, where higher values are observed during the day, attributed to the influences of photooxidation processes forming BrC through photochemical oxidation during the daytime. Overall, the BrC levels in the atmosphere are a complex result of primary sources and secondary processes (condensation, volatilization), mixing with other aerosol types (core-shell mixing), and effects from local meteorology and boundary-layer dynamics (Lambe et al. 2013; Li et al. 2018; Romonosky et al. 2016).

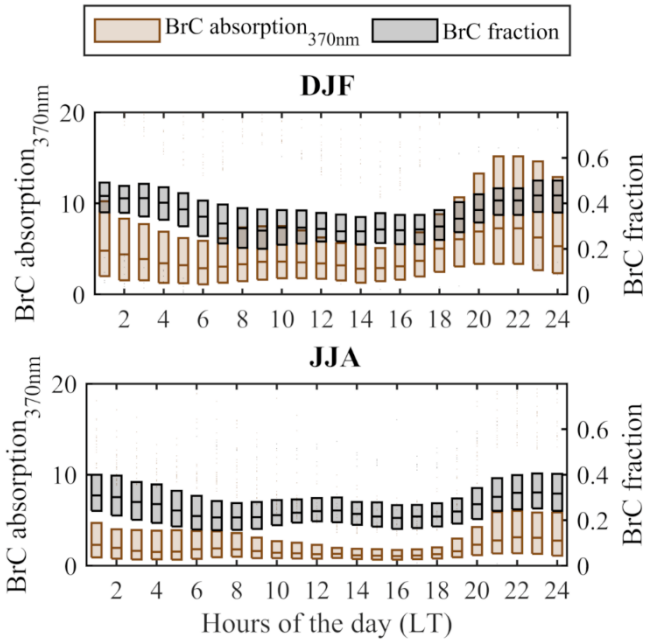

Figure 5: Diel cycle of BrC absorption (in Mm^{-1}) calculated at 370nm (y-axis left) and BrC fraction (y-axis right) at the ATOLL platform. The line is the median, whereas the box shows the interquartile range.

Combining in-situ observations and INTERPLAY allows us to analyze the effect of atmospheric aging on BrC lifetime. This analysis has focused only on the cold season, given the widespread use of wood combustion as residential heating during that period. As described in section 2, we further separate traffic and residential into fresh (BC emitted less than 24h) and aged (more than 24h). It is important to note that this analysis includes the two main sources during the cold period (Sep-Apr, traffic and residential correspond to 66% of BC according to INTERPLAY), however neglecting shipping and industrial emissions. Here, INTERPLAY has identified a comparable AAE of those sectors with traffic (~1.3), therefore, they were not included in this analysis which would increase the number of independent variables without a clear role in BrC loadings.

Figure 6a shows the relative contribution of fresh and aged BC from traffic and residential for the cold season, showing a relatively equilibrated contribution among the four categories (fresh being slightly higher with 28% for both sectors, whereas aged BC is higher for residential than traffic with 24% and 20%, respectively). Through Multiple Linear Regression, we identified that the dominating component for BrC is fresh residential (72%), followed by aged residential (16%) and aged traffic (12%), and no contribution from fresh traffic (Figure 6b). Thus, this analysis suggests that, after 24h of atmospheric aging, the BrC components associated with residential heating have strongly decreased. Generally, atmospheric observations report longer BrC absorption lifetimes (~1 day) (Forrister et al. 2015; Wang et al. 2016; Wong et al. 2019) than laboratory experiments (hours) (Saleh 2020). Forrister et al. (2015) and Selimovic et al. (2019) observed a substantial decay in aerosol UV light absorption in biomass-burning plumes, corresponding to a half-life of 9 to 15 h. Lin et al. (2017) reported the rapid evolution of both the BBOA composition and optical properties during a nationwide biomass-burning event in Israel, however, an important fraction of BrC persisted even after long aging times. Benedict et al. (2017) further observed that smoke impacts from a nearby wildfire had a much higher smoldering-to-flaming ratio at night than during the day, which then suggests the potential for increased BrC formation at night (Saide et al. 2015). It is also known that smoldering combustion of biomass emits many precursors, including monoterpenes furans, and cresol (Stockwell et al. 2015), which can react quickly with the major nighttime oxidant, NO_3, and ostensibly form UV-absorbing

organic nitrates that could augment BrC. Saleh et al., (2013) burned pocosin pine and oak, and found that photochemically aged aerosols were more absorbing than fresh emissions at 370 and 470 nm after 1 h. Zhong & Jang, (2014) tracked the absorption coefficients of BBOA during solar exposure in a smog chamber and observed an increase of 11 %–54 % in the integrated mass absorption cross section (280–600 nm) in the first half of the day, followed by a decrease in the afternoon. Furthermore, the FireLab from Missoula, Montana in the USA (Fleming et al. 2020), collected emitted biomass burning organic aerosol particles onto Teflon filters and analyzed them offline. Aiming to study the stability of the observed BrC compounds concerning photodegradation, BBOA particle samples were irradiated directly on filters with near UV (300–400 nm) radiation, followed by extraction and analysis. They found that the lifetimes of individual BrC chromophores depended on the fuel type and the corresponding combustion condition. Other studies (Lee et al. 2014; Sareen et al. 2010, 2010; Zhao et al. 2015; Zhong and Jang 2014) show that some types of BrC, depending on the precursor, can experience rapid photochemical degradation or formation via both direct photolysis and oxidation. Browne et al. (2019) and Sumlin et al. (2018) suggest that the photobleaching observed for smoldering biomass-combustion BrC in the aerosol phase has three key differences from secondary BrC: 1) combustion BrC exhibits a period photo enhancement before photobleaching (Wong et al. 2019; Wong, Nenes, and Weber 2017; Zhong and Jang 2014); 2) the decay of absorption occurs at longer timescales than secondary BrC (Wong, Nenes, and Weber 2017); and 3) a fraction of combustion BrC is resistant to photobleaching.

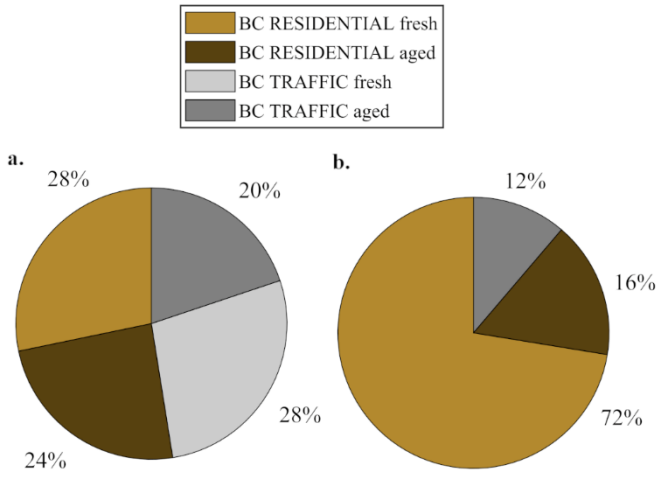

Figure 6: Brow carbon lifetime. a) Relative contribution to the mass of different Black Carbon sources (residential, traffic) emitted <24hrs (fresh) and >24hrs (aged). b) Relative contribution to light BrC absorption calculated at 470nm explained by the mass of different Black Carbon sources (residential, traffic) emitted <24hrs (fresh) and >24hrs (aged).

To summarize the literature survey above, much work has been done in terms of characterizing the optical properties of photochemically aged BBOA and surrogates. Although much of BrC lifetime has been studied previously and showed a plethora of results according to burning material and type of atmospheric aging, observational data arise mostly from laboratory-controlled experiments or summertime events associated with wildfires. Therefore, studies focusing on the ubiquitous wood-combustion usage as residential heating, particularly in Central Europe, were still lacking, to our knowledge. The data retrieved here suggests that despite generally low photochemistry during wintertime, there is a significant reduction in the BrC component of residential heating in this season after 24h since emission. This has not only climatic impacts but also direct consequences on the in-situ

source apportionment methods, leading to the misattribution of 24h-aged BC_{wb} to traffic, and thus less efficient pollution abatement strategies.

4 Conclusions and perspectives

In France, the limit values for PM concentration levels (15µg m^{-3} and 5µg m^{-3}, for PM_{10} and $PM_{2.5}$, recommended by the World Health Organization) are frequently exceeded, as in many European countries. The main origins of PM are residential wood burning (during the cold period), road transport (exhaust and non-exhaust) throughout the year, and other sources distributed more heterogeneously across regions, such as shipping and industrial emissions (Favez et al. 2021). Thus, in this work, we analyze origins (local, domestic-rest of the country, and transboundary) and associated optical properties of LAC influencing the ATOLL platform. Here, we performed a combined analysis of local winds and newly developed INTERPLAY (combining iN-situ obserERvations hysPLit And emission-inventorY), an approach merging multiannual coincident real-time submicron aerosols observations, individual back trajectories and emission inventories.

The in-situ aerosol absorption measurements performed by the aethalometer at ATOLL can be used to derive a simple BC source apportionment into fossil fuel and wood burning, the latter being assumed to have strong absorption in the UV and blue parts of the light spectrum from polycyclic aromatic hydrocarbons and humic-like substances (Sandradewi et al. 2008). The results of this approach exhibit differences in sources during the cold and warm seasons. For instance, during the cold season, peaks of BC_{ff} (0.98 µg m^{-1} -75^{th} percentile) are associated with all wind sectors during rush traffic hours while, BC_{wb} peaks (0.83 µg m^{-1} - 75^{th} percentile) are mostly associated with easterly winds, resulting of meteorology and arrival of continental air masses. During the warm season, increased dispersion and higher boundary layer height, combined with the holiday period lead to an average decrease of BC_{ff} decrease by about 37%, whereas a strong reduction in house heating (combined with the reasons above) is mostly associated with the 82% decrease in BC_{wb}.

In this analysis, we applied INTERPLAY to ~3 years of coincident in-situ measurements from 10/Dec/2016 – 31/Dec/2019 performed at the ATOLL platform. The latest monthly EDGAR emission inventory (Crippa et al. 2020) for black carbon was used. The monthly sector-specific grid maps include traffic (resuspended and no-resuspended), residential, shipping, industrial-manufacturing (combustion for manufacturing as well as oil refineries and transformation) agriculture waste burning, and power industry. Results of the BC footprint obtained with INTERPLAY show a reasonably good agreement with in-situ BC (R^2:0.36 with 12h baseline). The multiannual analysis of the spatial and relative contribution applying INTERPLAY exhibit 8% of the local contribution from the Lille area, 27% domestic (rest of the French territory), and 65% of transboundary (with Belgium 13%, North Sea 9%, Germany 8%, UK 7%, the Channel 6%, and others sea and countries making up the remainder). The main sectors contributing to the BC levels at the ATOLL platform are the traffic (31%), followed by the shipping (25%), the residential (21%), and the industry-manufacturing (17%) sectors. The agriculture waste burning (4%) and the power industry (2%) sectors contribute less.

During summer, the shipping sector is responsible for 38% of the contribution to BC in ATOLL, highlighting the importance of this sector in Northern France. In addition, during this season, an additional key sector to the contribution of BC in the region is the traffic sector (33%), yet, this sector remains the main contributor during spring (30%) and fall (32%). The residential sector is the main contributor to BC during winter, increasing its contribution up to 30% respective to summer. The INTERPLAY approach enriched the in-situ observations, allowing to identify and compare the associated BC source apportionment (BC_{ff}, BC_{wb}) and, the respective optical

properties ($AAE_{370\text{-}880nm}$) to the air masses reaching the site from different regions during the cold (Sep-Apr) and warm season (May-Aug), with at least 20% higher of the total BC footprint. Results regarding the regions showed an average concentration of black carbon from fossil fuels higher during the cold season for all regions, although differences between cold and warm seasons remain small. INTERPLAY identified a high average concentration of BC_{ff} and BC_{wb} coming from Germany during the cold season and warm seasons. Moreover, during the cold season, the $AAE_{370\text{-}880nm}$ reached its maximum value for all countries, mainly related to the growth in residential heating emissions, whereas, during the warm season, although the major source of emission is traffic related, the $AAE_{370\text{-}880nm}$ is higher (1.3) than the value expected (1) for pure BC, suggesting BrC formation. Looking at the $AAE_{370\text{-}880nm}$ by sectors, while INTERPLAY recognized an $AAE_{370\text{-}880nm}$ of 1.4 for the residential sector, the $AAE_{370\text{-}880nm}$ of 1.3 is associated with shipping, industry and traffic sectors. The $AAE_{370\text{-}880nm}$ values for air masses related to traffic emissions at the ATOLL platform are relatively higher than what has been reported by different authors (0.9 - 1.1) (Petit et al. 2021; Sandradewi et al. 2008; Zhang et al. 2019, Zhang et al. 2020; Zotter et al. 2017).

In this work, we analyzed the contribution and diurnal profile of BrC absorption in the UV range. The average contribution to absorption (29%) at the site is comparable with other European sites (e.g. Athens), increasing during winter by 9%. The BrC diurnal profile shows higher values during the late evening to early morning hours, reduced by 44% as the day progressed. This trend is the result of primary sources and secondary processes (condensation, volatilization), mixing with other aerosol types (core-shell mixing), and effects from local meteorology and boundary-layer dynamics. It is important to note that, the BrC levels may be impacted by the method applied to retrieve its absorption. For instance, assuming a constant value of AAE =1 for pure BC may be wrong. In fact, this analysis reported, for air masses associated with traffic sources, an average AAE value slightly higher than the one proposed by other authors. Further analysis should be done regarding the AAE associated with pure BC in the site.

Finally, we used the INTERPLAY approach to explore the lifetime and origins of BrC during the cold season. To do so, owing to the INTERPLAY approach, we separate air masses emitted 24hrs earlier (fresh aerosols) and more than 24hrs earlier (aged aerosols) from the BC-footprint for the traffic and residential sector. In general, the highest contribution to BC are from the fresh emissions for both, the residential (28 %) and traffic (28 %) sector while, aged emissions represent 24% and 20% for the residential and traffic sector, respectively. The BrC absorption was calculated at 470nm from the in-situ observations and used to calculate the contribution to the BrC absorption of fresh and aged aerosols from the residential and traffic sectors. By applying a multiple linear regression, we obtained 72% of the contribution to BrC absorption at 470nm by air masses emitted the 24 last hours from the residential sector, whereas, only 28% of the contribution is attributed to aged air masses emitted from the residential (16%) sector and traffic (12%). These results call attention to the bleaching effect after 24hrs of atmospheric transport.

Overall, this study offers the possibility to exploit the in-situ observations on a bigger scale via the INTERPLAY approach. Our multiannual and seasonal analysis employing INTERPLAY at the ATOLL platform highlights the possibility of quantifying and identifying the origins of light-absorbing aerosols and their associated optical properties. This work supports the evidence of high contribution to carbonaceous aerosols emitted by the traffic, shipping, and residential sectors in the region, where, residential has a strong seasonality mark. Furthermore, this chapter calls attention to the precautions needed when performing aerosol characterization and source

apportionment based on AAE values. Based on INTERPLAY results, the source apportionment of light-absorbing carbonaceous matter into fossil fuel, and wood burning fractions may be biased since the value of AAE not only depends on the class of combustion, type of fuel, and kind of wood burned, (e.g. high AAE by using high sulfur content as fuel in shipping emissions), but it also depends on the atmospheric transport giving a relatively low, yet highly variable, AAE values in wood combustion emissions. In addition, it points out the lack of studies of atmospheric aging based on atmospheric observations, relevant to the quantification of the radiative impact of organic species to be accounted for in climate calculations. This study opens the possibility to explore the aging of LAC employing atmospheric long-term in situ observations, it also recommends analyzing the aging by daytime and, it encourages the investigation of BrC aging during nighttime, when secondary reactions with precursors (e.g. NO_3) can lead to the formation of BrC.

Author acknowledgment

Conceptualization: JFB, AVG; Data Curation: AVG, JFB, SC, VR; Formal analysis: AVG, JFB, Funding acquisition: AVG, IC, VR; Investigation: AVG, JFB, SC, VR; Methodology: JFB, AVG; Project administration: IC, VR; Resources: VR; Software: AVG, JFB, Supervision: IC, VR; SC, Validation: JFB, SC, ET, EB, VR; Visualization: AVG; Writing – Original Draft: AVG, JFB; Writing – Review & Editing: SC, IC, VR.

The authors are really grateful to the staff at LOA, in particular Prof. P. Goloub, F. Auriol and R. De Filippi, for supporting the technical and logistical implementation of the instruments, and to Dr. L.-H. Rivellini (now at University of Toronto) for her early involvement. We thank T. Podvin (LOA) for providing the weather data at ATOLL, and Aude Bourin (IMT Nord Europe) for the execution of the back trajectories.

Funding acknowledgment

A. Velazquez Garcia's PhD grant is supported by CONACyT PhD grant (2019-000004-01EXTF-00001) and the Hauts-de-France Regional Council. IMT Nord Europe and LOA acknowledge financial support from the Labex CaPPA project, which is funded by the French National Research Agency (ANR) through the PIA (Programme d'Investissement d'Avenir) under contract ANR-11-LABX-0005-01, and the CLIMIBIO project, both financed by the Regional Council "Hauts-de-France" and the European Regional Development Fund (ERDF). IMT Nord Europe participated in the COST COLOSSAL Action CA16109. The ATOLL site is one of the French ACTRIS National Facilities and contributes to the CARA program of the LCSQA funded by the French Ministry of Environment.

References

Asmi, A. et al. 2011. "Number Size Distributions and Seasonality of Submicron Particles in Europe 2008–2009." Atmospheric Chemistry and Physics 11(11): 5505–38.

Barnaba, F., F. Angelini, G. Curci, and G. P. Gobbi. 2011. "An Important Fingerprint of Wildfires on the European Aerosol Load." Atmospheric Chemistry and Physics 11(20): 10487–501.

Bond, Tami. C. et al. 2013. "Bounding the Role of Black Carbon in the Climate System: A Scientific Assessment." Journal of Geophysical Research: Atmospheres 118(11): 5380–5552.

Bond, Tami C. et al. 2004. "A Technology-Based Global Inventory of Black and Organic Carbon Emissions from Combustion." Journal of Geophysical Research: Atmospheres 109(D14). https://onlinelibrary.wiley.com/doi/abs/10.1029/2003JD003697 (October 1, 2022).

Bovchaliuk, A. et al. 2013. "Variability of Aerosol Properties over Eastern Europe Observed from Ground and Satellites in the Period from 2003 to 2011." Atmospheric Chemistry and Physics 13(13): 6587–6602.

Browne, Eleanor C. et al. 2019. "Effect of Heterogeneous Oxidative Aging on Light Absorption by Biomass Burning Organic

Aerosol." Aerosol Science and Technology 53(6): 663–74.
Chen, Gang et al. 2022. "European Aerosol Phenomenology − 8: Harmonised Source Apportionment of Organic Aerosol Using 22 Year-Long ACSM/AMS Datasets." Environment International 166: 107325.
Chen, Lung-Wen Antony et al. 2021. "Brownness of Organic Aerosol over the United States: Evidence for Seasonal Biomass Burning and Photobleaching Effects." Environmental Science & Technology 55(13): 8561–72.
Chylek, Petr et al. 2019. "Mie Scattering Captures Observed Optical Properties of Ambient Biomass Burning Plumes Assuming Uniform Black, Brown, and Organic Carbon Mixtures." Journal of Geophysical Research: Atmospheres 124(21): 11406–27.
Corbin, J. C. et al. 2019. "Infrared-Absorbing Carbonaceous Tar Can Dominate Light Absorption by Marine-Engine Exhaust." npj Climate and Atmospheric Science 2(1): 1–10.
Crippa, M. et al. 2013. "Wintertime Aerosol Chemical Composition and Source Apportionment of the Organic Fraction in the Metropolitan Area of Paris." Atmospheric Chemistry and Physics 13(2): 961–81.
Crippa, Monica et al. 2020. "High Resolution Temporal Profiles in the Emissions Database for Global Atmospheric Research." Scientific Data 7(1): 121.
Cuesta-Mosquera, Andrea et al. 2021. "Intercomparison and Characterization of 23 Aethalometers under Laboratory and Ambient Air Conditions: Procedures and Unit-to-Unit Variabilities." Atmospheric Measurement Techniques 14(4): 3195–3216.
De Haan, David O. et al. 2011. "Formation of Nitrogen-Containing Oligomers by Methylglyoxal and Amines in Simulated Evaporating Cloud Droplets." Environmental Science & Technology 45(3): 984–91.
Denjean, Cyrielle et al. 2020. "Unexpected Biomass Burning Aerosol Absorption Enhancement Explained by Black Carbon Mixing State." Geophysical Research Letters 47(19): e2020GL089055.
Di Lorenzo, Robert A. et al. 2017. "Molecular-Size-Separated Brown Carbon Absorption for Biomass-Burning Aerosol at Multiple Field Sites." Environmental Science & Technology 51(6): 3128–37.
Drinovec, L. et al. 2015. "The 'Dual-Spot' Aethalometer: An Improved Measurement of Aerosol Black Carbon with Real-Time Loading Compensation." https://oa.tib.eu/renate/handle/123456789/765 (March 8, 2022).
European Environment Agency. 2013. "The Impact of International Shipping on European Air Quality and Climate Forcing — European Environment Agency." https://www.eea.europa.eu/publications/the-impact-of-international-shipping (August 18, 2022).
European Commission. 2019. "Top Cargo Ports in 2017." https://ec.europa.eu/eurostat/web/products-eurostat-news/-/DDN-20190711-1 (August 18, 2022).
Eurostat. 2022. "Population Statistics at Regional Level." https://ec.europa.eu/eurostat/statistics-explained/index.php?title=Population_statistics_at_regional_level (October 14, 2022).
Favez, Olivier. et al. 2010. "Inter-Comparison of Source Apportionment Models for the Estimation of Wood Burning Aerosols during Wintertime in an Alpine City (Grenoble, France)." Atmospheric Chemistry and Physics 10(12): 5295–5314.
Favez, Olivier et al. 2009. "Evidence for a Significant Contribution of Wood Burning Aerosols to PM2.5 during the Winter Season in Paris, France." Atmospheric Environment 43(22): 3640–44.
Favez, Olivier et al. 2021. "Overview of the French Operational Network for In Situ Observation of PM Chemical Composition and Sources in Urban Environments (CARA Program)." Atmosphere 12(2): 207.
Fleming, Lauren T. et al. 2020. "Molecular Composition and Photochemical Lifetimes of Brown Carbon Chromophores in Biomass Burning Organic Aerosol." Atmospheric Chemistry and Physics 20(2): 1105–29.
Flores, J. M. et al. 2014. "Complex Refractive Indices in the Near-Ultraviolet Spectral Region of Biogenic Secondary Organic Aerosol Aged with Ammonia." Physical Chemistry Chemical Physics 16(22): 10629–42.
Forrister, Haviland et al. 2015. "Evolution of Brown Carbon in Wildfire Plumes." Geophysical Research Letters 42(11): 4623–30.
Forster, Piers et al. 2021. "The Earth's Energy Budget, Climate Feedbacks, and Climate Sensitivity." In Climate Change 2021: The Physical Science Basis. Contribution of Working Group I to the Sixth Assessment Report of the Intergovernmental Panel on Climate Change, eds. Valérie Masson-Delmotte et al. Cambridge University Press.
Gao, Yuan et al. 2022. "Optical Properties of Mountain Primary and Secondary Brown Carbon Aerosols in Summertime." Science of The Total Environment 806: 150570.
Giles, D. M. et al. 2012. "An Analysis of AERONET Aerosol Absorption Properties and

Classifications Representative of Aerosol Source Regions." Journal of Geophysical Research: Atmospheres 117(D17). https://onlinelibrary.wiley.com/doi/abs/10.1029/2012JD018127 (August 18, 2022).

Golly, B. et al. 2019. "Organic Markers and OC Source Apportionment for Seasonal Variations of PM2.5 at 5 Rural Sites in France." Atmospheric Environment 198: 142–57.

Greene, Chad A. et al. 2019. "The Climate Data Toolbox for Matlab." https://zenodo.org/record/2590731 (April 5, 2022).

Haan, David O. De et al. 2009. "Secondary Organic Aerosol-Forming Reactions of Glyoxal with Amino Acids." Environmental Science & Technology 43(8): 2818–24.

Harrison, Mark A. J. et al. 2005. "Nitrated Phenols in the Atmosphere: A Review." Atmospheric Environment 39(2): 231–48.

He, Quanfu et al. 2021. "Optical Properties of Secondary Organic Aerosol Produced by Nitrate Radical Oxidation of Biogenic Volatile Organic Compounds." Environmental Science & Technology 55(5): 2878–89.

Helin, A. et al. 2021. "Variation of Absorption Ångström Exponent in Aerosols From Different Emission Sources." Journal of Geophysical Research: Atmospheres 126(10): e2020JD034094.

Hems, Rachel F. et al. 2021. "Aging of Atmospheric Brown Carbon Aerosol." ACS Earth and Space Chemistry 5(4): 722–48.

Kanakidou, M. et al. 2005. "Organic Aerosol and Global Climate Modelling: A Review." Atmospheric Chemistry and Physics 5(4): 1053–1123.

Kumar, Nivedita K. et al. 2018. "Production of Particulate Brown Carbon during Atmospheric Aging of Residential Wood-Burning Emissions." Atmospheric Chemistry and Physics 18(24): 17843–61.

Lambe, Andrew T. et al. 2013. "Relationship between Oxidation Level and Optical Properties of Secondary Organic Aerosol." Environmental Science & Technology 47(12): 6349–57.

Laskin, Alexander, Julia Laskin, and Sergey A. Nizkorodov. 2015. "Chemistry of Atmospheric Brown Carbon." Chemical Reviews 115(10): 4335–82.

Lee, Hyun Ji (Julie) et al. 2014. "Effect of Solar Radiation on the Optical Properties and Molecular Composition of Laboratory Proxies of Atmospheric Brown Carbon." Environmental Science & Technology 48(17): 10217–26.

Li, Sheng et al. 2018. "Filter-Based Measurement of Light Absorption by Brown Carbon in PM2.5 in a Megacity in South China." Science of The Total Environment 633: 1360–69.

Liakakou, E. et al. 2020. "Long-Term Brown Carbon Spectral Characteristics in a Mediterranean City (Athens)." Science of The Total Environment 708: 135019.

Lin, Peng et al. 2017. "Molecular Chemistry of Atmospheric Brown Carbon Inferred from a Nationwide Biomass Burning Event." Environmental Science & Technology 51(20): 11561–70.

Lin, Peng, Julia Laskin, Sergey A. Nizkorodov, and Alexander Laskin. 2015. "Revealing Brown Carbon Chromophores Produced in Reactions of Methylglyoxal with Ammonium Sulfate." Environmental Science & Technology 49(24): 14257–66.

Liu, Chao, Chul Eddy Chung, Yan Yin, and Martin Schnaiter. 2018. "The Absorption Ångström Exponent of Black Carbon: From Numerical Aspects." Atmospheric Chemistry and Physics 18(9): 6259–73.

Liu, Dantong et al. 2021. "Evolution of Aerosol Optical Properties from Wood Smoke in Real Atmosphere Influenced by Burning Phase and Solar Radiation." Environmental Science & Technology 55(9): 5677–88.

Liu, Jiumeng et al. 2016. "Optical Properties and Aging of Light-Absorbing Secondary Organic Aerosol." Atmospheric Chemistry and Physics 16(19): 12815–27.

Lu, Jessica W. et al. 2011. "Changes in the Optical Properties of Benzo[a]Pyrene-Coated Aerosols upon Heterogeneous Reactions with NO2 and NO3." Physical Chemistry Chemical Physics 13(14): 6484–92.

Lu, Zifeng et al. 2015. "Light Absorption Properties and Radiative Effects of Primary Organic Aerosol Emissions." Environmental Science & Technology 49(8): 4868–77.

Mbengue, Saliou et al. 2020. "Characterization of Equivalent Black Carbon at a Regional Background Site in Central Europe: Variability and Source Apportionment☆." Environmental Pollution 260: 113771.

Mohr, C. et al. 2012. "Identification and Quantification of Organic Aerosol from Cooking and Other Sources in Barcelona Using Aerosol Mass Spectrometer Data." Atmospheric Chemistry and Physics 12(4): 1649–65.

Moise, Tamar, J. Michel Flores, and Yinon Rudich. 2015. "Optical Properties of Secondary Organic Aerosols and Their Changes by Chemical Processes." Chemical Reviews 115(10): 4400–4439.

Moschos, Vaios et al. 2018. "Source Apportionment of Brown Carbon Absorption by Coupling Ultraviolet–Visible Spectroscopy with Aerosol Mass Spectrometry." Environmental Science & Technology Letters 5(6): 302–8.

Müller, T., M. Laborde, G. Kassell, and A. Wiedensohler. 2011. “Design and Performance of a Three-Wavelength LED-Based Total Scatter and Backscatter Integrating Nephelometer.” Atmospheric Measurement Techniques 4(6): 1291–1303.

Ng, Nga Lee et al. 2017. “Nitrate Radicals and Biogenic Volatile Organic Compounds: Oxidation, Mechanisms, and Organic Aerosol.” Atmospheric Chemistry and Physics 17(3): 2103–62.

Nguyen, Tran B., Alexander Laskin, Julia Laskin, and Sergey A. Nizkorodov. 2013. “Brown Carbon Formation from Ketoaldehydes of Biogenic Monoterpenes.” Faraday Discussions 165(0): 473–94.

Pani, Shantanu Kumar et al. 2021. “Brown Carbon Light Absorption over an Urban Environment in Northern Peninsular Southeast Asia.” Environmental Pollution 276: 116735.

Petit, Jean-Eudes et al. 2021. “Response of Atmospheric Composition to COVID-19 Lockdown Measures during Spring in the Paris Region (France).” Atmospheric Chemistry and Physics 21(22): 17167–83.

van Pinxteren, Dominik. et al. 2016. “Regional Air Quality in Leipzig, Germany: Detailed Source Apportionment of Size-Resolved Aerosol Particles and Comparison with the Year 2000.” Faraday Discussions 189(0): 291–315.

van Pinxteren, Dominik et al. 2019. “Trans-Boundary PM10: Quantifying Impact and Sources during Winter 2016/17 in Eastern Germany.” Atmospheric Environment 200: 119–30.

Pöhlker, Christopher et al. 2019. “Land Cover and Its Transformation in the Backward Trajectory Footprint Region of the Amazon Tall Tower Observatory.” Atmospheric Chemistry and Physics 19(13): 8425–70.

Potier, E. et al. 2019. “Characterizing the Regional Contribution to PM10 Pollution over Northern France Using Two Complementary Approaches: Chemistry Transport and Trajectory-Based Receptor Models.” Atmospheric Research 223: 1–14.

Pu, Wei et al. 2017. “Properties of Black Carbon and Other Insoluble Light-Absorbing Particles in Seasonal Snow of Northwestern China.” The Cryosphere 11(3): 1213–33.

Rehfeldt, M., E. Worrell, W. Eichhammer, and T. Fleiter. 2020. “A Review of the Emission Reduction Potential of Fuel Switch towards Biomass and Electricity in European Basic Materials Industry until 2030.” Renewable and Sustainable Energy Reviews 120: 109672.

Roig Rodelas, Roger et al. 2019. “Real-Time Assessment of Wintertime Organic Aerosol Characteristics and Sources at a Suburban Site in Northern France.” Atmospheric Environment 203: 48–61.

Romonosky, Dian E. et al. 2016. “Effective Absorption Cross Sections and Photolysis Rates of Anthropogenic and Biogenic Secondary Organic Aerosols.” Atmospheric Environment C(130): 172–79.

de Sá, Suzane S. et al. 2019. “Contributions of Biomass-Burning, Urban, and Biogenic Emissions to the Concentrations and Light-Absorbing Properties of Particulate Matter in Central Amazonia during the Dry Season.” Atmospheric Chemistry and Physics 19(12): 7973–8001.

Saide, Pablo E. et al. 2015. “Revealing Important Nocturnal and Day-to-Day Variations in Fire Smoke Emissions through a Multiplatform Inversion.” Geophysical Research Letters 42(9): 3609–18.

Saleh, Raward. et al. 2013. “Absorptivity of Brown Carbon in Fresh and Photo-Chemically Aged Biomass-Burning Emissions.” Atmospheric Chemistry and Physics 13(15): 7683–93.

Saleh, Rawad. 2020. “From Measurements to Models: Toward Accurate Representation of Brown Carbon in Climate Calculations.” Current Pollution Reports 6(2): 90–104.

Sandradewi, Jisca et al. 2008. “Using Aerosol Light Absorption Measurements for the Quantitative Determination of Wood Burning and Traffic Emission Contributions to Particulate Matter.” Environmental Science & Technology 42(9): 3316–23.

Sareen, N. et al. 2010. “Secondary Organic Material Formed by Methylglyoxal in Aqueous Aerosol Mimics.” Atmospheric Chemistry and Physics 10(3): 997–1016.

Satish, Rangu et al. 2017. “Temporal Characteristics of Brown Carbon over the Central Indo-Gangetic Plain.” Environmental Science & Technology 51(12): 6765–72.

Saturno, Jorge et al. 2018. “Black and Brown Carbon over Central Amazonia: Long-Term Aerosol Measurements at the ATTO Site.” Atmospheric Chemistry and Physics 18(17): 12817–43.

Sciare, Jean et al. 2011. “Large Contribution of Water-Insoluble Secondary Organic Aerosols in the Region of Paris (France) during Wintertime.” Journal of Geophysical Research: Atmospheres 116(D22). https://onlinelibrary.wiley.com/doi/abs/10.1029/2011JD015756 (October 21, 2022).

Selimovic, Vanessa, Robert J. Yokelson, Gavin R. McMeeking, and Sarah Coefield. 2019. “In Situ Measurements of Trace Gases, PM, and Aerosol Optical Properties during the 2017 NW US Wildfire Smoke Event.” Atmospheric Chemistry and Physics 19(6): 3905–26.

Shapiro, E. L. et al. 2009. “Light-Absorbing Secondary Organic Material Formed by Glyoxal in Aqueous Aerosol Mimics.” Atmospheric Chemistry and Physics 9(7): 2289–2300.

Stanaway, Jeffrey D. et al. 2018. “Global, Regional, and National Comparative Risk Assessment of 84 Behavioural, Environmental and Occupational, and Metabolic Risks or Clusters of Risks for 195 Countries and Territories, 1990–2017: A Systematic Analysis for the Global Burden of Disease Study 2017.” The Lancet 392(10159): 1923–94.

Stein, A. F. et al. 2015. “NOAA’s HYSPLIT Atmospheric Transport and Dispersion Modeling System.” Bulletin of the American Meteorological Society 96(12): 2059–77.

Stockwell, C. E., P. R. Veres, J. Williams, and R. J. Yokelson. 2015. “Characterization of Biomass Burning Emissions from Cooking Fires, Peat, Crop Residue, and Other Fuels with High-Resolution Proton-Transfer-Reaction Time-of-Flight Mass Spectrometry.” Atmospheric Chemistry and Physics 15(2): 845–65.

Sumlin, Benjamin J. et al. 2018. “Correction to Atmospheric Photooxidation Diminishes Light Absorption by Primary Brown Carbon Aerosol from Biomass Burning.” Environmental Science & Technology Letters 5(3): 193–193.

Sun, Jiaxing et al. 2021. “Light Absorption of Black Carbon and Brown Carbon in Winter in North China Plain: Comparisons between Urban and Rural Sites.” Science of The Total Environment 770: 144821.

Teich, Monique et al. 2017. “Contributions of Nitrated Aromatic Compounds to the Light Absorption of Water-Soluble and Particulate Brown Carbon in Different Atmospheric Environments in Germany and China.” Atmospheric Chemistry and Physics 17(3): 1653–72.

Velazquez-Garcia, Alejandra et al. 2023. “Deriving composition-dependent aerosol absorption, scattering and extinction mass efficiencies from multi-annual high time resolution observations in Northern France.” Atmospheric Environment. 298: (2023) 119613 https://doi.org/10.1016/j.atmosenv.2023.119613

Waked, Antoine et al. 2018. “Investigation of the Geographical Origins of PM10 Based on Long, Medium and Short-Range Air Mass Back-Trajectories Impacting Northern France during the Period 2009–2013.” Atmospheric Environment 193: 143–52.

Wang, Qiyuan et al. 2018. “Sources and Physicochemical Characteristics of Black Carbon Aerosol from the Southeastern Tibetan Plateau: Internal Mixing Enhances Light Absorption.” Atmospheric Chemistry and Physics 18(7): 4639–56.

Wang, Qiyuan et al. 2019. “High Contribution of Secondary Brown Carbon to Aerosol Light Absorption in the Southeastern Margin of Tibetan Plateau.” Geophysical Research Letters 46(9): 4962–70.

Wang, Xin et al. 2017. “Observations and Model Simulations of Snow Albedo Reduction in Seasonal Snow Due to Insoluble Light-Absorbing Particles during 2014 Chinese Survey.” Atmospheric Chemistry and Physics 17(3): 2279–96.

Wang, Xuan et al. 2016. “Deriving Brown Carbon from Multiwavelength Absorption Measurements: Method and Application to AERONET and Aethalometer Observations.” Atmospheric Chemistry and Physics 16(19): 12733–52.

Wong, Jenny P. S. et al. 2019. “Atmospheric Evolution of Molecular-Weight-Separated Brown Carbon from Biomass Burning.” Atmospheric Chemistry and Physics 19(11): 7319–34.

Wong, Jenny P. S., Athanasios Nenes, and Rodney J. Weber. 2017. “Changes in Light Absorptivity of Molecular Weight Separated Brown Carbon Due to Photolytic Aging.” Environmental Science & Technology 51(15): 8414–21.

Young, D. E. et al. 2015. “Investigating a Two-Component Model of Solid Fuel Organic Aerosol in London: Processes, PM1 Contributions, and Seasonality.” Atmospheric Chemistry and Physics 15(5): 2429–43.

Yttri, Karl Espen et al. 2020. “1 Trends, Composition, and Sources of Carbonaceous Aerosol in 2 the Last 18 Years at the Birkenes Observatory, Northern Europe.” : 45.

Yttri, Karl Espen, Christian Dye, Leiv Håvard Slørdal, and Ole-Anders Braathen. 2005. “Quantification of Monosaccharide Anhydrides by Liquid Chromatography Combined with Mass Spectrometry: Application to Aerosol Samples from an Urban and a Suburban Site Influenced by Small-Scale Wood Burning.” Journal of the Air & Waste Management Association 55(8): 1169–77.

Zhang, Qian et al. 2019. “Optical Properties and Source Identification of Black Carbon and Brown Carbon: Comparison of Winter and Summer Haze Episodes in Xi’an, Northwest China.” Environmental Science: Processes & Impacts 21(12): 2058–69.

Zhang, Xiaolin, Mao Mao, Yan Yin, and Shihao Tang. 2020. “The Absorption Ångstrom Exponent of Black Carbon with Brown Coatings: Effects of Aerosol Microphysics and Parameterization.” Atmospheric Chemistry and Physics 20(16): 9701–11.

Zhang, Yunjiang et al. 2019. “Six-Year Source Apportionment of Submicron Organic Aerosols

from near-Continuous Highly Time-Resolved Measurements at SIRTA (Paris Area, France).” Atmospheric Chemistry and Physics 19(23): 14755–76.

Zhang, Yunjiang et al. 2020. “Substantial Brown Carbon Emissions from Wintertime Residential Wood Burning over France.” Science of The Total Environment 743: 140752.

Zhao, R. et al. 2015. “Photochemical Processing of Aqueous Atmospheric Brown Carbon.” Atmospheric Chemistry and Physics 15(11): 6087–6100.

Zhong, M., and M. Jang. 2014. “Dynamic Light Absorption of Biomass-Burning Organic Carbon Photochemically Aged under Natural Sunlight.” Atmospheric Chemistry and Physics 14(3): 1517–25.

Zhu, Chong-Shu et al. 2021. “High Light Absorption and Radiative Forcing Contributions of Primary Brown Carbon and Black Carbon to Urban Aerosol.” Gondwana Research 90: 159–64.

Zotter, Peter et al. 2017. “Evaluation of the Absorption Ångström Exponents for Traffic and Wood Burning in the Aethalometer-Based Source Apportionment Using Radiocarbon Measurements of Ambient Aerosol.” Atmospheric Chemistry and Physics 17(6): 4229–49.

Annex 1: Chapter 3

		EU Air Quality Directives		
Pollutant	**Averaging period**	**Objective**	**Concentration**	**Comments**
$PM_{2.5}$	24-hour	Target value		
$PM_{2.5}$	Annual	Limit value	25 µg/m³	
$PM_{2.5}$	Annual	Indicative limit value	20 µg/m³	
PM_{10}	24-hour	Limit value	50 µg/m³	Not to be exceeded on more than 35 days/year
PM_{10}	Annual	Limit value	40 µg/m³	
O_3	Max. daily 8-hour mean	Target value	120 µg/m³	Not to be exceeded on more than 25 days/year (averaged over 3 years)
O_3	Max. daily 8-hour mean	Long-term objective	120 µg/m3	
O_3	8-hour	Target value		
O_3	Peak season [a]	Target value		
NO_2	Hourly	Limit value	200 µg/m³	Not to be exceeded on more than 18 hours/year
NO_2	Annual	Limit value	40 µg/m³	
NO_2	24-hour	Target value		
SO_2	Hourly	Limit value	350 µg/m³	Not to be exceeded on more than 24 hours/year
SO_2	24-hour	Limit value	125 µg/m³	Not to be exceeded on more than 3 days/year
CO	Max. daily 8-hour mean	Limit value	10 mg/m³	
CO	24-hour	Target value		
C_6H_6	Annual	Limit value	5 µg/m³	
BaP	Annual	Target value	1 ng/m³	Measured as content in PM_{10}
Pb	Annual	Limit value	0,5 µg/m³	Measured as content in PM_{10}
As	Annual	Target value	6 ng/m³	Measured as content in PM_{10}
Cd	Annual	Target value	5 ng/m³	Measured as content in PM_{10}
Ni	Annual	Target value	20 ng/m³	Measured as content in PM_{10}

A3 - 1 European Union Air Quality Directives (2008/50/EC, 2004/107/EC) Source: European Environmental Agency (https://www.eea.europa.eu/themes/air/air-quality-concentrations/air-quality-standards).

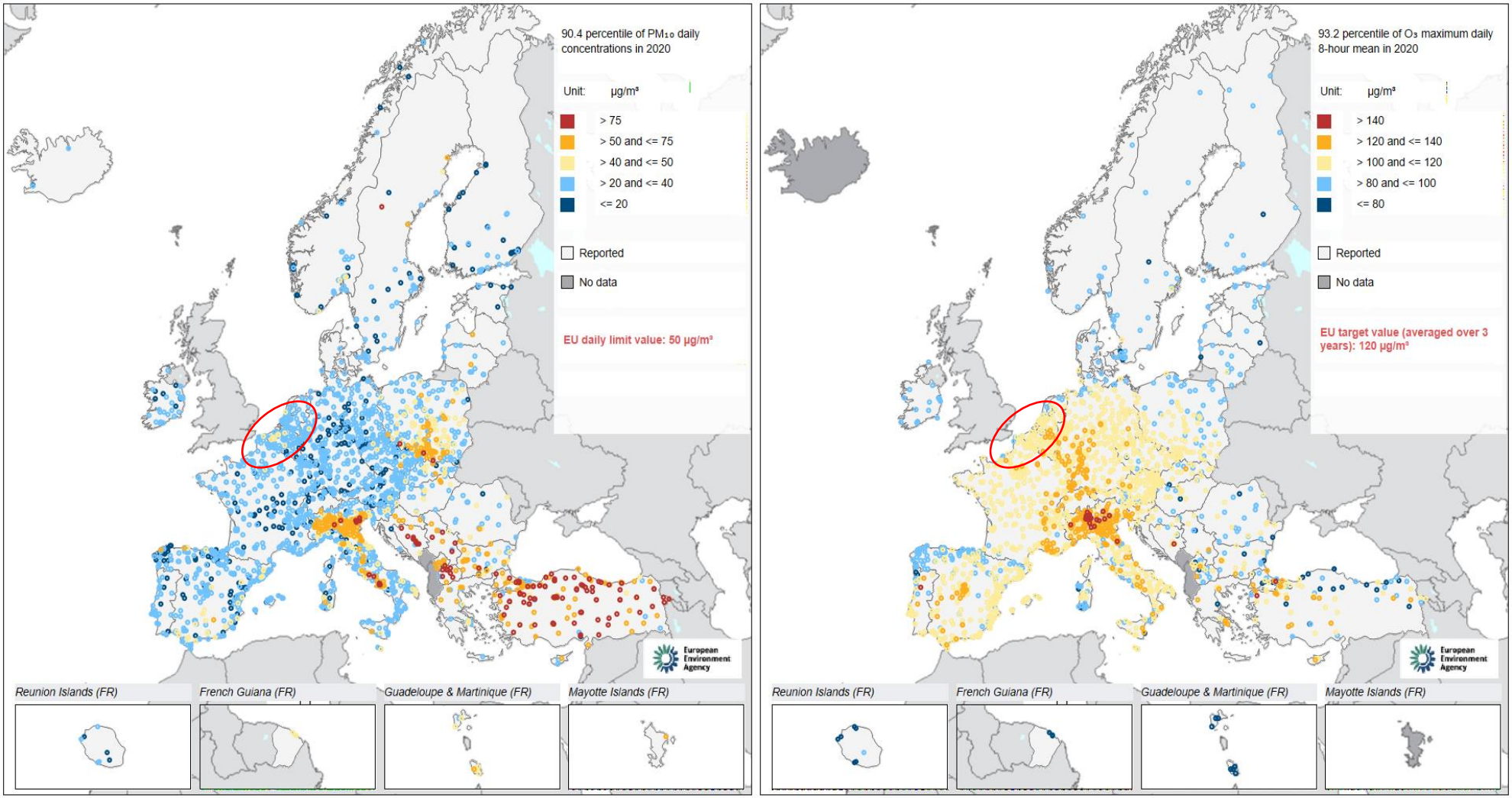

A3 - 2 Mass concentrations of PM_{10} (left) and O_3 (right). Source: Source: Europe's air quality status 2022, European Environment Agency. (https://www.eea.europa.eu//publications/status-of-air-quality-in-Europe-2022).

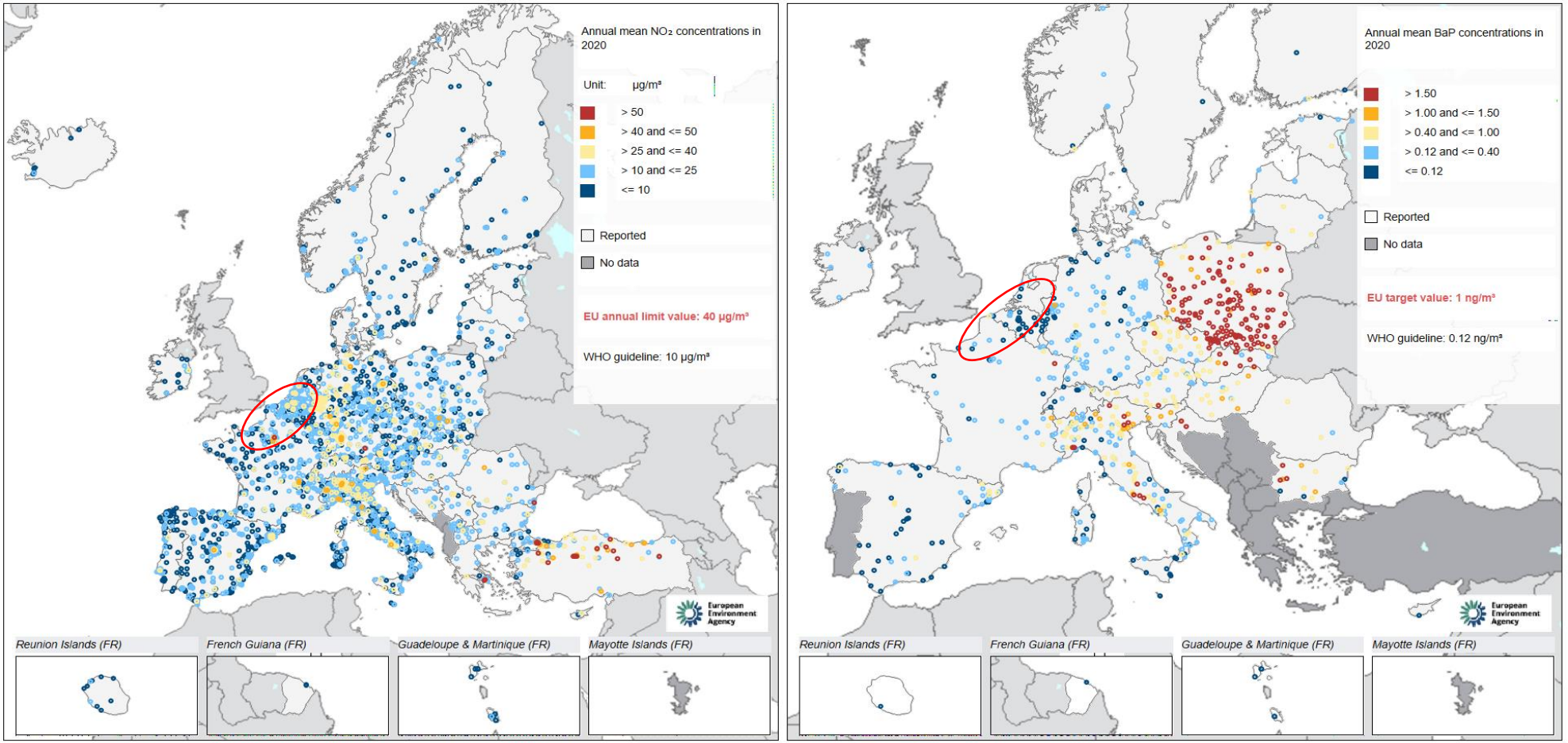

A3 - 3 Mass concentrations of NO_2 (left) and BaP (right). Source: Europe's air quality status 2022, European Environment Agency. (https://www.eea.europa.eu//publications/status-of-air-quality-in-Europe-2022)

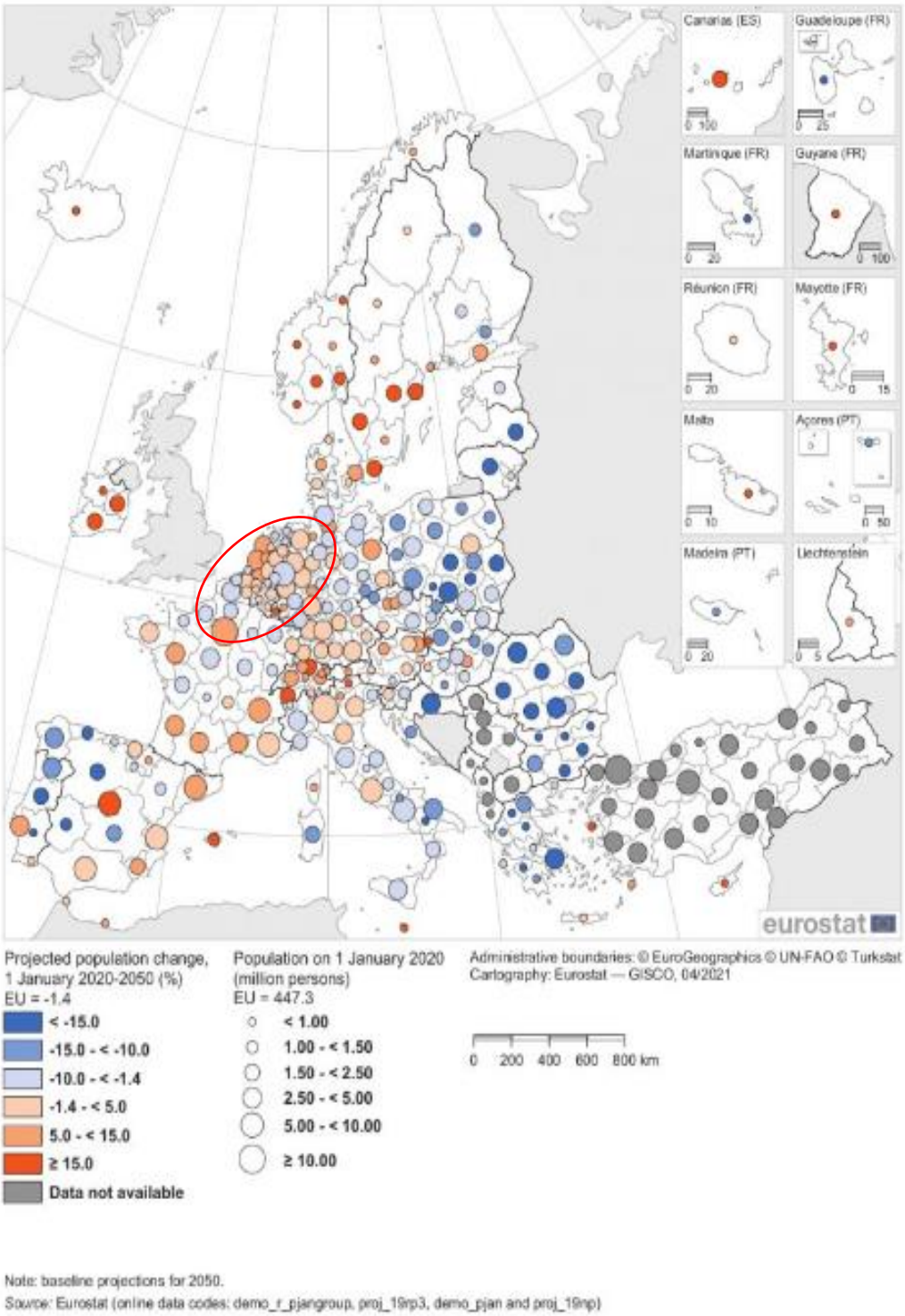

A3 - 4 Population on 1 January 2020 and projected population change 1 January 2020-250. Source: Eurostat (https://ec.europa.eu/eurostat/statistics-explained/index.php?title=Population_statistics_at_regional_level#Regional_populations, reviewed the 27 September 2022).

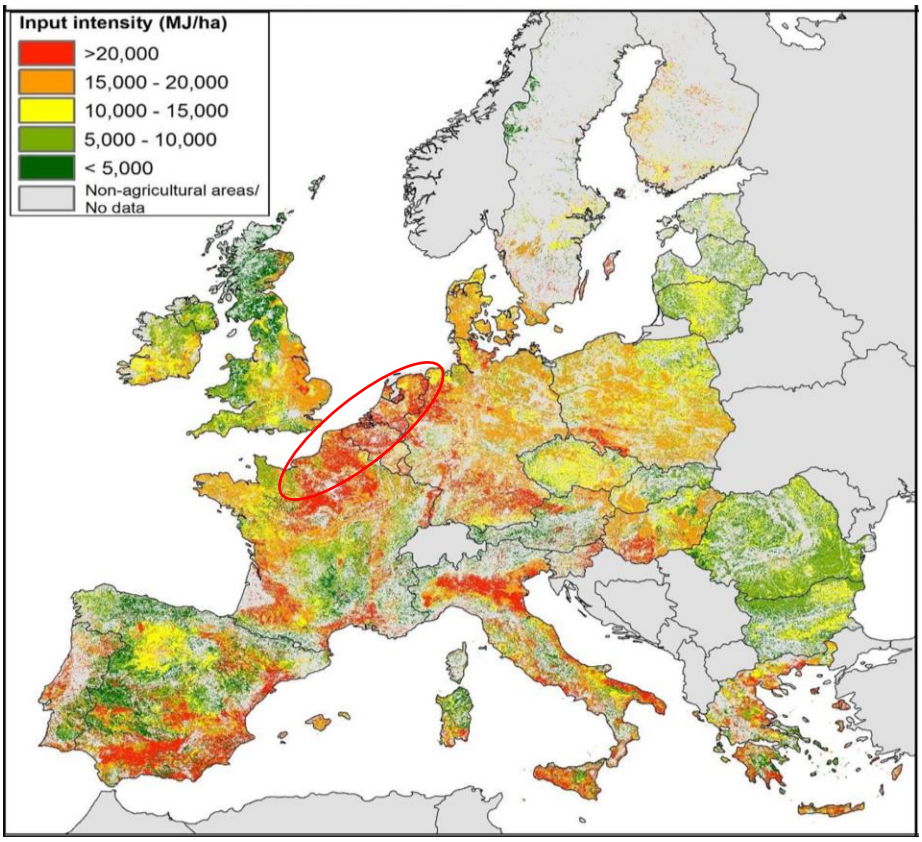

A3 - 5 Absolute intensity of agricultural management – energy input per ha.
Source: Rega et al. (2020)

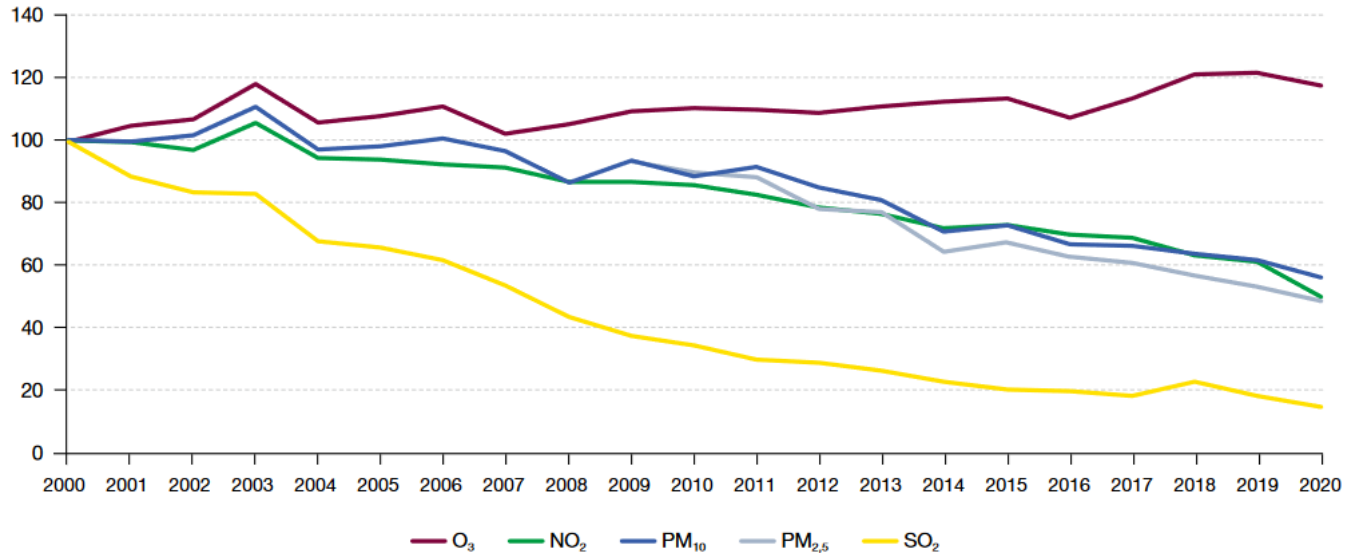

A3 - 6 Evolution of average annual mass concentrations (base 100 for year 2000) of SO_2 (yellow), NO_2 (green), O_3 (red), PM_{10} (blue) and $PM_{2.5}$ (gray) in urban environment. Source: MTE/SDES : Bilan de la qualité de l'air 2019, 16 sept. 2020 (p.8).

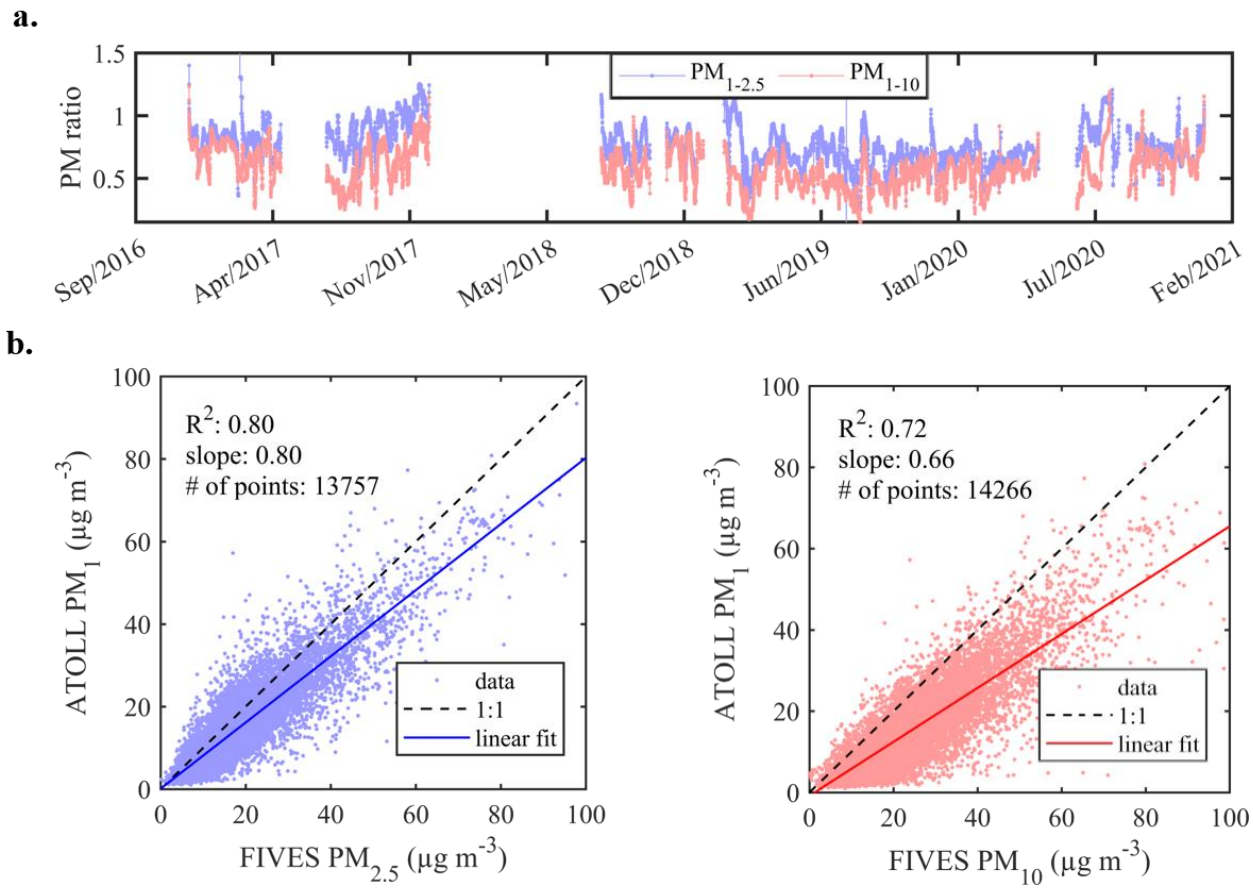

A3 - 7.Comparison of PM mass concentration between ATOLL and the Fives AtmoHdF station. a) Hourly time series of ratios between PM_1 vs $PM_{2.5}$ ($PM_{1\text{-}2.5}$, blue color) and PM_1 vs PM_{10} ($PM_{1\text{-}10}$, red color) b) Hourly scatterplots between PM_1 vs $PM_{2.5}$ (left) and PM_1 vs PM_{10} (right).

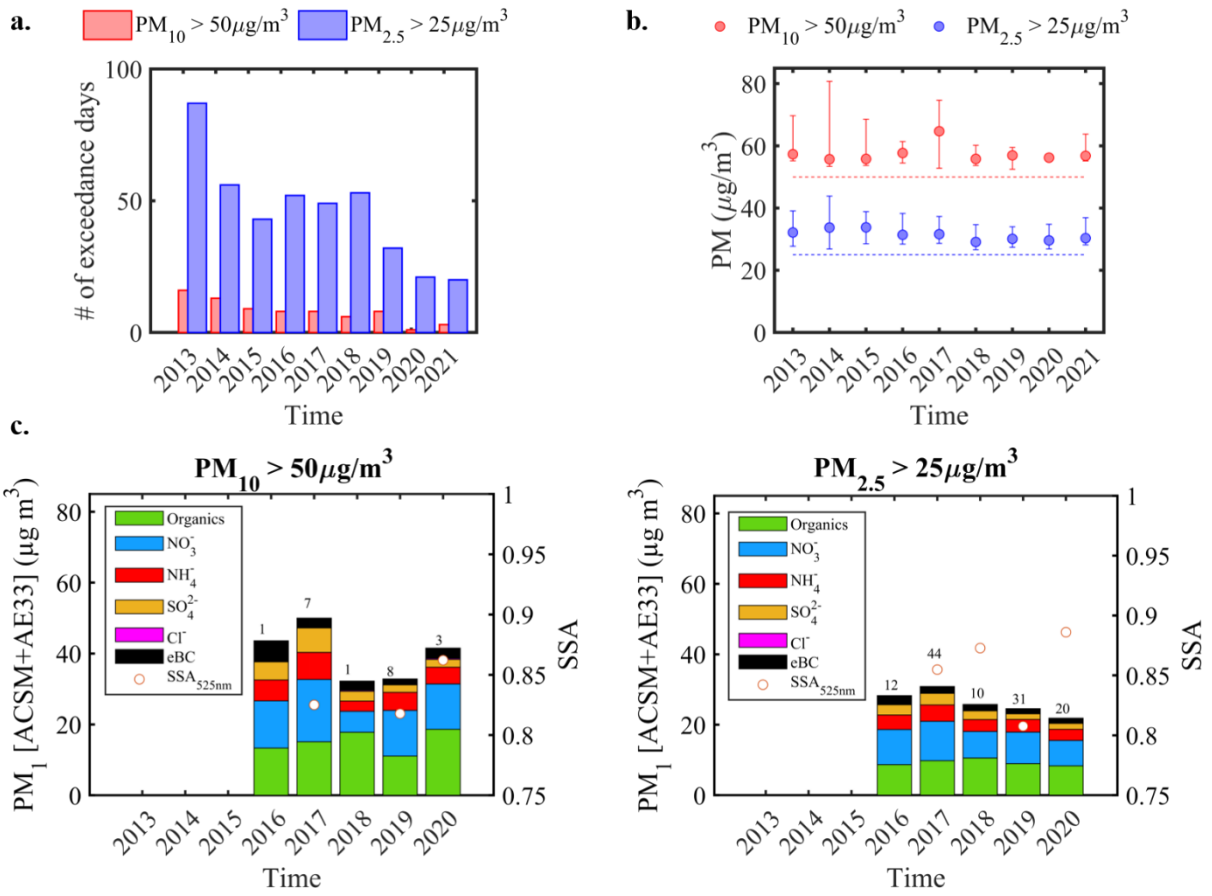

A3 - 8 Events of particle pollution at the ATOLL platform since 2013 until 2021 using the 2005 annual air quality guidelines from the World Health Organization (PM_{10} > 50µg m^{-3} & $PM_{2.5}$ >25 µg m^{-3}). a) Number of exceedance days of PM_{10} (in red) and $PM_{2.5}$ (in blue) concentration per year. b) Trend of PM_{10} (in red) and $PM_{2.5}$ (in blue) mass concentrations above the WHO guideline per year. c) Chemical composition (y axis left) and Single Scattering Albedo at 525 nm (y axis right) when the PM concentration exceed the WHO recommendations per year.

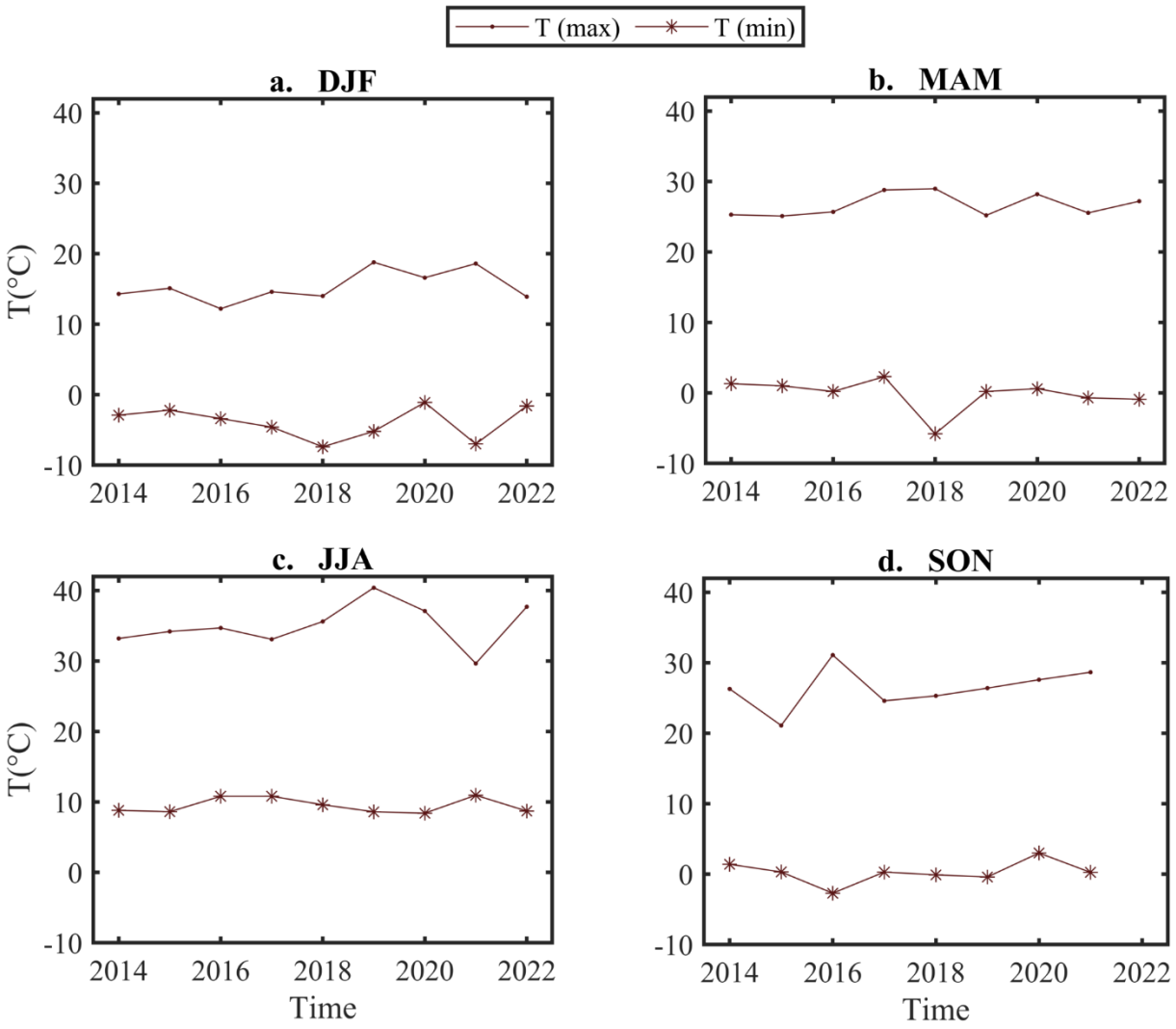

A3 - 9 Seasonal temperature (T) minimum and maximum values during the period January 2014 - August 2022 at the ATOLL platform.

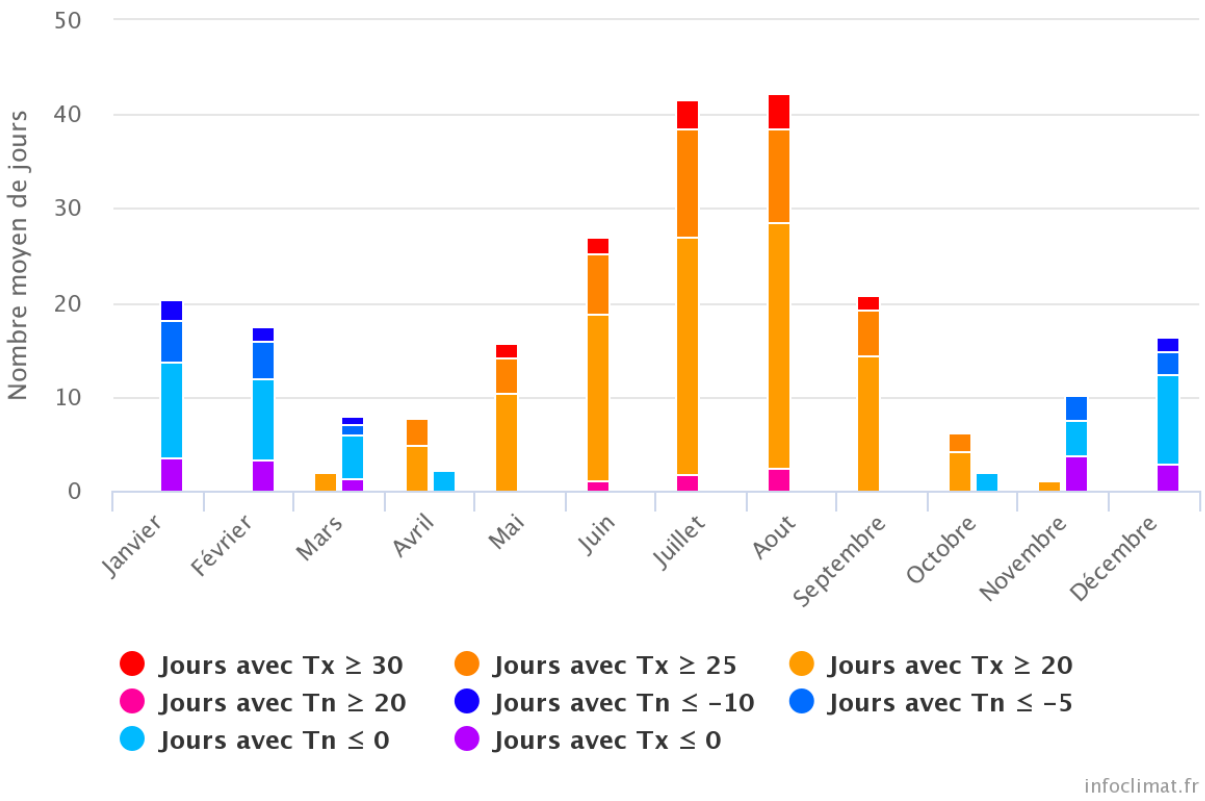

A3 - 10 Temperature-related phenomena for the period 1991-2022 at the Lille-Lesquin weather station. Source: https://www.infoclimat.fr/climatologie/normales-records/1991-2022/lille-lesquin/phenomenes/07015.html

Annex 2: Chapter 4

A4 - 1 Composition-dependent aerosol mass scattering, absorption and extinction efficiencies (MSE /MAE/ MEE) reported in the literature for different sites.

Location	λ (nm)	Temporal coverage	Approach	Size	Species					Reference
					$(NH_4)_2SO_4$	NH_4NO_3	Org	BC	Additional species	
Mass Scattering Efficiency, MSE ($m^2\ g^{-1}$)										
Eastern Mediterranean	545	26 July–23 August 2001	MLR	$PM_{2.5}$	2.7	4.2	-	-	-	Sciare et al 2005
USA	550	1990 - 2007	MLR	$PM_{2,5}$	2.8	2.8	2.5	-	-	Malm and Hand 2007
Xinken , China	550	Oct. - Nov. 2004	Theoretical	PM_1	7.1	7.6	6.7	4.2	4.1 (sea salt) 5.7 (residual)	Cheng et al 2008
Guangzhou, China	550	2 -31 Jul. 2006	MLR	$PM_{2.5}$	2.2	2.4	2.8	-	1.7 (sea salt) 0.6 (coarse mode) 1 ($PM_{2.5}$ – others)	Jung et al 2009
Granada, Spain	550	Mar. 2006 - Feb. 2007	MLR	PM_{10}	7.0	5.0	2.8	2.2	-	Titos et al 2012
Shanghai, China	525	Oct. 2012 - Nov. 2012	Theoretical	$PM_{2.5}$	3.5	4.3	4.5	-	-	Cheng et al 2014
Guangzhou, China	550	2009 - 2010	MLR	$PM_{2.5}$	*spring*					Tao et al 2014
					2.9	3.2	3.3		2.1 (sea salt) 1.1 (fine soil) 0.5 (coarse mode)	
					summer					
					2.5	2.6	2.8		1.5 (sea salt) 0.9 (fine soil) 0.6 (coarse mode)	
					fall					
					4.8	4.9	5.1		2.6 (sea salt) 1.3 (fine soil) 0.6 (coarse mode)	
					winter					
					5.3	5.5	6.2		2.4 (sea salt) 0.7 (fine soil) 0.5 (coarse mode)	
Bejing, China	550	24-31 Jan. 2013	MLR	PM_1	6.5	2.2	5.7	-	2.2 (NH_4HSO_4) 4.3 (NH_4Cl) 57.3 (residual)	Wang et al 2015

Xi'an, China	532	23 Dec. 2012 - 18 Jan. 2013	MLR	PM_1	*Visibility >5 km*					Zhou et al 2019
					3.6	8.9	4.1		3.9 (OOA)	
					Visibility <5 km					
					6.0	17.4	6.1		2.7 (OOA)	
Rio Branco, Brazil	450	Aug-Nov. 2018	MLR	PM_1	-	-	6.1 $(OOA_1)^+$ 6.6 $(OOA_2)^+$	7.4	13.9 $(BBOA)^+$	Ponczek et al 2022
	532						4.3 $(OOA_1)^+$ 4.8 $(OOA_2)^+$	6.1	9.1 $(BBOA)^+$	
	637						2.8 $(OOA_1)^+$ 3.3 $(OOA_2)^+$	4.7	5.7 $(BBOA)^+$	
Mass Absorption Efficiency, MAE ($m^2\ g^{-1}$)										
Xinken , China	550	Oct. - Nov. 2004	Theoretical	PM_1	-	-	0.06	9.3	0.2 (Residual)	Cheng et al 2008
Alabama, USA	365	Summer 2013	MLR	$PM_{2,5}$	-	-	1.3 $(BBOA)^+$ 0.3 $(LO\text{-}OOA)^+$ 0.01 $(MO\text{-}OOA)^+$ 0.01 $(Isoprene\text{-}OA)^+$	-	-	Washenfelder et al 2015
Guangzhou, China	365	Not reported	MLR	$PM_{2,5}$	-	-	0.7 $(WSOC)^{++}$ 0.75 $(HULIS)^{++}$ 1.4 $(ASOC)^{++}$ 2 $(MSOC)^{++}$	-	-	Li et al 2019
Guangzhou, China	370	Nov-Dec. 2014	MLR	$PM_{2,5}$	-	-	0.6 $(HOA)^+$ 3.4 $(BBOA)^+$ 1.0 $(LVOOA)^+$	-	-	Qin Y. M et al 2018
	470						0.3 $(HOA)^+$ 1.2 $(BBOA)^+$ 0.6 $(LVOOA)^+$			
	520						0.2 $(HOA)^+$ 0.6 $(BBOA)^+$ 0.4 $(LVOOA)^+$			
	590						0.1 $(HOA)^+$ 0.4 $(BBOA)^+$ 0.2 $(LVOOA)^+$			
	660						0.1 $(HOA)^+$ 0.2 $(BBOA)^+$ 0.2 $(LVOOA)^+$			
Manaus, Brazil	370	15 Aug - 15 Oct. 2014	MLR	PM_1	-	-	0.4 $(IEPOX\text{-}SOA)^+$ 0.4 $(MO\text{-}BBOA)^+$ 0.8 $(LO\text{-}BBOA)^+$	-	-	S. de Sá et al 2019

							1.5 $(HOA)^+$ 2.0 $(MO\text{-}OOA)^+$ 0.01 $(LO\text{-}OOA)^+$			
Xi'an, China	532	23 Dec. 2012 - 18 Jan. 2013	MLR	PM_1	-	-	*Visibility > 5 km*			Zhou et al 2019
							0.2	9.7	0.4 (OOA)	
							Visibility < 5 km			
							0.3	13.2	0.6 (OOA)	
Chiang Mai, Thailand	880	27 Feb. - 22 May 2019	MLR	$PM_{2,5}$	-	-	0.2	8.1	-	Tao et al 2020
	370						2.6	21.0	-	
Milan, Italy	880	Jan. - June 2016	MLR	PM_1	-	-	-	9.8 9.5	(winter) (summer)	Gilardoni et al 2020
	370						1.2 0.5	-	(winter) (summer)	
Karachi, Pakistan	632	Feb. 2015 - Mar. 2017	MLR	$PM_{2,5}$	-	-	0.97	6.5	-	Chen et al 2020
Singapore, Singapore	370	May- Jun. 2017	MLR	$PM_{2,5}$	-	-	0.9 $(HOA)^+$ 0.5 $(O\text{-}HOA)^+$ 0.06 $(COA)^+$ 0.6 $(LO\text{-}OOA)^+$ 0 $(MO\text{-}OOA)^+$	-	-	Kasthutiarachchi Y. N. et al 2020
	470				-	-	0.6 $(HOA)^+$ 0.3 $(O\text{-}HOA)^+$ 0.05 $(COA)^+$ 0.4 $(LO\text{-}OOA)^+$ 0.04 $(MO\text{-}OOA)^+$	-	-	
	520				-	-	0.3 $(HOA)^+$ 0.1 $(O\text{-}HOA)^+$ 0.03 $(COA)^+$ 0.1 $(LO\text{-}OOA)^+$ 0.06 $(MO\text{-}OOA)^+$	-	-	
	590				-	-	0.2 $(HOA)^+$ 0.1 $(O\text{-}HOA)^+$ 0.004 $(COA)^+$ 0.1 $(LO\text{-}OOA)^+$ 0.05 $(MO\text{-}OOA)^+$	-	-	
	660				-	-	0.1 $(HOA)^+$ 0.06 $(O\text{-}HOA)^+$ 0 $(COA)^+$ 0.03 $(LO\text{-}OOA)^+$ 0.04 $(MO\text{-}OOA)^+$	-	-	

Guangzhou, China	550	Apr., July, Oct. – Jan. 2018	MLR	$PM_{2.5}$	*spring*					Pei et al 2022
								11.0		
					summer					
								8.5		
					fall					
								10.4		
					winter					
								11.3		
Indo-gangetic Plain, India	365	23 Jun - 24 Jul. 2016	MLR	PM_{10}	-	-	0.6	-	-	Nayak et al 2022
Rio Branco, Brazil	370	Aug-Nov. 2018	MLR	PM_1	-	-	3.0	12.0	0.3 $(OOA_1)^+$ 0.2 $(OOA_2)^+$ 2.8 $(BBOA)^+$	Ponczek et al 2022
	470						0.97	8.8	0.9 $(OOA_1)^+$ 0.7 $(OOA_2)^+$ 2.0 $(HOA)^+$ 13.9 $(BBOA)^+$	
	520						0.47	7.39	0.2 $(OOA_1)^+$ 0.15 $(OOA_2)^+$ 0.24 $(HOA)^+$ 1.4 $(BBOA)^+$	
	637						0.13	5.5	0.1 $(OOA_1)^+$ 0.07 $(OOA_2)^+$ 0.01 $(HOA)^+$ 0.38 $(BBOA)^+$	
	880						-	3.5	-	
Mass Extinction Efficiency, MEE ($m^2\ g^{-1}$)										
Denver, USA	550	Nov. - Dec. 1978	Experimental	PM_1	6.6	2.8	4.4	3.2*	-	Groblicki et al. 1981
Several remote sites, USA	530	Mar. 1988 - Feb. 1991	Theoretical	PM	3.0	3.0	4.0	10.0	1 (fine soil)	Malm et al. 1994
									0.6 (coarse mass)	
									10 (residual)	
Several remote sites, USA	550	-	Theoretical	PM_1	2.2	2.4	2.8	10.0	1.7 (sea salt)	Pitchford et al. 2007
									0.6 (coarse mass)	
Xinken, China	550	Oct. - Nov. 2004	Theoretical	PM_1	7.5	8.0	7.1	11.0*	4.4 (sea salt)	Cheng et al. 2008
									6.2 (residual)	
Shenzhen, China	550	Jan. - Feb. 2009	Experimental	PM_1	2.3	2.3	4.5	9.2*	6.5 (residual)	Yao et al. 2010
	520		Experimental	$PM_{2.5}$	5.1	6.1	3.0	15.6*	1.3 (fine soil)	

Chengdu, China		Apr. 2011							0.8 (coarse mass)	Tao et al. 2014
		Jul. 2011			5.7	1.7	4.8	14.4*	1.0 (fine soil)	
									1.4 (coarse mass)	
		Oct. 2011			6.0	4.2	6.9	14.3*	0.9 (fine soil)	
									0.6 (coarse mass)	
		Jan. 2011			4.4	6.7	6.5	10.5*	0.8 (fine soil)	
									0.5 (coarse mass)	
Beijing, China	630	Oct. - Nov. 2012	Experimental	PM_1	7.0	7.0	1.1 (HOA)+ 1.3 (COA)+ 1 (CCOA)+ 4.6 (OOA)+	7.3	1 (NH_4Cl)	Wang et al. 2015
		Nov. - Dec. 2012			5.2	5.2	1 (COA)+ 1 (HOA)+ 5 (CCOA)+ 3 (OOA)+	7.3	2.7 (NH_4Cl)	
Po Valley, Italy	550	Nov. - Dec. 2015	Theoretical	$PM_{2.5}$	4.4	5.2	6.1	6.8*	3.2 (fine soil), Abs. coeff.	Valentini et al. 2018

* Elemental Carbon (EC, data derived from methods that are specific to the carbon content of carbonaceous matter)

+ Organic Aerosol (OA) – factors given by the source apportionment of Organics with Positive Matrix Factorization (PMF): Hydrocarbon-like Organic Aerosol (HOA), Biomass-Burning Organic Aerosol (BBOA), Cooking-like Organic Aerosol (COA), Coal Combustion Organic Aerosol (CCOA), Oxygenated Organic (OOA), Low-Oxygenated Organic (LOOA), More-Oxygenated Organic (MOOA). CCOA (main contributor to extinction in Wang et al. 2015 during the the non-heating period (NHP, Oct-Nov 2012) is not present at the ATOLL site (Chebaicheb et al. *in preparation*).

++ Organic Aerosol (OA) measure types – Methods of laboratory experiments to measure organics. Water Soluble Organic Carbon (WSOC), Soluble Humic-like Substances (HULIS), Alkanile Soluble Organic Carbon (ASOC), Methanol Soluble Organic Carbon (MSOC).

The references with gray background correspond to the literature values selected to evaluate the impact of using Fixed-MEE obtained for other sites together with ATOLL concentrations to retrieve the extinction coefficient based on IMPROVE eq.1 (Figure 4.1 in the main text)

A4 - 2 Retrieved values of Mass Scattering, Absorption and Extinction Efficiencies (MSE, MAE, MEE, respectively) from 370 to 950 nm based on MLR analysis at ATOLL by seasons.

	Season	**Winter (DJF)**				**Spring (MAM)**				**Summer (JJA)**				**Fall (SON)**			
	Wavelength (nm)	**AS**	**AN**	**Org**	**eBC**	**AS**	**AN**	**Org**	**eBC**	**AS**	**AN**	**Org**	**eBC**	**AS**	**AN**	**Org**	**eBC**
Mass Scattering Efficiency, MSE (m^2 g^{-1})	450	12.3	6.5	2.2	NA	9.6	3.7	0	NA	6.4	6.6	2.3	NA	7.0	6.8	2.3	NA
	525	11.3	4.9	1.5	NA	5.2	2.0	0	NA	4.7	5.1	1.6	NA	5.8	5.2	1.7	NA
	635	8.6	3.5	0.8	NA	5.2	2.1	0	NA	3.4	4.0	0.9	NA	5.4	4.0	1.2	NA
Mass Absorption Efficiency, MAE (m^2 g^{-1})	370	NA	NA	1.1	12.6	NA	NA	0.2	13.4	NA	NA	0.2	10.9	NA	NA	0.8	10.8
	470	NA	NA	0.4	10.3	NA	NA	0.1	10.3	NA	NA	0.2	8.6	NA	NA	0.4	8.4
	520	NA	NA	0.2	8.7	NA	NA	0.1	8.6	NA	NA	0.1	7.3	NA	NA	0.2	7.1
	590	NA	NA	0.1	7.5	NA	NA	0.1	7.4	NA	NA	0.1	6.5	NA	NA	0.2	6.2
	660	NA	NA	0.1	6.3	NA	NA	0	6.3	NA	NA	0.1	5.5	NA	NA	0.1	5.2
	880	NA	NA	0	4.5	NA	NA	0	4.5	NA	NA	0	4.0	NA	NA	0	3.8
	950	NA	NA	0	4.2	NA	NA	0	4.3	NA	NA	0	3.8	NA	NA	0	3.6
Mass Extinction Efficiency, MEE (m^2 g^{-1})	450	12.6	6.7	2.6	10.5	9.1	3.9	0	10.6	6.0	6.3	2.0	12.8	6.6	6.9	1.9	11.9
	525	11.7	5.1	1.5	9.2	7.1	3.2	0	7.1	4.4	4.8	1.3	11.2	5.7	5.3	1.2	9.8
	635	10.4	3.6	0.3	10.6	5.1	2.2	0	6.5	3.1	3.9	0.7	10.2	5.4	4.1	0.6	9.1

NA – not applicable; AS – Ammonium sulfate; AN- Ammonium nitrate; Org – Organic fraction; eBC – Equivalent black carbon

A non-zero intercept would physically mean that a certain amount of aerosol compounds would not be measured with our instrumental system (ACSM and AE-33) but would have a quite significant contribution to the optical parameters (scattering, absorption and/or extinction coefficients). Some authors (Crenn et al. 2015; Petit et al. 2015; Zhang et al. 2021) have shown that the sum of NR-PM_1 (Org, NO_3, NH_4, SO_4, Chl) and BC mass concentrations is similar to PM_1 measured from gravimetric measurements (with a variation around 14%) and/or optically derived from light scattering (around 17%). Therefore, the concentration of non-measured compounds in urban areas is expected to be low. One can also assume that the contribution of missing species to the optical parameters is relatively small since most of the light-absorbing or scattering compounds in this size fraction are detected. Thus, based on physical principles and previous studies, we decided not to include the intercept in the MLR equation (eq. 4.5). Nevertheless, to give an idea of the possible changes that a non-zero intercept would entail, we ran the MLR with and without an intercept. According to our results (Appendix - A4 - 3), the MAE, MSE and MEE are close to the values highlighted within the manuscript for all species with some remarkable differences. Certainly, the MSE_{AS} and MEE_{AS} show the largest differences (up to 29%) at 635nm, similar than the MSE_{org} and MEE_{org}, showing 20% of difference. The other compounds only show a change by less than 9% for all the wavelengths.

A4 - 3 Coefficients retrieved using *lsqlin* method at three different wavelengths (450, 525 and 635 nm) for major aerosol compounds (Ammonium Sulfate (AS), Ammonium Nitrate (AN), Organics (Org), and equivalent Black Carbon (eBC)). The first value correspond to a forced intercept of zero, while the value in parenthesis correspond to the calculations including a non-zero (free) intercept.

	Wavelength (nm)	Ammonium Sulfate	Ammonium Nitrate	Organics	eBC
Mass Scattering Efficiency, MSE (m^2 g^{-1})	450	7.1 (5.2)	4.6 (4.7)	3.1 (2.6)	-
	525	5.7 (4.1)	3.6 (3.7)	2.2 (1.8)	-
	635	4.8 (3.4)	2.7 (2.7)	1.5 (1.2)	-
Mass Absorption Efficiency, MAE (m^2 g^{-1})	370	-	-	0.7 (0.7)	11.6 (11.6)
	470	-	-	0.3 (0.3)	8.9 (8.9)
	520	-	-	0.2 (0.2)	7.5 (7.5)
	590	-	-	0.2 (0.2)	6.5 (6.5)
	660	-	-	0.1 (0.1)	5.5 (5.5)
	880	-	-	0.0 (0.0)	3.9 (3.9)
	950	-	-	0.0 (0.0)	3.7 (3.7)
Mass Extinction Efficiency, MEE (m^2 g^{-1})	450	5.8 (4.2)	4.6 (4.7)	2.9 (2.7)	13.5 (12.6)
	525	5.0 (3.6)	3.7 (3.7)	1.8 (1.7)	11.2 (10.4)
	635	4.5 (3.2)	2.7 (2.8)	1.0 (0.8)	10.7 (9.7)

Many previous studies have been using MLR (Ealo et al. 2018; Sciare et al. 2005; Tao et al. 2014; Titos, et al. 2012; Wang et al. 2015; Yao et al. 2010). They have been using different tests to evaluate the robustness of their calculations by looking at the residuals and the fractional bias (FB) both described in the following paragraphs.

Residuals:

The residuals (ϵ, in equation 5) correspond to the difference between the observed and the estimated extinction, scattering or absorption coefficients calculated from mass concentration and efficiency parameters (MEE, MSE or MAE). For ideal models, the residual values are 0. High residual values correspond to a model unable to properly estimate the tested parameter. The standardized residuals are used to test the robustness of the MLR method. If the absolute values of the standardized residuals are below 2, the MLR is robust, while larger values of the standardized residuals correspond to outliers (Islam et al. 2021; Kiebel et al. 1999; Schagen 2006). Figures 1-3 below show the standardized residuals obtained by applying the MLR to the retrieved individual coefficients for extinction (Appendix A4 – 4), scattering (Appendix A4 – 5) and absorption (Appendix A4 – 6) as reported in the manuscript (using *lsqlin* without intercept). The upper plot presents the cumulative probability of the standardized residuals, the 95% interval of confidence (below 2) represented by black dashed lines, and the number of points within the limit. The bottom plot shows the distribution of the standardized residuals probability, in which the percentage of points outside the limit (dashed lines) is shown. In all cases (extinction, scattering, absorption), the residuals are mostly centered to 0, and the percentage of outliers never exceed 6%.

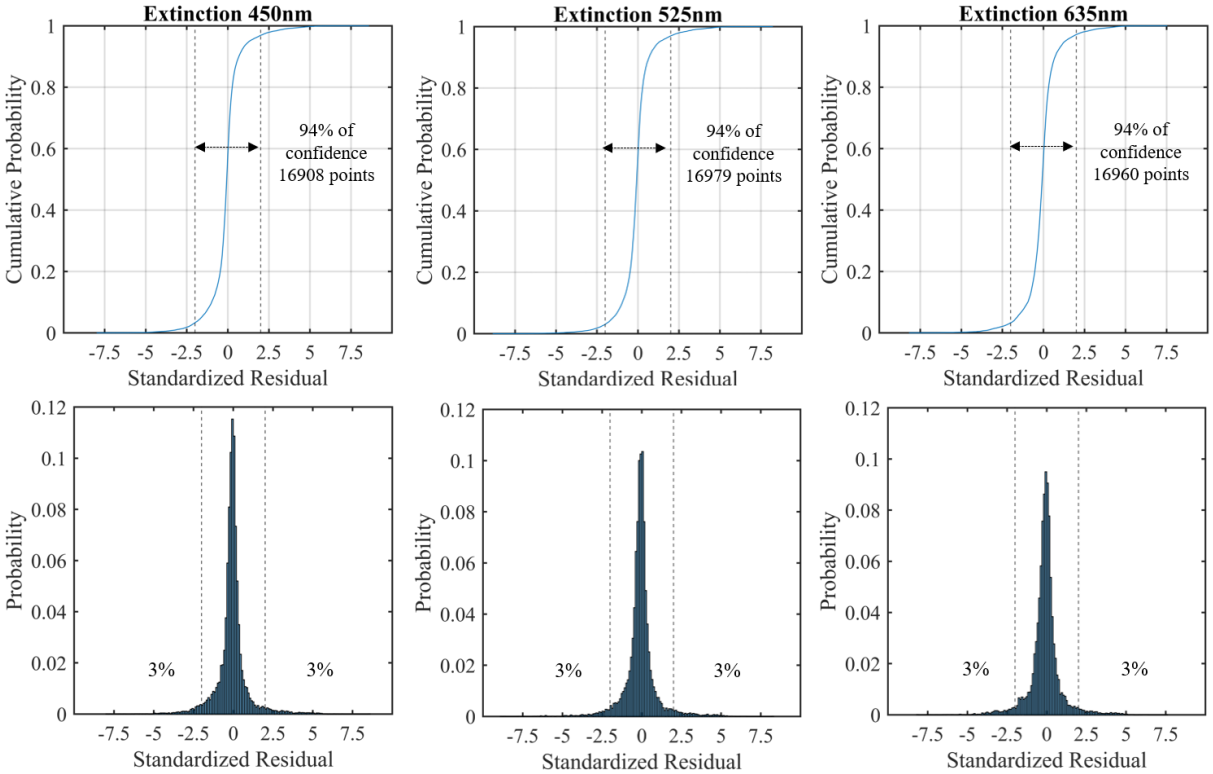

A4 - 4. Standardized residuals probability for extinction. The upper plot shows the cumulative probability while the bottom plot presents the distribution of the standardized residuals, obtained from the retrieval of MEE coefficients at three wavelengths (450, 525 and 635 nm).

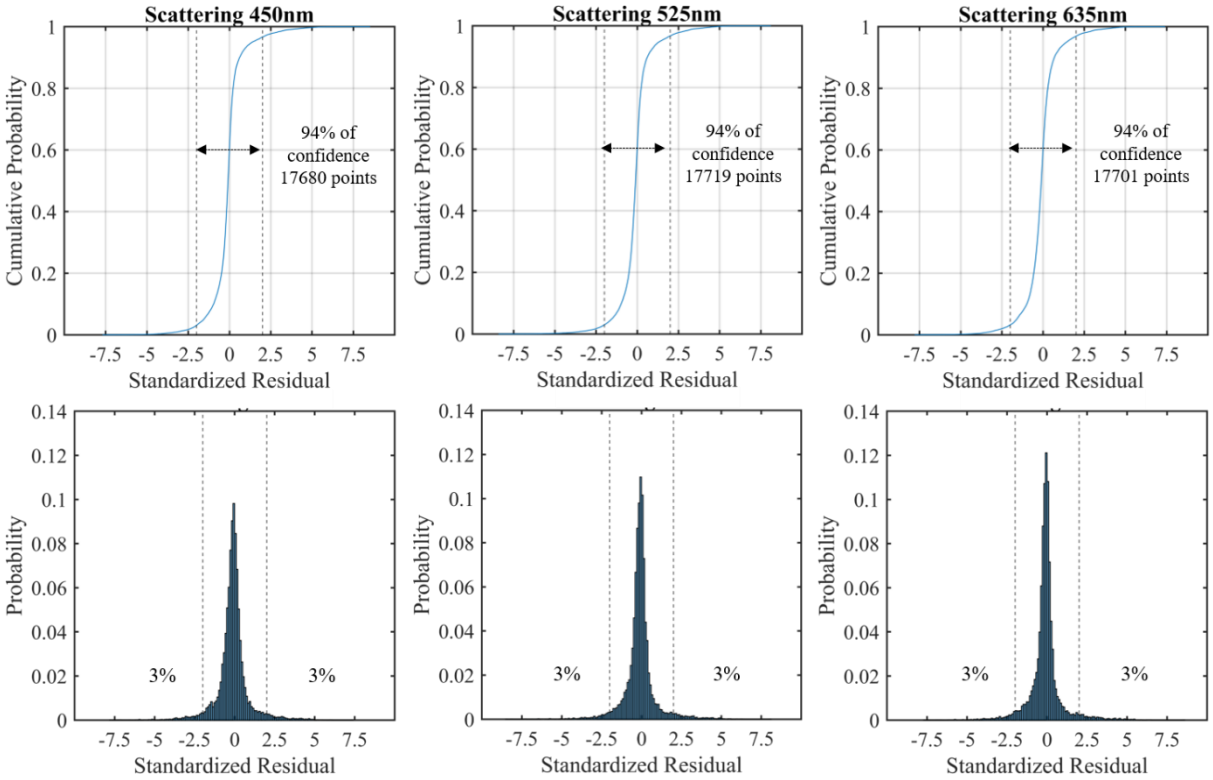

A4 - 5. Standardized residuals probability for scattering. The upper plot shows the cumulative probability while the bottom plot presents the distribution of the standardized residuals, obtained from the retrieval of MSE coefficients at three wavelengths (450, 525 and 635 nm).

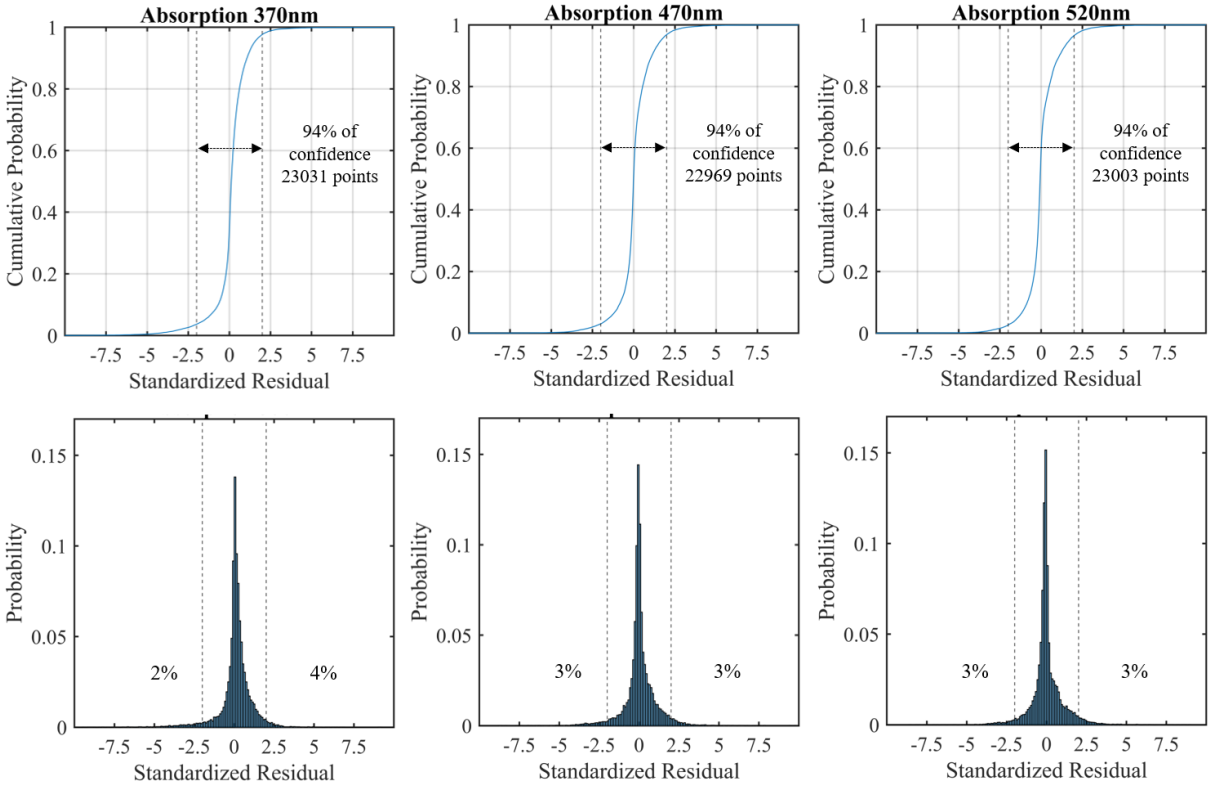

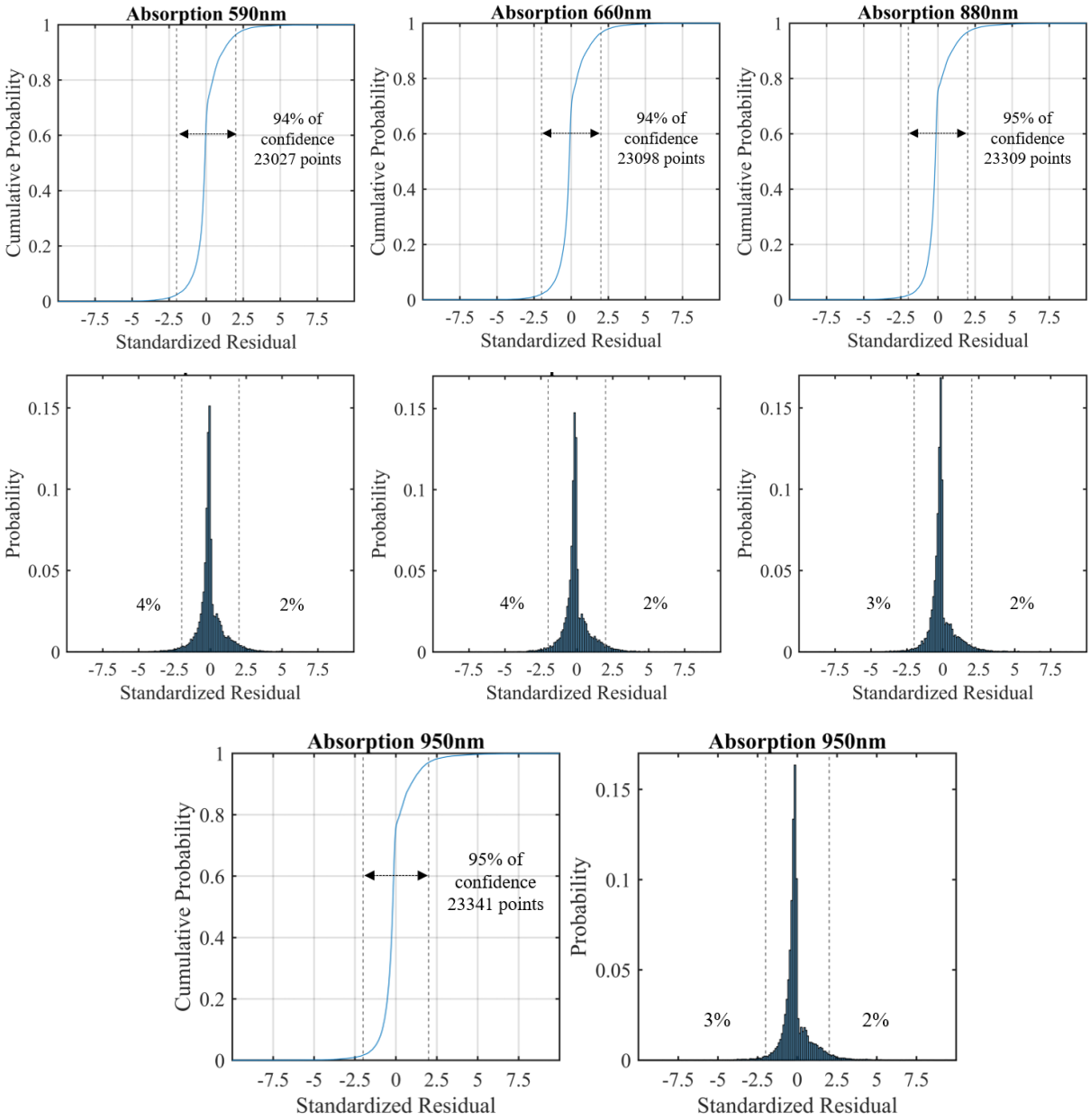

A4 - 6. Standardized residuals probability for absorption. The upper plot shows the cumulative probability while the bottom plot presents the distribution of the standardized residuals, obtained from the retrieval of MAE coefficients from 370 – 950 nm.

To conclude, the results discussed here confirms the robustness of the MLR technique to accurately estimate the optical parameters with at least 94% of values within 2σ and only 6% of outliers using 3 full years of measurements.

Fractional bias (FB):

The fractional bias is used by the IMPROVE (Interagency Monitoring of Protected Visual Environments, Ryan et al., 2005) community for evaluating the bias from the application of their formula to reconstruct light extinction in National Parks in the USA. Basically, estimated and measured scattering, absorption and, extinction coefficients are compared using the average FB, calculated with eq. a and eq. b

$$\overline{FB} = \frac{\sum_{ij} FB_{ij}}{\sum_{ij} 1} \quad \text{eq. a}$$

$$FB_{ij} = \frac{\sigma_{reconstructed\ ij} - \sigma_{observed\ ij}}{\sigma_{observed\ ij}} \quad \text{eq. b}$$

where,

FB_{ij} symbolizes the FB, the $\sigma_{observed\ ij}$ and $\sigma_{reconstructed\ ij}$ are the measured data and average estimates, respectively. The subscript j stands for a specific day and i stands for scattering, or absorption or, extinction coefficients. Results are shown in Appendix A4 - 7 where the fractional bias broken down by quintile from the lowest to the highest optical parameter (scattering, absorption, extinction coefficients) values reported in the manuscript. The larger values of FB highlight a large difference between the observed and modeled quantities tested, underlying the influence of the aerosol loading on the bias. According to Ryan et al. (2005) and references therein, a consistent overestimation was observed for all the modelled coefficients in the lower ranges, showing the highest bias in the 1st quintile. Biases are considerably reduced in the median range values, while a minor underestimation was observed for the highest values, 4th and 5th quintiles, with negative FB. At the ATOLL platform, we can observed what Ryan et al. (2005) described, larger overestimation (FB up to 1.62 at 635nm) is observed in the 1st quintile, biases are reduced in the median range values (95% for scattering and 35% for absorption) and, minor underestimation (FB down to -0.30 at 635nm) is observed in the 5th quintile. The higher FB observed in the 1st quintile might be linked to the fact that during low concentrations the instruments can get closer to the LoD. Besides, to the fact that those events occur after rain or, during summer time with strong dispersion conditions leading to clean air masses with different aerosol population, it might explain this bias at low (and to less extent, high) values. It is interesting to see that, for absorption, while the FB is significantly lower in the infrared, higher FB values are observed in UV, probably reflecting complexity of BrC dynamics.

Overall, the average FB of the 18 894 nephelometer data points is 0.027 and, about 0.29 for the 24 486 aethalometer data points (the average FB is 0.029). Ryan et al. (2005) report for the IMPROVE network a FB of 0.050 for scattering at 550nm, whereas Ealo et al. (2018) report, for a background site in Spain, a FB of 0.056 for the modelled absorption at 637nm and 0.040 for scattering at 525nm.

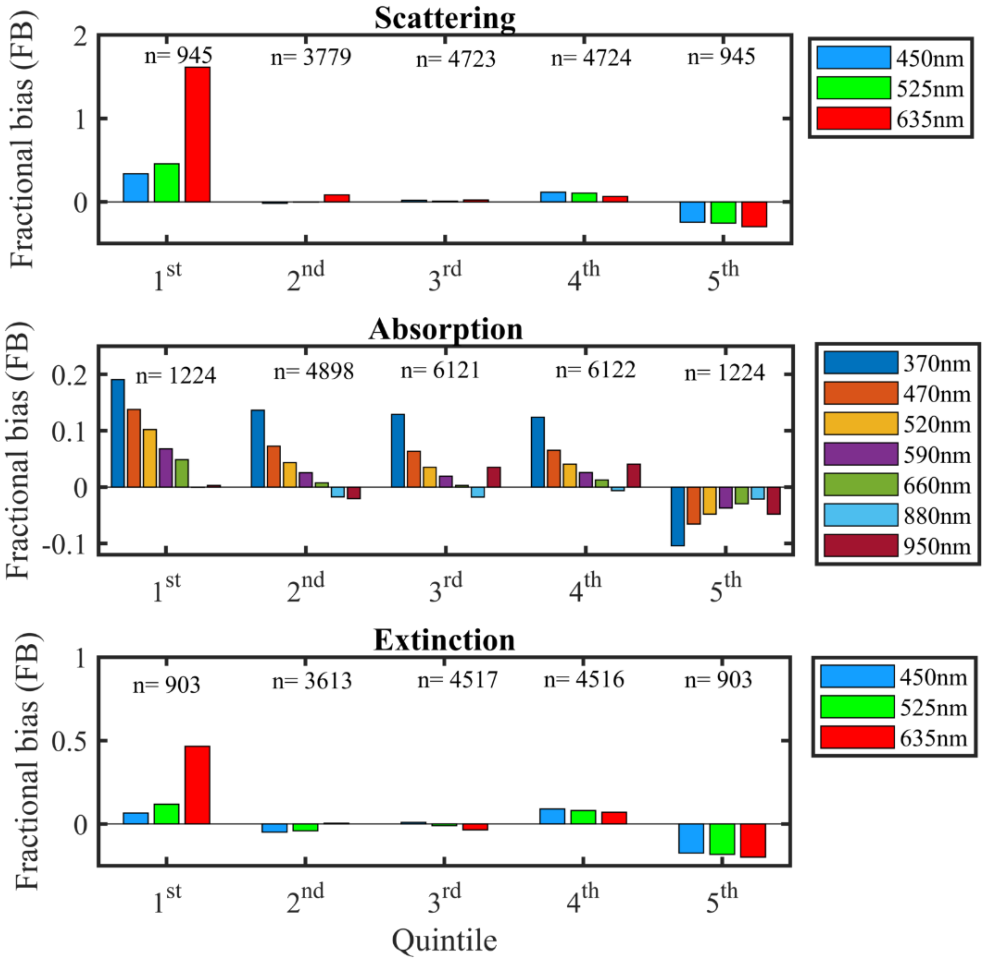

A4 - 7. Average fractional biases calculated for the observed modelled data pairs for scattering, absorption and extinction at the ATOLL platform broken down by quintiles from the lowest to highest aerosol optical coefficient values. n corresponds to the number of data points used in every quintile.

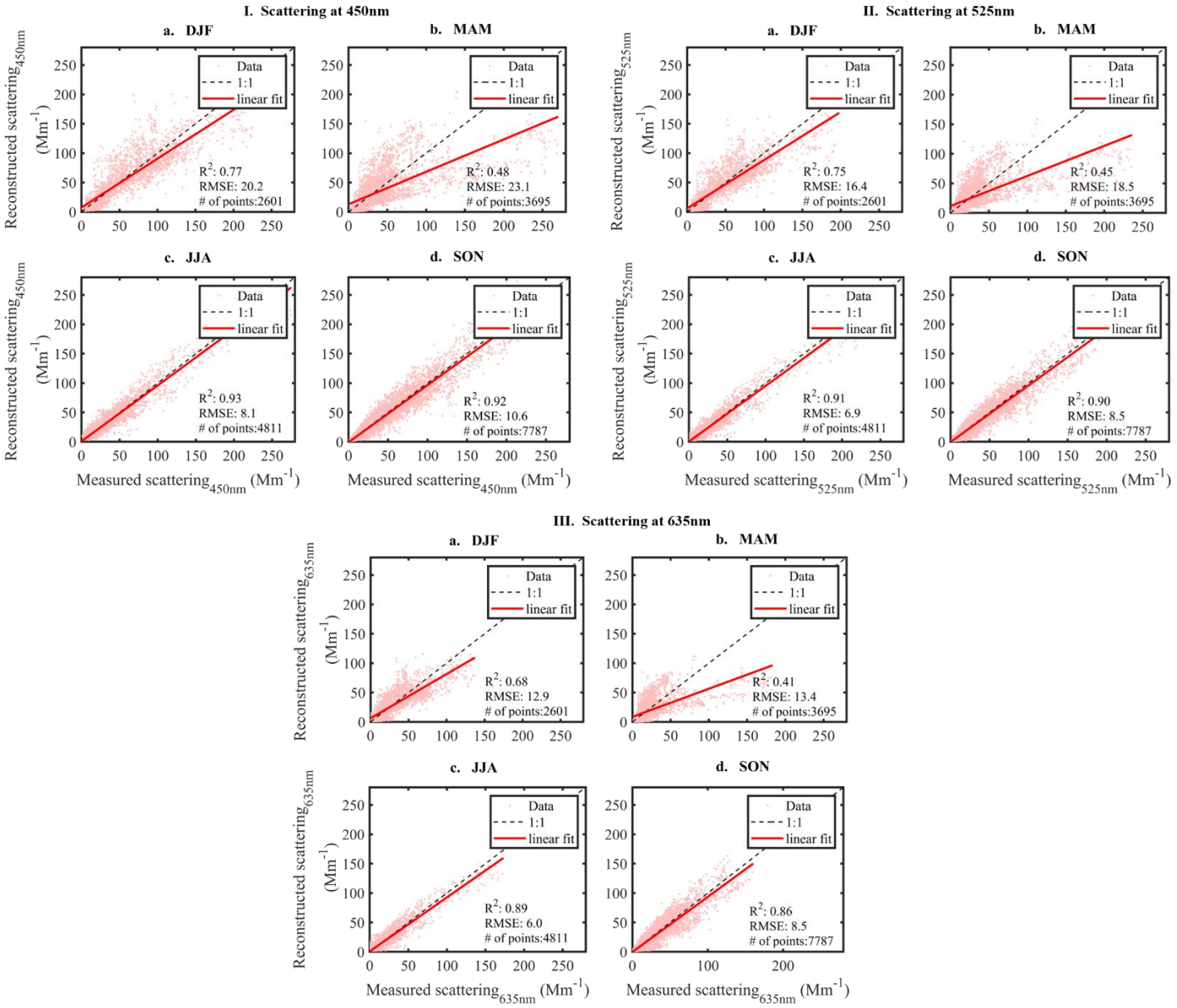

A4 - 8.Scattering reconstructed (y axis) and measured (x axis) by seasons at 450 nm (I), 525 nm (II) and 635 nm (III)

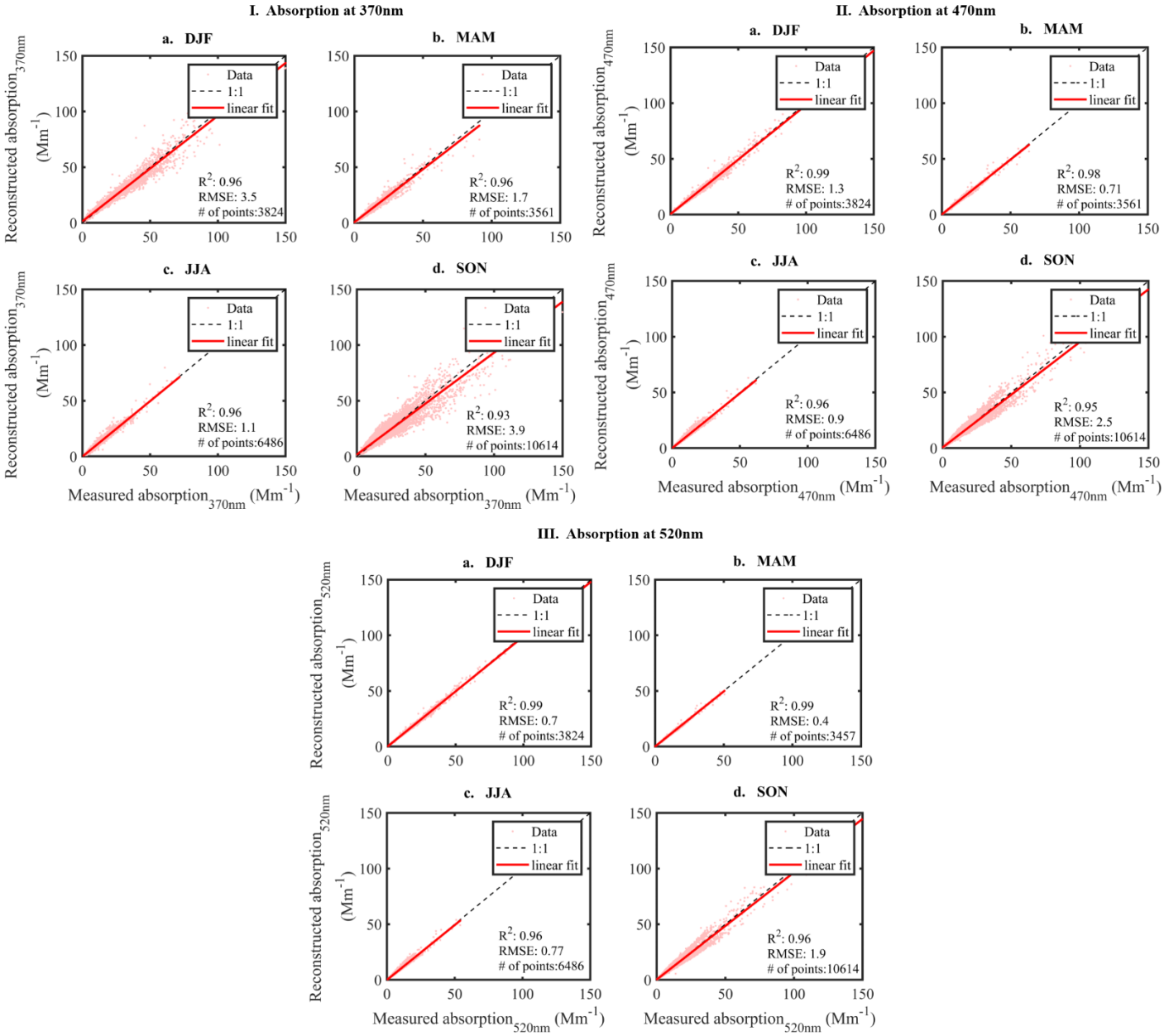

A4 - 9 Absorption reconstructed (y axis) and measured (x axis) at 370 nm (I), 470 nm (II), 520 nm (III)

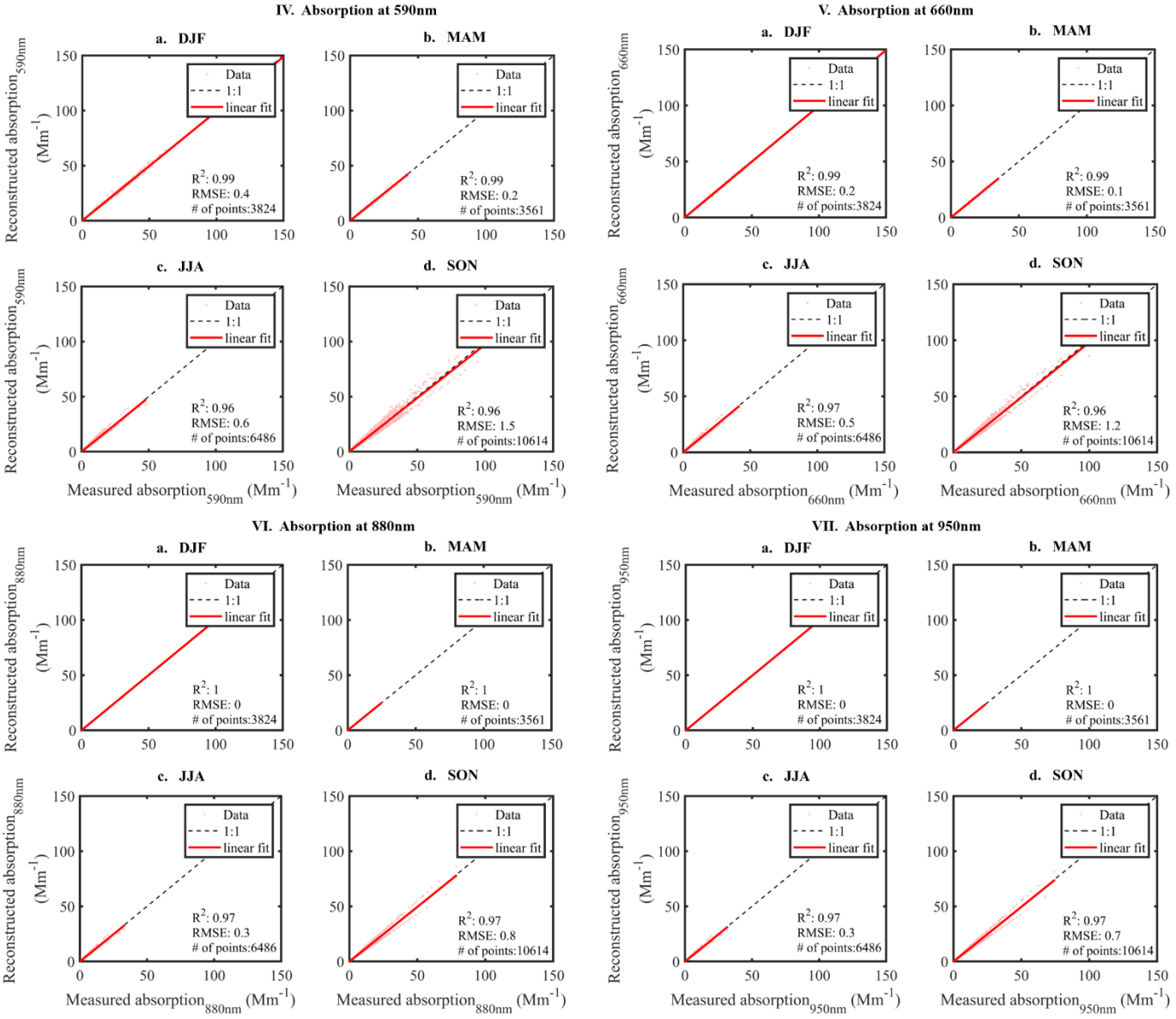

A4 - 10 Absorption reconstructed (y axis) and measured (x axis) at 590 nm (IV), 660 nm (V), 880 nm (VI) and 950 nm (VII

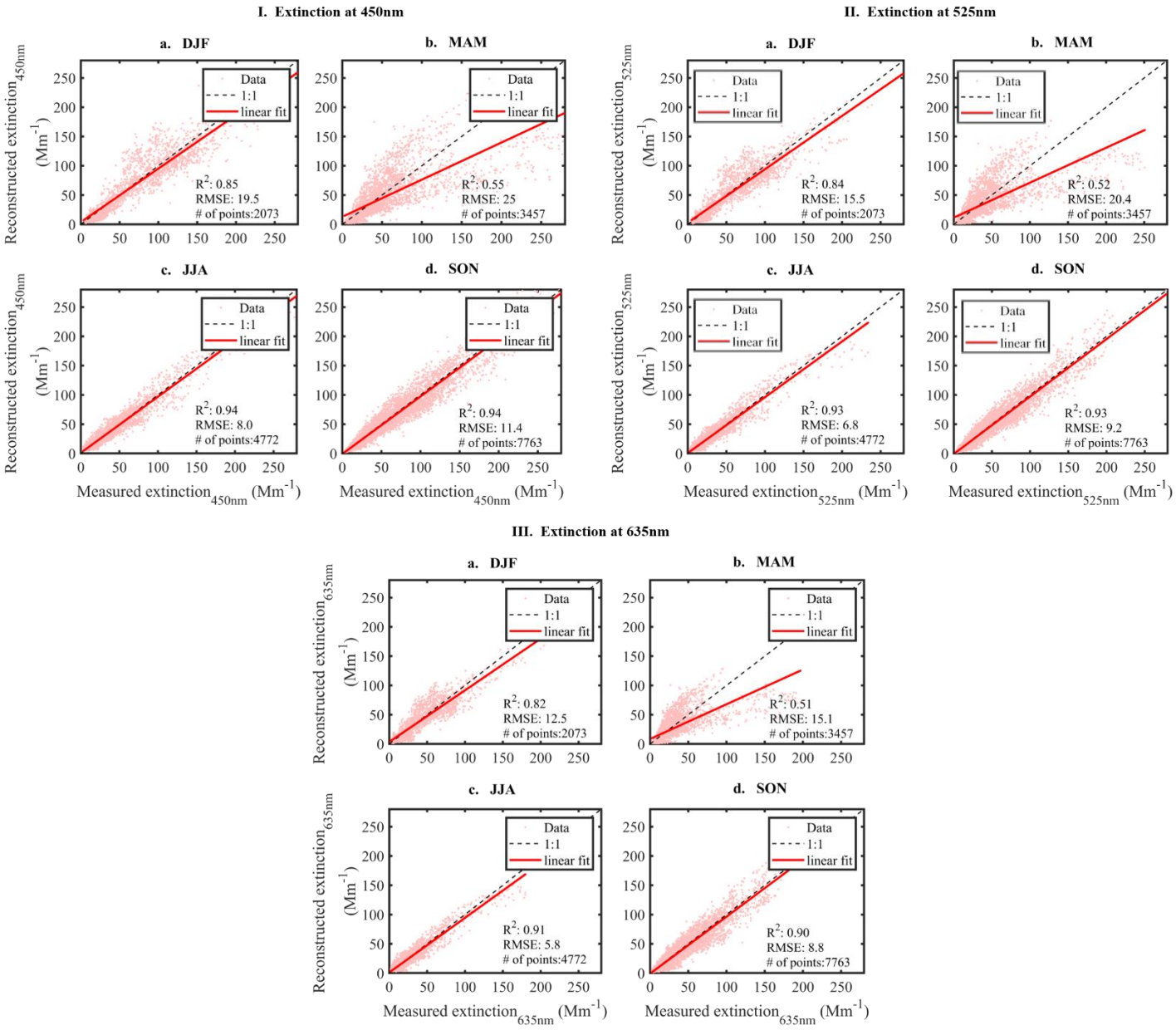

A4 - 11 Extinction reconstructed (y axis) and measured (x axis) at 450 nm (I), 525 nm (II), 635 nm (III).

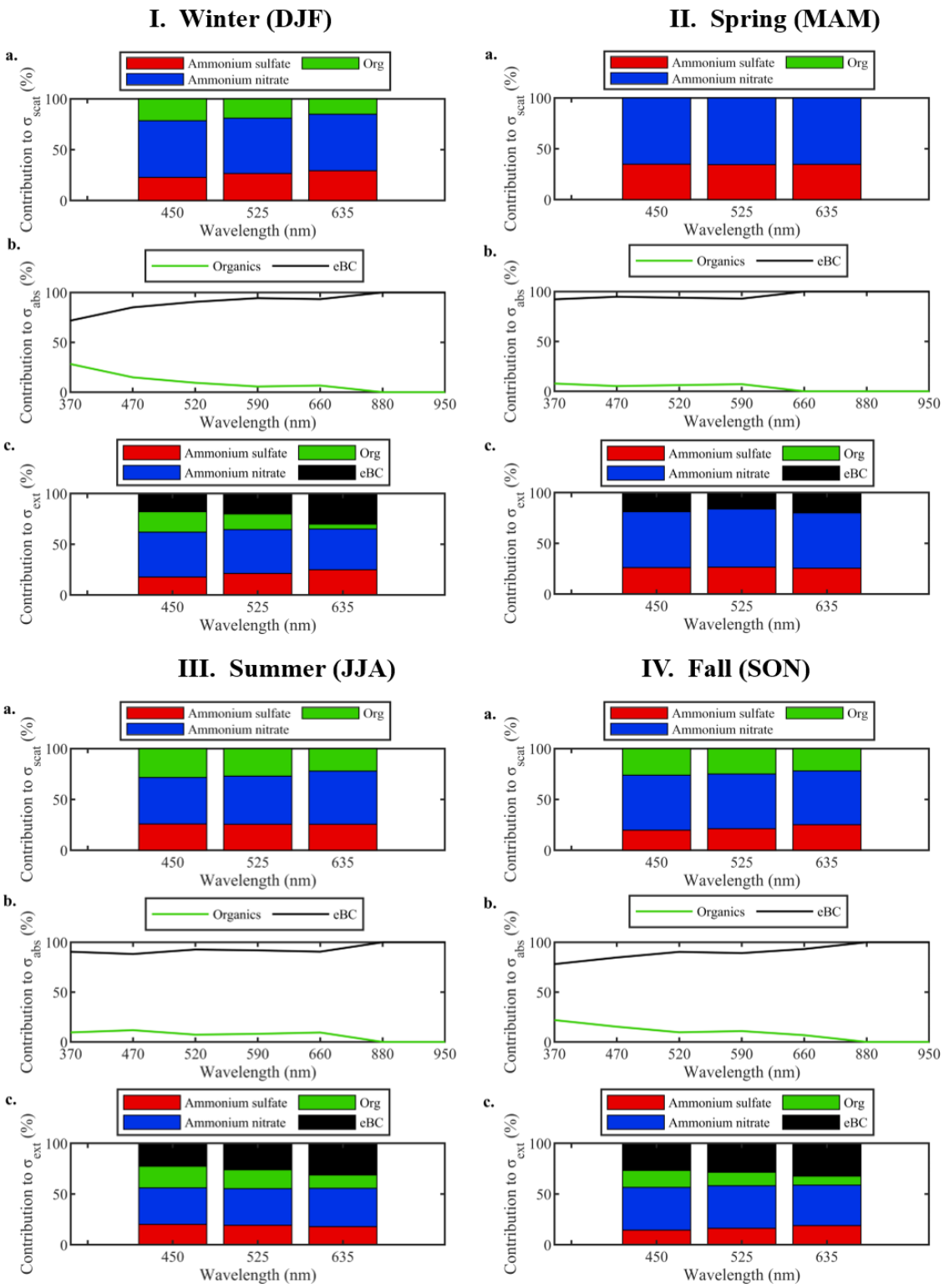

A4 - 12 Seasonal (I-winter, II- spring, II- summer IV- fall) contributions of chemical species to aerosol optical properties: scattering (a) absorption (b) and extinction (c) at all wavelengths

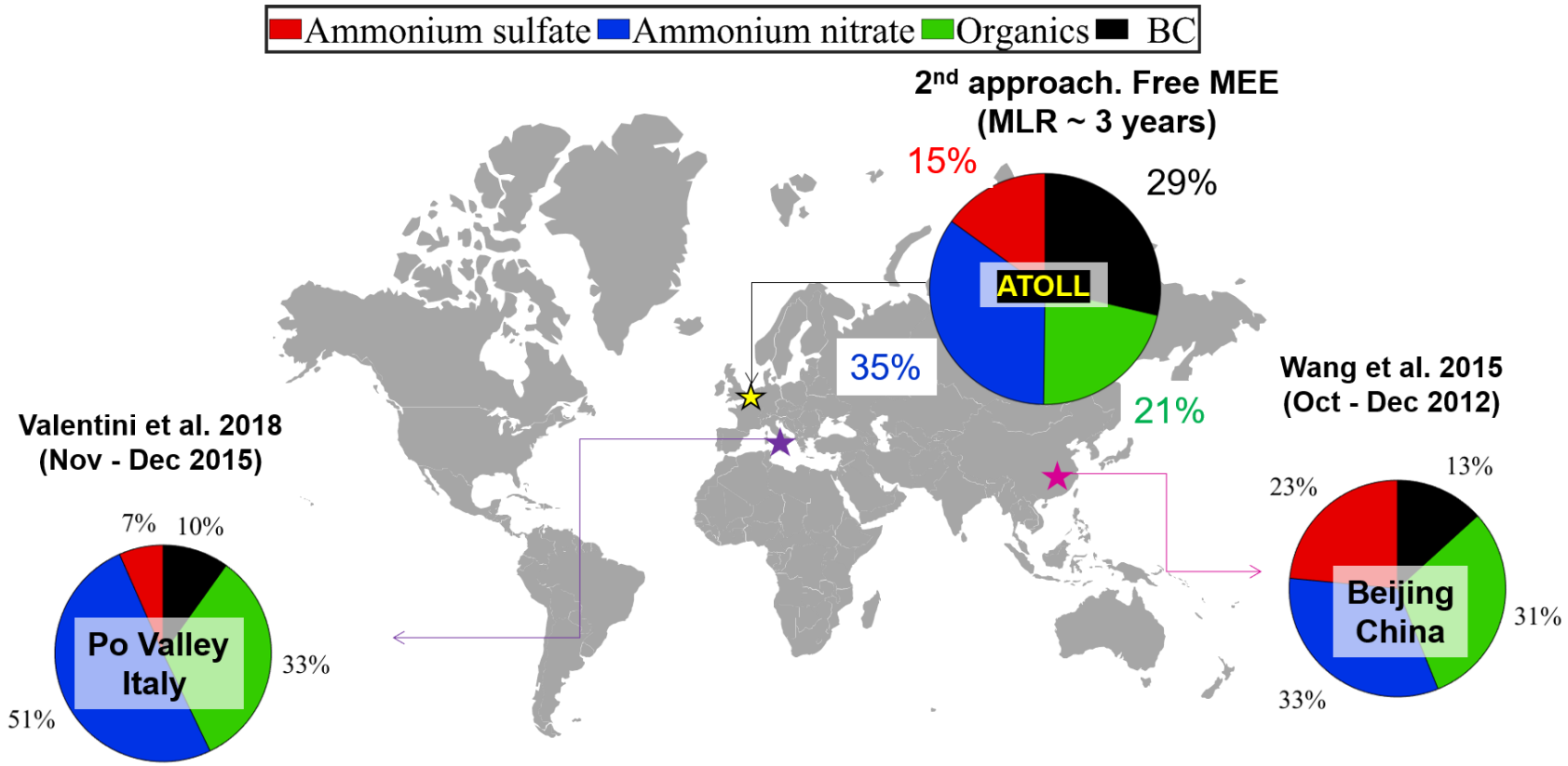

A4 - 13 Comparison of the chemical contribution to extinction in the visible range (525-550nm) at the ATOLL platform with other sites located in the Po Valley, Italy (Valentini et al. 2018) and Beijing, China (Wang et al. 2015).

Annex 3: Chapter 5

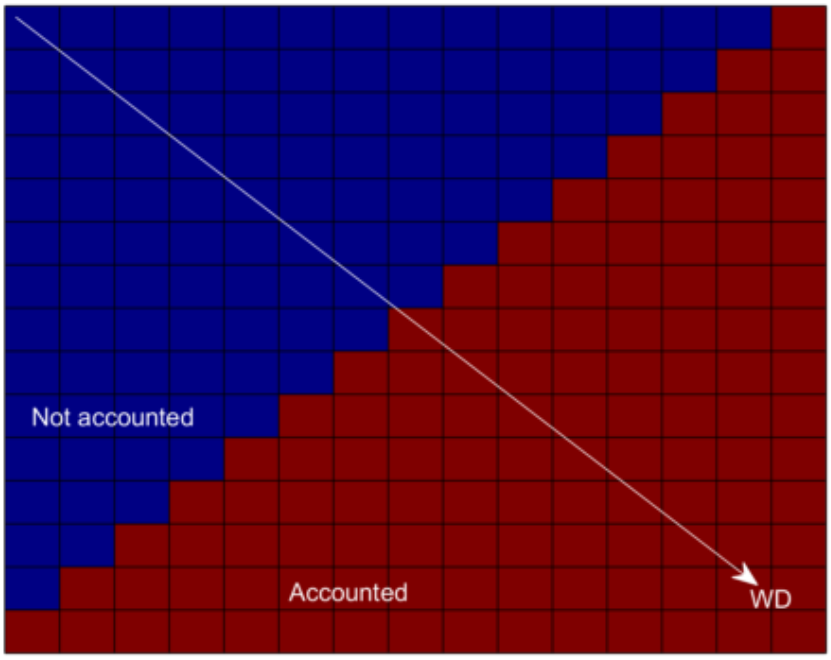

A5 - 1 Diagram of INTERPLAY. The figure represents the arrival sector drawn (arrow) in the vicinity of the ATOLL platform (red area). WD: Wind direction.

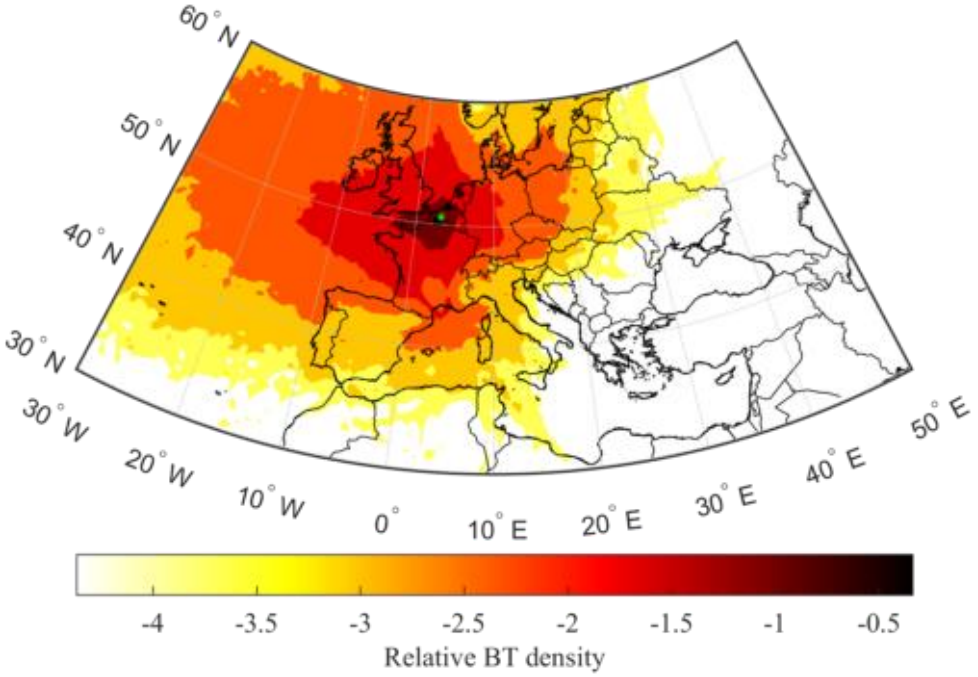

A5 - 2 HYSPLIT backward trajectory (BT) ensembles showing the large-scale trade wind circulation influence at the ATOLL platform by means of air mass residence time maps. The BT ensembles comprise all 26 808 individual BTs, spanning a multi-year time period from Dec 2016 to Dec 2019.

Top 20 cargo ports and other main cargo ports in 2017

(Gross weight of goods handled)

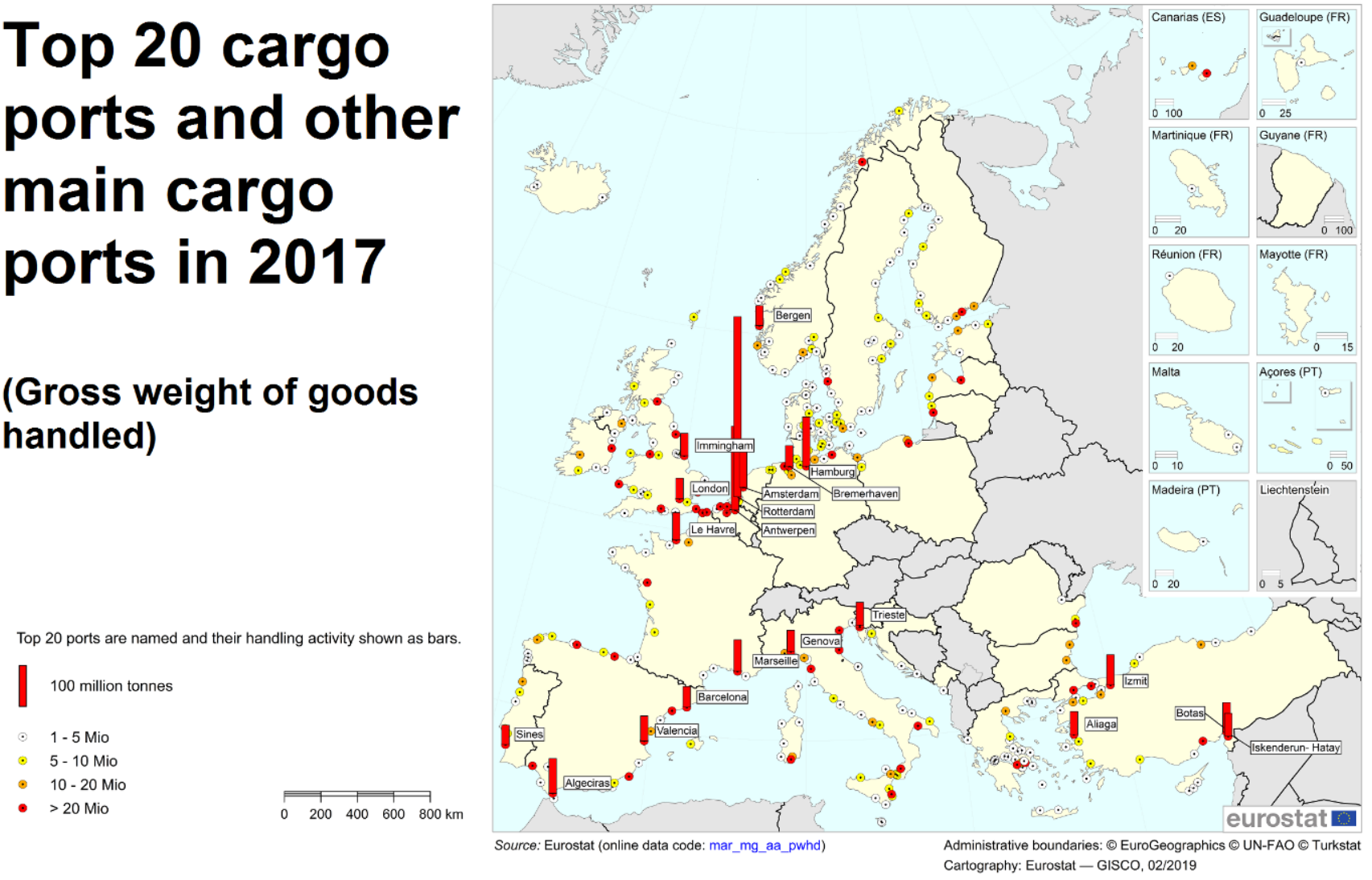

A5 - 3 Top 20 cargo ports and other main cargo ports in 2017. Soure: Eurostat 2019.

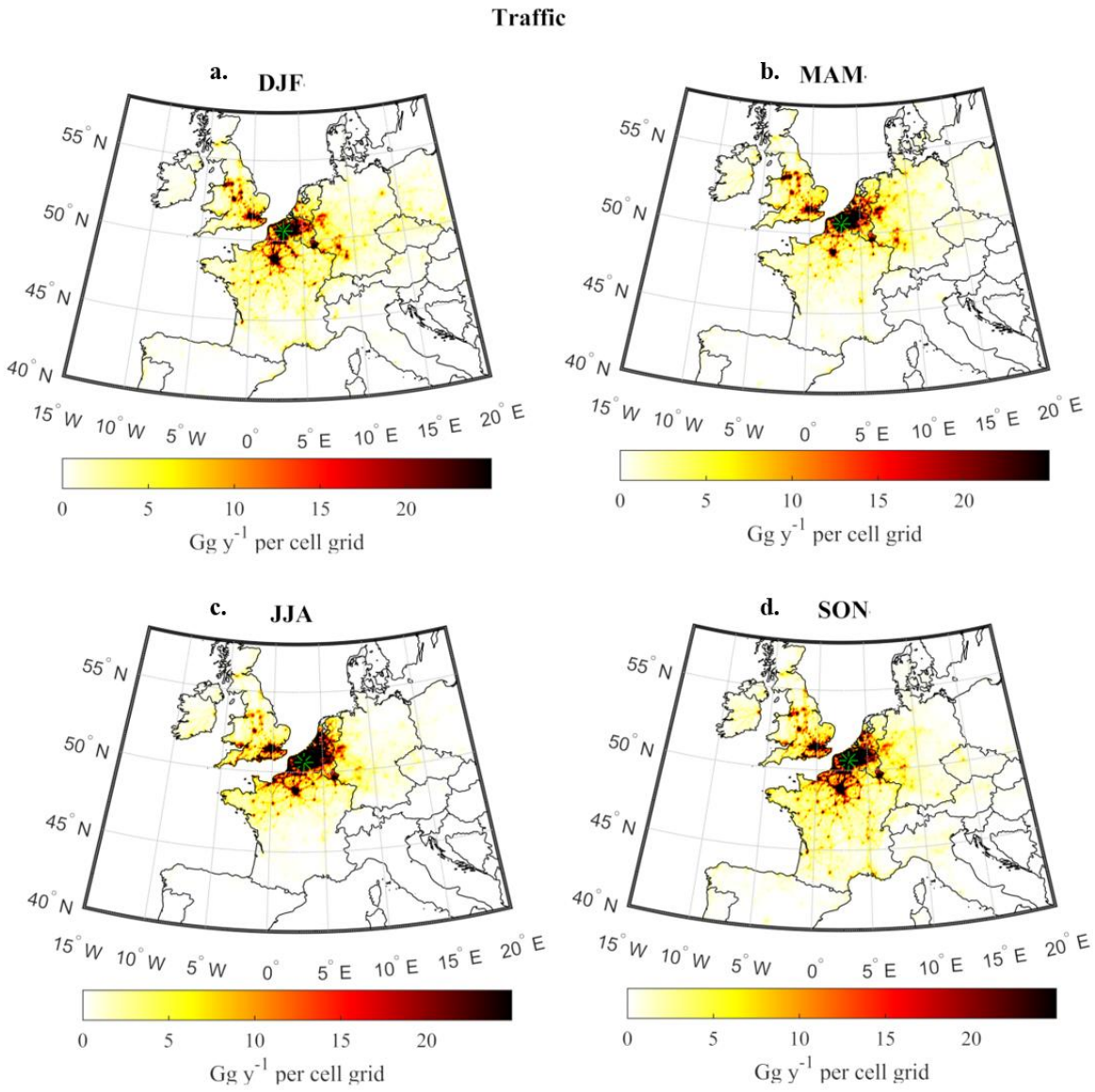

A5 - 4 Seasonal spatial allocation of BC contribution by the traffic sector at the ATOLL platform for the period Dec 2016 – Dec 2019.

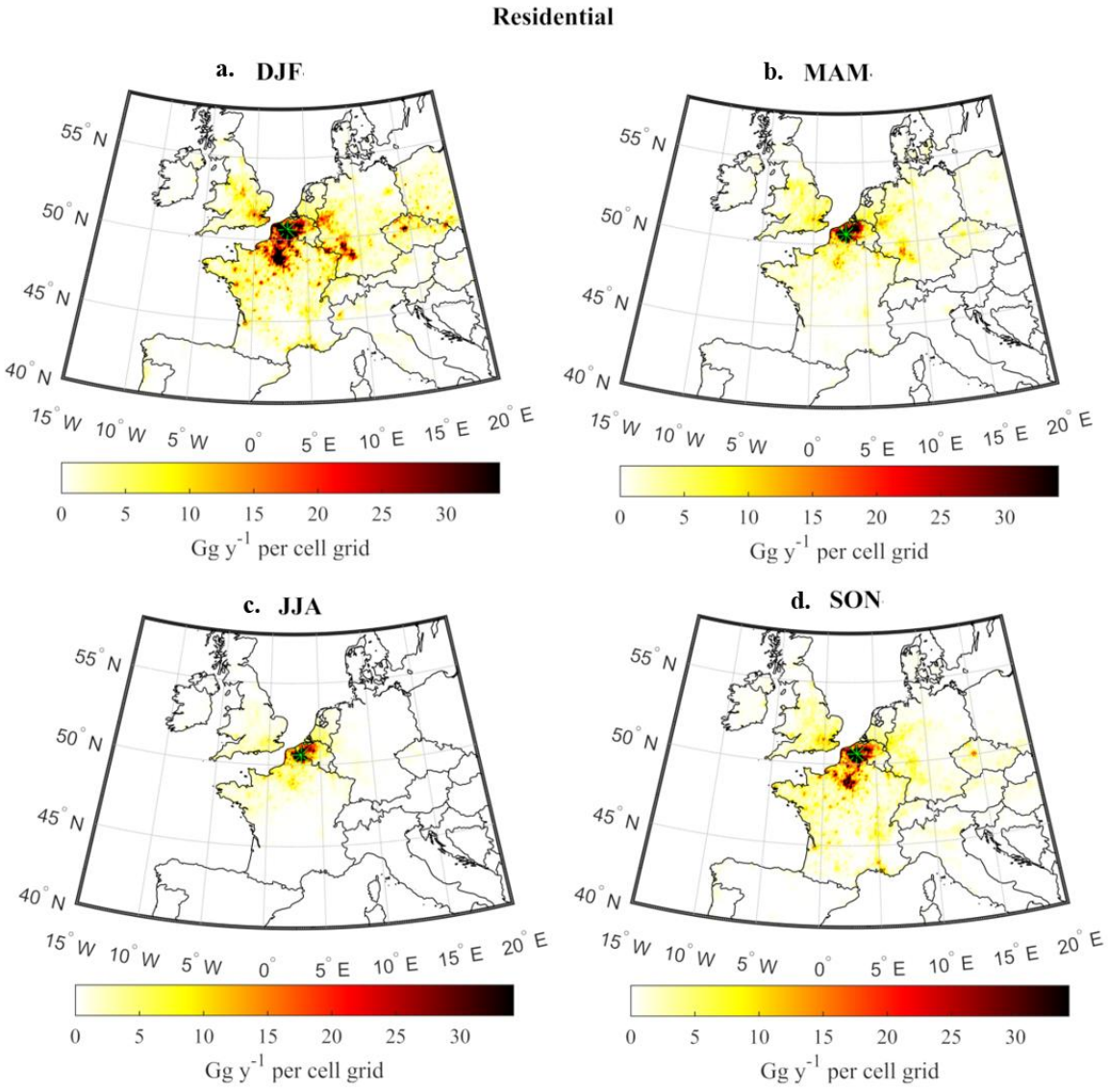

A5 - 5 Seasonal spatial allocation of BC contribution by the residential sector at the ATOLL platform for the period Dec 2016 – Dec 2019

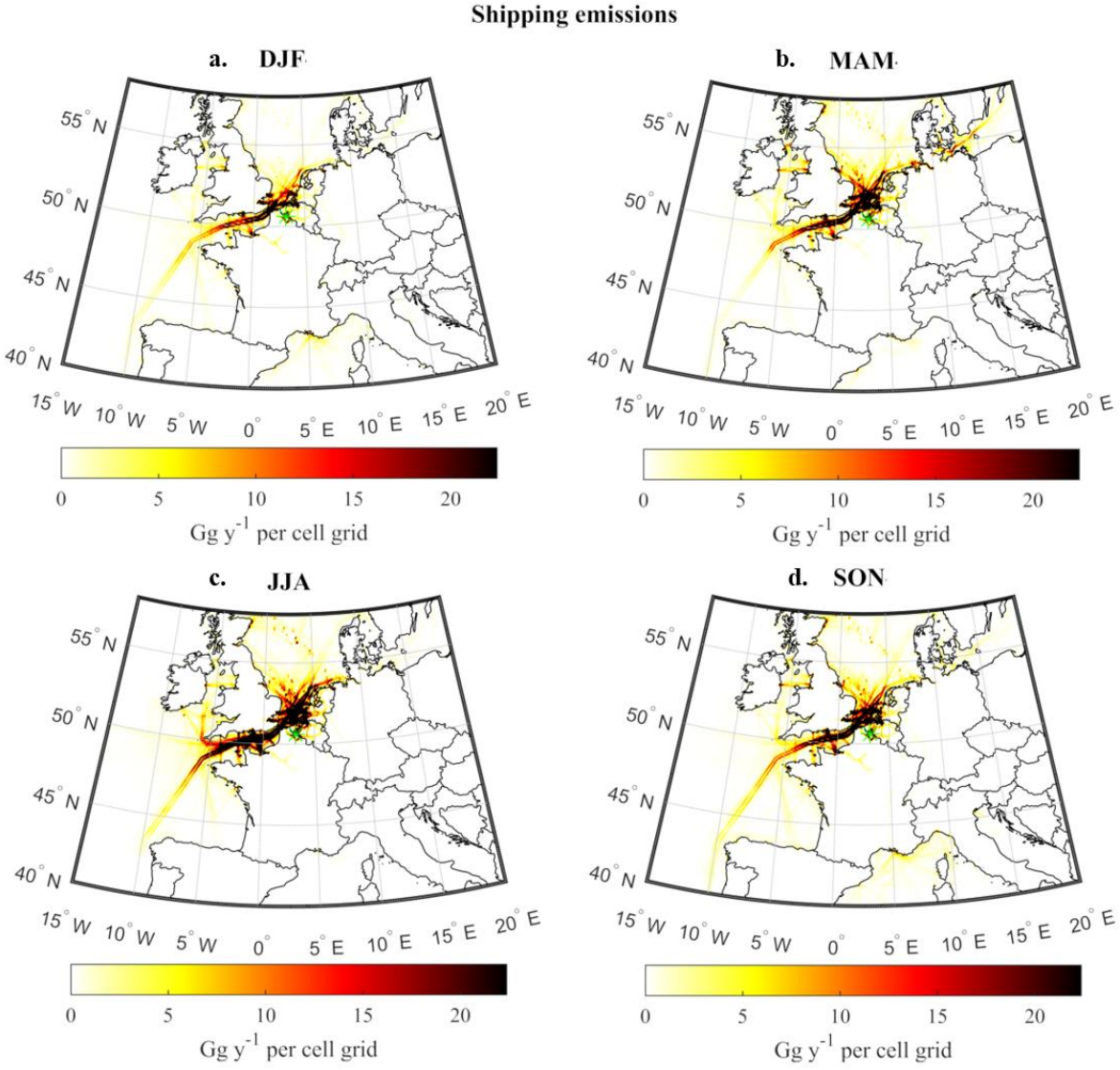

A5 - 6 Seasonal spatial allocation of BC contribution by the shipping sector at the ATOLL platform for the period Dec 2016 – Dec 2019

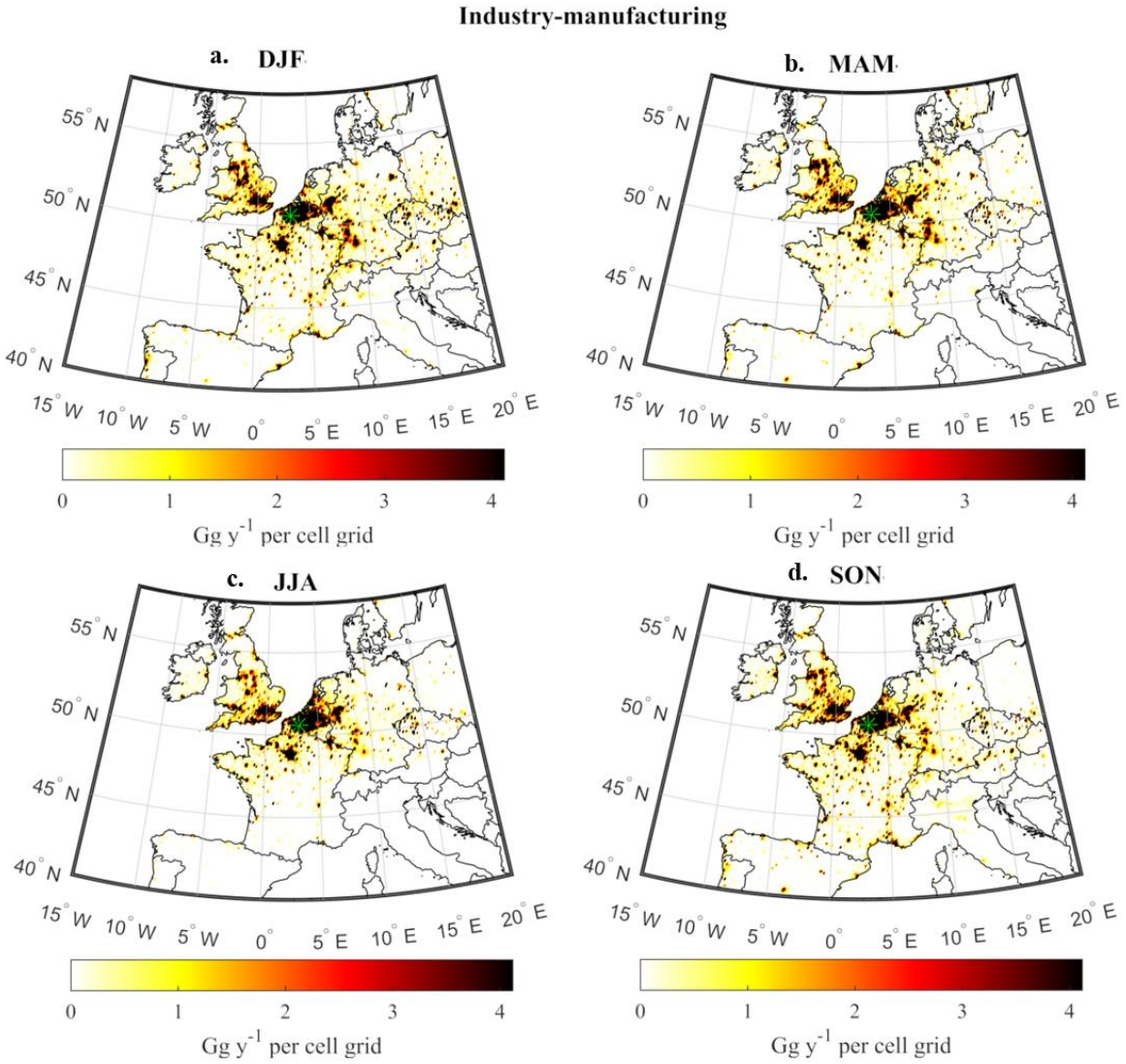

A5 - 7 Seasonal spatial allocation of BC contribution by the industry-manufacturing sector at the ATOLL platform for the period Dec 2016 – Dec 2019

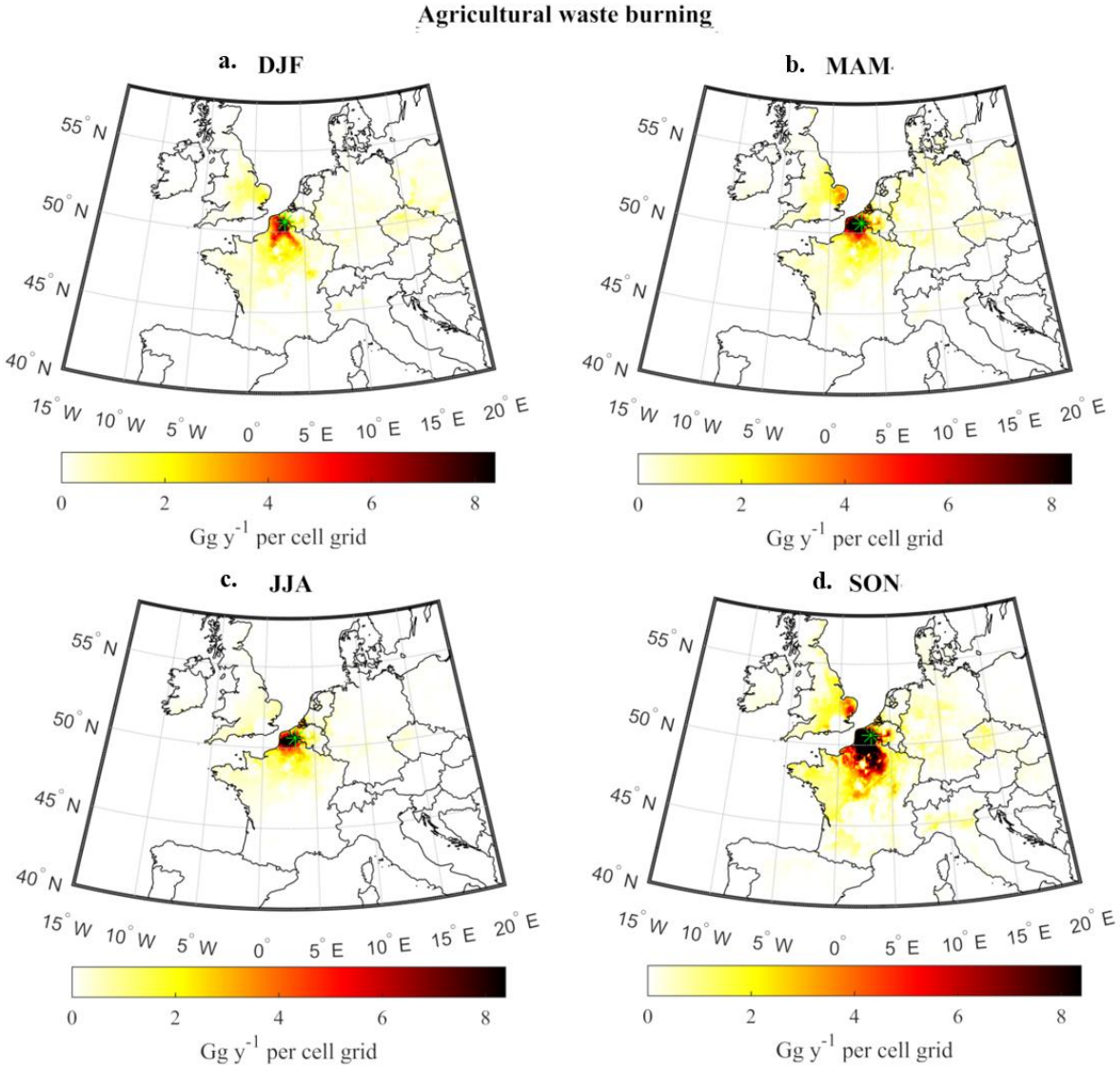

A5 - 8 Seasonal spatial allocation of BC contribution by the agricultural waste burning sector at the ATOLL platform for the period Dec 2016 – Dec 2019

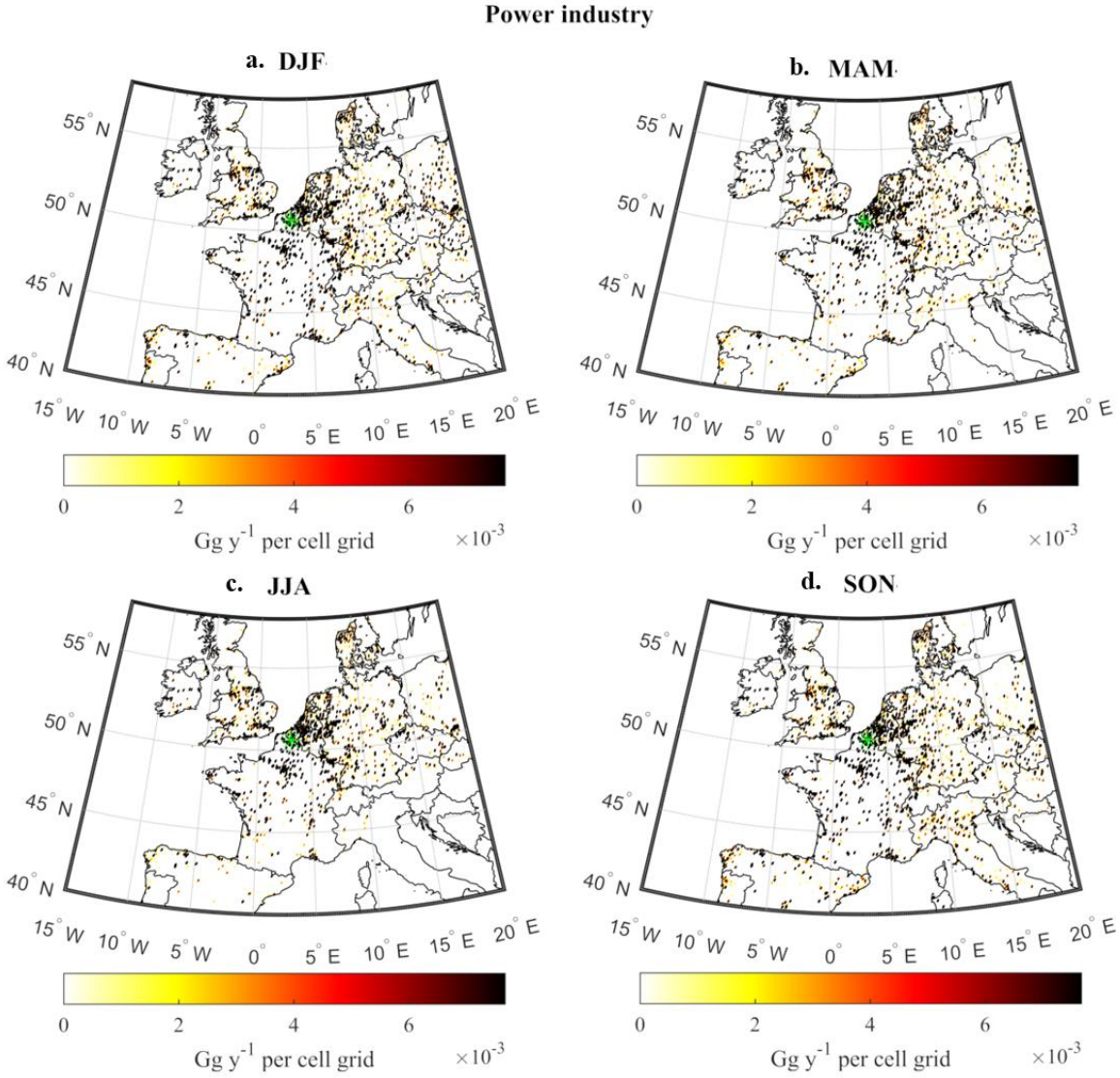

A5 - 9 Seasonal spatial allocation of BC contribution by the power industry sector at the ATOLL platform for the period Dec 2016 – Dec 2019.

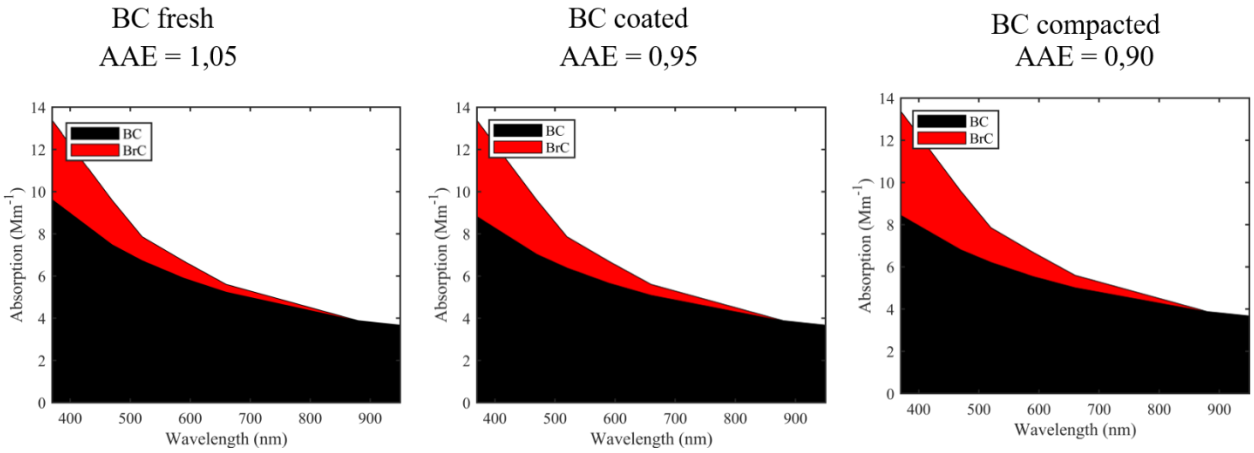

A5 - 10 Sensivity test of AAE values for BC applying values reported by Liu et al. 2018

Sources	MAE at 370 nm (m^2 g^{-1})	MAE at 470 nm (m^2 g^{-1})
Residential fresh	0.26	1.14
Residential aged	0.07	0.03
Traffic fresh	-	-
Traffic aged	0.043	0.02

A5 - 11 Mass Absorption Efficiency retrieved with an MLR

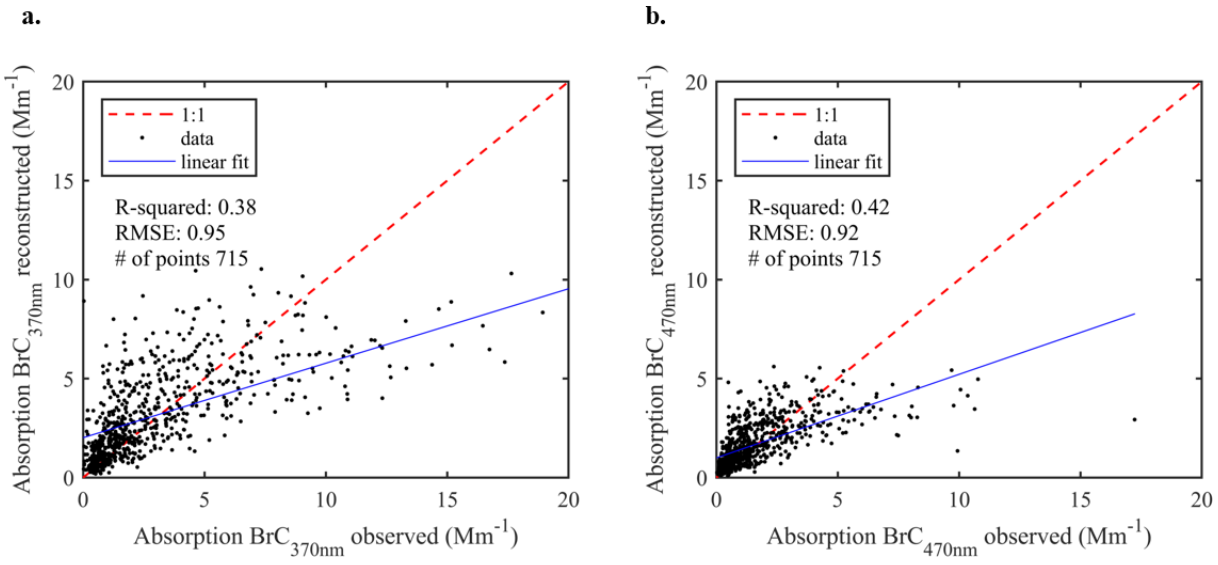

A5 - 12 Linear fit of Brown Carbon retrieved through MLR
at 370 nm (a) and 470 nm (b) vs Brown carbon observed by the aethalometer.